POLITECNICO DI MILANO

School of Civil, Environmental and Land Management Engineering

Master of Science in **Civil Engineering**

–

School of Industrial and Information Engineering

Master of Science in **Mathematical Engineering**

ON CARDIOVASCULAR MODELING, BALLISTOCARDIOGRAPHIC ANALYSIS AND BED SENSORING

Advisor: Prof. Engr. **Riccardo Sacco**
Dept. of Mathematics, Politecnico di Milano.

co-Advisor: Prof. Engr. **Giovanna Guidoboni**
Dept. of Mathematics, University of Missouri, USA.

MASTER OF SCIENCE THESIS

Raul Invernizzi - 899208

- ACADEMIC YEAR 2020/2021 -

Special thanks

Alla **mia famiglia** che mi ha sempre supportato e sopportato durante tutto il mio percorso universitario.

Ringrazio tutti i miei **compagni di percorso al Poli**.
In particolare, quelli più storici e duraturi: Bao e Giulietta.

Ringrazio **Marta**, piacevole scoperta accessoria durante la mia permanenza negli USA, che è poi divenuta la mia quotidianità.

Ringrazio il **prof. Sacco**, per aver accettato di farmi da relatore ed avermi fatto da perfetto caronte fra le due diverse ingegnerie.

Ringrazio la **professoressa Guidoboni** per la meravigliosa esperienza che mi ha permesso di vivere negli USA.

Infine, ringrazio la mia stessa indole che mi ha permesso di non cedere mai nonostante le numerose difficoltà incontrate lungo il percorso, alzando pure la posta tentando (e terminando con successo) questo doppio titolo magistrale.

Grazie a tutti!

Sintesi

Questo documento rappresenta la *Tesi di laurea specialistica* dell'autore, atta a conseguire il Doppio Titolo di Laurea Magistrale in *Ingegneria Civile* e in *Ingegneria Matematica* presso il Politecnico di Milano.

Il lavoro riportato in questa tesi deriva da un'esperienza lavorativa fatta all'estero dall'autore come *visiting scholar researcher* presso i laboratori di Ingegneria Elettrica e Informatica dell'Università del Missouri (Columbia, USA), durante il semestre primaverile dell'anno accademico 2018-2019.

L'elaborato è diviso in due parti principali contenenti, rispettivamente, tre e due capitoli. Tutti i capitoli riguardano essenzialmente la modellizzazione cardiovascolare, l'analisi ballistocardiografica e la misurazione sperimentale di quest'ultima utilizzando sensori applicati ad un letto. In particolare, la prima parte introduce la teoria, le tecniche di modellazione e illustra il modello matematico considerato. La seconda parte riguarda invece le misure sperimentali, sviluppate ed acquisite durante lo svolgimento di questa tesi e utilizzate per ottenere quantità che sono state successivamente confrontate con quelle ottenute dal modello virtuale.

Nel **primo capitolo** viene brevemente introdotta l'analogia fluido-elettrica, attraverso la quale i vasi sanguigni possono essere modellati come *resistori*, degli *induttori* possono essere utilizzati per includere gli effetti inerziali del fluido nei vasi e dei *condensatori* simulano l'effetto della dilatazione dei vasi.

Nel **secondo capitolo**, che rappresenta il centro del lavoro, l'attenzione è focalizzata su come modellare dettagliatamente un sistema cardiovascolare. Sfruttando l'analogia richiamata nel primo capitolo, viene preso come riferimento un modello della letteratura e vengono fatte *analisi incrementali* e di causa-effetto su di esso. Si studiano modelli più semplici comparandoli ai risultati del modello di riferimento così da capire se tutte le parti descritte da quest'ultimo servono e in che misura modificano i risultati.

Nel **terzo capitolo**, viene eseguita un'*analisi di sensitività* del modello proposto. Questo viene fatto approssimando il modello reale attraverso un meta-modello basato sulla

polynomial chaos expansion grazie al quale vengono poi valutati gli *indici di Sobol* delle variabili di input considerate, capendo quindi il contributo che generano nell'output.

Nel **quarto capitolo**, il primo della seconda parte, l'accuratezza del modello matematico viene verificata rispetto a *misurazioni sperimentali*. Si definisce nel dettaglio la procedura seguita dall'autore per acquisite queste misure, attraverso l'uso di celle di carico, e si analizza il modo utilizzato per convalidare il modello di riferimento.

Nel **quinto capitolo**, infine, viene analizzato l'effetto della presenza di un materasso sul letto. Vengono in particolare riportate misurazioni di parametri fisici di alcuni materassi, ottenute dall'autore, con l'obiettivo in futuro di sviluppare un protocollo di misurazione e di testing più preciso che consideri anche l'influenza del materasso.

Contributi dell'autore

Il primo capitolo si rifà alla letteratura. Nel secondo capitolo l'autore considera un modello matematico presente in letteratura ma ne estende fortemente le possibilità di comprensione e simulazione (vedi ad esempio BCGz, a pagina 46, le analisi incrementali della Sezione 2.3 e le considerazioni sul filtering della Sezione 2.5.1). Nel terzo capitolo, l'autore si avvale di avanzate tecniche di analisi della sensitività per svolgere ulteriori analisi sul modello di riferimento mai svolte in precedenza.

La quarta e la quinta parte rappresentano, invece, una completa novità sperimentale nel campo, poiché facendo uso di misure in laboratorio, ideate ed ottenute direttamente dall'autore, viene presentata e discussa una validazione del modello di riferimento e infine viene riportata la stima di alcuni parametri meccanici legati ai materassi, col fine di aiutare i futuri sviluppi nel settore.
Quest'ultima parte di tesi è già stata inoltre pubblicata dall'autore, insieme ad altri, in forma di capitolo in un libro scientifico edito dalla Springer. (R. Invernizzi, 2021)

Parole chiave

Ballistocardiogramma; Ballistocardiografia; BCG; BCGz; Modellazione cardiovascolare; Modellazione fisiologica; Arterie; Vasi sanguigni; Sensori per letto; Cuore; Salute cardiovascolare; Malattie cardiovascolari; Celle di carico; Analisi di sensitività; Indici di Sobol; Polynomial Chaos Expansion (PCE); Monitoraggio cardiaco; Materasso;

Abstract

This document is the author's *second-level degree thesis* for the achievement of the Double Master of Science degree in *Civil Engineering* and in *Mathematical Engineering* at the Politecnico di Milano.

The material reported in this thesis is the result of a work experience made by the author as a *visiting scholar researcher* at the laboratories of the Electrical Engineering & Computer Science of the University of Missouri (Columbia, USA), during the spring semester of the 2018-2019 academic year.

The work is divided in two main parts, containing three and two chapters, respectively. All the chapters essentially concern the cardiovascular modeling, the ballistocardiography analysis and the experimental measurement of the latter by using bed sensors. In particular, the first part introduces the theory, the modeling techniques and illustrates a mathematical model taken as a reference. The second part, instead, concerns the experimental measurements, developed and acquired during the carrying out of this thesis, and used to obtain quantities which were subsequently compared with those obtained from the virtual model.

In the **first chapter** the **electric analogy to fluid flow** is briefly introduced, in the analogy, blood vessels can be modeled as resistors, inductors can be used to include inertial effects of the fluid, and capacitors simulate the dilatation effect of the vessel's walls.

In the **second chapter**, which represents the core of the work, the focus is on **how to model a detailed cardiovascular system**. By exploiting the analysis recalled in the first chapter, a model from the literature is taken as a reference and incremental and cause-effect analyzes are carried out on it. Simpler models are studied and compared to the reference model in order to understand if all the parts described by the latter are needed and to what extent they modify the results.

In the **third chapter**, a **sensitivity analysis** of the proposed model is performed. This is done by approximating the model through a forefront meta-model based on poly-

nomial chaos expansion thanks to which the Sobol indices of the input variables considered are then evaluated, leading to the understanding of the contribution they generate in the output.

In the **fourth chapter**, the first of the second part, the accuracy of the analyzed mathematical model is **verified with respect to experimental measurements**. Taken directly by the author through the use of load cells, these measures are then used to validate the model.

In the **fifth chapter**, finally, the effect of the presence of a mattress on the bed is analyzed. Measurements of physical parameters of some mattresses, obtained by the author, are reported with the aim in the future of developing a more precise measurement and testing protocol that also considers the influence of the mattress.

Author's contributions

The first chapter recalls the needed literature. In the second chapter the author considers a published model and greatly extends its understanding and simulation possibilities (see e.g. BCGz, at page 48, build-up analysis of Section 2.3, filtering considerations of Section 2.4.1). In the third chapter, the author makes use of advanced sensitivity analysis techniques to improve the comprehension of the reference model.

The fourth and fifth parts, instead, represent a complete experimental novelty in the field. By making use of in-lab measures, conceived and obtained directly by the author, a validation of the reference model is presented and discussed. finally, the estimate of some mechanical parameters related to the mattresses is reported, in order to help future developments in the sector.

This last part of the thesis has also already been published by the author, together with others, in the form of a chapter in a scientific book published by Springer. (R. Invernizzi, 2021)

Keywords

Ballistocardiogram; Ballistocardiography; BCG; BCGz; Cardiovascular modeling; Physiological modeling; Arteries; Blood vessels; Bed sensors; Heart; Cardiovascular health; Cardiovascular diseases; Load cells; Sensitivity analysis; Sobol indices; Polynomial Chaos Expansion (PCE); Heart monitoring; Mattress.

Index

ON CARDIOVASCULAR MODELING, BALLISTOCARDIOGRAPHIC ANALYSIS AND BED SENSORING

Figures and tables index

Figures index

X

Tables index

Introduction

The context

Cardiovascular diseases (CVDs) represent the **first leading cause of death** world-wide[1]. Of the 56.9 million deaths worldwide in 2016, ischemic heart disease and stroke are the world's biggest killers, accounting for a combined **15.2 million deaths** in 2016. These diseases have remained the leading causes of death globally in the last 15 years.
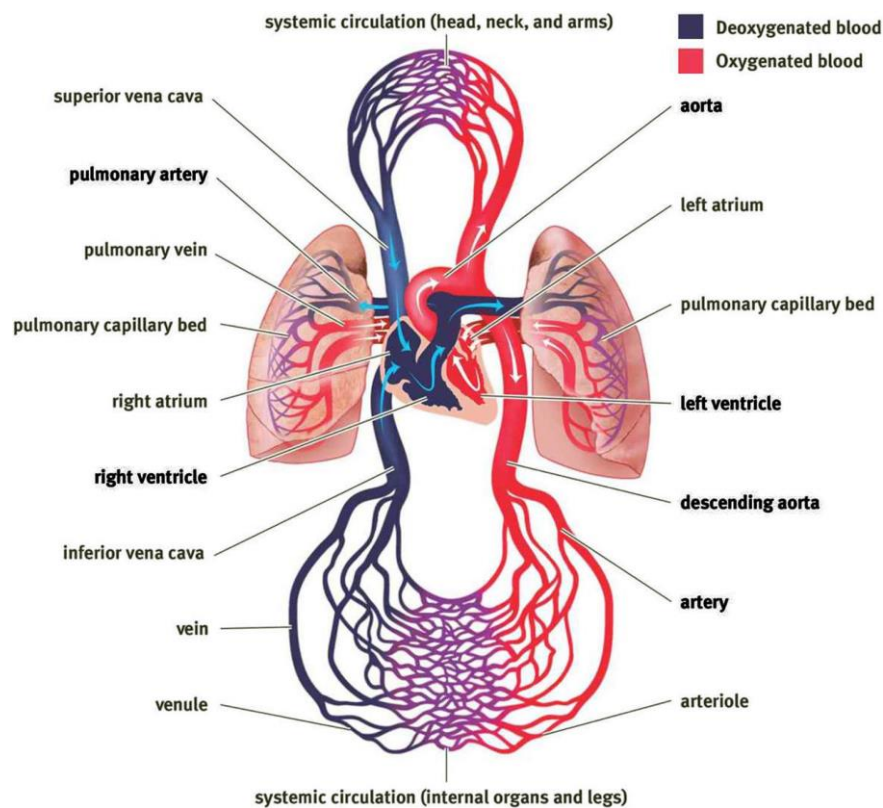
Figure 0.1 – General scheme of the human cardiovascular system.
(Adapted from The Princeton Review's MCAT® Biology Review)

---

[1] World Health Organization. 2018. The top 10 causes of death. (2018).
https://www.who.int/news-room/fact-sheets/detail/the-top-10-causes-of-death
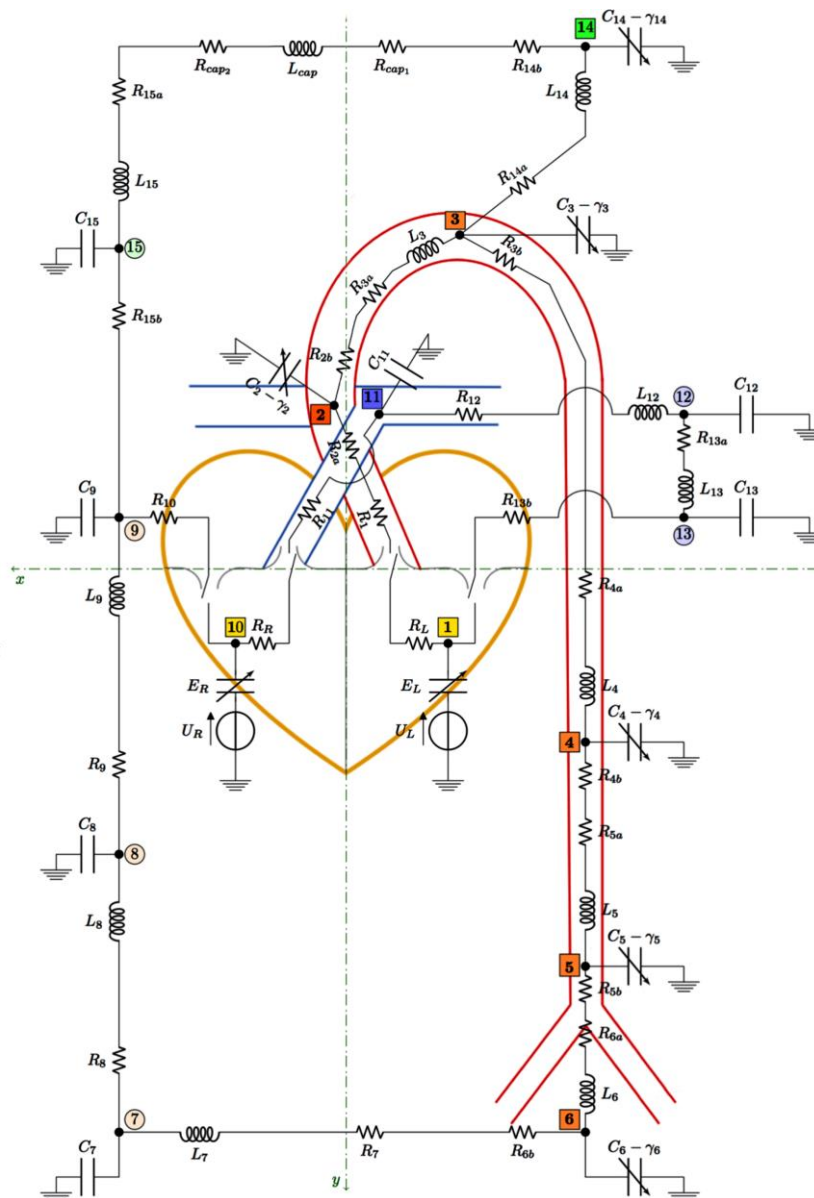
Figure 0.2 – Schematic representation of the closed-loop model describing the flow of blood through the circulatory system. The model leverages the electric analogy to fluid flow, where resistors, capacitors and inductors represent hydraulic resistance, compliance and inertial effects, respectively. (Guidoboni, et al., 2019)

Progression of a patient's CVD is often gradual and subtle. **Early detection of CVD progression is crucial** to intervene effectively, optimize a patient's treatment and mitigate negative outcomes. A noncontact approach to monitor cardiovascular health is offered by ballistocardiography, whose signal, the **ballistocardiogram (BCG)**, captures the repetitive motion of the center of mass of the human body resulting from

the blood motion within the circulatory system. Interestingly, BCG-based monitoring of CVD does not require body contact and <u>the signal can reflect the status of the whole cardiovascular system</u>.

A variety of different sensors has been developed to capture the BCG; several are now available commercially. BCG sensors are often utilized to monitor heart rate, respiration rate and other parameters for tracking sleep quality. **The morphology of BCG waveforms has also been studied for the purpose of tracking changes in cardiovascular health, such as changes in blood pressure and heart function**.

A quantitative approach to interpret BCG waveforms on the basis of fundamental mechanisms in cardiovascular physiology has been developed recently in (Guidoboni, et al., 2019). The approach relies on a **closed-loop mathematical model** of the cardiovascular system including 4 main interconnected compartments representing the heart, the systemic circulation, the pulmonary circulation and the cerebral circulation, see Figure 0.2.

Results obtained through virtual models simulations can be used as a theoretical guide to optimize BCG sensors and/or select the sensing technology that is best suited to detect BCG changes associated with a specific condition.

The work done

In this master thesis work, a closed-loop mathematical model is taken as a reference and a detailed analysis of each part of the model is presented and discussed.

The capability of the model is verified with experimental measures in the head-to-toe direction, computing the so-called BCGy signal. Then, given new experimental results obtained by the author, a newly ballistocardiography computation in the *z* direction is proposed and implemented. The obtained results are then compared to in-lab measurements of the BCGz through the use of load cells positioned under a bed as done for the BCGy.

A build-up analysis tries to assess the cause-to-effect relations of the various parts of the closed-loop model with respect to the ballistocardiogram plot and to some considered physiological quantities. The role of the activation function, the function describing the heart pumping action, is investigated along with the role of arterial viscoelasticity into the model. With respect to this latter issue, a comparison between

different signal filtering and smoothing techniques is performed, and an original standardized filtering protocol, is proposed.
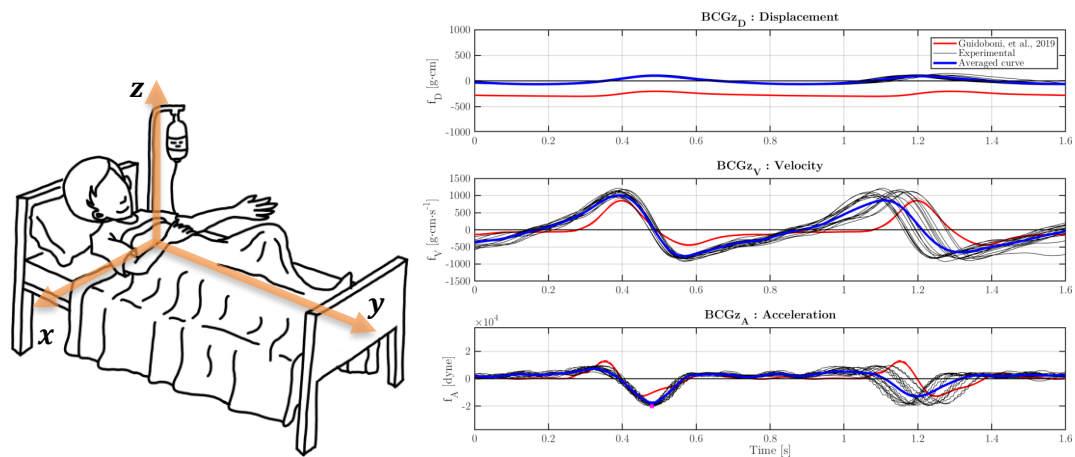
Figure 0.3 – Ballistocardiogram reference axis and BCGz curves.

A full chapter is devoted to the theory of sensitivity analysis; after an extensive theoretical introduction clarifying all the aspects involved in this study, a sensitivity and uncertainty analysis is performed over specific input parameters of the referenced model.

In the last part, the interaction between mattress and measurements is discussed. Measurements of mechanical parameters of different mattresses are reported aiming to future developments on this research direction.

Practical and social utility of the research

The main purpose of this line of research is to develop a standardized methodology and related technology, which will enable to measure, with a non-direct-contact device, someone's body natural vibrations. These measures are a mean to assess the cardiovascular health state of the subject, preventing the sudden onset of cardiovascular diseases and thus making this research have the potential of saving many lives.

The problems and results discussed in this thesis are particularly relevant for situations where a patient's cardiovascular disease must be monitored accurately but limiting the contact with the patient's body. In fact, by using load cells as experimented

in this work, an instrumented bed can be used for health monitoring without negatively affecting the patient's life.

Using load cell technology together with the developed algorithms allows us to capture body signals which, if compared with the signals predicted by the mathematical model, permits to assess the patient's cardiovascular health state in a new reliable way.

This non-invasive method can be utilized in a hospital monitoring environment, deployed on hospitalized beds, but also in a home setting, mounted in people's own beds, or, extending the possibilities for easy monitoring in everyday life, even in chairs or armchairs.

This technology promises to be of extraordinary value and it is ensured that this will have a decisive role in a future in which deaths from cardiovascular diseases are significantly reduced thanks to the constant unobtrusive monitoring of the state of the cardiovascular system of every human being.

PART I :

CARDIOVASCULAR MODELING

1 – ELECTRIC ANALOGY TO FLUID FLOW

In this chapter a connection is drawn between fluid and electric variables, describing the *hydraulic meaning* of **passive electric elements** such as resistors, capacitors and inductors, as well as **active electric elements** such as independent sources of current and voltage.

In order to simplify the mathematical description of a fluid-dynamic-based problem, it is convenient to <u>connect the associated main hydraulic variables to some corresponding fictitious electric variables</u>.

Due to its extensive utilization in electronic engineering, the lumped electric circuit theory is very well established, see e.g. (Desoer & Kuh, 2010). Thus, if a physical problem can be described with the same mathematical formulation used in lumped electric circuits, then, a vast spectrum of theoretical and computational techniques already developed for electronic applications can be readily applied for its solution.

An application of lumped electric circuit theory to Life Sciences and Bioengineering can be found in (Sacco, et al., 2019).

Lumped passive electric circuit elements, such as resistors, capacitors and inductors, can be easily <u>used to assemble a circuit</u> connected by analogy to the fluid dynamic system that is under investigation. In addition, even active components such as those prescribing a volumetric flow rate (corresponding to an independent current source), or a pressure difference (corresponding to an independent voltage source), can be used instead of their analogous hydraulic components.

The aim of this chapter is to establish the fundamental correspondence between electric and hydraulic quantities by means of the continuum-based theory. These computations are based on Chapter 15 of (Sacco, et al., 2019).

In the following sections, the main electric elements are described in detail.

1.1 Hydraulic resistors
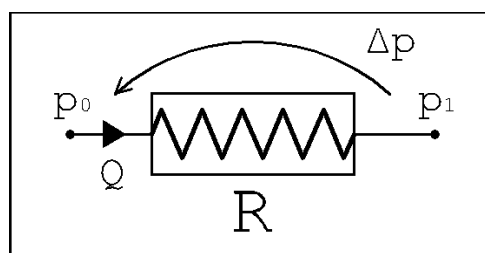
Figure 1.1 – Circuit representation of a resistive element.

It is well known that the *Ohm law* establishes a linear relationship between voltage and current. In hydraulic, the *Poiseuille law* establishes an analogous linear relationship between the pressure drop at the ends of a rigid cylindrical tube and the volumetric flow rate of fluid running through the tube. However, if the tube is not rigid, the relationship between pressure drop and volumetric flow rate ceases to be linear. In the following, both linear hydraulic resistances, characterizing rigid tubes, and nonlinear hydraulic resistances, characterizing compliant and collapsible tubes, are reported, since they are often utilized to model vascular segments.

1.1.1 Linear case: Poiseuille law

Let us consider the Poiseuille flow of a Newtonian viscous fluid in a rigid cylindrical tube of radius r and length l, see Figure 1.2.
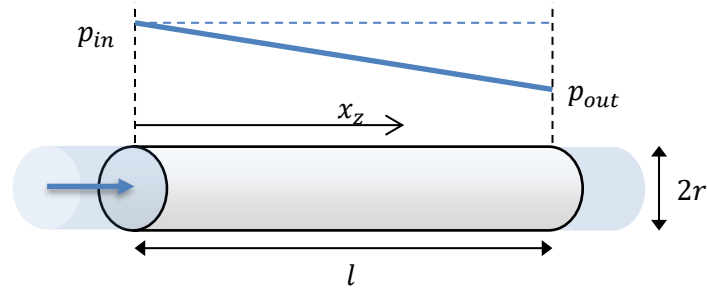
Figure 1.2 – Representative cylindrical tube of length l and cross-section of radius r.

In general, assuming a stationary and incompressible fluid flow in a tube, the pressure can be considered following a linear distribution along the tube axis:

$$p(x_z) = A\, x_z + B \tag{1.1}$$

where x_z denotes the axial coordinate of the tube, as shown in Figure 1.2.

Note that, by writing this, we are already assuming that the pressure is also constant over each cross-section and that does not depend on time.

Assuming to prescribe a pressure at the inlet and outlet boundaries (constant over the cross-section), the two constants A and B can be determined:

$$[\ p(0) = p_{in}\ ;\ \ p(l) = p_{out}\ ]\ \ \rightarrow\ \ \left[\ A = \frac{p_{out} - p_{in}}{l}\ ;\ \ B = p_{in}\ \right]$$

As a result, the pressure field along the tube can be written as:

$$\boxed{p(x_z) = -\frac{p_{in} - p_{out}}{l} x_z + p_{in}} \tag{1.2}$$

The velocity of the fluid inside the tube, assuming that it is not accelerating (so it is constant along the longitudinal direction of the tube) can be written in the form:

$$\underline{v}(\underline{x}) = V(x_r)\ \underline{e}_z \tag{1.3}$$

where x_r is the radial coordinate, $\underline{e}_z$ is the unit vector along the tube axis and the function $V(x_r)$ can be obtained from the balance of linear momentum as:

$$V(x_r) = -\frac{A}{4\,\mu}(r^2 - x_r^2) \tag{1.4}$$

Thus, the velocity field of the fluid can be expressed as:

$$\underline{v} = \frac{p_{in} - p_{out}}{4\,\mu\,l}(r^2 - x_r^2)\,\underline{e_z}$$

(1.5)

Let us define the volumetric flow rate as:

$$Q_v = \int_S \underline{v} \cdot \underline{n}\, dS$$

(1.6)

where S is any cross-section of the tube, and $\underline{n}$ is the unit normal vector to S.

If S can be considered constant along the tube, the resulting Q_v is constant along the tube:

$$
\begin{aligned}
Q_v &= \int_0^r \int_0^{2\pi} V(x_r)\,\underline{e_z} \cdot \underline{e_z}\, x_r\; dx_r\, dx_\theta \\
&= \frac{(p_{in} - p_{out})\,\pi}{2\,\mu\,l} \int_0^r (r^2 - x_r^2)\, x_r\, dx_r \\
&= \frac{(p_{in} - p_{out})\,\pi}{2\,\mu\,l} \left(\frac{r^4}{2} - \frac{r^4}{4} \right)
\end{aligned}
$$

(1.7)

where x_θ is the angular coordinate, and the renown **Poiseuille law** is obtained:

$$Q_v = \frac{\pi\, r^4}{8\,\mu\,l} \underbrace{(p_{in} - p_{out})}_{\Delta p}$$

(1.8)

It can be easily seen that this law has <u>the same mathematical structure as the Ohm law describing a linear resistor</u>, upon establishing the correspondence: $Q_v \leftrightarrow i$, and $\Delta p \leftrightarrow v$.

Noticing also that Q_v represents the fluid volume per unit time passing through the tube cross-section and i represents the electric charge per unit time passing through the circuit branch, we can establish a further correspondence between fluid volume V and electric charge Q.

In addition, since the electric voltage v is defined as the difference between the value of the electric potential ψ at the end nodes of the circuit branch, we establish a correspondence between ψ and the fluid pressure p.

$$[\,Q_v\,] \text{ volumetric flow rate } \Longleftrightarrow [\,i\,] \text{ electric current}$$
$$[\,\Delta p\,] \text{ pressure drop } \Longleftrightarrow [\,v\,] \text{ electric voltage}$$
$$[\,V\,] \text{ fluid volume } \Longleftrightarrow [\,Q\,] \text{ electric charge}$$
$$[\,p\,] \text{ fluid pressure } \Longleftrightarrow [\,\psi\,] \text{ electric potential}$$

(1.9)

In this perspective, we can define a hydraulic conductance G_{hyd} and a hydraulic resistance $R_{hyd} = G_{hyd}^{-1}$ as:

$$G_{hyd} = \frac{\pi\, r^4}{8\,\mu\, l} \quad ; \quad \boxed{R_{hyd} = \frac{8\,\mu\, l}{\pi\, r^4}}$$

(1.10)

so that:

$$\boxed{\Delta p = R_{hyd} \cdot Q_v}$$

(1.11)

1.1.2 Non-linear case: deformable tubes

One of the main assumptions in the derivation of the Poiseuille law is the fact that <u>the tube is a rigid circular cylinder</u>. However, many applications of interest in bioengineering and life sciences involve <u>tubes that are not rigid</u>. Some examples in the human body are blood vessels in the cardiovascular system and airways in the lungs.

Let us consider a straight cylinder Ω with cross-section S (of general shape, not necessarily circular) and length l, see Figure 1.3.

Let $\underline{e}_i$ with $i = 1,2,3$ be the unit vectors in the x_1, x_2, x_3 axis respectively, and let $\underline{e}_3$ be directed along the tube axis.
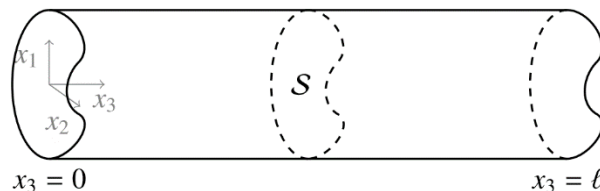
Figure 1.3 – Representative cylinder Ω in the Cartesian coordinate system (x_1, x_2, x_3) with cross-section S and length l. Adapted from (Sacco, et al., 2019).

Let us assume that the motion inside the cylinder Ω can be described by the Stokes equations:

$$\begin{cases} \nabla_x \cdot \underline{v} = 0 \\ -\nabla_x \, p + \mu \, \Delta_x \, \underline{v} = \underline{0} \end{cases} \tag{1.12}$$

where: $\nabla_x \cdot \underline{v}$ is the divergence of the velocity field $\underline{v}$ defined as
$$\nabla_x \cdot \underline{v} = \frac{\partial v_1}{\partial x_1} + \frac{\partial v_2}{\partial x_2} + \frac{\partial v_3}{\partial x_3}$$

$\nabla_x \, p$ is the pressure gradient defined as $\nabla_x \, p = \left[\frac{\partial p}{\partial x_1} \quad \frac{\partial p}{\partial x_2} \quad \frac{\partial p}{\partial x_3} \right]^T$

$\Delta_x \, \underline{v}$ is a vector field representing the Laplacian of $\underline{v}$,
where the components of the Laplacian are defined as:
$$\Delta_x \, \underline{v} = \begin{cases} \Delta_{\underline{x}} v_1 = \frac{\partial^2 v_1}{\partial x_1{}^2} + \frac{\partial^2 v_1}{\partial x_2{}^2} + \frac{\partial^2 v_1}{\partial x_3{}^2} \\ \Delta_{\underline{x}} v_2 = \frac{\partial^2 v_2}{\partial x_1{}^2} + \frac{\partial^2 v_2}{\partial x_2{}^2} + \frac{\partial^2 v_2}{\partial x_3{}^2} \\ \Delta_{\underline{x}} v_3 = \frac{\partial^2 v_3}{\partial x_1{}^2} + \frac{\partial^2 v_3}{\partial x_2{}^2} + \frac{\partial^2 v_3}{\partial x_3{}^2} \end{cases}$$

μ is the dynamic viscosity which is assumed to be a positive constant.

Note: the first equation in (1.12) is also called "*incompressibility condition*", whereas the second equation in (1.12) is the "*balance of linear momentum*".

Let us assume that the following boundary conditions are prescribed:

$$\begin{cases} p = p_{in} & \text{at } x_3 = 0 \\ p = p_{out} & \text{at } x_3 = l \end{cases} \tag{1.13}$$
$$\{ \ \underline{v} = \underline{0} \quad \text{on } \partial S \ (\text{no} - \text{slip condition}) \tag{1.14}$$

where ∂S denotes the boundary of S.

Let us further assume that:

A1. The shape of the cross-section S is constant along the tube.
A2. Fluid pressure is constant on each cross-section $\rightarrow p = p(x_3)$.
A3. Fluid axial velocity can be written as: $v_3 = \overline{v}(x_3) \, f(S)$, where $\overline{v}(x_3)$ represents the average velocity on the cross-section S, and $f(S)$ is an appropriate shape function satisfying $\int_S f(S) \, dS = A$.
A4. Axial motion is predominant: $\|\underline{v}_S\| \ll |v_3|$ (where $\| \cdot \|$ can be the *maximum norm*).

With these assumptions, a model reduction can be performed by integrating the equations in system (1.13) on the cross-section S as follows.

Let us define the volumetric flow rate Q_v through the cross-section S as:

$$Q_v(x_3) = \int_S v_3 \, dS \tag{1.15}$$

Now, considering assumption (A3), the incompressibility condition (1.12), the no-slip boundary condition (1.14) and assumption (A1), we obtain:

$$\frac{d \, Q_v(x_3)}{dx_3} = 0 \tag{1.16}$$

The above relation implies that the volumetric flow rate must be constant along the tube.

In addition, let us assume that:

A5. The viscous dissipation in the axial direction is negligible.
A6. The pressure is linear in x_3, so that: $p(x_3) = -\frac{p_{in} - p_{out}}{l} x_3 + p_{in}$.

Then it is possible to write:

$$\frac{A}{l}(p_{in} - p_{out}) - k_r \, \overline{v} = 0 \tag{1.17}$$

with the factor k_r that depends on the specific profile $f(S)$, chosen a priori for the fluid motion. In the case of parabolic velocity profile, such as the one exhibited in the Poiseuille flow, we have $k_r = 8 \, \pi \, \mu$.

Thus, the balance of linear momentum in the axial direction leads to:

$$\boxed{\Delta p = \frac{k_r \, l}{A^2} \, Q_v} \tag{1.18}$$

Note: it is immediate to verify that, in the case of a rigid tube with a circular cross-section of radius r, the expression (1.17) coincides with the Poiseuille law (1.8). However, in the case of deformable tubes, the cross-sectional area A depends on the pressure difference across the tube wall. More precisely, denoting by p_{ext} the external pressure acting on the tube, we need to provide a constitutive equation characterizing the mechanical behavior of the tube wall, also referred to as *tube law*.

To this purpose, let us introduce for simplicity the *dimensionless cross-sectional area* $\alpha = A/A_{ref}$, where A_{ref} is a reference value for the cross-sectional area. Then, characterizing the *tube law* consists in defining a function $P = P(\alpha)$ such that:

$$P(\alpha) = \frac{\overline{p} - p_{ext}}{k_p} \qquad (1.19)$$

where: $\overline{p}$ is the mean pressure in the tube (Hp. $\overline{p} = \frac{p_{in} + p_{out}}{2}$);

k_p is a constant that accounts for geometrical and mechanical properties of the tube.

The explicit form of the constitutive function $P(\alpha)$ depends on the particular system under consideration.

Two types of tubes cases will be considered: the *compliant tube* and the *collapsible tube*.

• *Compliant tubes*

In the case of compliant tubes, the cross-section is assumed to be circular and to remain circular after the deformation, see Figure 1.4. In this case, the radial displacement η is computed using the membrane law:

$$\eta = \frac{(1 - v^2)\, r_{ref}^{\,2}\, (\overline{p} - p_{ext})}{E\, h} \qquad (1.20)$$

where: E, v are the elastic constants the tube: Young modulus and Poisson ratio;

h is the tube wall thickness;

r_{ref} is the reference radius.
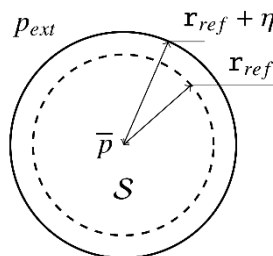
Figure 1.4 – Deformation of a compliant tube for a positive transmural pressure difference $p - p_{ext} > 0$. The cross-section S remains circular after the deformation and the radial displacement is denoted by η.

In addition, the *reference area* is defined as $A_{ref} = \pi \, r_{ref}{}^2$.

The expression (1.20) can be rewritten using the following parameters:

$$\alpha = \frac{A}{A_{ref}} \quad ; \quad k_p = \frac{1}{r_{ref}{}^3} \cdot \frac{E \, h^3}{12 \, (1 - v^2)} \quad ; \quad k_L = 12 \left(\frac{r_{ref}}{h}\right)^2 \tag{1.21}$$

obtaining:

$$k_L \left(\alpha^{1/2} - 1\right) = \frac{\overline{p} - p_{ext}}{k_p} \tag{1.22}$$

Comparing (1.21) with (1.19), it is possible to characterize $P = P(\alpha)$ as follows:

$$\boxed{P(\alpha) = k_L \left(\alpha^{1/2} - 1\right)} \tag{1.23}$$

The above expression represents the *tube law* for a compliant tube whose deformation is described by the membrane law (1.20).

Recalling that $\alpha = A/A_{ref}$, it is possible to solve the expression (1.22) for A, obtaining:

$$A = A_{ref} \left(\frac{\overline{p} - p_{ext}}{k_p \, k_L} + 1\right)^2 \tag{1.24}$$

Substituting (1.24) into (1.18) leads to the equation:

$$\boxed{\Delta p = R_{comp} \, Q_v} \tag{1.25}$$

where $R_{comp} = R_{comp}(\overline{p})$ is a nonlinear function of the fluid pressure that characterizes the hydraulic resistance of a compliant tube:

$$\boxed{\boxed{R_{comp} = \frac{k_r \, l}{A_{ref}{}^2} \left(\frac{\overline{p} - p_{ext}}{k_p \, k_L} + 1\right)^{-4}}} \tag{1.26}$$

• *Collapsible tubes*

In the case of collapsible tubes, the cross-section S exhibits a marked change in shape depending on whether the pressure $\overline{p}$ inside the tube is larger or smaller than the external pressure p_{ext}. Experiments on collapsible tubes have shown that S changes shape from circular, to elliptic to highly collapsed as the transmural pressure difference $\overline{p} - p_{ext}$ decreases, as illustrated in Figure 1.5. The phenomenon of tube collapse under negative transmural pressure difference is also known as *Starling resistor effect* and plays a crucial role in veins and airways.
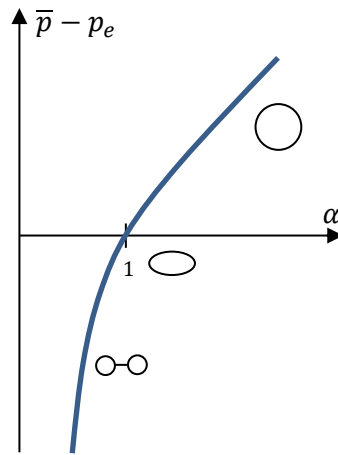
Figure 1.5 – Schematic illustration of experimental results for a collapsible tube. The cross-section shape changes from circular to elliptic to highly collapsed as the transmural pressure difference $\overline{p} - p_e$ decreases. Adapted from (Sacco, et al., 2019).

It is possible to observe that when the transmural pressure difference is positive, the vessel dilates and maintains a circular cross-section. However, when the transmural pressure difference is negative, the cross-section changes shape, first becoming elliptical and then collapsing until two opposite sides of the inner wall touch each other. In this region, the vessel is more resistant and thus large changes in the transmural pressure difference yield small changes in the cross-sectional area. This behavior is mathematically represented by the following constitutive equation:

$$P(\alpha) = \begin{cases} 1 - \alpha^{-3/2} & \text{for } \alpha \leq 1 \\ k_L(\alpha^{1/2} - 1) & \text{for } \alpha > 1 \end{cases} \tag{1.27}$$

In particular, we notice that a collapsible tube is assumed to behave in the same way as a compliant tube if $\alpha > 1$. Next, an expression for α can be obtained by manipulating (1.27). Recalling that $\alpha = A/A_{ref}$, it is possible to substitute the expression (1.27) into (1.18), obtaining:

$$\boxed{\Delta p = R_{coll}\, Q_v} \tag{1.28}$$

where $R_{coll} = R_{coll}(\overline{p})$ is a nonlinear function of the fluid pressure that characterizes the hydraulic resistance of a collapsible tube:

$$\boxed{R_{coll} = \begin{cases} \dfrac{k_r\, l}{A_{ref}^{\;2}} \left(\dfrac{\overline{p} - p_{ext}}{k_p} \right)^{4/3} & \text{for } \alpha \leq 1 \\[2em] \dfrac{k_r\, l}{A_{ref}^{\;2}} \left(\dfrac{\overline{p} - p_{ext}}{k_p} + 1 \right)^{-4} & \text{for } \alpha > 1 \end{cases}} \tag{1.29}$$

Remark: In the case of an electric resistor, energy is received from the electric circuit and dissipated under the form of heat via the *Joule effect*. In the case of a hydraulic resistor, energy is received from the hydraulic circuit and dissipated under the form of heat via the viscous effect of *internal friction*.

1.2 Hydraulic capacitors
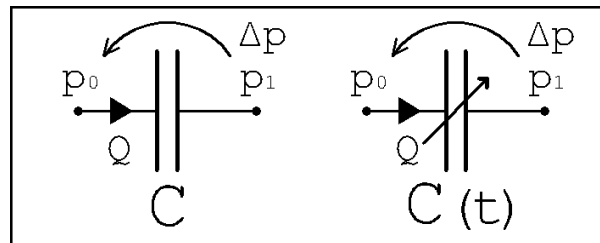
Figure 1.6 – Circuit representation of a capacitive element.

An electric capacitor is a passive two-terminal electronic component that stores electrical energy in an electric field which, in the case of linear time-invariant capacitor of capacitance C can be written as:

$$\varepsilon_C = \frac{1}{2} C v^2 \tag{1.30}$$

Since the electric equivalent of the voltage drop v is the pressure drop Δp, the *electrical energy* described above corresponds to a *potential energy*.
Thus, the correspondence between electric and hydraulic capacitors should be sought in the potential part of the fluid equations.

The general constitutive law characterizing a capacitor in the context of lumped electric circuits is:

$$\boxed{i = \frac{dQ}{dt}} \quad Q = Q(v) \tag{1.31}$$

where: i is the electric current passing through the capacitor;
            Q is the electric charge stored in the capacitor;
            v is the voltage drop across the capacitor.

The basic correspondence between electric and hydraulic variables established in the scheme (1.9) tells us that a hydraulic capacitor must be described by a constitutive law of the form:

$$\boxed{Q_v = \frac{dV}{dt}} \quad V = V(\Delta p) \tag{1.32}$$

where: Q_v is the volumetric flow rate passing through the capacitor;
         V is the fluid volume stored in the capacitor;
         Δp is the pressure drop across the capacitor.

Thus, an hydraulic capacitor is capable of <u>storing and releasing fluid volume dynamically</u>, thereby creating a fluid flow through the element.
This implies that:

1. a hydraulic capacitor must be able to deform and accommodate changes in fluid volume with time;

2. the constitutive relationship between fluid volume and pressure drop across the capacitor characterizes the behavior of the specific element.

• *Tubes as hydraulic capacitors*

In Sections 1.1.1 and 1.1.2 we have considered the fluid flow in rigid and deformable tubes from the point of view of their hydraulic resistances. Since rigid tubes cannot alter their shape, they cannot accommodate changes in volume and, as a consequence, cannot be modeled as hydraulic capacitors. Conversely, <u>deformable tubes can change their shape and therefore act as hydraulic capacitors</u>. Let us consider the cases of compliant and collapsible tubes that were discussed in Section 1.1.2.

We recall that A is the cross-sectional area of the tube, which is assumed to be constant along the length l of the tube.

Thus, the tube volumes in the deformed and reference configurations, denoted by V and V_{ref} respectively, can be written as:

$$V = A\,l \quad \text{and} \quad V_{ref} = A_{ref}\,l \tag{1.33}$$

Thus, the constitutive law characterizing a compliant tube as a hydraulic capacitor can be obtained from (1.24) leading to:

$$V = \begin{cases} V_{ref}\left(1 - \dfrac{\Delta p}{k_p}\right)^{-2/3} & \text{for } V \le V_{ref} \\[4mm] V_{ref}\left(\dfrac{\Delta p}{k_p\,k_L} + 1\right)^{2} & \text{for } V > V_{ref} \end{cases} \tag{1.34}$$

In both compliant and collapsible cases, the pressure difference Δp across the hydraulic capacitor is the transmural pressure difference $\Delta p = \overline{p} - p_{ext}$, with $\overline{p}$ denoting the average pressure inside the tube.

Remark: In the case of an electric capacitor, energy is received from the electric circuit and stored under the form of *electric energy*. In the case of a hydraulic capacitor, energy is received from the hydraulic circuit and stored under the form of *potential energy associated with the volume change*.

1.3 Hydraulic inductors
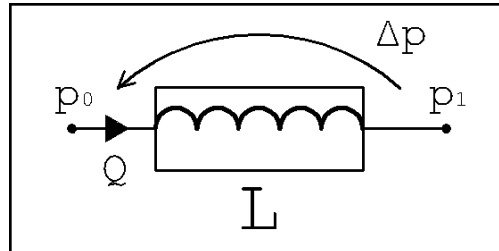
Figure 1.7 – Circuit representation of an inductive element.

The constitutive law characterizing a linear time-invariant inductor in the context of lumped electric circuits is:

$$v = L \frac{di}{dt} \tag{1.35}$$

where: i is the electric current passing through the inductor;
v is the voltage drop across the inductor.

An electric inductor receives energy from the circuit and stores it under the form of **magnetic energy** which, in the case of a linear time-invariant inductor of inductance L can be written as:

$$\varepsilon_L = \frac{1}{2} L i^2 \tag{1.36}$$

Since the electric equivalent of the electric current i is the volumetric flow rate Q_v, the *magnetic energy* described above corresponds to a *kinetic energy*.
Thus, <u>the correspondence between electric and hydraulic inductors should be sought in the inertial part of the fluid equations</u>.

For the sake of simplicity, let us consider a rigid tube of length l and circular cross-section S of radius r.

Let us start from the Navier-Stokes equations [2]:

$$\begin{cases} \nabla_{\underline{x}} \cdot \underline{v} = 0 \\[2mm] \rho \dfrac{\partial \underline{v}}{\partial t} + \rho (\underline{v} \cdot \nabla_{\underline{x}}) \, \underline{v} = -\nabla_{\underline{x}} \, p + \mu \, \Delta_{\underline{x}} \, \underline{v} \end{cases} \tag{1.37}$$

Let us simplify system (1.37) by making the same assumptions A1-A6 as in Section 1.1.2 with the difference that now $v_3 = v_3(x_3, t) \cdot f(S)$ and $p = p(x_3, t)$.

Thus, the balance of linear momentum can be reduced to its axial component:

$$\rho \frac{\partial v_3}{\partial t} = -\frac{\partial p}{\partial x_3} + \mu \left(\frac{\partial^2 v_3}{\partial x_1^2} + \frac{\partial^2 v_3}{\partial x_2^2} \right) + \mu \frac{\partial^2 v_3}{\partial x_3^2} \tag{1.38}$$

Integrating (1.38) over the cross-section S yields:

$$\rho \frac{dQ_v}{dt} = \frac{A}{l} (p_{in} - p_{out}) - \frac{k_r}{A} Q_v \tag{1.39}$$

In the *inviscid case*, we can set $k_r = 0$ to obtain:

$$\boxed{\Delta p = \frac{\rho \, l}{A} \frac{dQ_v}{dt}} \qquad \Delta p = p_{in} - p_{out} \tag{1.40}$$

from which it is possible to obtain a characterization of the hydraulic conductance as:

$$\boxed{\boxed{L_{hyd} = \frac{\rho \, l}{A}}} \tag{1.41}$$

Note that the hypothesis of *inviscid flow* is reasonable considering the aim of the section, since the viscosity resistances to motion are accounted by using equivalent resistors.

---

[2] As a general remark, it may be useful to recall that a linearized version of the Navier-Stokes equations is represented by the "Stokes equations", which reads:

$$\begin{cases} \nabla_{\underline{x}} \cdot \underline{v} = 0 \\[2mm] \mu \, \Delta_{\underline{x}} \, \underline{v} - \nabla_{\underline{x}} \, p = f \end{cases}$$

1.4 Hydraulic active elements
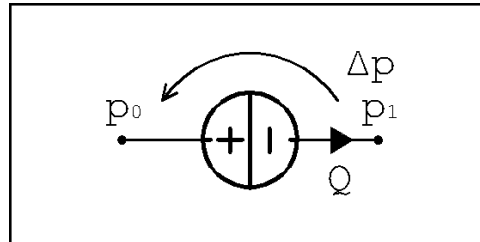
Figure 1.8 – Circuit representation of a prescribed voltage source.

Electric active elements <u>provide prescribed sources of electric current or voltage</u>. In analogy, we can use electric active elements to model the action of hydraulic devices that establishes a <u>prescribed volumetric flow rate Q_v</u> (corresponding to an independent current source), or a <u>prescribed pressure difference Δp</u> (corresponding to an independent voltage source). Thus, hydraulic active elements include **pumps** and **injectors**.
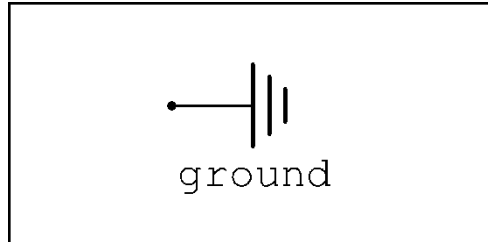
Figure 1.9 – Circuit representation of a ground connection element.

To conclude, it can be useful to remark that the **circuit ground** symbol corresponds to a node where the electric potential, or the fluid pressure in the hydraulic analogy, is set equal to zero.

2 – MODELING AND ANALYSIS OF THE CARDIOVASCULAR SYSTEM

Taking into considerations the connections analyzed in Chapter 1 between hydraulic elements and electric elements, (Guidoboni, et al., 2019) developed a **closed-loop circuit model of the cardiovascular system** with the aim of virtually recreating the Ballistocardiogram (BCG) of a patient (see "Chapter 2.2 - Ballistocardiogram analysis" for definitions).

The modeling of the cardiovascular system through a lumped model has a long history. Different models have been proposed to treat different aspects of the cardiovascular system. In the following, other closed-loop models will be considered, for instance the one developed by (Avanzolini, et al., 1988); however the closed-loop model proposed in Section 2.1 is the first model that has been developed with the purpose of performing computational ballistocardiography simulations.

In **Section 2.1**, the closed-loop circuit model proposed by (Guidoboni, et al., 2019) simulating the blood flow inside the cardiovascular system is introduced and analyzed. In **Section 2.2** the same model is used to perform a simulation of the Ballistocardiogram (BCG).

In **Section 2.3** and **Section 2.4**, the role of a particular function called *activation function* is investigated as well as the role of vessel *viscoelasticity*.

Finally, In **Section 2.5** the referenced model is compared to previous models and a causal-relation analysis is performed to establish relations between BCG parts and circuital compartments.

2.1 Closed-loop model for the cardiovascular system

Blood circulation is modeled using the analogy between electric circuits and hydraulic networks as described in Chapter 1. In this context, *electric potentials* correspond to *fluid pressures*, *electric charges* correspond to *fluid volumes* and *electric currents* correspond to *volumetric flow rates*, see (1.9).

By making use of circuit elements, a model is built which leads to a system of nonlinear ordinary differential equations whose solution provides the <u>time-dependent profiles of pressures and volumes at the circuit nodes</u> and <u>flow rates through the circuit branches</u>.

2.1.1 Detailed circuital description of the model

The closed-loop model analyzed in this section consists of a network of resistors, capacitors, inductors, voltage sources and switches arranged into <u>4 main interconnected compartments</u> representing the **heart**, the **systemic circulation**, the **pulmonary circulation** and the **cerebral circulation**, as reported in Figure 2.1.

The **circuit nodes** have been marked by thick black dots and numeric labels from 1 to 15. The anatomical meaning of the circuit nodes has been summarized in Table 2.1. In the model, *resistors*, *capacitors* and *inductors* represent *hydraulic resistance*, *wall compliance* and *inertial effects*, respectively. <u>Variable capacitors</u>, indicated with arrows in Figure 2.1, are utilized to describe the wall viscoelasticity in large arteries and the nonlinear properties of the heart muscle fibers. Cerebral capillaries are assumed to be non-compliant. The four heart valves are modeled as ideal switches. <u>The ventricular pumps are modeled as time-dependent voltage sources</u>.

The model depicted in Figure 2.1 will be also called in the following "Model 5 (Guidoboni, et al.)". The reason for the number "5" will be explained in **Section 2.5**.
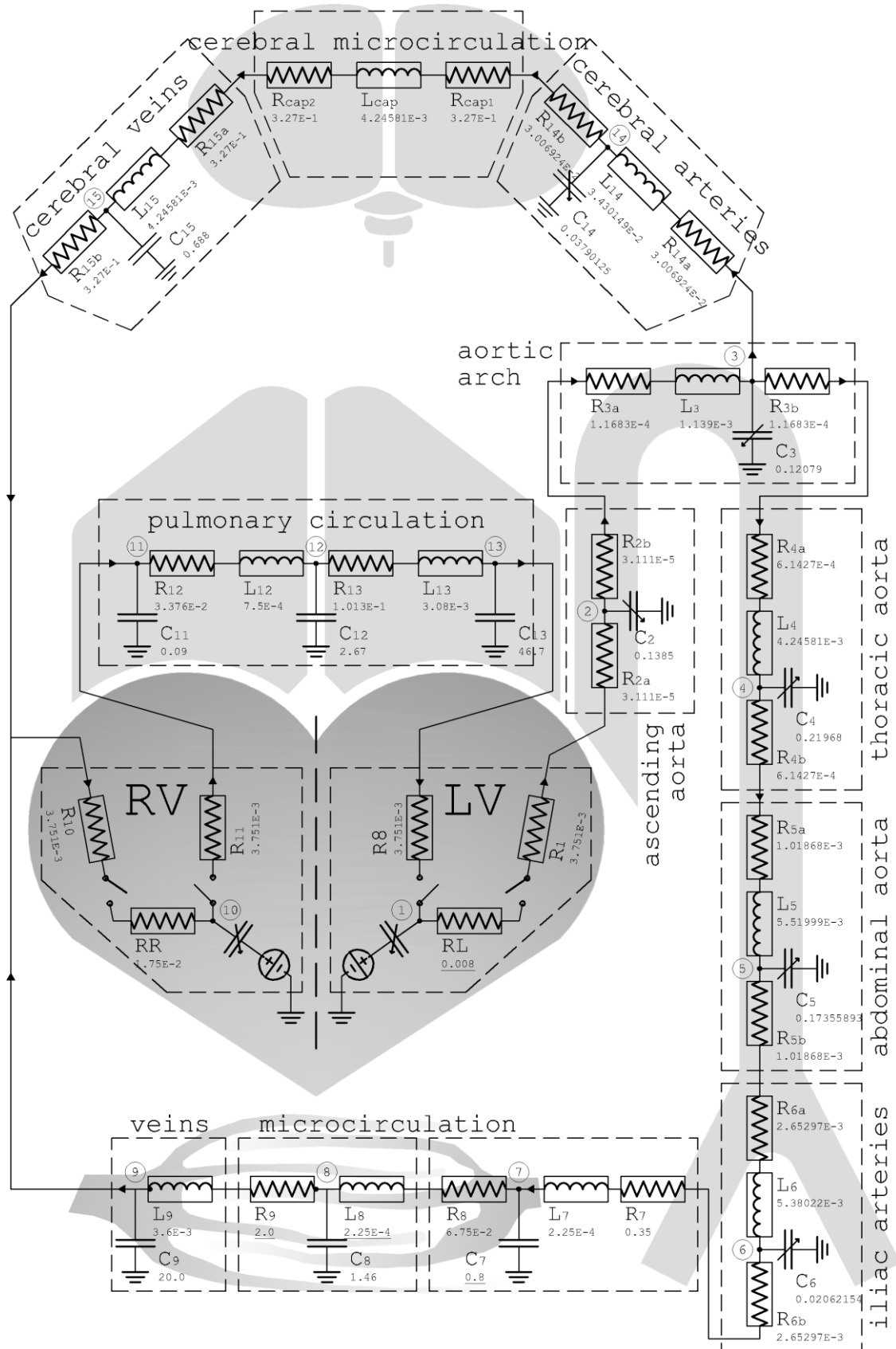
Figure 2.1 – Cardiovascular circuit model taken as reference (Guidoboni, et al., 2019).

Node	Compartment	Segment
1	Heart	Left Ventricle
2	Systemic	Ascending Aorta
3	Systemic	Aortic Arch
4	Systemic	Thoracic Aorta
5	Systemic	Abdominal Aorta
6	Systemic	Iliac arteries
7	Systemic	Small arteries
8	Systemic	Capillaries
9	Systemic	Veins
10	Heart	Right Ventricle
11	Pulmonary	Pulmonary Arteries
12	Pulmonary	Capillaries
13	Pulmonary	Veins
14	Cerebral	Cerebral Arteries
15	Cerebral	Veins

Table 2.1 – Anatomical meaning of the circuit nodes.

• *System of differential equations*

The closed-loop model in Fig. 2 can be written as a system of ordinary differential equations (ODEs) of the form:

$$\underline{\underline{M}}\left(\underline{Y}(t)\right)\frac{d\underline{Y}(t)}{dt} = \underline{\underline{A}}\left(\underline{Y}(t)\right)\cdot\underline{Y}(t) + \underline{b}\left(\underline{Y}(t)\right) \qquad t \in [0,T] \tag{2.1}$$

where: $\underline{Y}(t) = \left[\underline{V}(t); \ \underline{Q}(t)\right]^T$ is the m−dimensional column vector of unknowns;

$\underline{V}(t)$ denote the vector of fluid volumes stored in the capacitors;

$\underline{Q}(t)$ denote the vector of volumetric flow rate through the inductors;

$\underline{\underline{M}}$ and $\underline{\underline{A}}$ are $m \times m$ tensors;

$\underline{b}$ is the m−dimensional column vector of given forcing terms.

We anticipate that $\underline{\underline{M}}$, $\underline{\underline{A}}$ and $\underline{b}$ nonlinearly depend on the vector of state variables $\underline{Y}$. The specific expressions for $\underline{Y}$, $\underline{\underline{M}}$, $\underline{\underline{A}}$ and $\underline{b}$ follow from the constitutive equations characterizing the circuit elements and the *Kirchhoff laws* of currents and voltages, as detailed in (Guidoboni, et al., 2019).

• *Electrical elements*

The theory of the circuit elements used to build the closed-loop model was introduced in Chapter 1. The constitutive laws characterizing these elements are here summarized in Table 2.2.
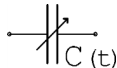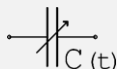
Figure	Element	Constitutive law
R	Linear resistor	$Q = \dfrac{\Delta p}{R}$
R	Linear resistor + ideal switch	$Q = \sigma_{P_0 - P_1} \dfrac{\Delta p}{R}$
C	Linear capacitor	$Q = \dfrac{dV}{dt}$; $V = C\,\Delta p$
C (t)	Variable capacitor	$\Delta p = \dfrac{V}{C} + \gamma \dfrac{dV}{dt}$
C (t)	Variable capacitor (Ventricular elastance)	$\Delta p = E(t) \cdot V$
	Voltage source	$P_1(t) = U(t)$
L	Linear inductor	$L \dfrac{dQ}{dt} = \Delta p$

Table 2.2 – Constitutive laws of the circuit elements in the closed-loop model.

with:

	V	Fluid volume;
	$\Delta p = P_0 - P_1$	Pressure difference;
	$\sigma_{P_0 - P_1} = \begin{cases} 1 & \text{if } \Delta p > 0 \\ 0 & \text{if } \Delta p \leq 0 \end{cases}$	Switch function;
	C	Capacitance constant;
	γ	Viscoelastic constant;
	$E(t)$	Ventricular elastance (depending on the *activation function*);
	$U(t)$	Pressure function (depending on the *activation function*);
	L	Inductance constant.

The values of the main parameters pertaining to each circuit element are reported directly in Figure 2.1.

- The parameter values pertaining to the <u>heart</u>, the <u>systemic microcirculation</u> and the <u>pulmonary circulation</u> have been adapted from (Avanzolini, et al., 1988)].

- The parameter values pertaining to the <u>main arteries</u> have been computed using the following constitutive equations, (Canic, et al., 2006):

Resistance:

$$R = \frac{8 \pi l \eta}{S^2}$$

(2.2)

Inductance:

$$L = \frac{\rho_b \, l}{S}$$

(2.3)

Capacitance:

$$C = \frac{3 \, l \, S \, (a + 1)^2}{E \, (2a + 1)} \quad ; \quad \gamma = \frac{\delta}{C}$$

(2.4)

where: $a = r/h$ is the ratio between vessel radius r and wall thickness h;

            l is the vessel length;

            $S = \pi \, r^2$ is the vessel cross-sectional area;

            ρ_b is the blood density;

            η is the blood viscosity;

            E, δ are the Young modulus and the viscoelastic parameter characterizing the vessel wall.

In (Guidoboni, et al., 2019), it is assumed that:

$\rho_b = 1.05$ [g/cm^3]; $\eta = 0.035$ [g cm^{-1} s^{-1}];

$E = 4 \cdot 10^6$ [dyne/cm^2]; $\delta = 1.56 \cdot 10 - 3$ [s].

The values of the remaining geometrical parameters utilized to determine R, L, C and γ for each of the main arterial segments have been adapted from (Noordergraaf & al., 1963) and are reported in Table 2.3.

Arterial Segment	l [cm]	r [cm]	h [cm]
Ascending Aorta	4.0	1.44	0.158
Aortic Arch	5.9	1.25	0.139
Thoracic Aorta	15.6	0.96	0.117
Abdominal Aorta	15.9	0.85	0.105
Iliac artery	5.8	0.52	0.076
Carotid artery	20.8	0.39	0.064

Table 2.3 – Geometrical parameters used for the main arterial segments.

• *Activation function*

The **activation function** $A(t)$ is a function characterizing the ventricular contractions. It is the function governing the *pumping timing* of the heart ventricles. This special function must be tailored to the specific circuit and it must be able to make the circuit reproduce physiological waveforms of *volumes*, *pressures* and *flow rates*.

Figure 2.2 shows the values of the activation function $A(t)$ in time, as defined in (2.5), and some related timing functions t_a and t_b.
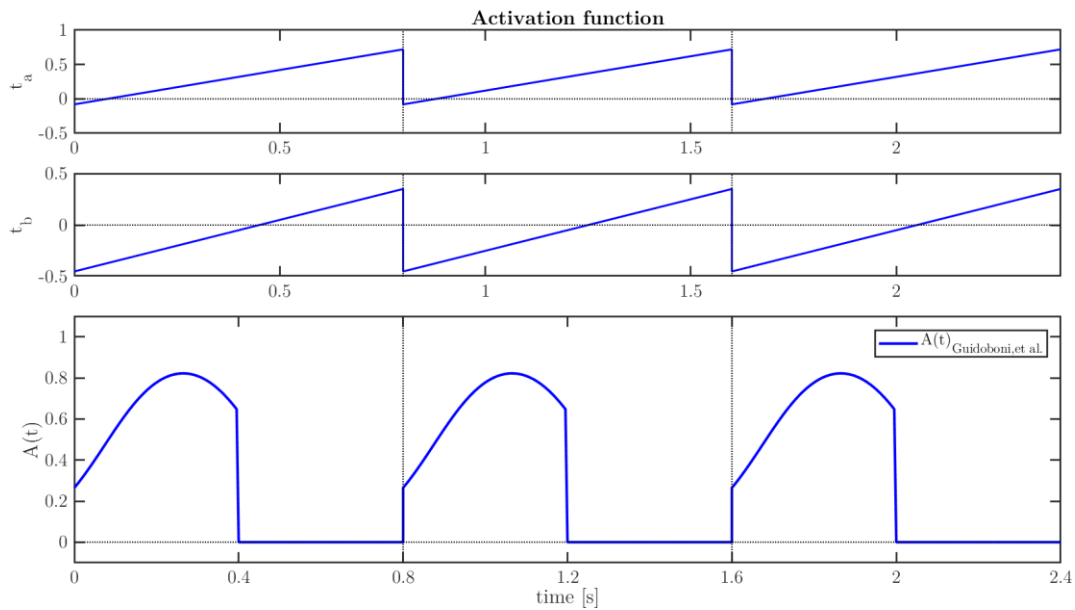
Figure 2.2 – Graphical representation of the activation function $A(t)$ and some related timing functions t_a and t_b.

In (Guidoboni, et al., 2019) the activation function was defined as:

$$A(t)_{IEEE\ Std} = \begin{cases} \dfrac{1}{2}\left[\tanh\left(q_{L/R} \cdot t_a\right) - \tanh\left(q_{L/R} \cdot t_b\right)\right] & \text{if } t_m < T_s \\ \\ 0 & \text{if } t_m \geq T_s \end{cases} \tag{2.5}$$

where the parameters considered in the formula are defined as:

$q_L = q_R = 2\pi$ are given constants [l/s];

$T_C = 0.8 \text{ s}$ is the length of one cardiac cycle;

$T_S = 0.16 + 0.3 \cdot T_C$ is the length of the systolic part of the cardiac cycle;

$t_m = mod\,(time,\,Tc)$ is the time related to the cardiac cycle;

$t_{a/b} = t_m - T_{a/b}$ are timing depending on T_a and T_b, which are given time constants that can be characterized via *electrocardiography* (ECG). Specifically, $T_a = 0.08$ s corresponds to the T wave peak time and $T_b = 0.45$ s corresponds to the T wave offset time with respect to the R wave peak, see Figure 2.3.
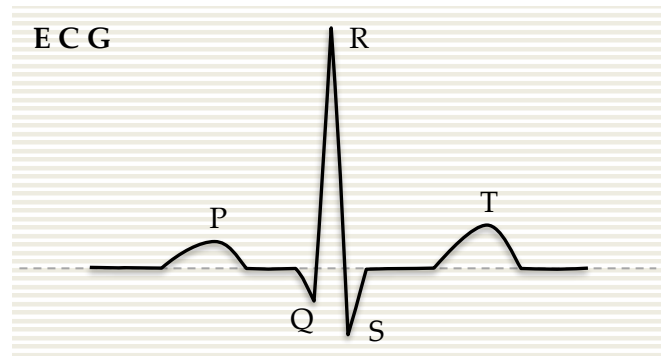
Figure 2.3 – Standard ECG signal.

► **Variable capacitors:**

Capacitors in the ventricular part of the circuit characterizing the *ventricular elastance* depend on the activation function through the formulas:

$$C(t) : \begin{cases} E_L(t) = E_{D,L} + E_{S,L} \cdot A(t) \\[2mm] E_R(t) = E_{D,R} + E_{S,R} \cdot A(t) \end{cases} \tag{2.6}$$

where $E_{D,L}$, $E_{S,L}$ (resp. $E_{D,R}$, $E_{S,R}$) are given constants characterizing the diastolic and systolic elastances of the left ventricle (resp. right ventricle).

► **Voltage sources:**

The hydraulic analog of a voltage source is an element that imposes the nodal pressure as $P_1(t) = U(t)$, where $U(t)$ is a given function. Following (Avanzolini, et al., 1988), it is assumed that:

$$v(t) : \begin{cases} U_L(t) = U_{L,O} \cdot A(t) \\ U_R(t) = U_{R,O} \cdot A(t) \end{cases} \tag{2.7}$$

where $U_{L,O}$ and $U_{R,O}$ are positive constants and $A(t)$ is given in equation (2.5).

•*Modeling software programs*

The mathematical model described so far has been implemented in **OpenModelica[3]**, an open source Modelica-based modeling and simulation environment of complex dynamic systems. Model results have been obtained using a differential algebraic system solver, DASSL, with a tolerance of 10^{-6} and a time step of $0.001\ s$.
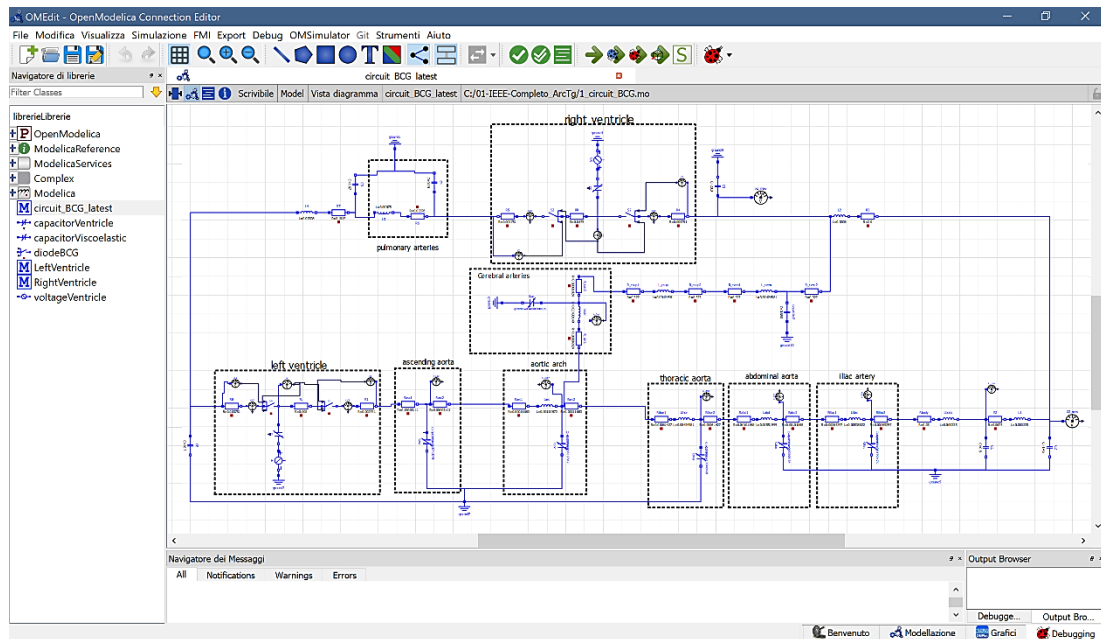
Figure 2.4 – OpenModelica 1.13.2 64bit, Connector Editor main screen.

The simulations are performed over **8 cardiac cycles**, each of duration equal to $0.8\ s$, for a total simulation time of $6.4\ s$, in order to obtain a periodic solution and avoid the initial transient needed to reach sustained periodic conditions.

The results reported in the majority of the graphs in this thesis correspond to the **last of the 8 simulated cardiac cycles**.

Simulation results were then post-processed using **MATLAB[4]**, a commercial software to analyze data, develop algorithms and implement mathematical models.

---

[3] https://openmodelica.org/

[4] https://it.mathworks.com/products/matlab.html

2.1.2 Capability of the model: cardiovascular physiology

The capability of the proposed closed-loop model to capture some of the main features of the cardiovascular system is shown in (Guidoboni, et al., 2019) by comparing theoretical results to experimental measurements.

•*Ventricle-related parameters*

A qualitative description of **left ventricular function** is shown in Figure 2.5, which reports the volume-pressure relationship in the left ventricle during one cardiac cycle simulated via the closed-loop model. Results show that the model correctly captures the four basic phases of ventricular function: *ventricular filling* (phase A), *isovolumetric contraction* (phase B), *ejection* (phase C), and *isovolumetric relaxation* (phase D).
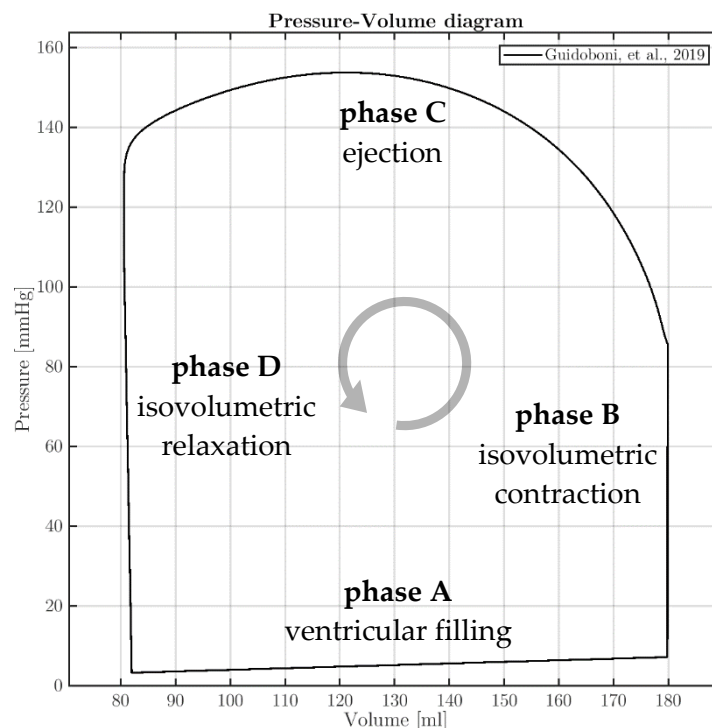
Figure 2.5 – Pressure-volume cycle obtained with the model in (Guidoboni, et al., 2019). The model captures the four phases of ventricular function: *ventricular filling* (phase A), *isovolumetric contraction* (phase B), *ejection* (phase C), and *isovolumetric relaxation* (phase D).

Another qualitative representation of ventricular function is given by the **Wiggers diagram**, where the <u>volume waveform of the left ventricle</u> is portrayed together with the <u>pressure waveforms of the left ventricle</u> and the ascending aorta. The Wiggers

33

diagram simulated via the closed-loop model, see Figure 2.6, shows the typical features of isovolumetric contraction and relaxation exhibited by physiological waveforms (Klabunde, 2011).
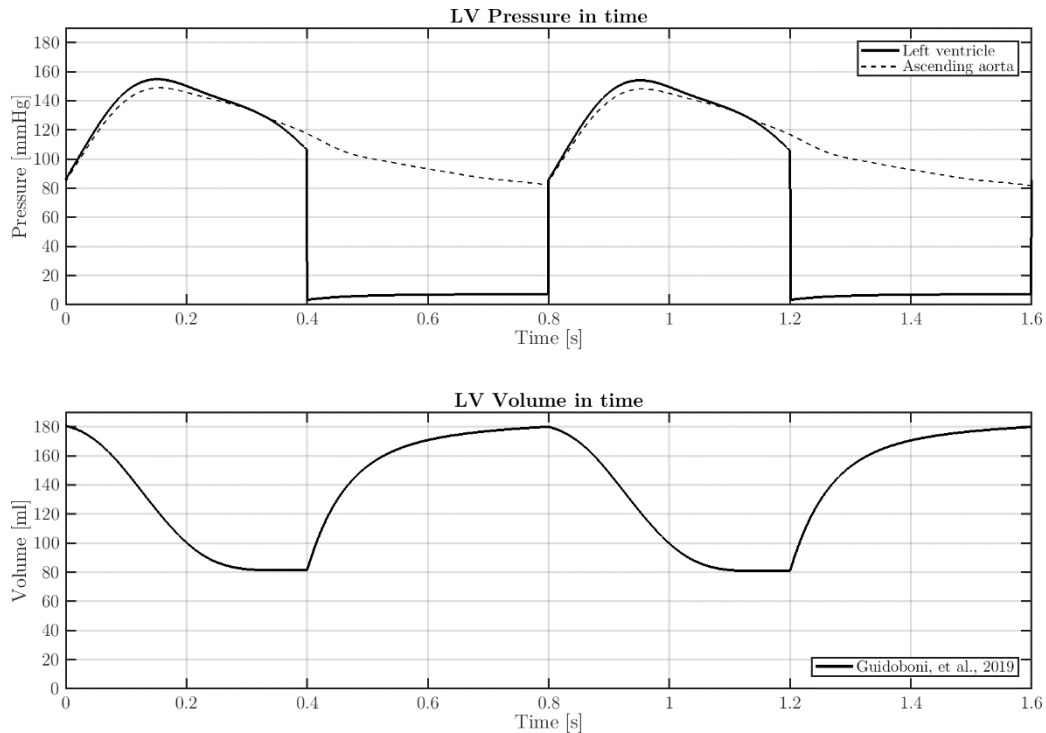
Figure 2.6 – Wiggers diagram simulated via the closed-loop model. Results show the typical features of isovolumetric contraction and relaxation (Klabunde, 2011).

• *Cardiovascular parameters*

Quantitative parameters describing cardiovascular physiology include: *end-diastolic volume* (EDV), *end-systolic volume* (ESV), *stroke volume* (SV), *cardiac output* (CO) and *ejection fraction* (EF) associated with the left and right ventricles.

- EDV and ESV are computed as the maximum and minimum values of the ventricular volumes during the cardiac cycle, respectively.
- SV is given by the difference $SV = EDV - ESV$.
- EF is given by the relative difference $EF = 100 \cdot (EDV - ESV) / EDV$, which can also be written as $EF = 100 \cdot SV / EDV$.
- Denoting by T_C the length of the heartbeat measured in seconds, the *heart rate* HR and the *cardiac output CO* are computed as $HR = 60 / T_C$ and $CO = HR \cdot SV / 1000$.

Table 2.4 provides the values of the above parameters for the left and right ventricles as reported in the clinical literature and the values simulated via the closed-loop model. Specifically, the clinical studies in (Maceira & al., 2006) and (Maceira & al., 2006) utilized cardiovascular magnetic resonance to assess left and right ventricular functions on 120 healthy individuals. All the simulated values fall within the ranges reported in the clinical literature, thereby validating the capability of the closed-loop model to reproduce the main features of the heart function.

Parameter	Unit	Normal Clinical Range		Closed-Loop Model		
		Left Ventricle	*Right Ventricle*	*Left Ventricle*	*Right Ventricle*	
End-Diastolic Volume (EDV)	[ml]	142 (102-183)	144 (98-190) 130 (100-160)	**155.6**	**157.7**	✔
End-Systolic Volume (ESV)	[ml]	47 (27-68)	50 (22-78) 75 (50-100)	**67.3**	**68.8**	✔
Stroke Volume (SV)	[ml/beat]	95 (67-123) (60-100)	94 (64-124) 80 (60-100)	**88.2**	**88.8**	✔
Cardiac Output (CO)	[l/min]	6 (4-8)	6 (4-8)	**6.6**	**6.6**	✔
Ejection Fraction (EF)	[%]	67 (58-76)	66 (54-78) 50 (40-60)	**56.7**	**56.3**	✔

Table 2.4 – Cardiovascular physiology: left and right ventricles reference values compared to the simulated ones.
Clinical references: (Maceira & al., 2006), (Maceira & al., 2006), (Lifesciences, 2014)

• *Pressure and volume of the cardiovascular compartments*

The **pressure** and **volume waveforms** pertaining to the main segments of the systemic arteries simulated via the closed-loop model are reported in Figure 2.7. Results show that the model captures the typical features of peak magnification and time delay exhibited by physiological waveforms.

In addition, in Figure 2.8 all the main aortic pressures are superposed all together in order to better investigate the general trend predicted by the simulation. It can be seen that the ascending aorta has a lower pressure, while pressure increases in the farthest zones of the aorta and the iliac arteries. This behavior is physiological (McDonald, 1974) and confirms the capability of this model to simulate the buildup changes in pressure and waveforms.
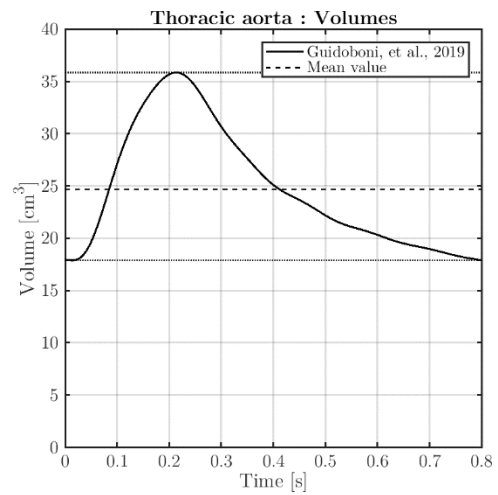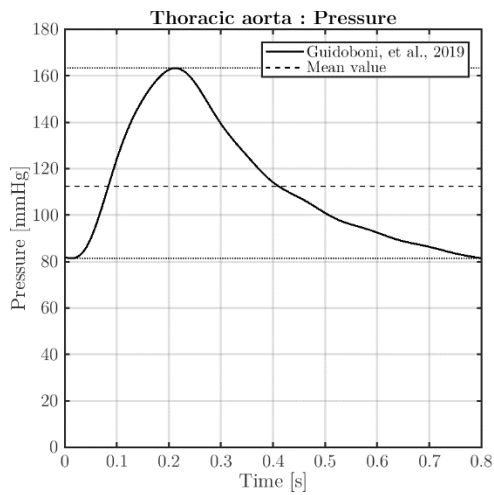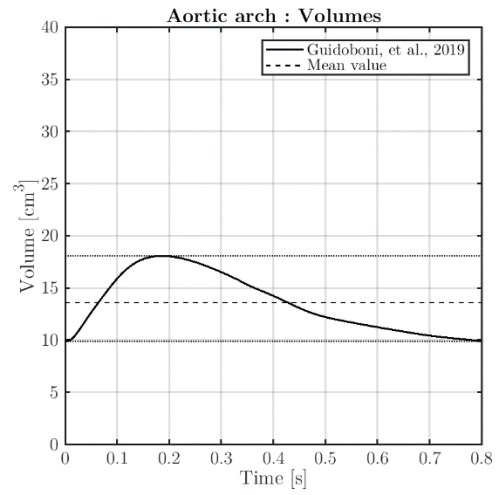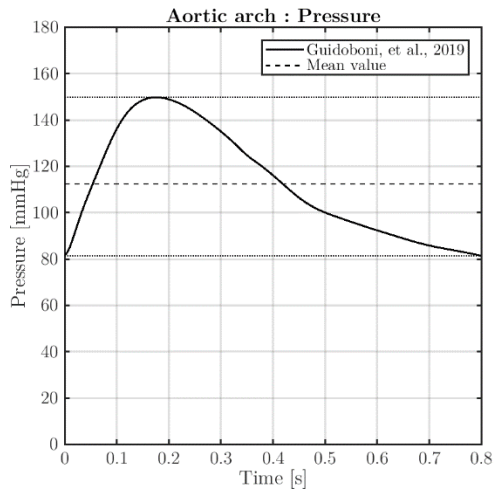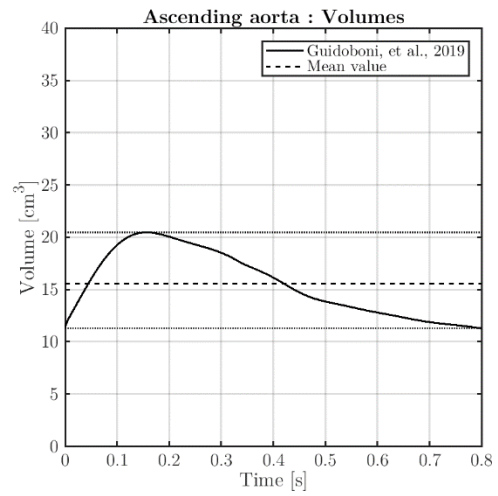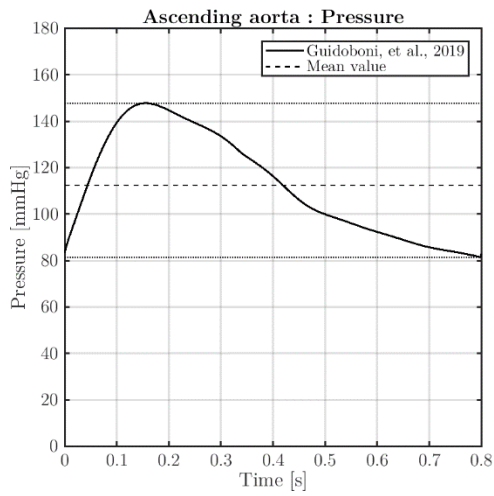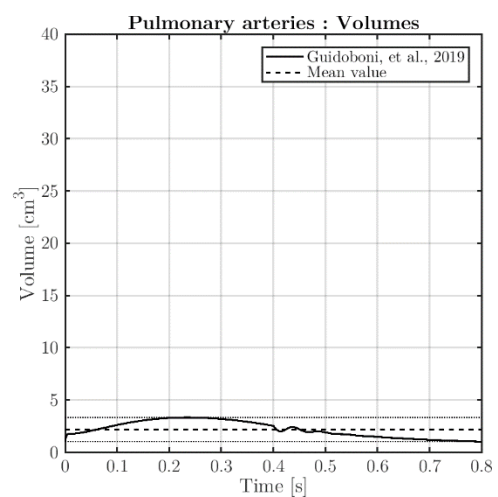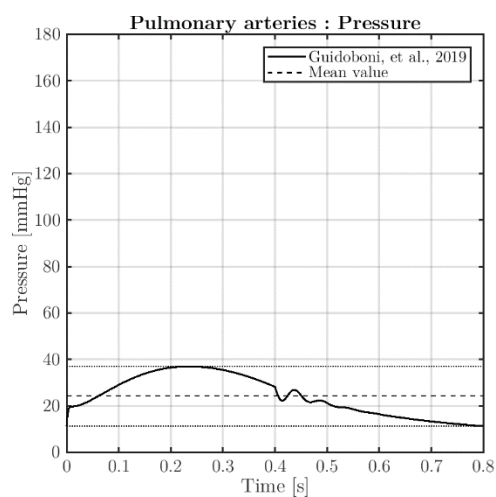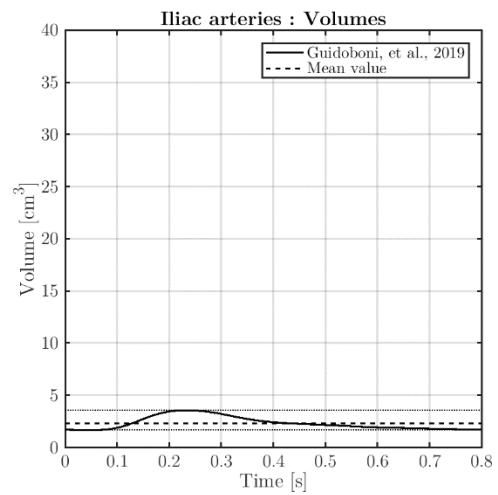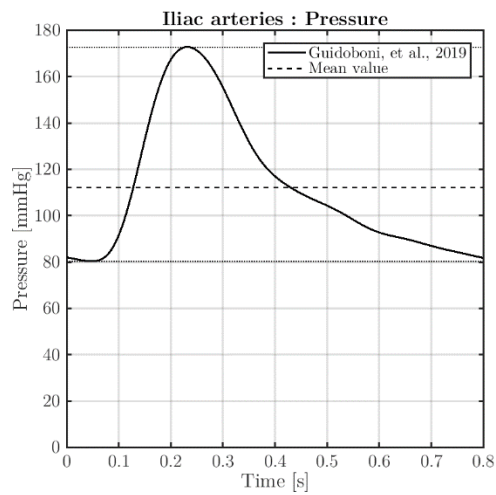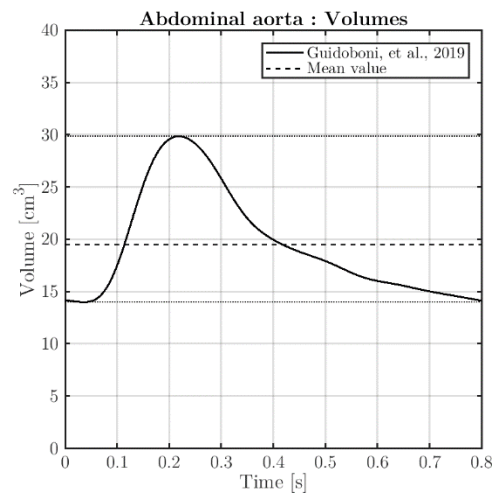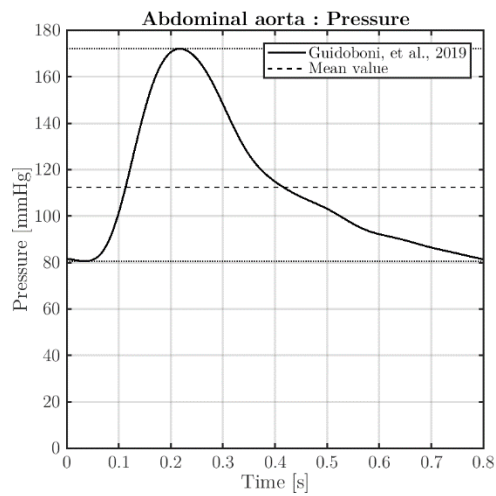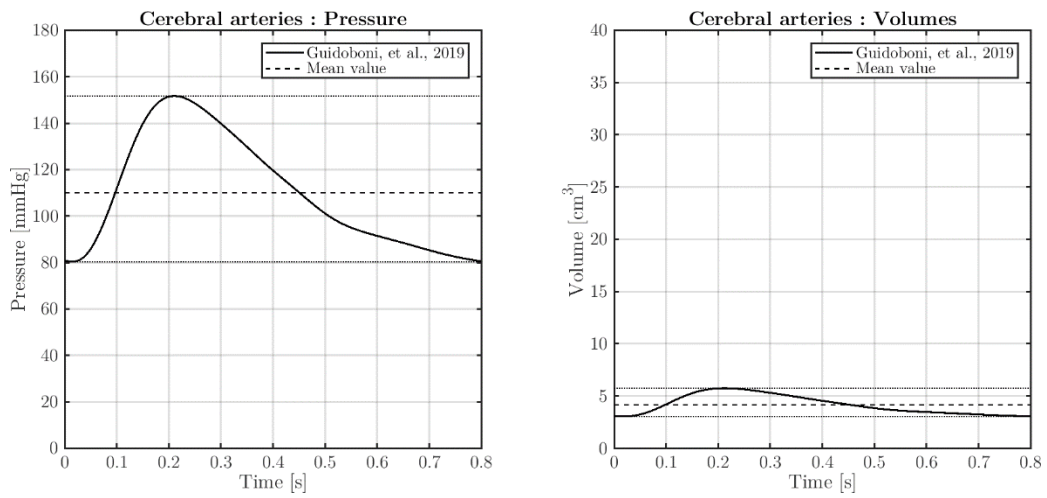
Figure 2.7 – Time evolution of pressure (left columns) and volume (right columns) in time (with respect to the last cardiac cycle simulated) of seven vascular compartments: ascending aorta, aortic arch, thoracic aorta, abdominal aorta, iliac arteries, pulmonary arteries, cerebral arteries.
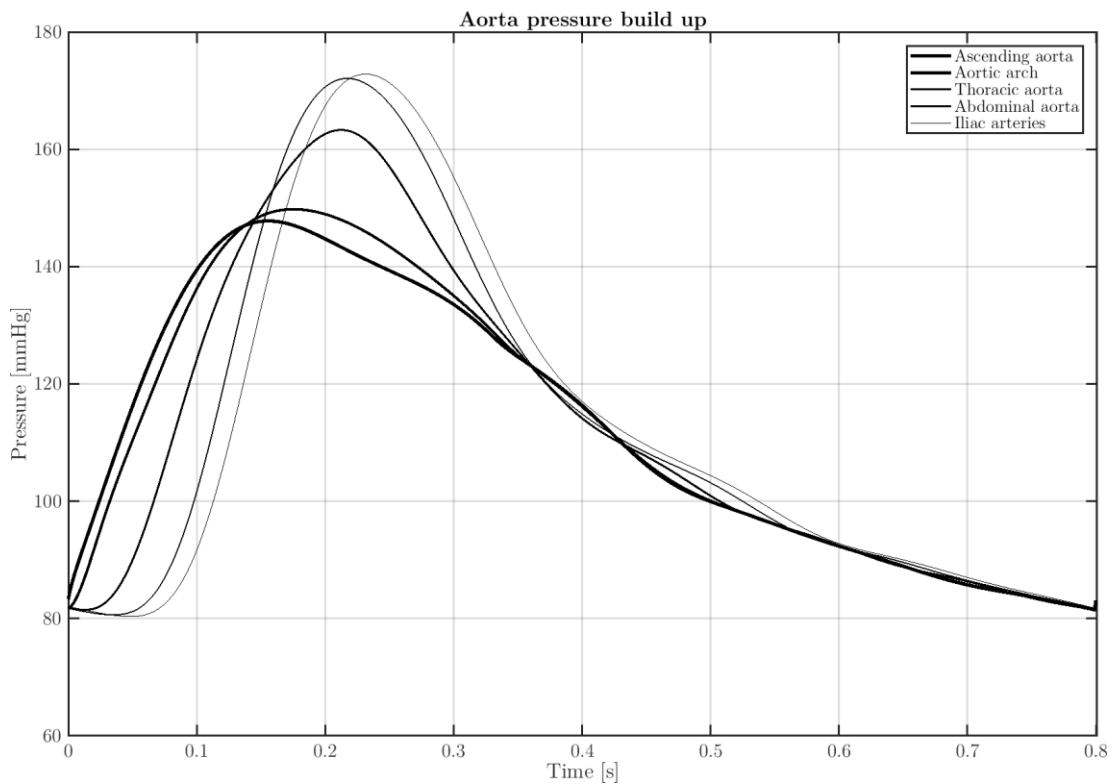
Figure 2.8 – Pressure waves of the five main arterial compartments of the torso superposed: ascending aorta, aortic arch, thoracic aorta, abdominal aorta, iliac arteries.

Additional validations of the model are proposed in (Guidoboni, et al., 2019).

Overall, the results presented in (Guidoboni, et al., 2019) provide evidence of the capability of the proposed closed-loop model to capture prominent features of cardiovascular physiology and support the utilization of the model output to construct a theoretical BCG, as discussed next.

2.2 Ballistocardiogram analysis

Ballistocardiography captures the signal generated by the repetitive motion of the human body due to sudden ejection of blood into the large vessels with each heartbeat (Starr & Noordergraaf, 1967). The signal is called ***ballistocardiogram* (BCG)**. Extensive research work by Starr and Noordergraaf showed that the effect of main heart malfunctions, such as congestive heart failure and valvular disease, would alter the BCG signal (Starr & Noordergraaf, 1967) (Starr & Wood, 1961) (Pinheiro & al, 2010), thereby yielding a great potential for passive, noncontact monitoring of the cardiovascular status.

As seen in Section 2.1.2, simulated arterial pressure waveforms and ventricular functions are in good qualitative and quantitative agreement with those reported in the clinical literature. The proposed closed-loop model should therefore be able to capture the predominant features of BCG signals and could be potentially used to predict pathological changes on the basis of fundamental mechanisms in cardiovascular physiology.

2.2.1 BCG theoretical background

Starr and Noordergraaf provided the theoretical foundations to interpret BCG signals by **expressing the displacement of the center of mass of the human body** as a function of the blood volumes occupying different vascular compartments at a given time during the cardiac cycle (Starr & Noordergraaf, 1967). Specifically, the coordinate Y of the center of mass of the body along the head-to-toe direction at any given time t can be written as:

$$Y(t) = \frac{\rho_b}{M} \sum_{i=1}^{N} V_i(t) \cdot y_i + c \tag{2.8}$$

where: ρ_b is the blood density;

M is the total body mass;

N is the total number of vascular compartments in the model;

$V_i(t)$ is the blood volume filling the compartment i at the time t;

y_i is the coordinate of the compartment i with respect to the heart plane;

c is a constant term representing the body frame.

In essence, <u>the Y motion of the body is obtained by multiplying the relative mass of each vascular compartment over the total body mass</u> ($\rho_b \cdot V_i(t) / M$) <u>by the coordinate y_i of the same vascular compartment</u>.

Since the term c in (2.8) is constant for a given person, the BCG signal associated with the **center of mass displacement** in the head-to-toe direction is defined as:

$$BCG_{disp}(t) := \frac{\rho_b}{M} \sum_{i=1}^{N} V_i(t) \cdot y_i \qquad (2.9)$$

The BCG signals associated with **velocity** and **acceleration** of the center of mass can be obtained via *time differentiation* as:

$$BCG_{vel}(t) = \frac{\rho_b}{M} \sum_{i=1}^{N} \frac{dV_i(t)}{dt} \cdot y_i \qquad (2.10)$$

$$BCG_{acc}(t) = \frac{\rho_b}{M} \sum_{i=1}^{N} \frac{d^2V_i(t)}{dt^2} \cdot y_i \qquad (2.11)$$

In our body, the waveforms $V_i(t)$ are the results of the complex interplay between the <u>blood volume ejected from the heart</u>, the <u>resistance to flow that blood experiences</u> across the cardiovascular system and the <u>pressure distribution</u> within it (Guidoboni, et al., 2019).

Starr and Noordergraaf characterized the volume waveforms $V_i(t)$ by means of experimental measurements at each location y_i (Starr & Noordergraaf, 1967).
Guidoboni, et al. instead, shown that the waveforms associated with $V_i(t)$ can be computed by means of a mathematical model based on the physical principles governing vascular physiology, thereby paving the way to the use of quantitative methods to interpret BCG signals and identify cardiovascular abnormalities in a given patient (Guidoboni, et al., 2019).

The first computer-aided approach for quantitative interpretation of BCG signals was proposed by Noordergraaf et al in (Noordergraaf & al., 1963), where the electric analogy to fluid flow was leveraged to describe the motion of blood through the arterial system during the cardiac cycle and calculate the resulting BCG signal. Since then, only a few studies have been directed to the theoretical construction and interpretation of BCG signals.

Wiard, et al. utilized a three-dimensional finite element model for blood flow in the thoracic aorta to show that the traction at the vessel wall appears to be of similar magnitude to recorded BCG forces (Wiard, et al., 2009).

Kim, et al. proposed a simplified model based on the equilibrium forces within the aorta to show that blood pressure gradients in the ascending and descending aorta are major contributors to the BCG signal (Kim, et al., 2016).

Despite their different approaches to blood flow modeling, the aforementioned studies share the common feature of focusing only on the arterial side of the cardiovascular system, thereby leading to *open-loop models* of the circulation.

In reality, though, our blood circulates within a **closed-loop system** and, as a consequence, hemodynamic changes observed at the level of the major arteries might be the result of changes occurring elsewhere within the closed-loop system. For example, left ventricular heart failure leads to an increase in fluid pressure that is transferred back to the lungs, ultimately damaging the right side of the heart and causing right heart failure (Bogaard & al., 2009). Another example is given by venothromboembolism, a disorder manifested by deep vein thrombosis and pulmonary embolism. Deep vein thrombosis occurs when a blood clot forms in a vein, most often in the leg, but they can also form in the deep veins of the arm, splanchnic veins, and cerebral veins (Di Nisio & al., 2016). A pulmonary embolism occurs when a clot breaks loose and travels to the pulmonary circulation, causing thrombotic outflow obstruction and a sudden strain on the right ventricle (Jolly & Phillips, 2018). Sequelae of such an event include decreased right ventricular cardiac output, poor overall cardiac output, and decreased systemic blood pressure.

The <u>main goal of developing a rich model</u> in terms of vascular compartments descriptions is to <u>include sufficient elements to reproduce theoretically the BCG signal and predict changes associated with specific pathological conditions</u> and to afford a *reference model* promising to serve as a <u>virtual laboratory</u> where cardiovascular dysfunctions can be simulated and their manifestation on the BCG signal can be characterized.

• *BCG-related model features*

The closed-loop model is utilized to <u>construct the BCG signal theoretically</u> by substituting in (2.9), (2.10) and (2.11) the volume waveforms computed via the solution of the mathematical model.

The following nine contributions, ($N = 9$), are included in the calculations for the BCG signal:

- The volume waveforms pertaining to the left and right ventricles (nodes 1, 10),
- Four aortic segments (nodes 2, 3, 4, 5),
- Iliac arteries (node 6),
- Pulmonary arteries (node 11),
- Cerebral arteries (node 14).

In Figure 2.9 the main systemic arteries are shown.
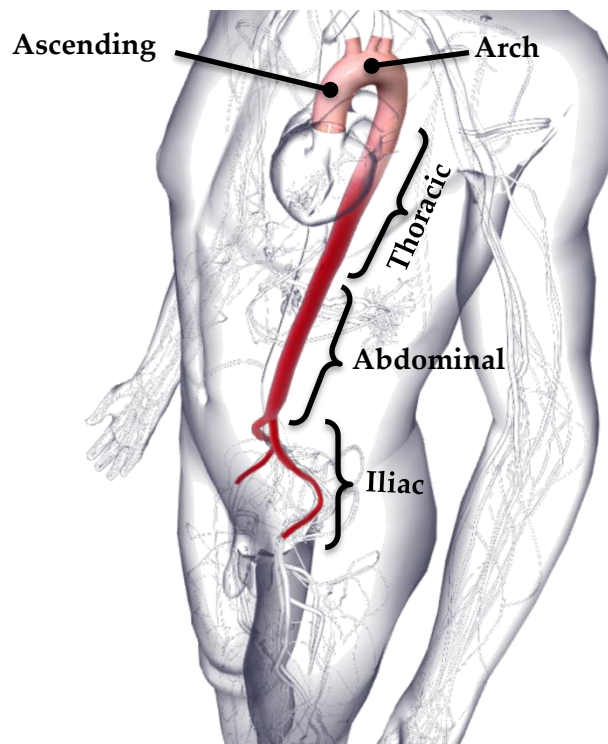
Figure 2.9 – 3D image of the body[5]. The main arteries included in the closed-loop model are highlighted in red.

---

[5] Image generated with the human.biodigital widget:
https://human.biodigital.com/widget/?m=production/maleAdult/male_complete_anatomy_08.json

The calculation of the BCG signal requires the values of the coordinates representing the distance of each compartment of interest from an ideal plane.

The movement of the blood inside the main vessels is tridimensional and so is the movement of the center of mass of a subject. Traditionally, head-to-toe BCG (called BCGy, by considering the y-direction associated to head-to-toe direction) is the only signal reported and is the most studied. Since the main vessels go along the head-to-toe direction, BCGy is the stronger signal but we will see that is worth considering also the BCGz (which is the signal associated to the movement of the center of mass of the body with respect to the back-front direction). It can be noticed from experiments that the weaker signal is the BCGx, probably due to the greater symmetry of the vessels with respect to the left-right direction, and so is not taken into account for our computations.

For the computation of the BCGy, the considered reference plane is the *ventricular valves plane*, see Figure 2.10. For the computation of the BCGz, instead, the reference plane is positioned at the *centroid of the thoracic aorta* adjacent to the vertebral column.

The values adopted in this work are summarized in Table 2.5.
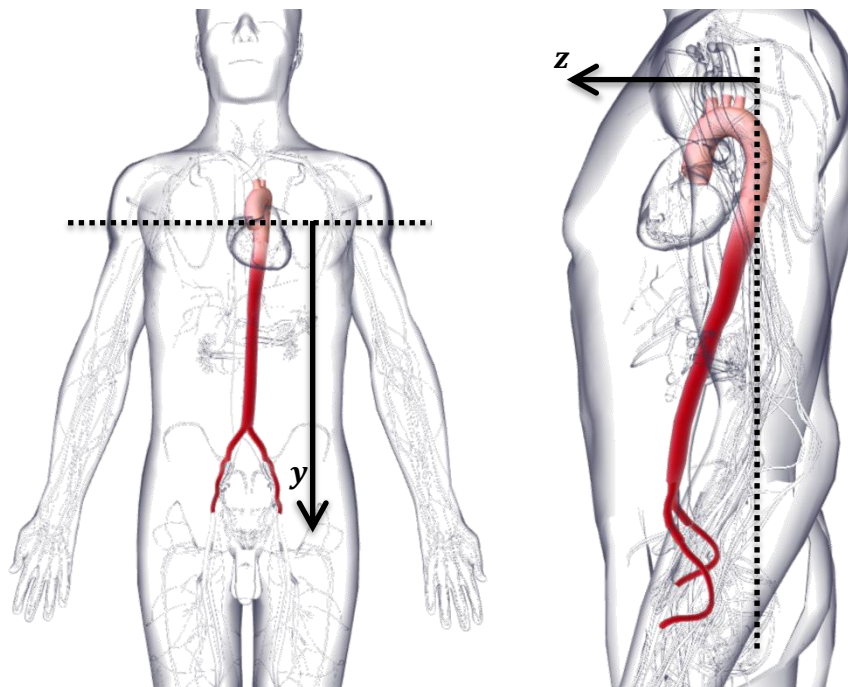
Figure 2.10 – Main arteries included in the closed-loop model with reference planes.

Node	Compartment	Segment	y_i [cm]	z_i [cm]
1	Heart	Left Ventricle	+0.5	-
10	Heart	Right Ventricle	+0.5	-
2	Systemic	Ascending Aorta	-2	-
3	Systemic	Aortic Arch	-7	+1
4	Systemic	Thoracic Aorta	+20	-
5	Systemic	Abdominal Aorta	+35	+4
6	Systemic	Iliac arteries	+45	+6
11	Pulmonary	Pulmonary Arteries	-5	-
14	Cerebral	Cerebral Arteries	-10	+4

Table 2.5 – Circuit nodes considered for BCG computations with specified y_i and z_i positions.

2.2.2 Simulated BCG

The volume waveforms simulated using the closed-loop model (see Figure 2.1) can be substituted in (2.9) to calculate theoretically the waveform $BCG_{disp}(t)$ associated with the displacement of the center of mass.

The BCG waveforms for velocity and acceleration, namely $BCG_{vel}(t)$ and $BCG_{acc}(t)$, are obtained from $BCG_{disp}(t)$ via <u>discrete time differentiation</u>.

Following (Starr & Noordergraaf, 1967) and (Guidoboni, et al., 2019), the BCG waveforms are reported by means of the **auxiliary functions** f_D, f_V and f_A defined as:

$$BCGy : \begin{cases} \boldsymbol{f_D(t)} = \left(M \cdot BCGy_{disp}(t) \right) = \boxed{\rho_b \sum_{i=1}^{N} V_i(t)\, y_i} & [g\ cm] \\[2ex] \boldsymbol{f_V(t)} = \left(M \cdot BCGy_{vel}(t) \right) = \boxed{\rho_b \sum_{i=1}^{N} \frac{dV_i(t)}{dt}\, y_i} & [g\ cm\ s^{-1}] \\[2ex] \boldsymbol{f_A(t)} = \left(M \cdot BCGy_{acc}(t) \right) = \boxed{\rho_b \sum_{i=1}^{N} \frac{d^2V_i(t)}{dt^2}\, y_i} & [dyne] \end{cases} \qquad (2.12)$$

These auxiliary functions are independent of the value of the mass M and, as a consequence, they <u>allow for a fair comparison between BCG waveforms</u> reported in different studies.

Figure 2.11 reports the simulated BCG in terms of the auxiliary functions (2.12) presented above over two consecutive cardiac cycles (the last two of the simulation including 8 cycles).
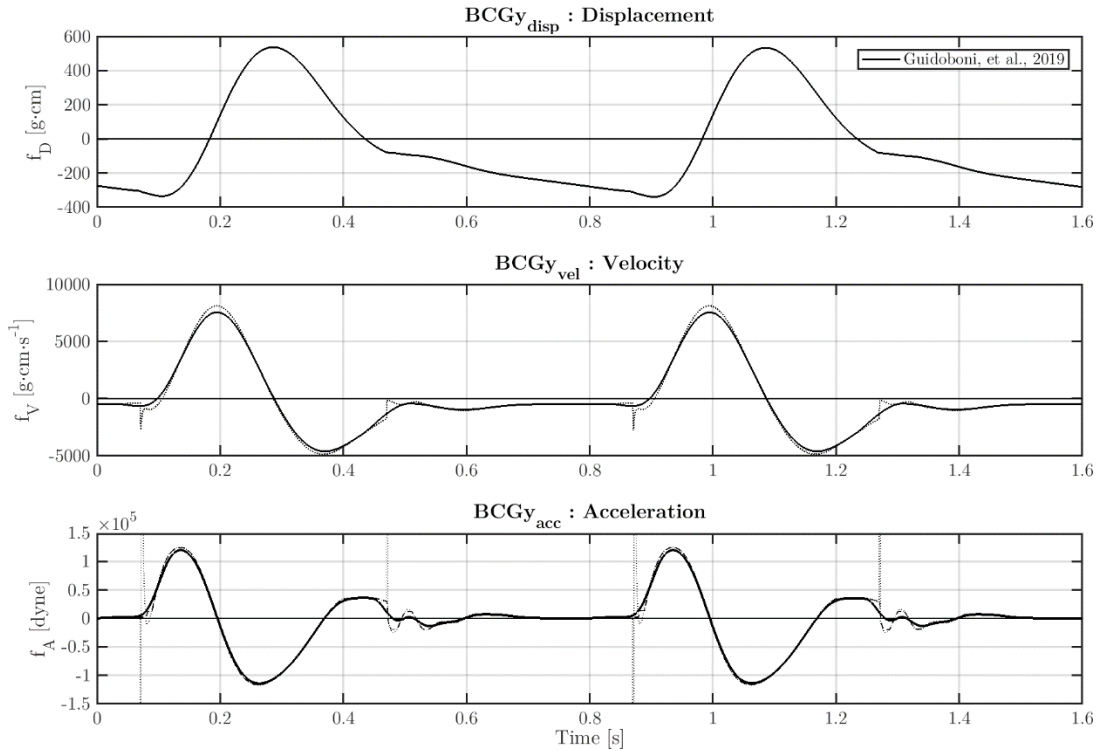
Figure 2.11 – Ballistocardiogram with displacement, velocity and acceleration associated with the closed-loop circuit model.

Figure 2.12 reports a zoom of the $f_A(t)$ function, simulated via the closed-loop model over one cardiac cycle. Note that the bold curve is the result of a filtering process, better described in Section 2.4.1, which takes the "rough curve" obtained directly from the model and applies high peaks cleaning and appropriate other signal filters. The waveform exhibits the typical **I**, **J**, **K**, **L**, **M** and **N** peaks and valleys that characterize BCG signals measured experimentally, as in (Starr & Noordergraaf, 1967), thereby confirming the capability of the closed-loop model to capture the fundamental cardiovascular mechanisms that give rise to the BCG signal.

In this perspective, the closed-loop model presented in (Guidoboni, et al., 2019) could be used to perform a sensitivity analysis to identify the cardiovascular parameters that influence the BCG signal the most. In addition, the output of the proposed closed-

loop model could be coupled with models describing the functioning principles of the specific measuring device in order to better interpret the acquired BCG signal.
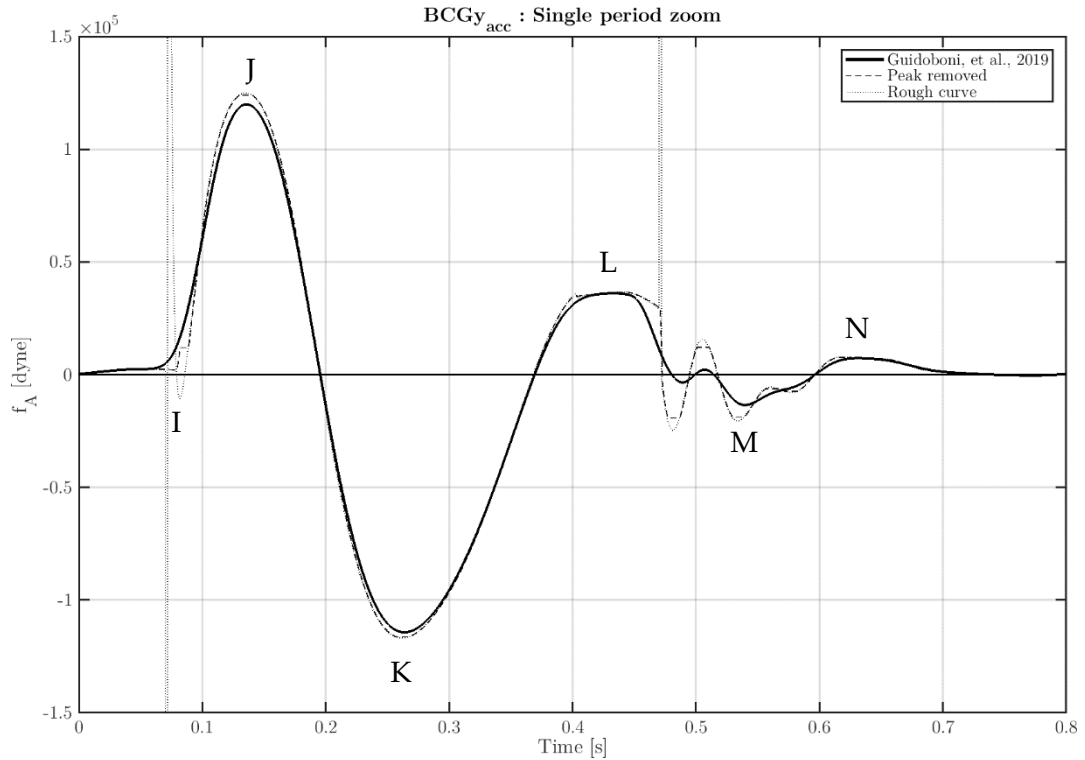
Figure 2.12 – Acceleration BCG over one cardiac cycle associated with the closed-loop circuit model.

• *BCGz*

Using the same theoretical background presented above, also the ballistocardiogram in the *z* direction can be simulated using the closed-loop model. This part is a partial novelty in the field since, in the available literature, the BCGz is always disregarded.

Making reference to the set of equations (2.12), the following set of equations can be derived by analogy for the **BCGz computation**:

$$BCGz : \begin{cases} \boldsymbol{f_D}(\boldsymbol{t}) = \left(M \cdot BCGz_{disp}(t) \right) = \boxed{\rho_b \sum_{i=1}^{N} V_i(t) \, z_i} & [g \; cm] \\[2em] \boldsymbol{f_V}(\boldsymbol{t}) = \left(M \cdot BCGz_{vel}(t) \right) = \boxed{\rho_b \sum_{i=1}^{N} \frac{dV_i(t)}{dt} \, z_i} & [g \; cm \; s^{-1}] \\[2em] \boldsymbol{f_A}(\boldsymbol{t}) = \left(M \cdot BCGz_{acc}(t) \right) = \boxed{\rho_b \sum_{i=1}^{N} \frac{d^2V_i(t)}{dt^2} \, z_i} & [dyne] \end{cases} \quad (2.13)$$
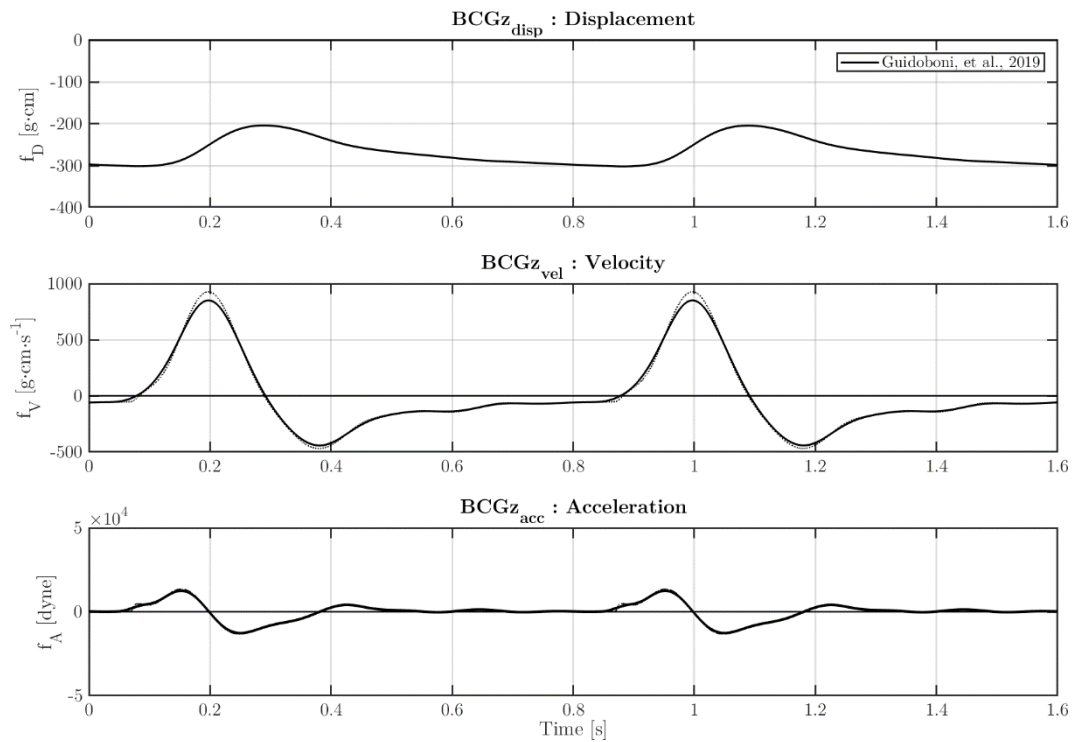
Figure 2.13 – Ballistocardiogram in the *z* direction (BCGz) with displacement, velocity and acceleration associated with the closed-loop circuit model.
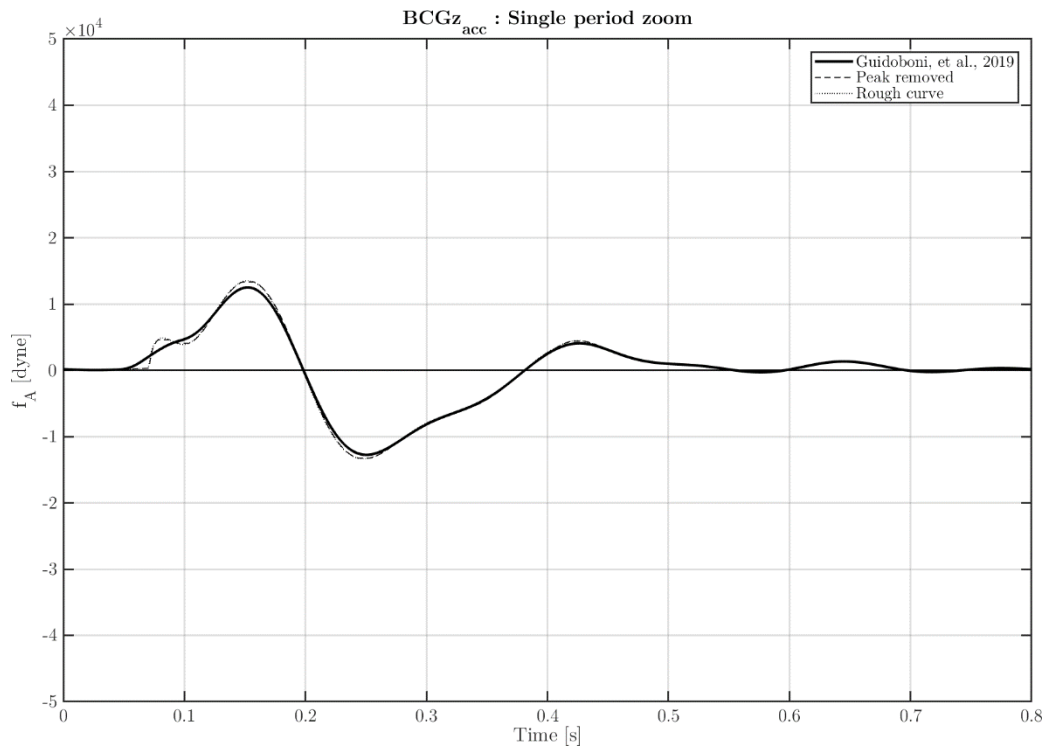
Figure 2.14 – Acceleration BCGz over one cardiac cycle associated with the closed-loop cir-cuit model.

The coordinates z_i are reported in Table 2.5 as well.

The simulated BCGz, computed using the closed-loop model, is presented in Figure 2.13 and Figure 2.14. Please note that the comparisons are done with respect to the bold curve which is the final curve obtained after a filtering process better described in Section 2.4.1.

Combined 2D movement:

Having at this point the BCG signals computed along 2 spatial directions, it is possible to plot the movement of the computed center of mass of the subject as well as its associated velocity and acceleration in a 2D plot along the y-z plane. See Figure 2.15.
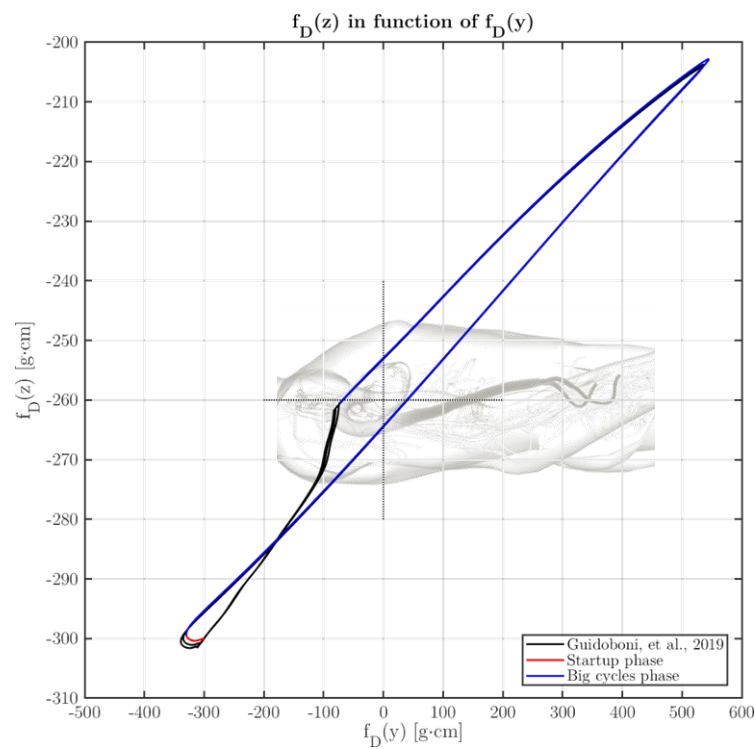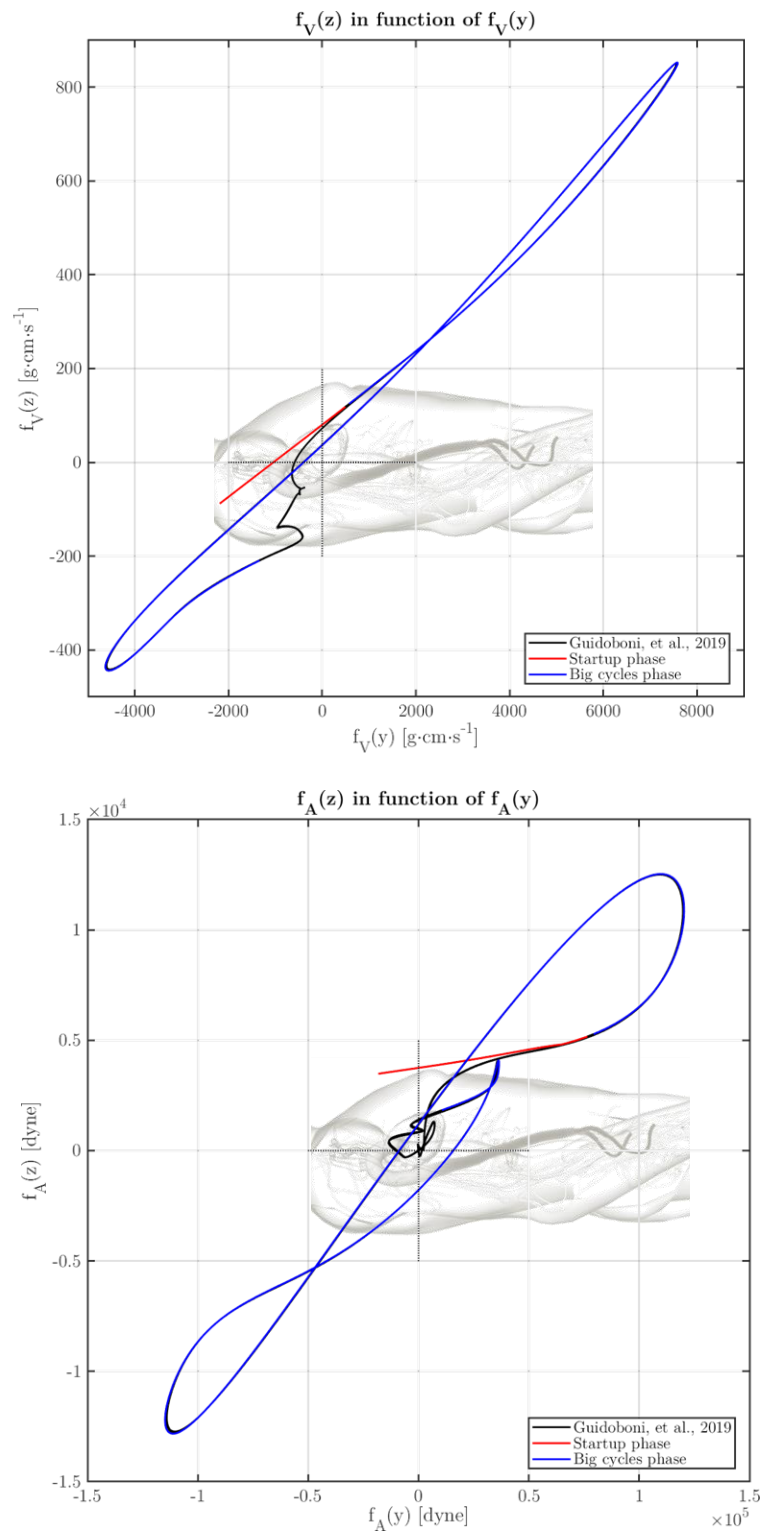
Figure 2.15 – Movement of the computed center of mass of the subject, its associated velocity and its acceleration in a 2D plot on the y-z plane.

2.3 Role of the activation function

As already introduced in Chapter 2.1 (Closed-loop model for the cardiovascular system), the **activation function** is a function characterizing <u>ventricular contractions</u>. It is also the function governing the pumping timing.

As mentioned, each activation function should be tailored to the specific circuit. For Model 5 (Guidoboni, et al.) it is the function $A(t)$ expressed in Chapter 2.1.1 and recalled here for reference, see (2.5):

$$A(t)_{Guidoboni,et\ al.} = \begin{cases} \boxed{\dfrac{1}{2}\left[\tanh(q_{L/R} \cdot t_a) - \tanh(q_{L/R} \cdot t_b)\right]} & \text{if } t_m < T_s \\ 0 & \text{if } t_m \geq T_s \end{cases} \qquad (2.5)$$

Considering instead one of the first example of closed loop models Model 0 (Avanzolini, et al.), which is better analyzed in Section 2.5.1, it has a completely different activation function, it is:

$$A(t)_{Avanzolini} = \begin{cases} \boxed{\dfrac{1}{2}\left[1 - \cos\left(2\pi\dfrac{t_m}{T_s}\right)\right]} & \text{if } t_m < T_s \\ 0 & \text{if } t_m \geq T_s \end{cases} \qquad (2.14)$$

Figure 2.16 shows a comparison between the two considered activation functions.
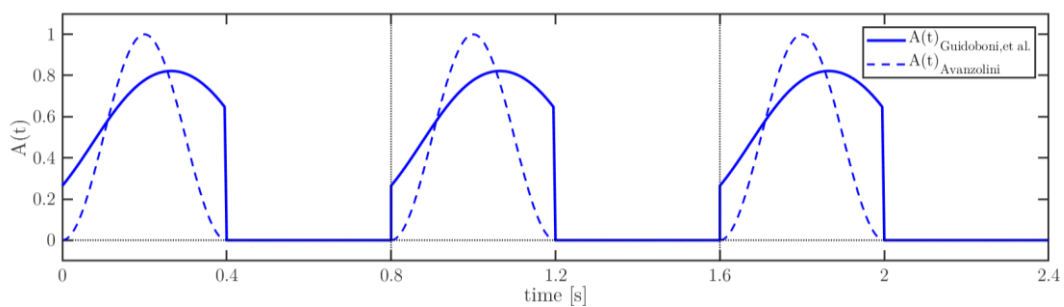
Figure 2.16 – Activation function comparison.

• *Simulated BCG and activation function's role*

For comparison purposes, in this section the BCG simulated by Model 0 (Avanzolini, et al.) and by the reference model Model 5 (Guidoboni, et al.), called here "Model 5" <u>using swapped activation functions</u> (Model 0 uses relation (2.5) and Model 5 relation (2.14)), are reported and compared.

It can be clearly seen from Figure 2.18 and from Figure 2.19 that the activation function can modify the response in terms of BCG curves, but it is not enough to make Model 0 (Avanzolini, et al.) suitable for BCG computations.

In addition, from Figure 2.20 and Figure 2.21 it can be noticed how crucial the definition of a specifically tailored activation function may be. In fact, Model 5 (Guidoboni, et al.), associated with the activation function of Model 0 (Avanzolini, et al.), brings to greatly inaccurate BCG curves, the curves goes even out of scale in this case! Whereas the same circuit with the tailored activation function allows accurate characterization of the BCG signal.

Finally, the pressure-volume curve is reported in Figure 2.17 to emphasize the modifications in the amplitude brought to the model by an incorrect activation function:
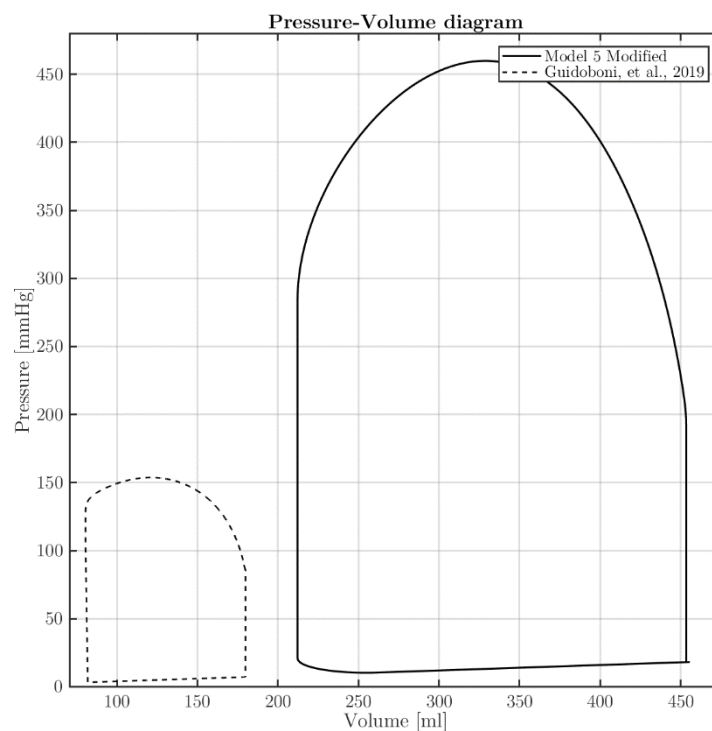
Figure 2.17 – Pressure over volume cycle of Model 5 (Guidoboni, et al.) implemented with the Avanzolini activation function (2.14) compared to the standard Model 5 (Guidoboni, et al.).
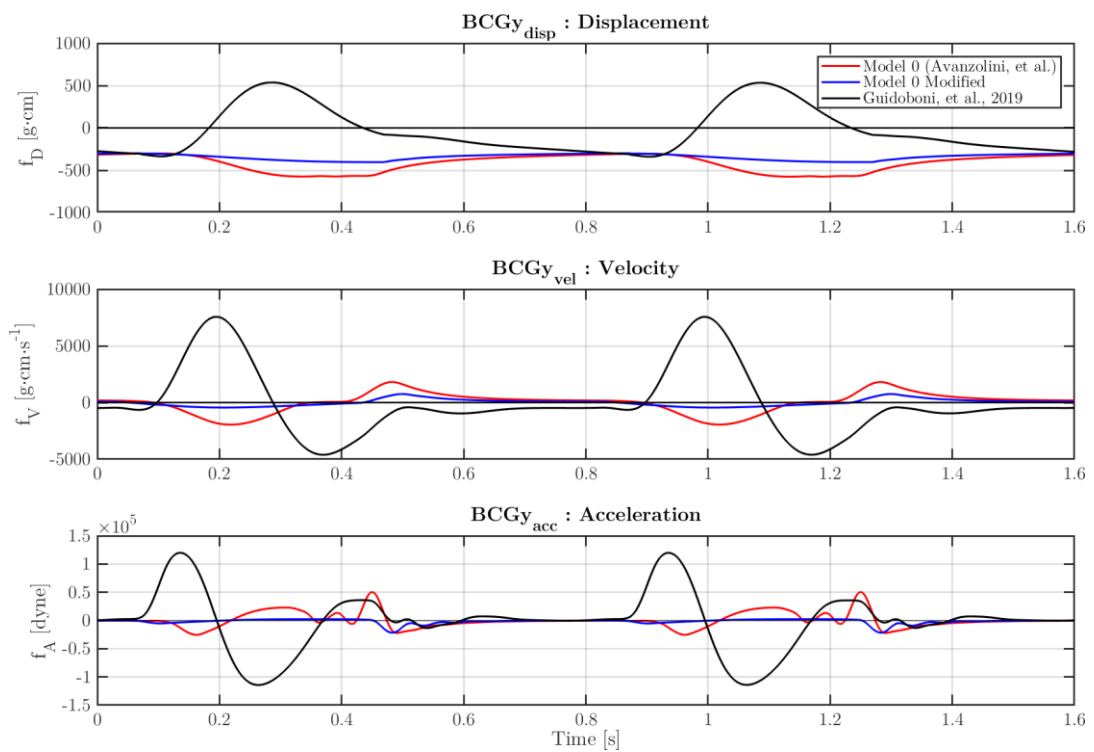
Figure 2.18 – Simulated BCG obtained from: (I) standard Model 0 (Avanzolini, et al.), (II) Model 0 (Avanzolini, et al.) implemented with the activation function of Model 5 (Guidoboni, et al.) (2.5), (III) Model 5 (Guidoboni, et al.).
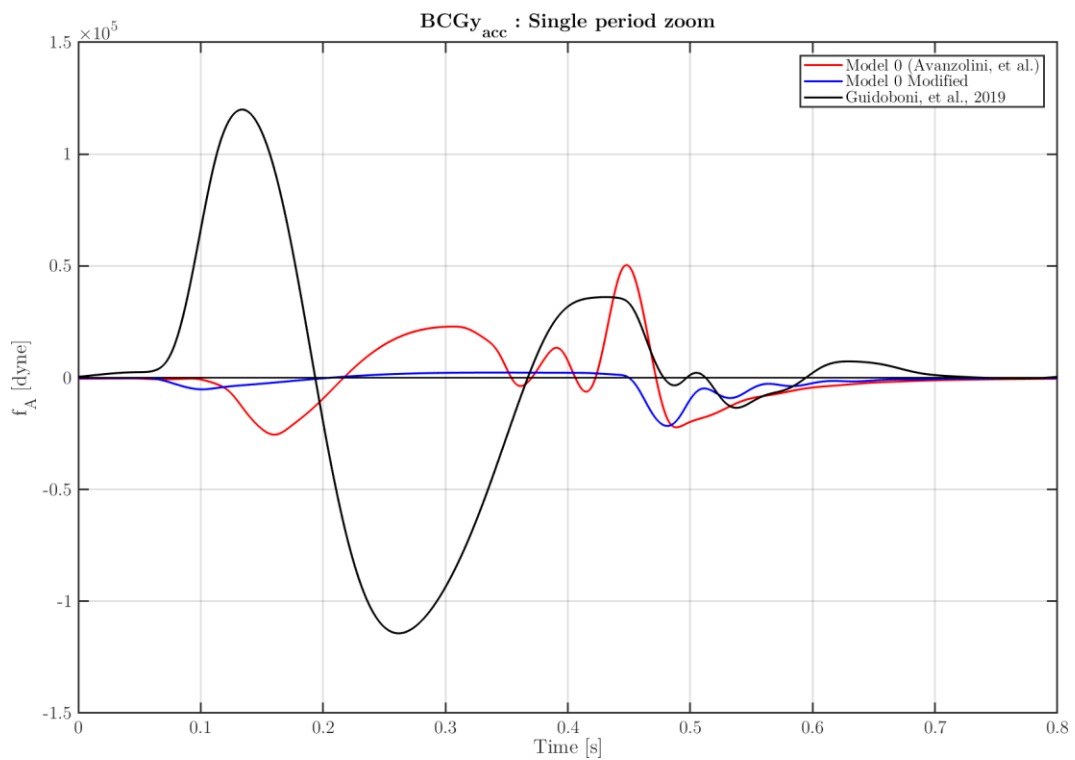
Figure 2.19 – Acceleration BCG over one cardiac cycle of the previous Figure 2.18.
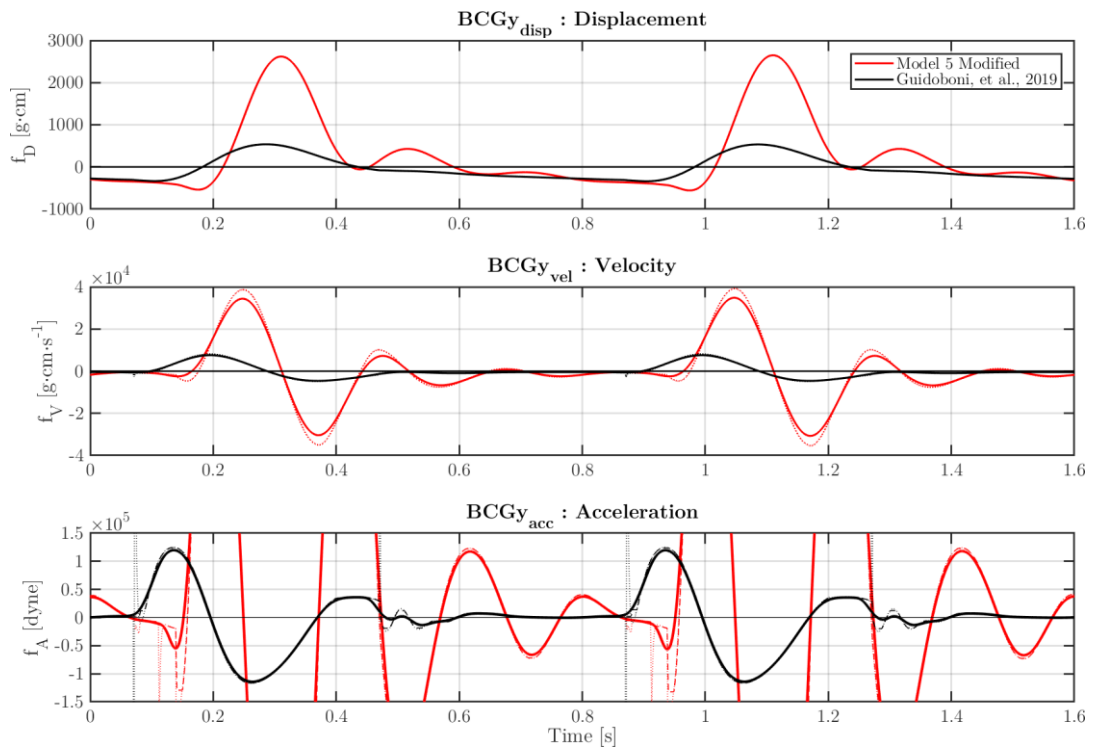
Figure 2.20 – Simulated BCG obtained from: (I) Model 5 (Guidoboni, et al.), (II) Model 5 (Guidoboni, et al.) implemented with the activation function of Model 0 (Avanzolini, et al.) (2.14).
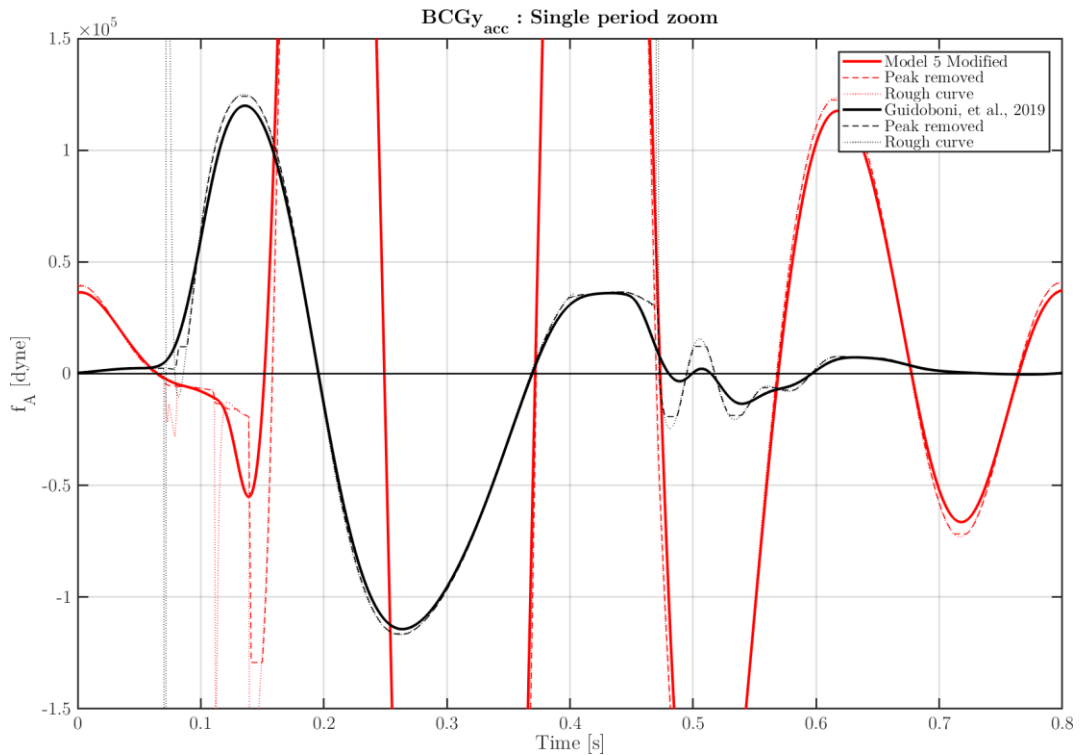
Figure 2.21 – Acceleration BCG over one cardiac cycle of the previous Figure 2.20.

54

2.4 Role of viscoelasticity

In Chapter 2.1 (Closed-loop model for the cardiovascular system) the mathematical description of the *viscoelasticity feature,* brought to the model by using *variable capacitors*, was discussed.

In this section a deeper analysis about the viscoelasticity role is performed.

The expression of the circuit component responsible for the viscoelastic property of the arterial wall (the *variable capacitor*) is here reported, see (2.15) (see Table 2.2 for additional references).
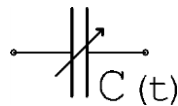
$$\Delta p = \frac{V}{C} + \gamma \frac{dV}{dt} \tag{2.15}$$

with: V Fluid volume;

         C Capacitance constant;

         γ Viscoelastic constant.

If the viscoelastic constant is null, $\gamma = 0$, the system will exhibit a purely elastic behavior, with deformations synchronous to stresses, without the natural smoothing provided by viscoelastic effects.

In the following, Model 5 (Guidoboni, et al.) is analyzed by setting $\gamma = 0$ (no viscoelasticity) in every capacitor, see the results in Figure 2.22 and Figure 2.23.

It can be seen from the BCG that a strong <u>oscillatory pattern</u> arises and it is not smoothed even after eight cardiac cycle simulations as it normally would be.
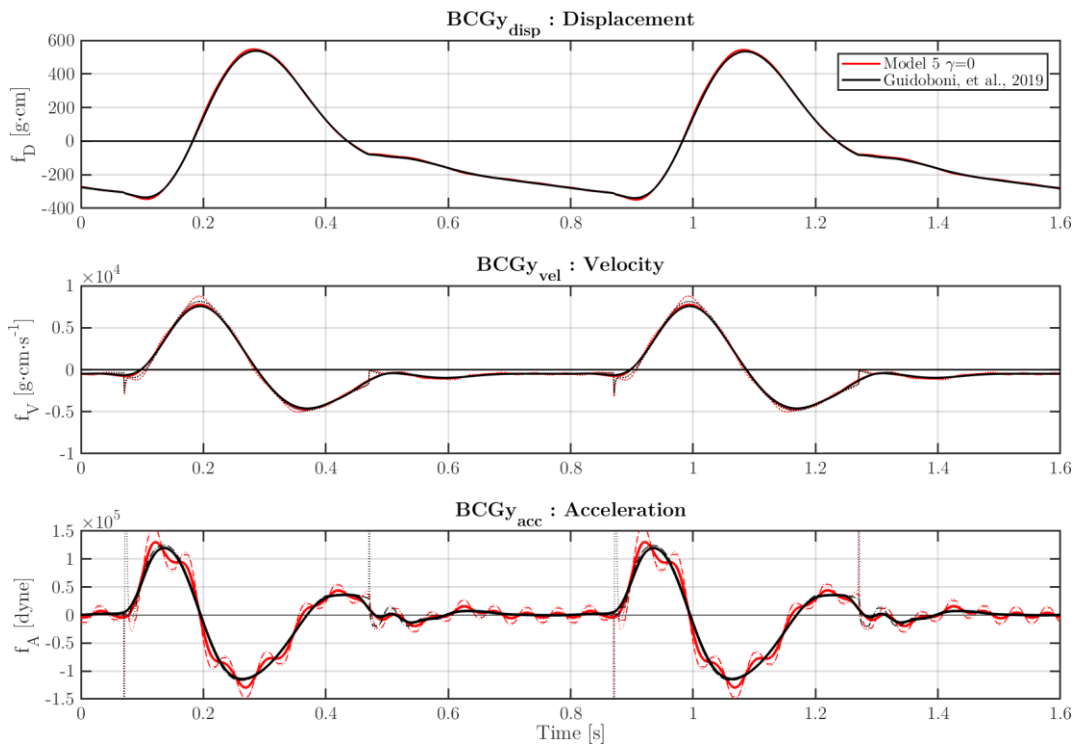
Figure 2.22 – Simulated BGG of Model 5 (Guidoboni, et al.) not including viscoelasticity ($\gamma = 0$), compared to the standard Model 5 (Guidoboni, et al.).
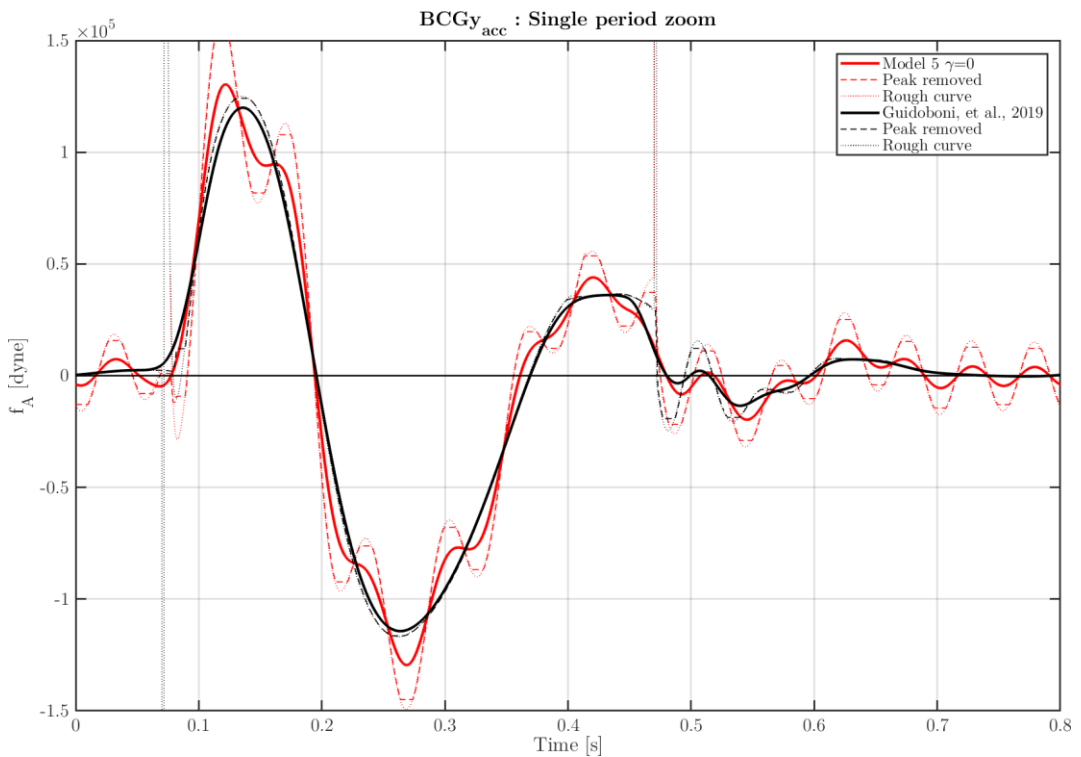
Figure 2.23 – Acceleration BCG over one cardiac cycle of the previous Figure 2.22.

The pressure-volume curve is also obtained and reported in Figure 2.24. It can be noticed that this time, the plot is not significantly modified by the viscoelasticity effects. This is because this graph is referred to the ventricle, and thus it is not affected directly by the arteries stiffness modification.
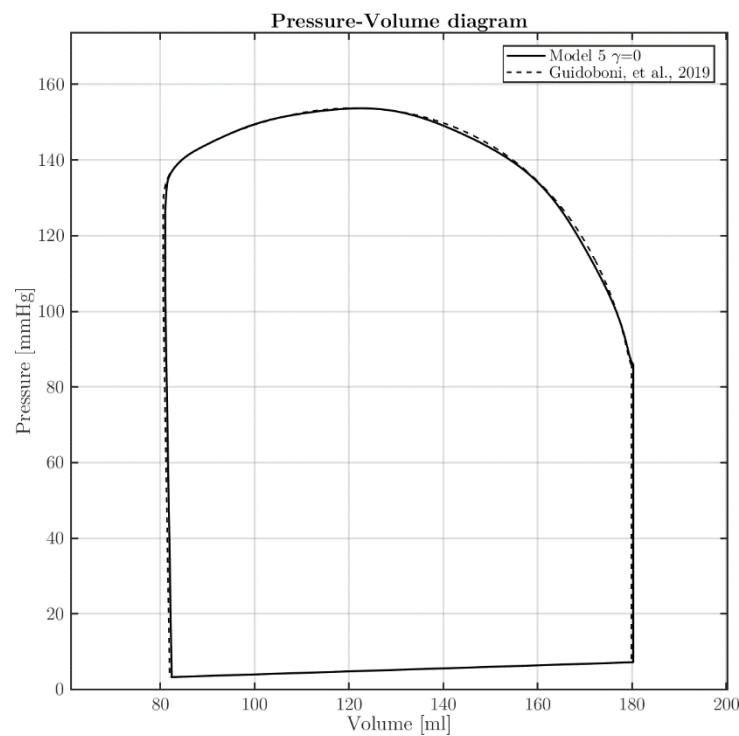
Figure 2.24 – Pressure over volume cycle of Model 5 (Guidoboni, et al.) not including viscoelasticity ($\gamma = 0$), compared to the standard Model 5 (Guidoboni, et al.).

From computing instead the pressure and volume curves related to the main compartments considered, see Figure 2.25, it can be noticed the occurrence of an **oscillatory pattern** (in the absence of viscoelasticity) as already observed analyzing the BCG signal. This behavior can be explained considering that $\gamma = 0$ means that the model does not have a natural smoothing capability, and therefore any perturbation is propagated being only partially damped.

Figure 2.25 – Simulated pressure and volume changes in time, measured in the aortic arch part (on the top) and in the abdominal aorta part (on the bottom), associated with Model 5 (Guidoboni, et al.) deprived of the viscoelasticity feature ($\gamma = 0$).

2.4.1 Signal processing, filtering and smoothing

Considering the natural filtering role played by viscoelasticity, it results immediately clear that the signal processing technique is important to get reliable results.

The smoothing and filtering procedure applied in every BCG curve present in this thesis are reported here below:

1. Obtain the **rough BCG curve**, which is the curve directly obtained solving the model using OpenModelica;

2. Remove the sharp spikes from it by using a **peak removal tool** (in this case a median filter applied over a moving window including 20 samples)

3. Smooth the obtained curve without spikes with a linear fit **smoothing filter** operating over a moving window of 60 samples at a time.

Figure 2.26 shows a comparison between 3 BCG curves:
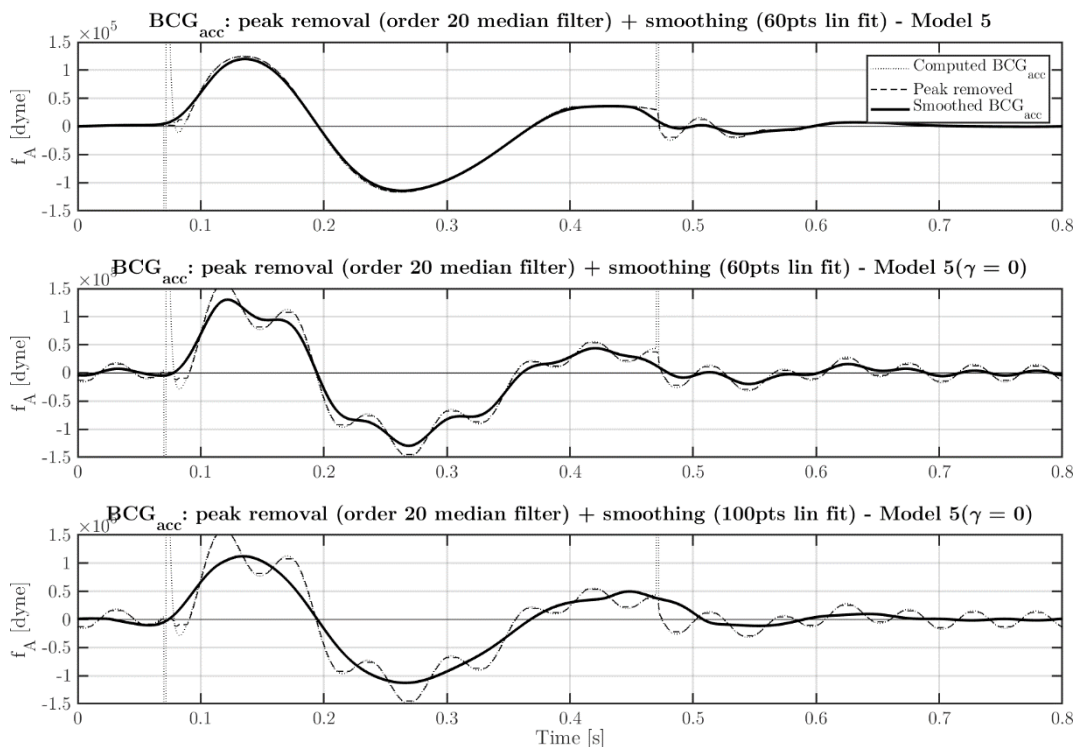
Figure 2.26 – Simulated BCG obtained from Model 5 (Guidoboni, et al.) with different filtering and smoothing techniques applied.

- The **first curve** is the standard BCG obtained from Model 5 (Guidoboni, et al.) introduced in Chapter 2.2, with applied the spike removal filter and the smoothing filter with 60 samples resolution (the "standard reference" from now on).

- The **second curve** is obtained from Model 5 (Guidoboni, et al.) not including viscoelasticity ($\gamma = 0$), with a peak-removal filter and the smoothing filter with 60 samples resolution as done in the other graphs. It can be seen that, despite the curve is smoothed, the difference in the final curve compared to the first one is clear and the small waves can be effectively identified.

- The **third curve** is obtained from the same rough data used for the second one, but in this case a larger smoothing <u>filter operating over 100 samples</u> is applied. The result is a curve very similar to the first one. <u>This filtering can be very dangerous</u>, in fact from the final curve no small waves can be seen, and so a condition of reduced elasticity of the arteries, simulated by the model by a reduced viscoelasticity, cannot be assessed!

2.5 Origins and analysis of the closed-loop model

In this section, the reference closed-loop model is compared with alternative simpler versions.

Starting from the first model proposed by (Avanzolini, et al., 1988), which includes only a lumped description of the main arteries, other models with increasing levels of detail in the main arteries and the cerebral arteries are analyzed step-by-step.

Since the BCGz was not implemented in the considered references, the analysis concerns the BCGy signal only (along the head-to-toe direction).

The following Table 2.6 shows the considered models characteristics:

Model type	Heart LV+RV	Pulmonary circulation	Asc	Arc	Thor	Abd	Iliac	Body	Cerebral circulation
Model 0 (Avanzolini, et al.)	✔	✔						✓	✗
Model 1	✔	✔	Group **1**		Group **2**			✓	✗
Model 2	✔	✔	✓	✓	✓	Group **3**		✓	✗
Model 3	✔	✔	Group **1**		Group **2**			✓	✔
Model 4	✔	✔	✓	✓	✓	Group **3**		✓	✔
Model 5 (Guidoboni, et al.)	✔	✔	✓	✓	✓	✓	✓	✓	✔

Table 2.6 – Closed-loop models considered features.

2.5.1 MODEL 0: A first example of closed-loop circuit model

The starting point for the development of the closed-loop model presented in Section 2.1 is the model proposed by Avanzolini in 1988 (Avanzolini, et al., 1988). Figure 2.27 shows the original circuital scheme, and Figure 2.28 shows the relative anatomical interpretation.
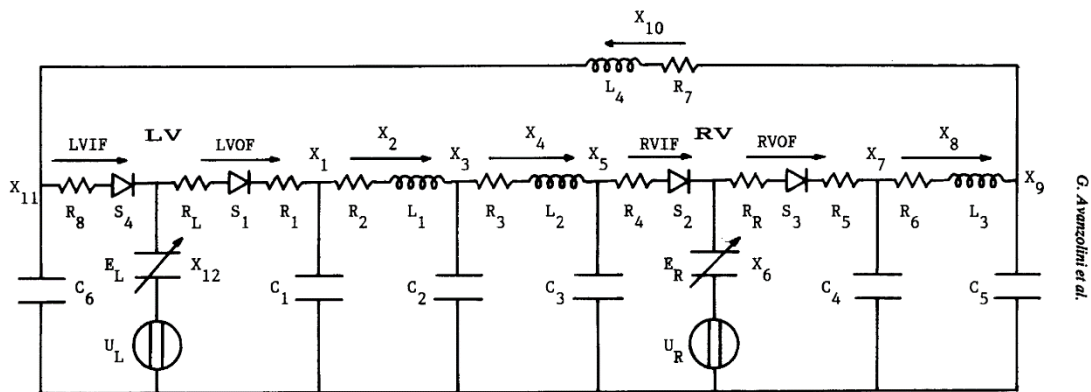
Figure 2.27 – Electric analog model of the closed-loop cardiovascular system proposed in (Avanzolini, et al., 1988).

The main feature of Model 0 (Avanzolini, et al.) is the utilization of a closed-loop network that allows to simulate feedback phenomena in the cardiovascular system.

In the following we illustrate how to use the scheme of Figure 2.27 to simulate the ballistocardiogram signal.

• Simulated BCG

Computing the ballistocardiogram associated with Model 0 (Avanzolini, et al.), and superposing it to Model 5 (Guidoboni, et al.), brings to the curves in Figure 2.29 and Figure 2.30.

It is important to note that, to compute the BCGy of this model, the y_i coordinates of the considered compartments are mantained the same as Table 2.5 (neglecting the coordinates of the parts not present in the model).
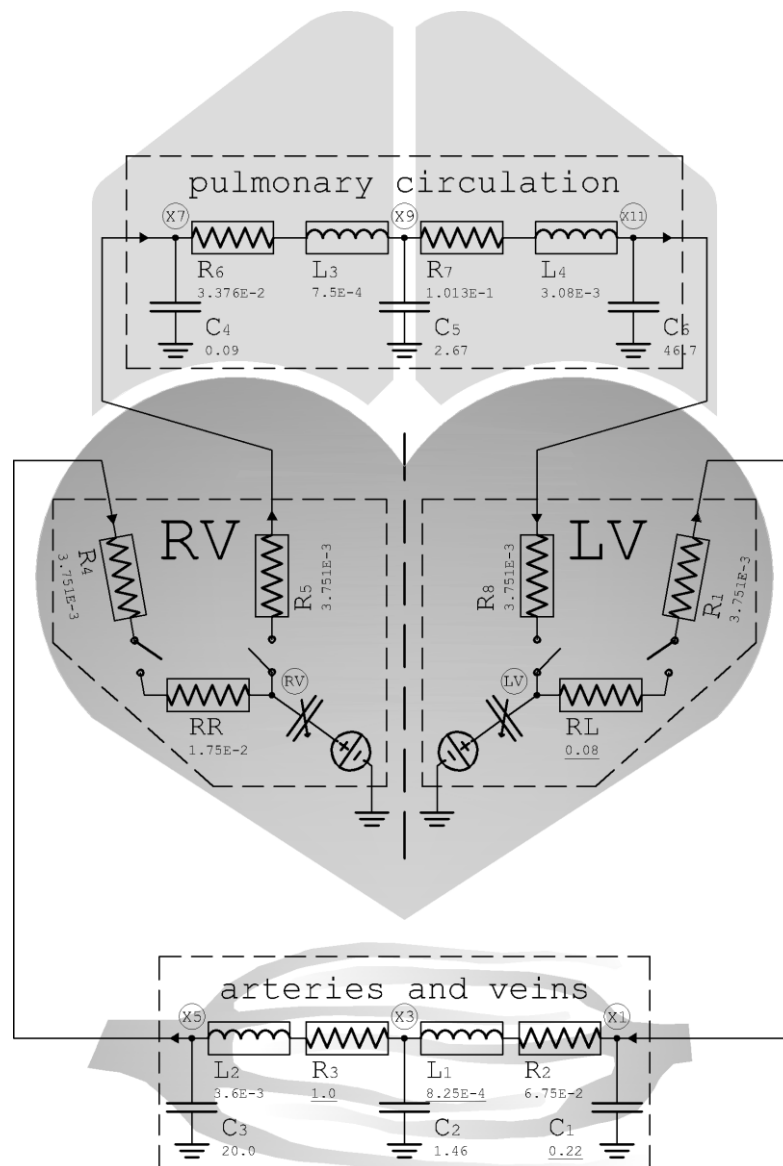
Figure 2.28 – Anatomical interpretation of the closed-loop model proposed in (Avanzolini, et al., 1988).

The figures show that the model by Avanzolini, et al. does not include enough details in order to capture the BCG curve. In fact, only the M peak can barely be seen, while the other peaks even appear reversed in sign.

The differences can be easily explained considering that Model 0 (Avanzolini, et al.) does not contain an extensive description of the main arteries, therefore the dynamic effect of the volume of fluid moving in them cannot contribute to the construction of the ballistocardiogram.
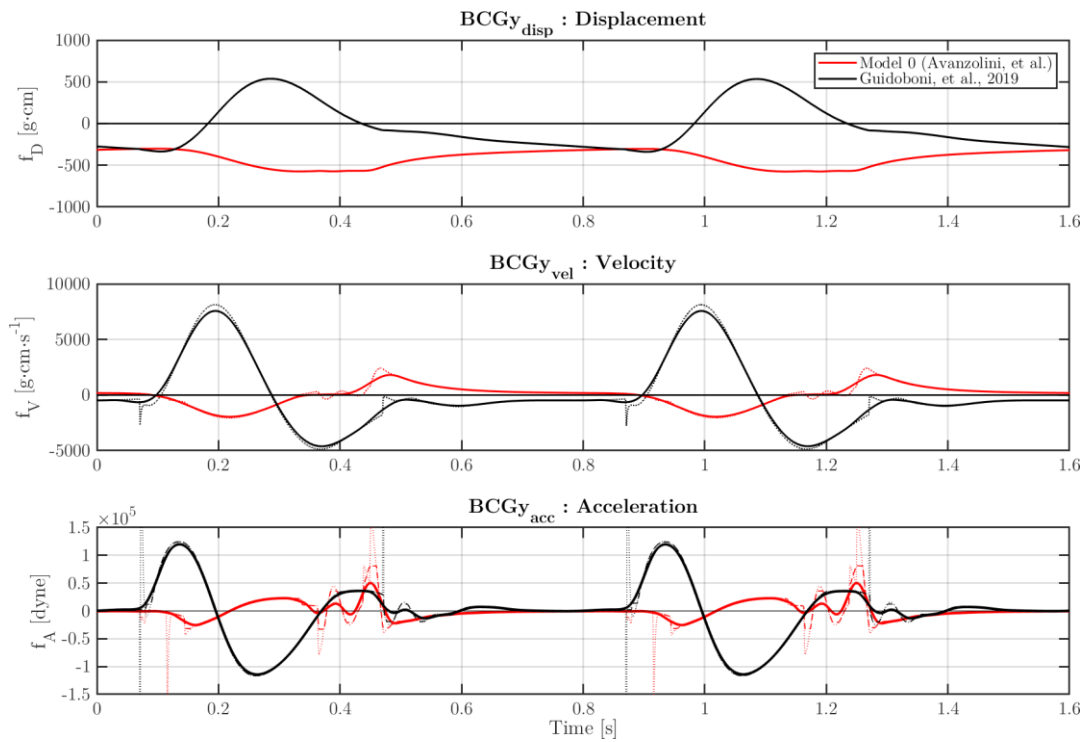
Figure 2.29 – Simulated BCG of Model 0 (Avanzolini, et al.), compared to Model 5 (Guidoboni, et al.).
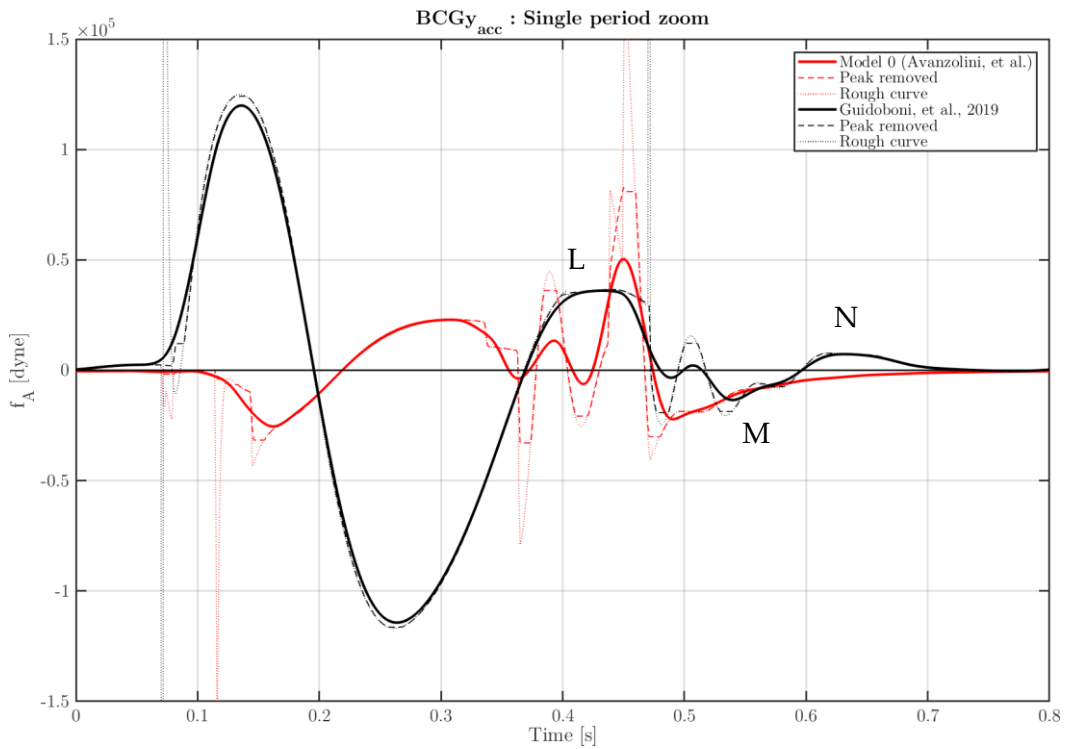
Figure 2.30 – Acceleration BCG over one cardiac cycle, Model 0 (Avanzolini, et al.).

2.5.2 MODEL 1: Two arterial compartments, without cerebral description

Making a step toward a more detailed description of the cardiovascular circuit, a model including two main arterial compartments can be considered:

- Compartment 1 (Group 1): Ascending aorta and aortic arch.
- Compartment 2 (Group 2): Thoracic, abdominal aorta and iliac arteries.
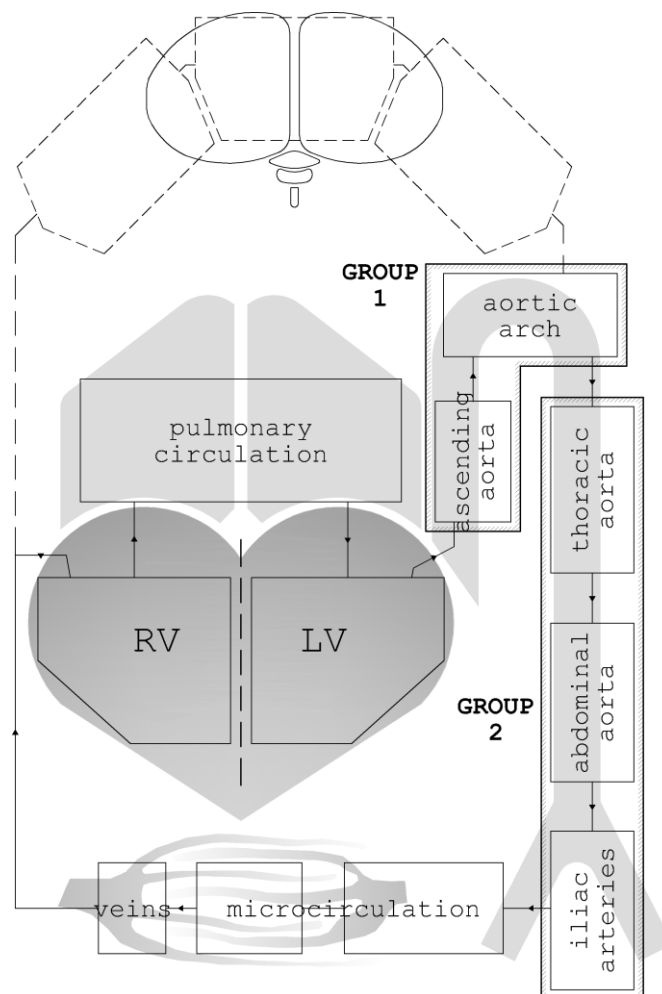
Figure 2.31 – Simplified circuit model considering the main arteries composed by two main groups and without cerebral description (Model 1).

In order to compare the behavior of Model 1 with respect to Model 5 (Guidoboni, et al.), the two compartments are modeled as a **basic arterial tract**, as depicted in Figure 2.32, with values of the resistors, inductor and capacitors obtained by summing the

65

ones used in Model 5 (Guidoboni, et al.) obtaining an equivalent arterial compartment group.

The values of the y_i coordinates of the considered compartments are mantained the same as Table 2.5. In particular, Group 1 is considered lumped at the <u>aortic arch</u>, and Group 2 at the <u>abdominal aorta</u> (neglecting the coordinates of the parts not present in the model).

The values used to model Group 1 and Group 2 are reported in Table 2.7.
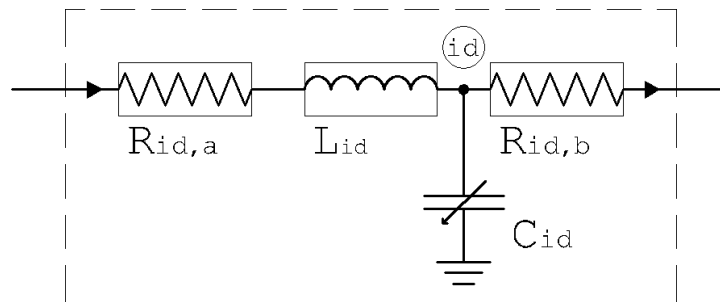
Figure 2.32 – Basic circuital unit modeling an artery. The unit is composed by two resistors, one inductor and a variable capacitor.

Group	Element	Formula	Value	
Group 1	Resistors	$R_{eq} = R_{asc} + R_{arch}$	$1.479E - 04$	mmHg $\cdot$ s / cm^3
	Inductor	$L_{eq} = L_{arch}$	$1.139E - 03$	mmHg $\cdot$ s^2 / cm^3
	Capacitor	$C_{eq} = C_{asc} + C_{arch}$	$2.593E - 01$	cm^3 / mmHg
		$\gamma_{eq} = \gamma_{asc} + \gamma_{arch}$	$8.831E - 02$	mmHg / cm^3
Group 2	Resistors	$R_{eq} = R_{thor} + R_{abd} + R_{iliac}$	$4.286E - 03$	mmHg $\cdot$ s / cm^3
	Inductor	$L_{eq} = L_{thor} + L_{abd} + L_{iliac}$	$1.515E - 02$	mmHg $\cdot$ s^2 / cm^3
	Capacitor	$C_{eq} = C_{thor} + C_{abd} + C_{iliac}$	$4.139E - 01$	cm^3 / mmHg
		$\gamma_{eq} = \gamma_{thor} + \gamma_{abd} + \gamma_{iliac}$	$1.565E - 02$	mmHg / cm^3

Table 2.7 – Equivalent values of resistances, inductances and capacitances of Group 1 and Group 2.

The results in terms of BCG computation are reported in Figure 2.33 and Figure 2.34.
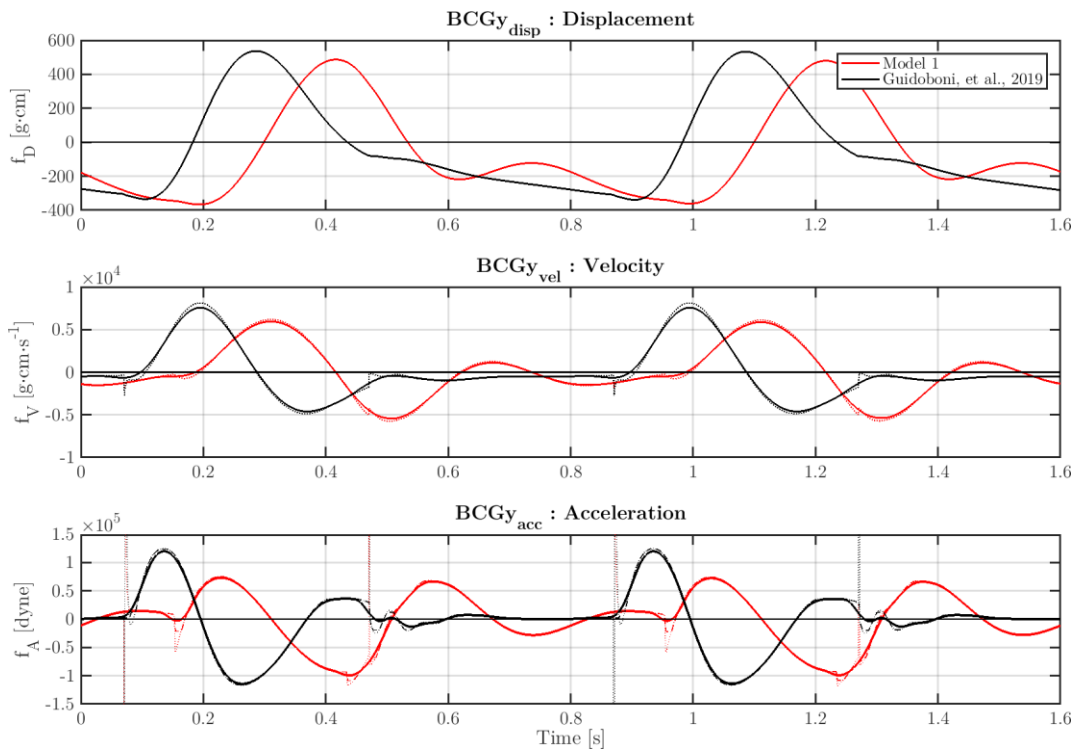
Figure 2.33 – Simulated BGG of Model 1, compared to Model 5 (Guidoboni, et al.).
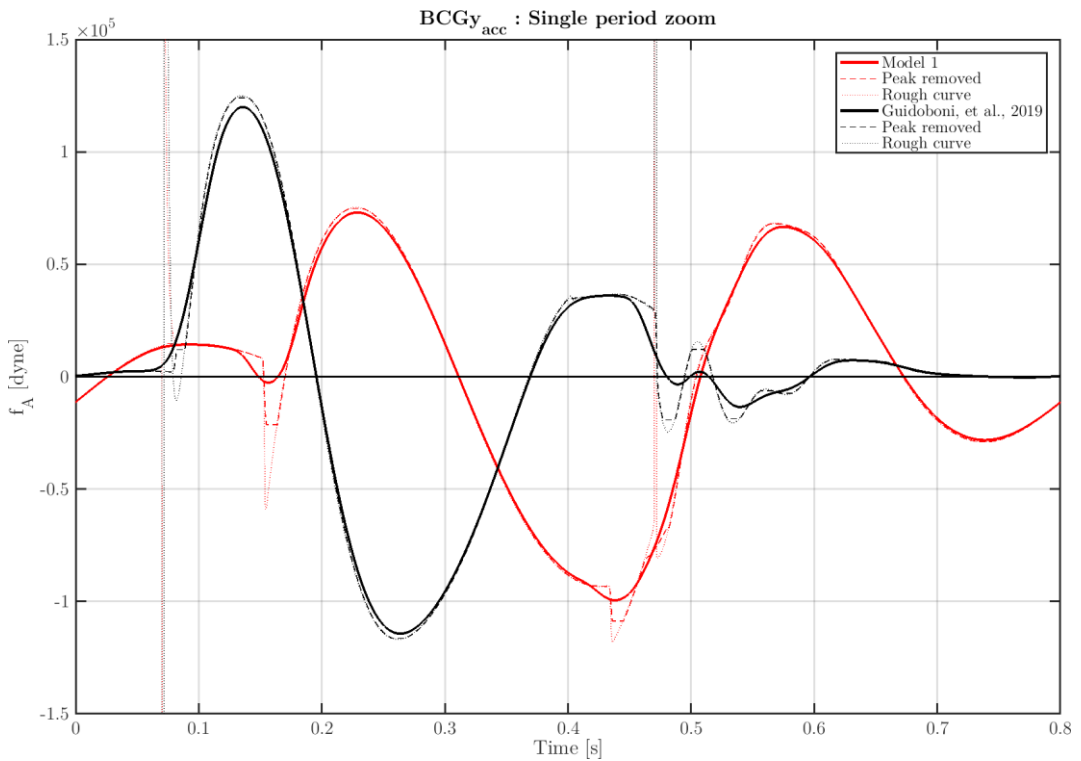
Figure 2.34 – Acceleration BCG over one cardiac cycle of Model 1.

In addition to the BCG it is also useful to analyze the pressures and volumes in the various compartments. The pressure-volume curve pertaining to the left ventricle is particularly relevant in cardiovascular physiology.
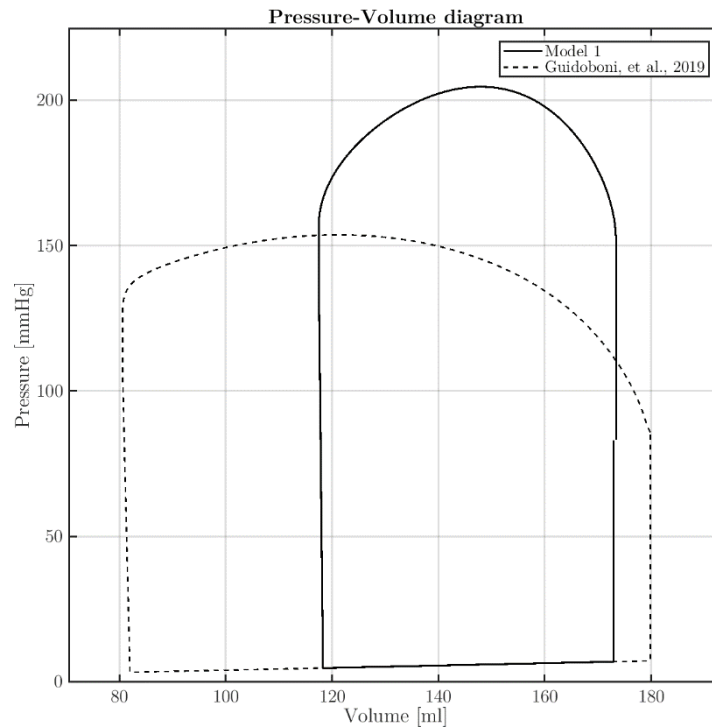
Figure 2.35 – Pressure-volume diagram for the left ventricle of Model 1 compared to Model 5 (Guidoboni, et al.).

It can be immediately seen that, by adding a very simple description of the aorta, the BCG signal exhibits a remarkable improvement in quality.
A time shift can be noticed, compared to Model 5 (Guidoboni, et al.), but substantially the BCG signal shape starts to be recognizable.

Despite this improvement with the BCG signal, the pressures analyzed in Figure 2.35 and Figure 2.36 shows much higher values than physiological values. This may be caused by the fact that the pressure is not slowly distributed among multiple vessel segments compartments and thus smoothed out, but it is reduced too quickly inside the few compartments considered, which results in step-wise curves instead of gradually reducing ones.

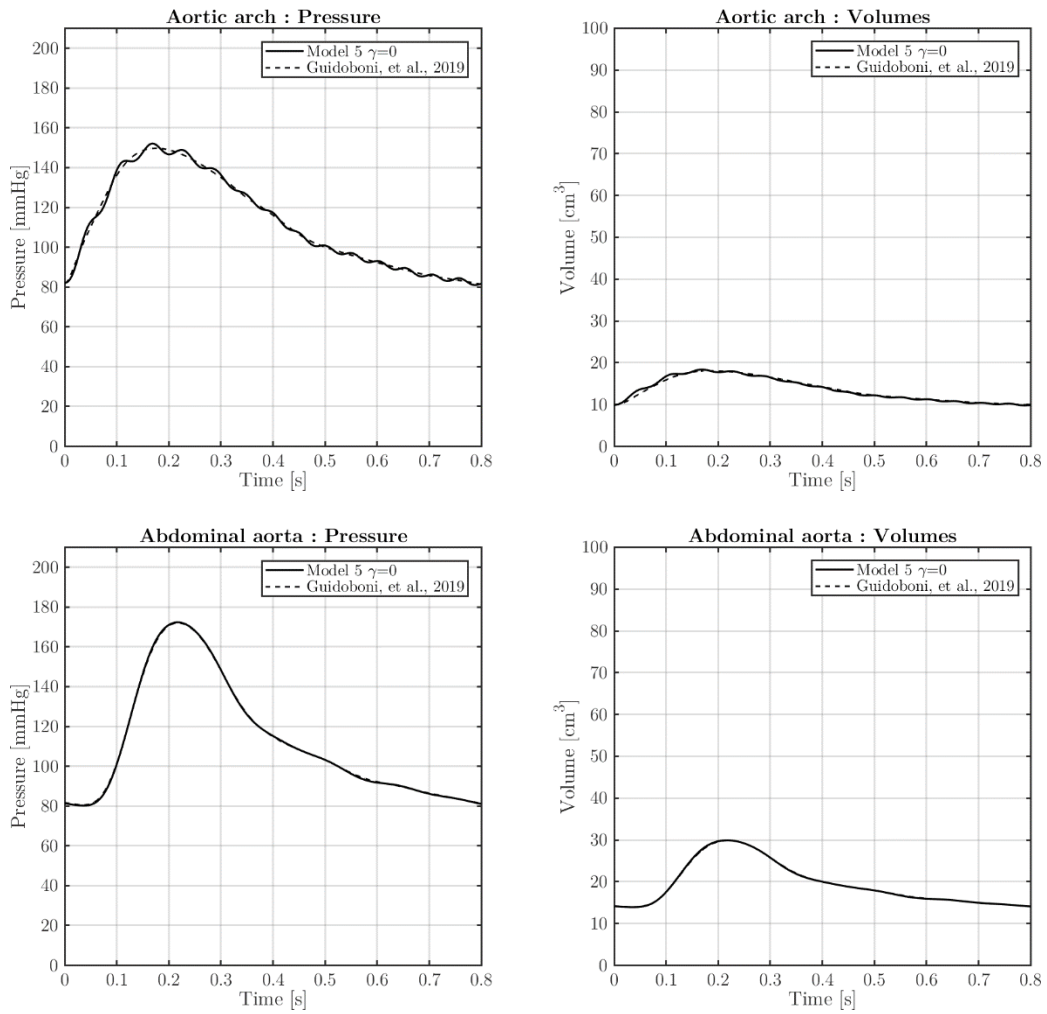For this reason, additional models are considered in the following.
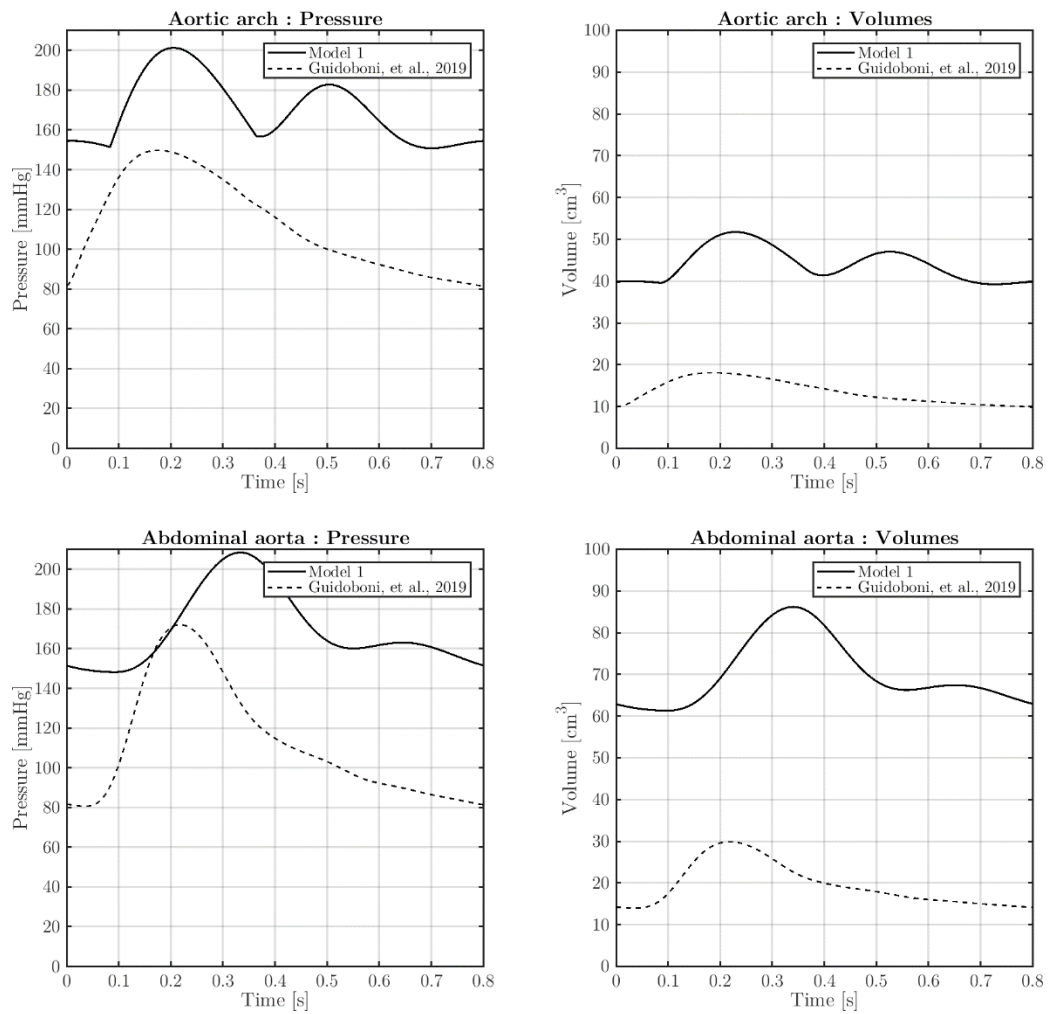
Figure 2.36 – Simulated pressure and volume changes in time, measured in the aortic arch part (on the top) and in the abdominal aorta part (on the bottom), associated with Model 1.

2.5.3 MODEL 2: Four arterial compartments, without cerebral description

Making another step toward a more detailed description of the cardiovascular circuit, the main considered arteries are made of 4 different compartments:

- Compartment 1: Ascending aorta.
- Compartment 2: Aortic arch.
- Compartment 3: Thoracic aorta.
- Compartment 4 (Group 3): Abdominal aorta and iliac arteries.
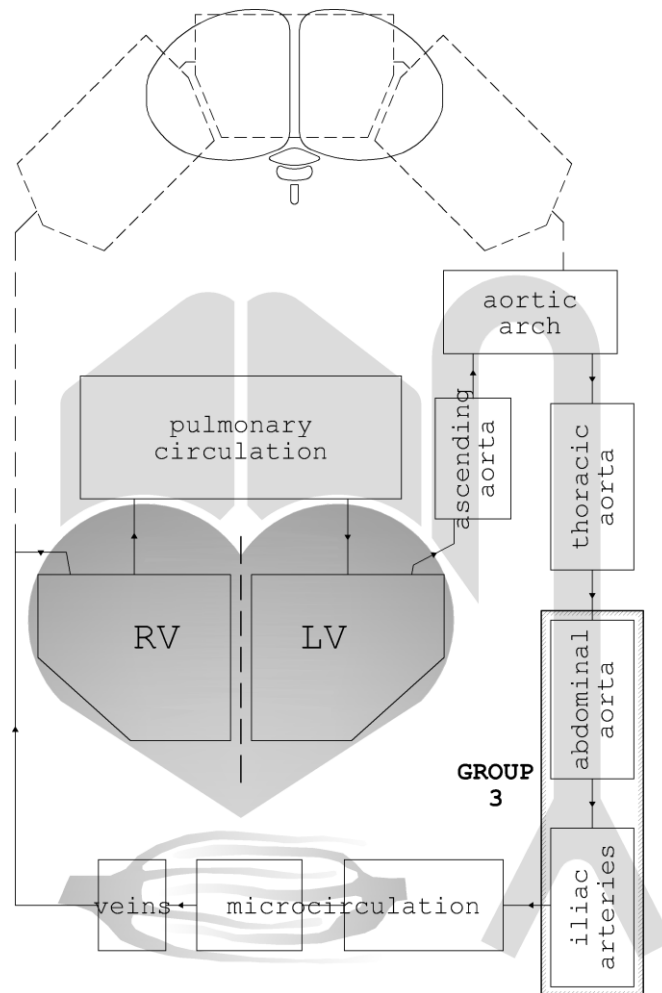
Figure 2.37 – Simplified circuit model considering the main arteries composed by four main parts, without cerebral description (Model 2).

Again, in order to compare the behavior of this model to Model 5 (Guidoboni, et al.), the "group compartment" is modeled as an arterial tract, as depicted in Figure 2.32, with values of the resistors, inductor and capacitors obtained by summing the ones used in Model 5 (Guidoboni, et al.) obtaining an equivalent arterial compartment group.

The values of the y_i coordinates of the considered compartments are mantained the same as Table 2.5. In particular, Group 3 is considered lumped at the <u>abdominal aorta</u> (neglecting the coordinates of the parts not present in the model).

The values used to model Group 3 are reported in Table 2.8.

Group	Element	Formula	Value	
Group 3	Resistors	$R_{eq} = R_{iliac} + R_{abd}$	$3.672E-03$	mmHg $\cdot$ s / cm^3
	Inductor	$L_{eq} = L_{iliac} + L_{abd}$	$1.090E-02$	mmHg $\cdot$ s^2 / cm^3
	Capacitor	$C_{eq} = C_{iliac} + C_{abd}$	$1.942E-01$	cm^3 / mmHg
		$\gamma_{eq} = \gamma_{iliac} + \gamma_{abd}$	$2.680E-02$	mmHg / cm^3

Table 2.8 – Equivalent values of resistance, inductance and capacitance of Group 3.

The results in terms of BCG computation are reported in Figure 2.38 and Figure 2.39.

It can be noticed that the <u>situation does not significantly improve</u> by simply adding arterial parts. The BCG still exhibits a non-standard pattern and the pressures in the compartments are still above the references, although much more smoothed in shape. Despite this, the great improvement in having a more detailed description of the main arteries is that pathological conditions affecting only a compartment can be effectively simulated.

For these reasons, additional models are considered in the following, concentrating on adding compartments no more related to the aorta only.

71
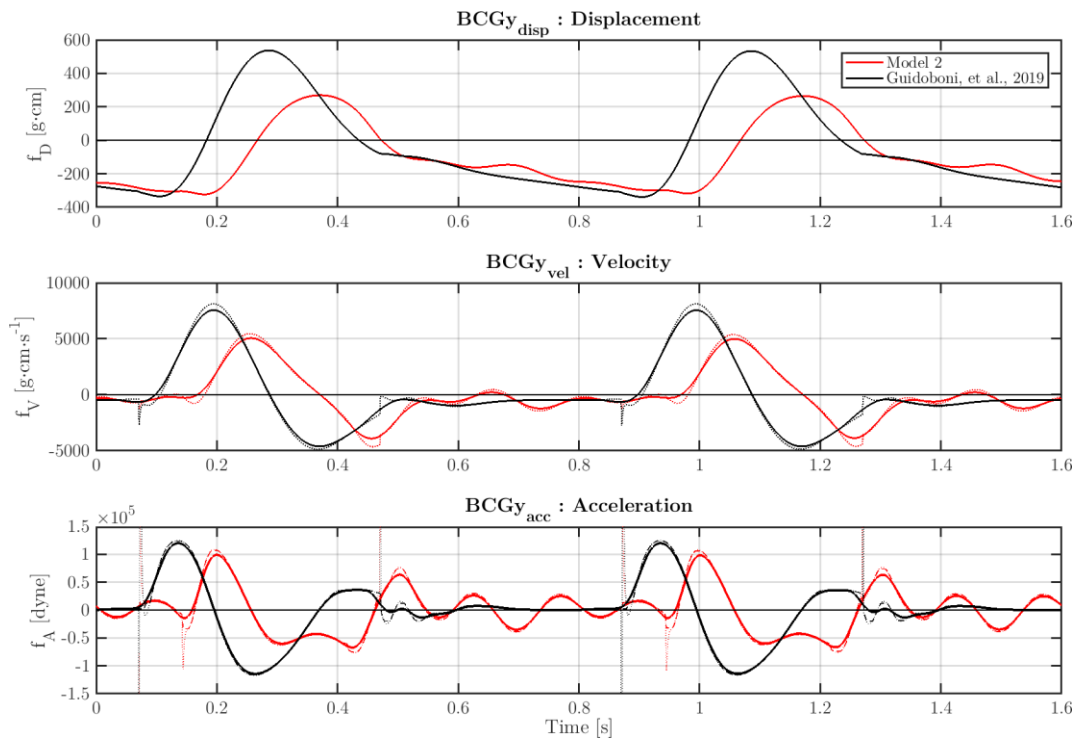
Figure 2.38 – Simulated BGG of Model 2, compared to Model 5 (Guidoboni, et al.).
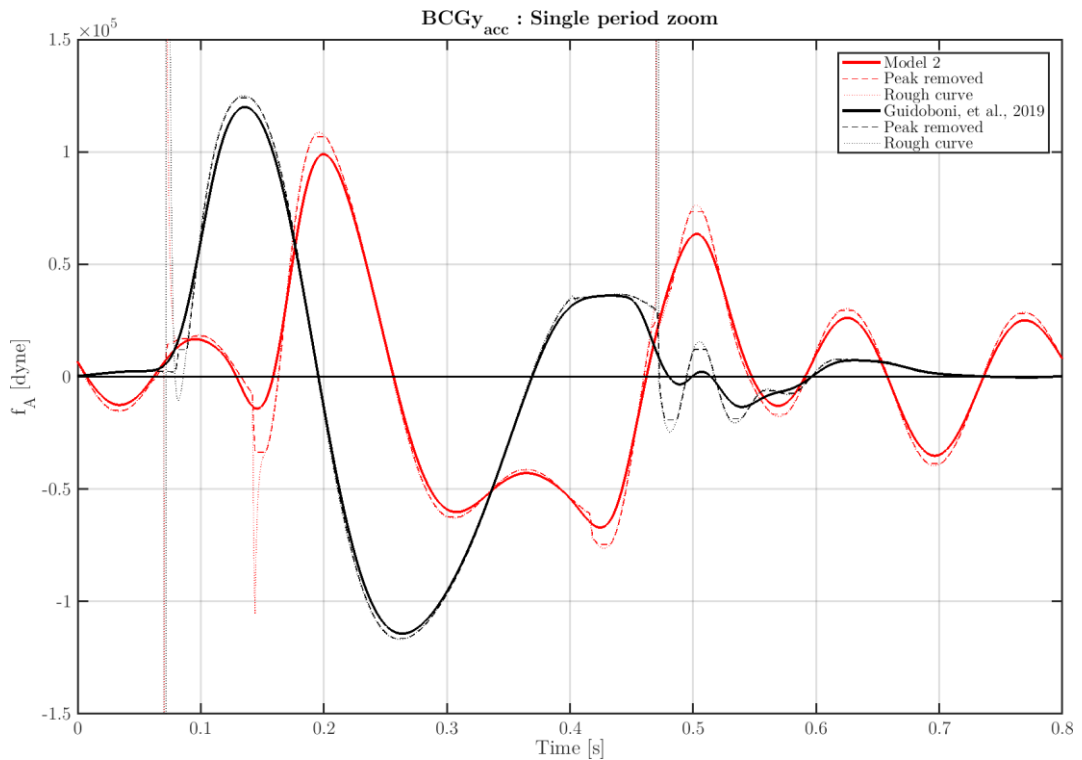
Figure 2.39 – Acceleration BCG over one cardiac cycle of Model 2.

Also the pressure-volume curve is obtained and here reported:
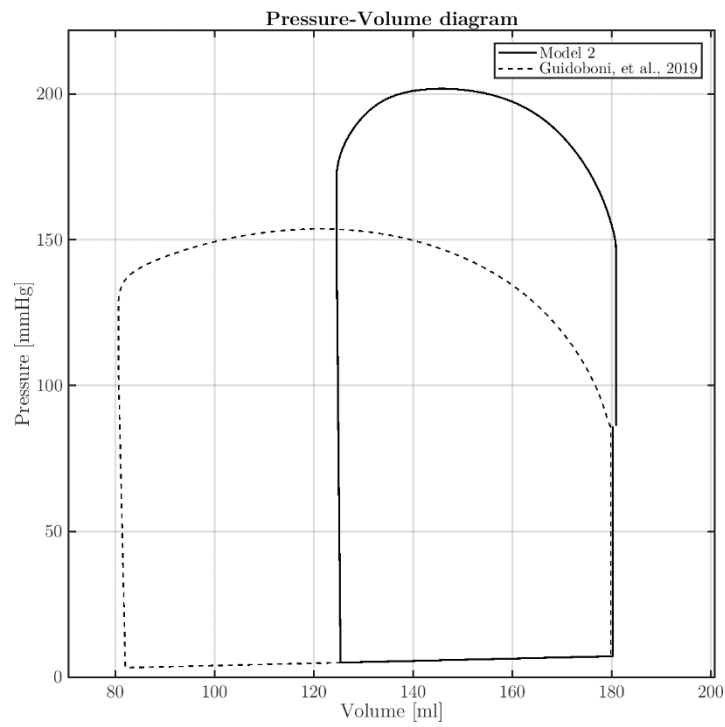
Figure 2.40 – Pressure-volume cycle of Model 2 compared to Model 5
(Guidoboni, et al.).
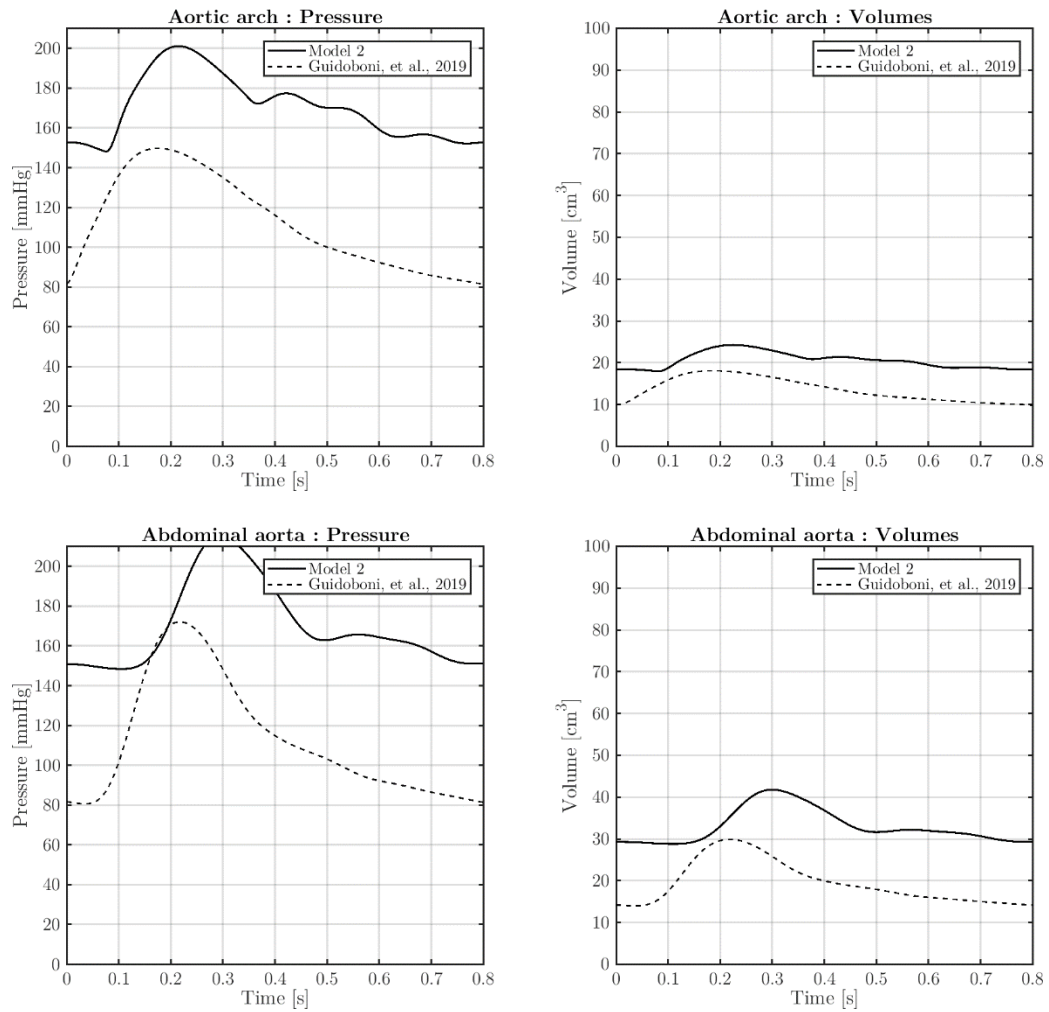
Figure 2.41 – Simulated pressure and volume changes in time, measured in the aortic arch part (on the top) and in the abdominal aorta part (on the bottom), associated with Model 2.

2.5.4 MODEL 3: Two arterial compartments, with detailed cerebral description

In order to better capture BCG features, the analysis of a simple model with the <u>addition of a circulatory compartments situated above the ventricular line</u> may be of interest.

With this purpose, the model in Figure 2.42 is introduced, having the same arterial description as in Figure 2.31, but with the detailed description of the cerebral circulation, already introduced for Model 5 (Guidoboni, et al.) shown in Figure 2.1.
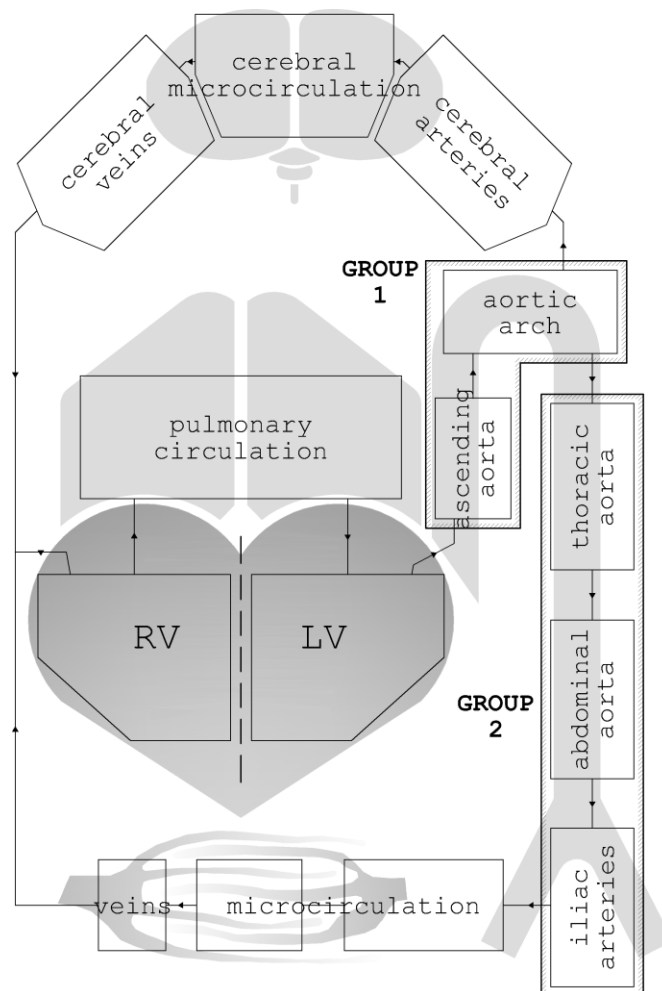
Figure 2.42 – Simplified circuit model considering the aorta composed by two main parts with also a detailed cerebral description (Model 3).

The results in terms of BCG computation are reported in Figure 2.43 and Figure 2.44:
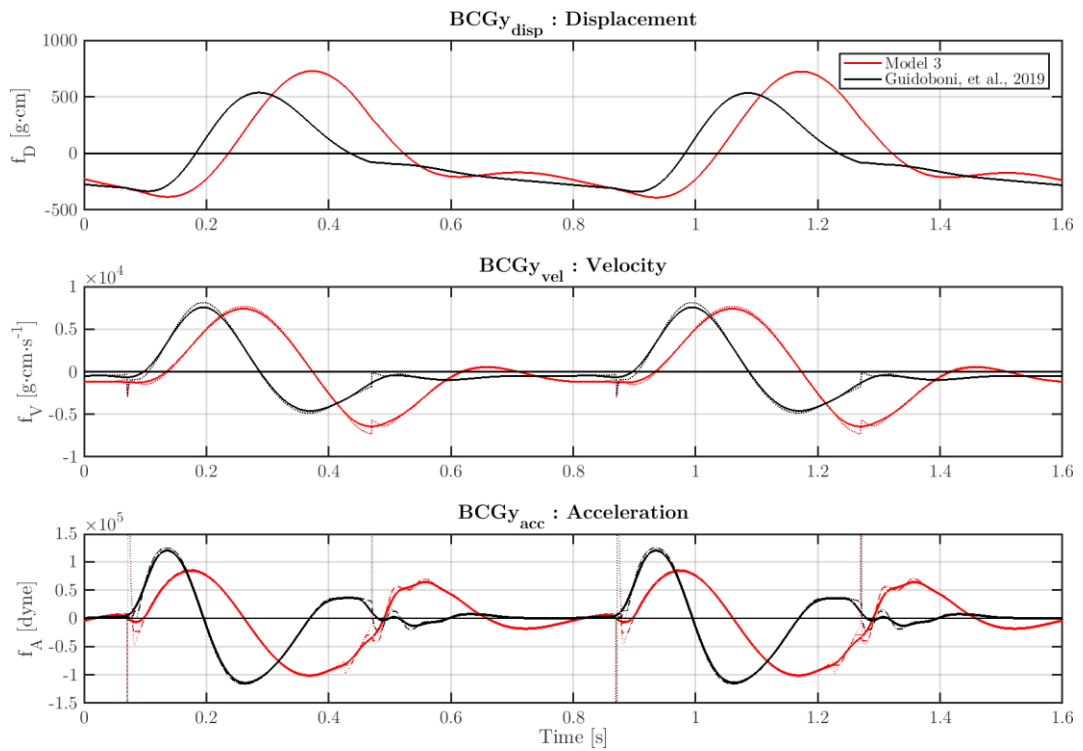
Figure 2.43 – Simulated BGG of Model 3, compared to Model 5 (Guidoboni, et al.).
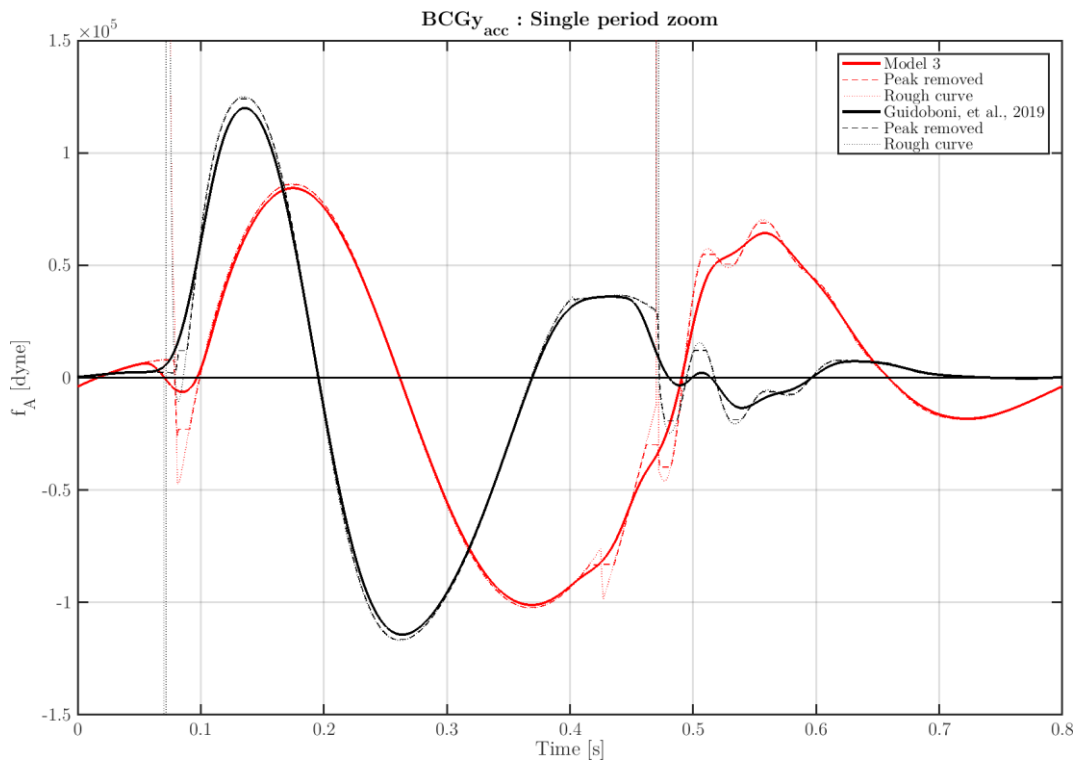
Figure 2.44 – Acceleration BCG over one cardiac cycle of Model 3.

Also the pressure-volume curve is obtained, see Figure 2.45.
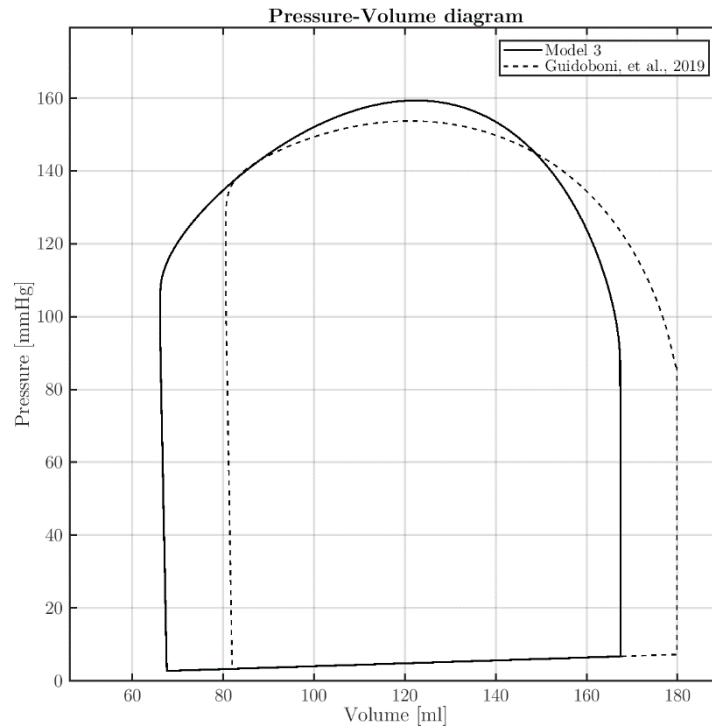
Figure 2.45 – Pressure over volume cycle of Model 3 compared to Model 5 (Guidoboni, et al.).

as well as the pressure and volumes curves inside two compartments, see Figure 2.46.

It can be seen that adding the cerebral part not only improves the quality of the BCG signal (which however still exhibits a time shift), but also uniforms the pressures in every compartment.

In the next section the richer four compartments model introduced in Section 2.5.3 is analyzed with the addition of a detailed cerebral modeling.
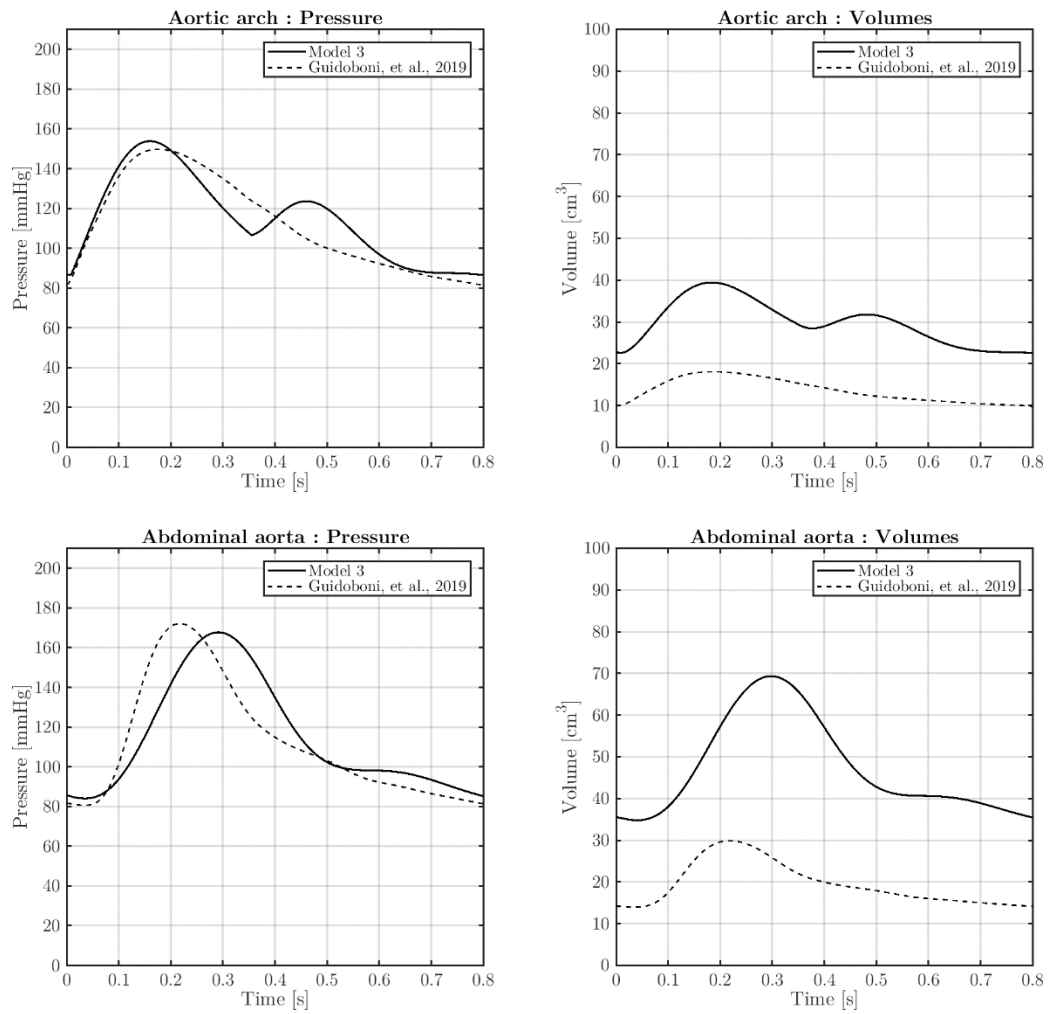
Figure 2.46 – Simulated pressure and volume changes in time, measured in the aortic arch part (on the top) and in the abdominal aorta part (on the bottom), associated with Model 3.

2.5.5 MODEL 4: Four arterial compartments, with detailed cerebral description

Following the line of Section 2.5.4 (Model 3), in this part the *four compartment model* introduced in Section 2.5.3 (Model 2) is updated with the addition of a detailed cerebral description and analyzed. With this purpose the model in Figure 2.47 is introduced.
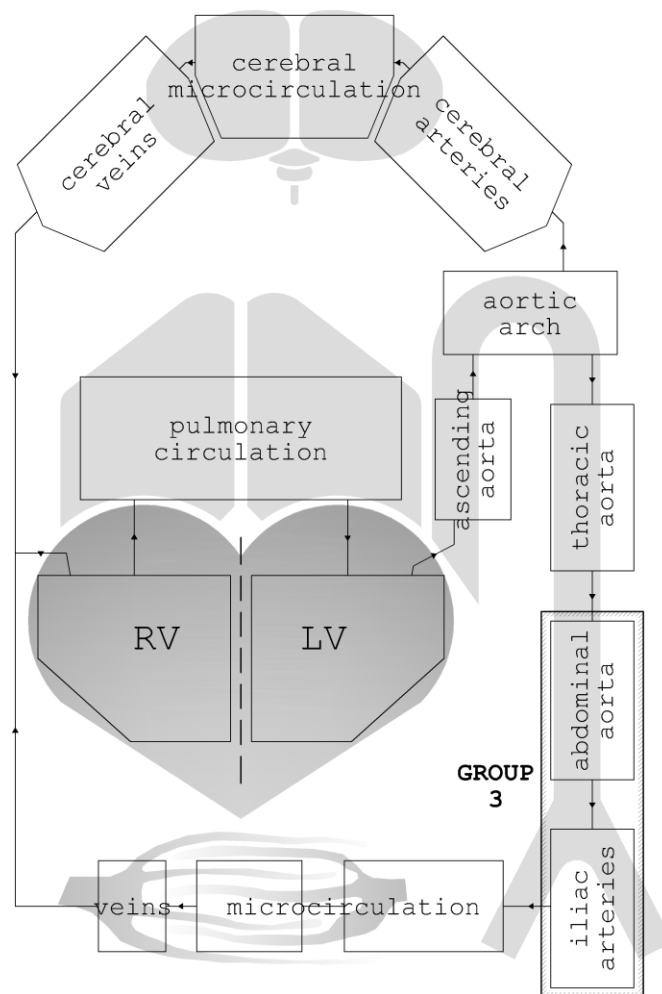
Figure 2.47 – Simplified circuit model considering the aorta composed by 4 main parts with also a detailed cerebral description (Model 4).

The results in terms of BCG computation are reported in Figure 2.48 and Figure 2.49:

79
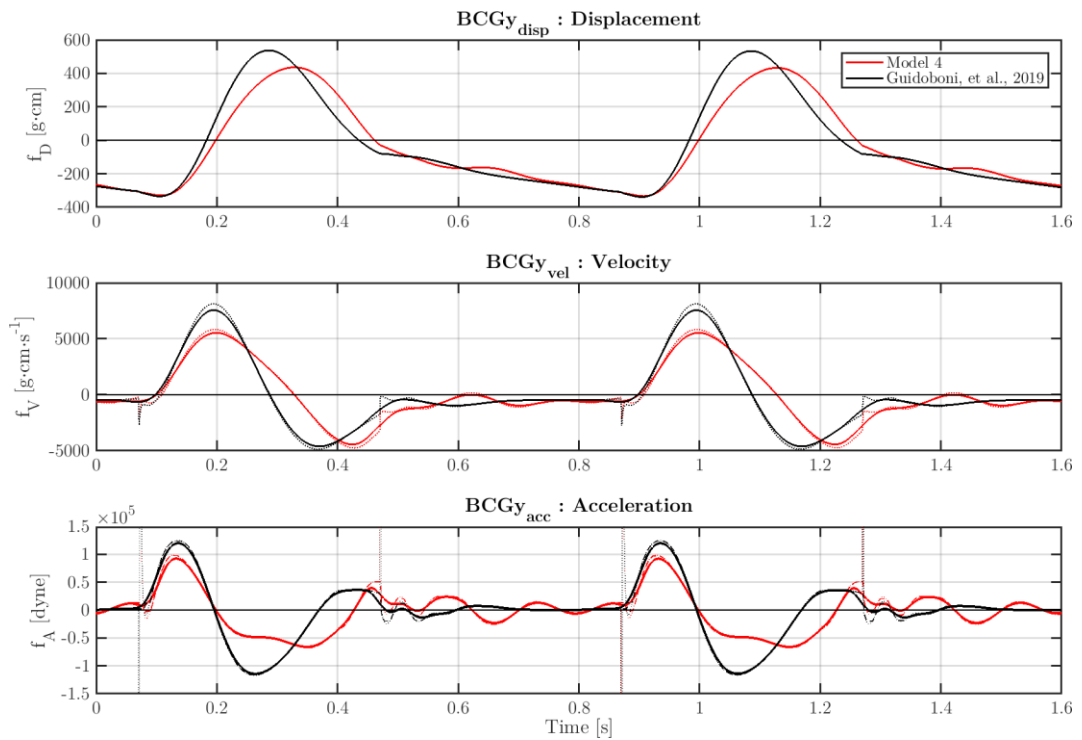
Figure 2.48 – Simulated BGG of Model 4, compared to Model 5 (Guidoboni, et al.).
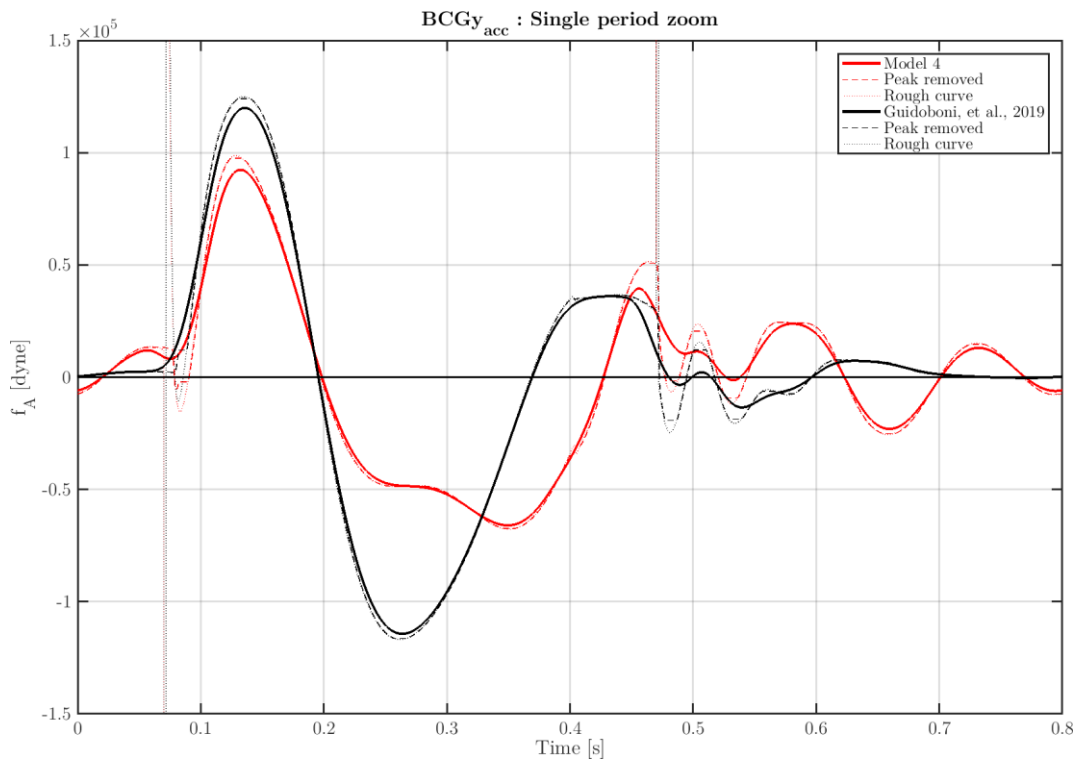
Figure 2.49 – Acceleration BCG over one cardiac cycle of Model 4.

The pressure-volume curve is again obtained and reported in Figure 2.50.
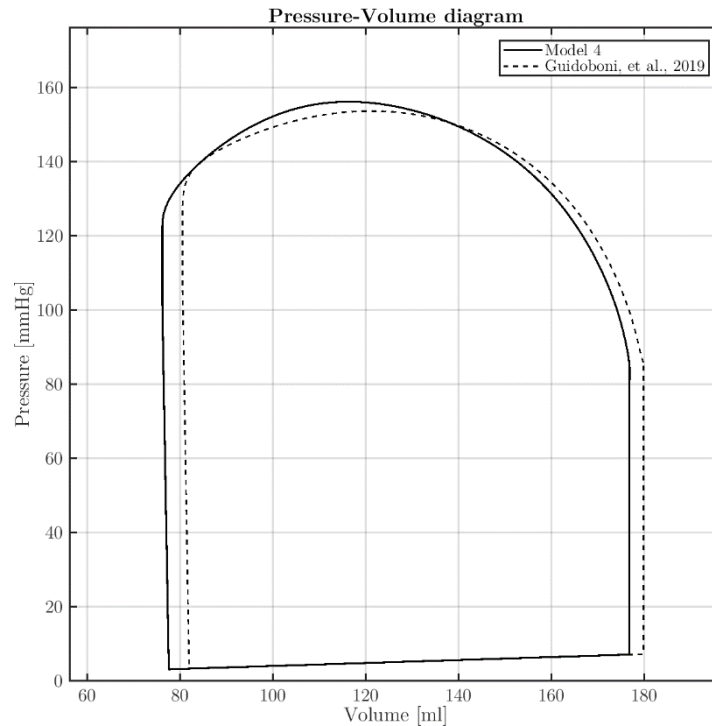
Figure 2.50 – Pressure over volume cycle of Model 4 compared to Model 5 (Guidoboni, et al.).

The pressure and volume curves for the two main compartments are also obtained, see Figure 2.51.

It can be noticed this time that with this Model 4 the obtained BCG graph is <u>very similar to the one obtained with Model 5 (Guidoboni, et al.)</u>. The pressures and volumes are also very similar.

With the addition of the iliac arteries the imperfections in the curves are solved and the graphs would be the same as the one used as reference.

The above results show that **every piece of the considered reference model is useful in order to obtain a convincing BCG simulated signal**. Looking at the various sub-models previously considered help clarify the role of each part in contributing to the final result.
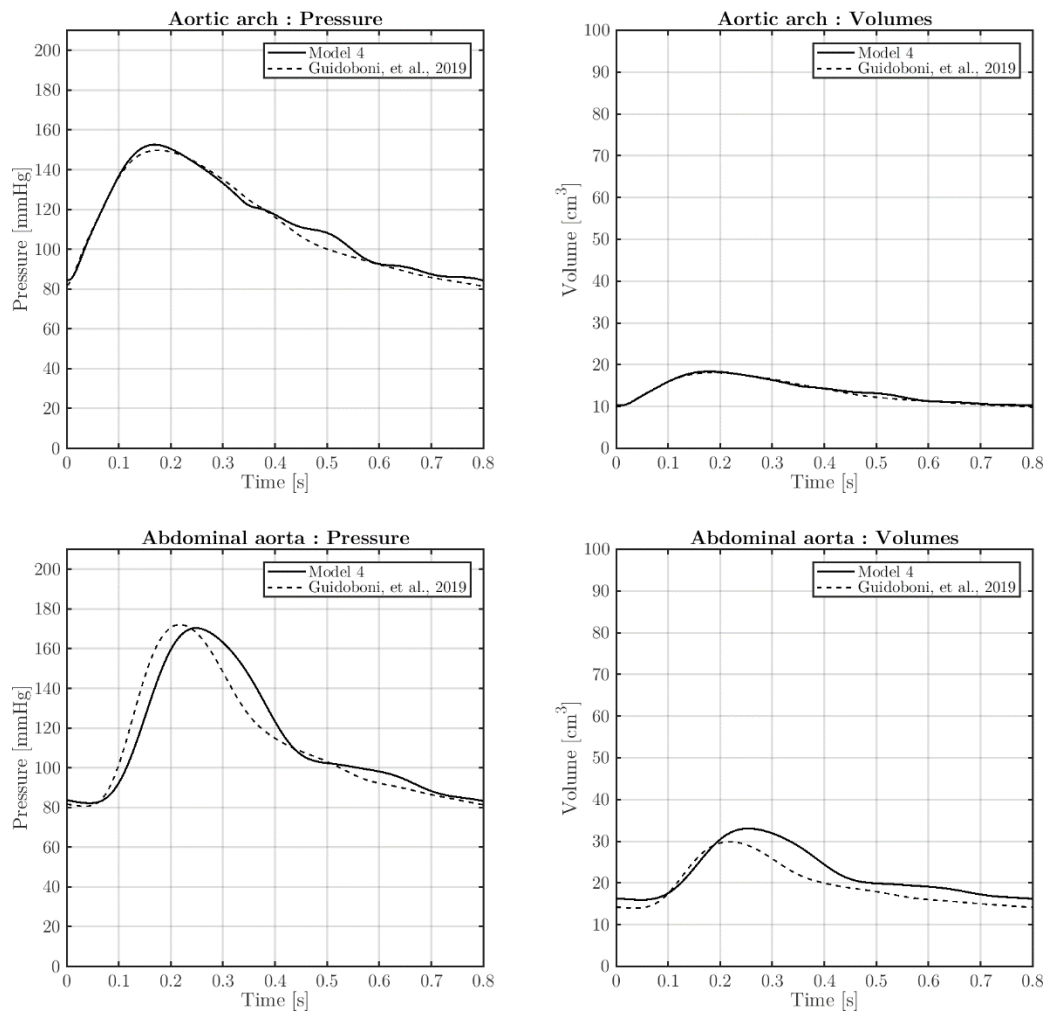
Figure 2.51 – Simulated pressure and volume changes in time, measured in the aortic arch part (on the top) and in the abdominal aorta part (on the bottom), associated with Model 4.

3 – SENSITIVITY ANALYSIS

Sensitivity Analysis is a tool that is increasingly used in modeling practice to analyze how the different values of a set of variables affect a specific dependent variable under certain specific conditions. In general, Sensitivity Analysis is used in a wide range of fields, ranging from biology and geography to economics and engineering.

It is especially useful in the study and analysis of "black box processes" where the output is an *opaque function* of several inputs. This is the case of a process that for some reasons cannot be studied and analyzed directly, usually because it very complex and the exact relationship between the inputs and outputs are not clearly identified and well understood.

In this chapter a theoretical background of the concepts behind the sensitivity analysis are firstly introduced, ranging from its purposes, its problems, how it works, and how the simulation processes involved into the computations of some specific indices used to describe the input variables importance can be simplified.

At the end of the theoretical part, some examples are also provided in order to facilitate the interpretation of the final resulting plots.

Finally some parameters of the closed-loop model presented in Chapter 2 are analyzed in a sensitivity analysis context in order to assess their relative importance over a specific chosen output.

3.1 Sensitivity analysis: Theoretical background

Sensitivity analysis is the study of <u>how the uncertainty in the output can be related to different uncertainties in the inputs</u> of a mathematical model or system. **Uncertainty analysis**, ideally run together with sensitivity analysis, focuses on uncertainty quantification and on <u>how the uncertainties are propagated from the input to the output of the model</u>.

Sensitivity analysis is usually conducted by recalculating the outcomes of a model under alternative assumptions as inputs, to determine the impact of an input variable on the output.

Sensitivity analysis can be useful for a vast range of purposes, including:

- **Understanding of the relationships** between input and output variables in a model.
- **Testing the robustness of the output** results of a model in the presence of input uncertainty.
- **Reducing the output uncertainty** of a model by identifying the main model's inputs that cause significant uncertainty (inputs that should therefore be the focus of the attention in order to increase robustness).
- **Searching for errors in the model** (by unveiling unexpected relationships between inputs and outputs).
- **Simplifying a model** by fixing model inputs that have no effect on the output, or identifying and removing redundant parts of the model structure.
- **Optimizing the model** by finding regions in the space of input factors for which the model output is either maximum or minimum or meets some optimum criterion.
- **Calibrating models** with large number of parameters, in fact a primary sensitivity test can ease the calibration stage by focusing on the sensitive parameters only.

A mathematical model can be highly complex, and as a result its relationships between inputs and outputs may be poorly understood. In such cases, the model can be viewed as a **black box** (i.e. the output is an "opaque" function of its inputs), see Figure 3.1.
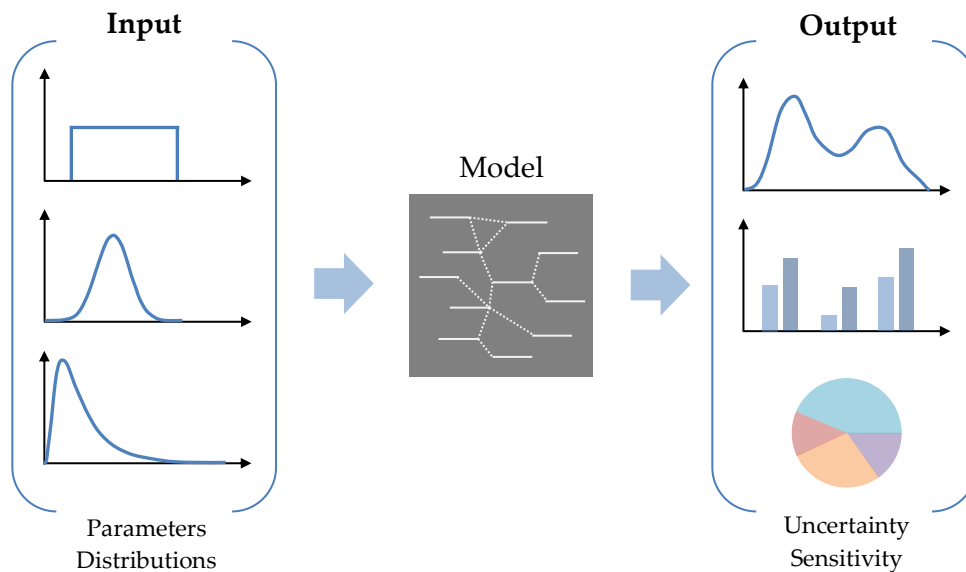
Figure 3.1 – General scheme of a sampling-based sensitivity analysis.
Uncertainty arising from different sources (data distributions, parameter estimation) are propagated through the model (which can have alternative model structures) to the output. Outputs are then used for <u>uncertainty analysis</u>, by analyzing their distributions, and <u>sensitivity analysis</u> by quantifying their relative importance.

Usually, some or all the model inputs are subject to **uncertainty**. Sources of uncertainties may be:

- Variables stochastic by nature (aleatory/randomly determined processes),
- Measurement errors,
- Scarcity of information,
- Poor or partial understanding of the driving forces and model mechanisms.

<u>This uncertainty imposes a limit on our confidence in the response or output of the model</u>.

Good modeling practice requires the modeler to provide an <u>evaluation of the confidence in the model</u>. This requires, first, a quantification of the uncertainty in any model results (**uncertainty analysis**); and second, an evaluation of how much each input is contributing to the output uncertainty, ordering by importance the strength and relevance of the inputs in determining the variation in the output (**sensitivity analysis**).

In models involving many input variables, sensitivity analysis is an essential ingredient of model building and quality assurance. National and international agencies involved in impact assessment studies have included sections devoted to sensitivity analysis in their guidelines.

• *Potential challenges of the sensitivity analysis*

Sensitivity analysis typically involves several challenges or constraints. Some of the most common are:

- **Computational expense:** Sensitivity analysis is almost always performed, through a sampling-based approach, by running the model many times. This can be a significant challenge when:
  - A single run of the model takes a <u>significant amount of time</u> (minutes, hours or longer). This is not unusual with very complex models.
  - The model has a <u>large number of uncertain inputs</u>. Sensitivity analysis is essentially the exploration of the multidimensional input space, which grows exponentially in size with the number of inputs.

  Computational expense is a problem also in many practical sensitivity analyses. In general this issue can be faced in two ways:
  - Deal with the high computational cost by **increasing computational power**, or adopting a **parallel implementation**.
  - **Reduce model complexity** in order to decrease the time cost of each simulation.

  Some methods to reduce the computational expense include the use of *emulators* (for large models), *screening methods* (for reducing the dimensionality of the problem), or *event-based sensitivity analysis* methods (i.e. input variable selection (IVS), used mainly for time-constrained applications).

- **Correlated inputs:** Most common sensitivity analysis methods assume independence among model inputs, but sometimes inputs can be strongly correlated. This is still an immature field of research and definitive methods have yet to be established. Two main approaches are used in this context:
  - **Avoid correlated inputs** (if it is possible to know it a-priori).
  - Use **polynomial expansions** (approximating the unknown model function linking the considered inputs to the considered outputs).

86

- **Nonlinearity:** Some sensitivity analysis approaches, such as those based on linear regression, can inaccurately measure sensitivity when the model response is nonlinear with respect to its inputs. In such cases, variance-based measures are more appropriate.

- **Model interactions:** Interactions occur when the perturbation of two or more inputs simultaneously causes a variation in the output that is greater than that of varying each of the inputs alone. Such interactions are present in any model that is non-additive, but will be neglected by methods such as scatterplots and one-at-a-time perturbations. The effect of interactions can be measured by the total-order sensitivity index.

- **Multiple outputs:** Virtually, all sensitivity analysis methods consider a single univariate model output, yet many models have as output a large number of possibly spatially-dependent or time-dependent data. Note that this does not preclude the possibility of performing different sensitivity analyses for each output of interest. However, for models in which the outputs are correlated, the sensitivity measures can be hard to interpret. Particular attention must be posed to the interpretation of the results.

- **Given data:** In most cases the analyst has access to the model and can perform simulations choosing the inputs. In some case, however, sensitivity analysis must be performed with "given data", this may occur when the analysis has to be performed retrospectively, perhaps using data from an optimization or uncertainty analysis, or when data comes from a discrete source.

3.1.1 **Variance-based sensitivity analysis: Sobol index analysis**

Variance-based sensitivity analysis (often referred to as the **Sobol method** or **Sobol indices**[6]) is a form of global sensitivity analysis. Working within a probabilistic framework, <u>it decomposes the variance of the output of the model or system into fractions which can be attributed to inputs or sets of inputs.</u>

For example, given a model with two inputs and one output, one might find that 70% of the output variance is caused by the variance in the first input, 20% by the variance in the second, and the remaining 10% due to interactions between the two, see Figure 3.2. These percentages are directly interpreted as *measures of sensitivity*. Variance-based measures of sensitivity are attractive because they <u>measure sensitivity across the whole input space</u> (it is so called *global method*), they <u>can deal with nonlinear responses</u>, and they <u>can measure the effect of interactions</u> in non-additive systems.
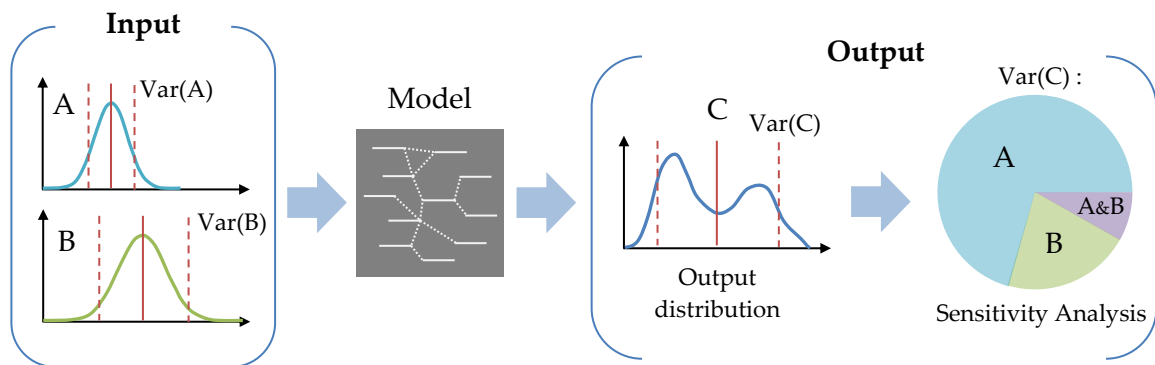
Figure 3.2 – Graphical example of a sensitivity analysis. Given two input A and B and one output C, the output variance is caused by the variance of the first input by an amount of 70%, of the second input by 20%, and by the interaction between the two by 10%.

---

[6] Ilya Meyerovich **Sobol** (15 August 1926) is a Russian mathematician of Jewish Lithuanian origin, known for his work on Monte Carlo methods. His research spans several applications, from nuclear studies to astrophysics, and has contributed significantly to the field of sensitivity analysis. His contributions to sensitivity analysis include the development of the sensitivity indices which bear his name "Sobol indices", including global sensitivity indices.

• *Decomposition of variance*

Any mathematical model can be viewed as a function of the type:

$$\boxed{Y = f(X)}$$

(3.1)

where: $X = \{X_1, X_2, \ldots, X_d\} \in \mathbb{R}^d$ is a vector of uncertain model inputs;

   $Y \in \mathbb{R}^w$ is the chosen univariate model output (vector of multiple outputs);

   $f(\,): \mathbb{R}^d \rightarrow \mathbb{R}^w$ is the mathematical model.

Note: Multiple outputs can be analyzed only by multiple independent sensitivity analyses, therefore scalar model outputs are typically considered. In this case $w = 1$.

Furthermore, <u>it will be assumed that the inputs are independently and uniformly distributed</u> within the unit hypercube of dimension d, thus $X_i \in [0, 1]$ for $i = 1, 2, \ldots, d$. This assumption does not lead to loss of generality because any input space can be transformed onto this unit hypercube.

► *Decomposition of the model function:*

The function $f(X)$ may be decomposed in a sum of sub-functions each referred to a single input variable X_i at a time, or to mixed variables (X_i, X_j), in the following way:

$$\boxed{Y = f_0 + \sum_{i=1}^{d} f_i(X_i) + \sum_{i<j}^{d} f_{ij}(X_i, X_j) + \cdots + f_{1,2,\ldots,d}(X_1, X_2, \ldots, X_d)}$$

(3.2)

where: d is the dimension of the input space (number of input terms);

   f_0 is a constant term;

   f_i is a function of a direct input X_i;

   f_{ij} is a function of mixed inputs X_i and X_j.

For example, if $d = 3$ the relation (3.2) becomes:

$$Y = f_0 + \underbrace{\left(f_1(X_1) + f_2(X_2) + f_3(X_3)\right)}_{\Sigma_{i=1}^{d} f_i(X_i)} +$$
$$+ \underbrace{\left(f_{12}(X_1, X_2) + f_{13}(X_1, X_3) + f_{23}(X_2, X_3) + f_{123}(X_1, X_2, X_3)\right)}_{\Sigma_{i<j}^{d} f_{ij}(X_i, X_j) + \cdots + f_{1,2,\ldots,d}(X_1, X_2, \ldots, X_d)}$$

(3.3)

This decomposition is valid if the following condition holds:

89

$$\int_0^1 f_k(X_1, X_2, \dots X_d) \, dX_k = \mathbf{0} \quad \text{for} \quad k = (1, 2, \dots, d) \tag{3.4}$$

which means that all the terms in the functional decomposition (3.2) are *orthogonal*.

Note: when performing statistical analysis, *independent variables* that affect a particular *dependent variable* are said to be *orthogonal* if they are *uncorrelated*. If correlation is present, the factors are not orthogonal.

►*Expected values, conditional expectation and variance:*

- Let X be a discrete **random variable** with a finite number of finite outcomes $x_1, x_2, \dots, x_n$ occurring with probabilities $p_1, p_2, \dots, p_n$, respectively. The **expected value** of X (sometime also known as the *average value, mean value,* or *first moment*) is defined as:

$$\boxed{E(X) = \sum_{i=1}^n x_i \cdot p_i} = (x_1 \, p_1 + x_2 \, p_2 + \dots + x_n \, p_n) \tag{3.5}$$

Note: since all probabilities p_i add up to 1 ($p_1 + p_2 + \dots + p_k = 1$), the expected value is the *weighted average*, p_i's being the weights. If all outcomes x_i are equiprobable (that is, $p_1 = p_2 = \dots = p_n$), then the weighted average coincides with the *simple average*. The law of large numbers states that the *arithmetic mean* of the values a variable can assume (for example the mean all the numbers printed on a dice) almost surely converges to the *expected value* as the number of repetitions approaches infinity (in fact, the *expected value* in rolling a six-sided die is 3.5 as the number of rolls approaches infinity, because the average of all the integers between 1 and 6 equal to 3.5, see (3.6)).

$$\frac{(1 + 2 + 3 + 4 + 5 + 6)}{6} = \frac{21}{6} = 3.5 \tag{3.6}$$

- In addition, let us introduce the **conditional expectation** (or *conditional expected value, conditional mean*) of a random variable as its expected value given that a certain set of "conditions" is known to occur. In the case when the random variable is defined over a discrete probability space, the "conditions" are a partition of this probability space.
  Let us define the **conditional expectation** of a discrete random variable Y given an event H with strictly positive probability $P(H) > 0$ (which may be

the event that a random variable assumes a particular value $X = X_i$), as the weighted average of the values that Y can take, where each possible value is weighted by its respective conditional probability. It is denoted $E(Y \mid H)$ or $E(Y \mid X = X_i)$, $E(Y \mid X_i)$, and it is a fixed value.

$$E(Y \mid H) = \sum_x \frac{P(Y = Y_i \wedge H)}{P(H)}$$

(3.7)

where: $P(H)$ is the probability of an event H;

$\wedge$ is the logic AND.

- Let us also introduce the concept of **variance** which is the expectation of the squared deviation of a random variable from its mean. Informally, it measures how far a set of (random) numbers are spread out from their average value.

$$Var(X) = E[(X - \mu)^2]$$

(3.8)

where: $\mu = E[X]$ is the mean of the values of X.

►*Decomposition of the output variance:*

Having introduced the concepts of *expected value* and of *conditional expectation*, we are in a position to define the **terms of the functional decomposition** expressed in (3.2) in terms of *conditional expected values*, see (3.9).

$$\begin{cases} f_0 = E(Y) \\ f_i\,(X_i) = E(Y \mid X_i) - f_0 \\ f_{ij}\,(X_i, X_j) = E(Y \mid X_i, X_j) - f_0 - f_i - f_j \end{cases}$$

(3.9)

from which it can be seen that:

- f_i is the effect of varying X_i alone (known as the *main effect* of X_i, a term used in opposition to *interaction effects*),
- f_{ij} is the effect of varying X_i and X_j simultaneously, additional to the effect of their individual variations. This is known as a *second-order interaction*. Higher-order terms have analogous definitions.

Now, further assuming that $f(\boldsymbol{X})$ is square-integrable, the functional decomposition (3.2) may be squared and integrated to give,

91

$$\int_0^1 f^2(\boldsymbol{X})\, d\boldsymbol{X} - f_0{}^2 = \sum_{s=1}^{d} \sum_{i_1 < \cdots < i_s}^{d} \int \left(f_{i_1 \ldots i_s}\right)^2 \left(dX_{i_1} \ldots dX_{i_s}\right) \qquad (3.10)$$

Notice that the left hand side is equal to the variance of Y, and the terms on the right hand side are variance terms, now decomposed with respect to sets of the X_i. This finally leads to the **decomposition of variance expression**,

$$Var(Y) = \sum_{i=1}^{d} V_i + \sum_{i<j}^{d} V_{ij} + \cdots + V_{1\,2\,\ldots\,d} \qquad (3.11)$$

where: $V_i = Var_{X_i}\left(E_{X_{\sim i}}(Y \mid X_i)\right);$

   $V_{ij} = Var_{X_{ij}}\left(E_{X_{\sim ij}}(Y \mid X_i, X_j)\right) - V_i - V_j\,;$

   $X_{\sim i}$ indicating the set of all variables *except* X_i .

The above variance decomposition shows <u>how the variance of the model output can be decomposed into terms that can be associated with each input</u>, as well as the <u>interaction effects between them</u>. Together, all terms sum to the total variance of the model output.

• *Sobol indices*

► **First-order indices:**
A direct variance-based measure of sensitivity S_i, called the "*first-order sensitivity index*", or "*main effect index*" is stated as follows,

$$S_i = \frac{V_i}{Var(Y)} \qquad (3.12)$$

This is the contribution to the output variance of the main effect of X_i, therefore it measures the effect of varying X_i *alone*, but averaged over variations in other input parameters. It is standardized by the total variance to provide a fractional contribution. Higher-order interaction indices (S_{ij}, S_{ijk} and so on) can be formed by dividing other terms in the variance decomposition by $Var(Y)$. Note that this has the implication that the sum of the first-order indices must be unitary,

$$\sum_{i=1}^{d} S_i + \sum_{i=1}^{d} S_{ij} + \cdots + S_{1\,2\,\ldots\,d} = 1 \qquad (3.13)$$

► **Total-effect index:**

Using the S_i, S_{ij} and higher-order indices given above, it is possible to build a global picture of the importance of each variable in determining the output variance.

However, since this requires the evaluation of $(2^d - 1)$ indices, when the number of variables is large, it can be too computationally demanding.

For this reason, a measure known as the "*Total-effect index*" or "*Total-order index*", S_{Ti}, is used. This index measures the contribution to the output variance of X_i, *including all variances caused by its interactions, of any order, with any other input variable*. It is given as,

$$\boxed{S_{Ti} = \frac{E_{X_{\sim i}}\left(Var_{X_i}(Y \mid X_{\sim i})\right)}{Var(Y)}} = 1 - \frac{Var_{X_{\sim i}}\left(E_{X_{\sim i}}(Y \mid X_{\sim i})\right)}{Var(Y)} \tag{3.14}$$

Note: unlike the first order index S_i, the sum of all the total-effect indices may result greater than unity, $\sum_{i=1}^{d} S_{Ti} \geq 1$. This is due to the fact that the interaction effect between e.g. X_i and X_j is counted in both S_{Ti} and S_{Tj}, in fact, the sum of the S_{Ti} will be equal to 1 only when the model is purely additive.

• *Calculation of the indices*

For analytically tractable functions, the indices above may be calculated analytically by evaluating the integrals in the decomposition. However, in the vast majority of cases they are estimated through computational methods. This is usually done using the **Monte Carlo method**.

Monte Carlo simulations are a broad class of computational algorithms that rely on repeated random sampling to obtain numerical results. Their approach is based on the generation of a sequence of randomly distributed points (pseudorandom points generated inside a unit hypercube), then it transforms them then into a continuously distributed guessed probability function that is used to feed the model input, in order to finally get a large number of outputs that can be statistically analyzed.

In practice, considering sequence generation, it is common to substitute random sequences with low-discrepancy sequences to improve the efficiency of the estimators. This is then known as the *quasi-Monte Carlo method*. Some low-discrepancy sequences commonly used in sensitivity analysis include the *Sobol sequence* and the *Latin hypercube* design.
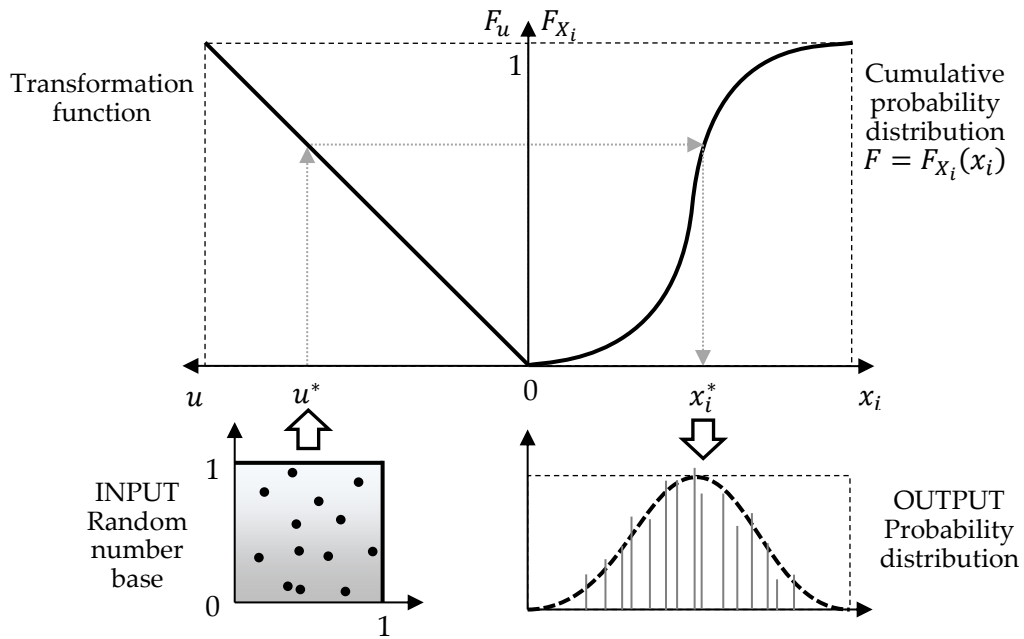
Figure 3.3 – Schematic representation of the Monte Carlo simulation method.

To calculate the Sobol indices using the quasi-Monte Carlo method, the following steps are followed:

Let N be the number of tests performed for each input variable, and d be the number of considered inputs of the model.

1. <u>Generate an $N \times 2d$ *sample matrix*</u> (this should be done with respect to the probability distributions of the input variables).

2. Use the first d columns of the matrix as matrix A, and the remaining d columns as matrix B (this effectively gives two <u>independent samples of N points</u> in the d-dimensional unit hypercube), see (3.15).

$$
\begin{bmatrix}
a_{1,1} & a_{1,2} & a_{1,3} & b_{1,1} & b_{1,2} & b_{1,3} \\
a_{2,1} & a_{2,2} & a_{2,3} & b_{2,1} & b_{2,2} & b_{2,3} \\
a_{3,1} & a_{3,2} & a_{3,3} & b_{3,1} & b_{3,2} & b_{3,3} \\
... & ... & ... & ... & ... & ... \\
a_{N,1} & a_{N,2} & a_{N,3} & b_{N,1} & b_{N,2} & b_{N,3}
\end{bmatrix}
\qquad (3.15)
$$

$$\underbrace{\phantom{a_{1,1} \ a_{1,2} \ a_{1,3}}}_{A} \qquad \underbrace{\phantom{b_{1,1} \ b_{1,2} \ b_{1,3}}}_{B}$$

3. <u>Build d further $N \times d$ matrices $A_B^{(i)}$</u>, for $i = (1, 2, \ldots, d)$, such that the ith column of $A_B^{(i)}$ is equal to the ith column of B, and the remaining columns are from A, see (3.16).

$$A_B^{(1)} = \begin{bmatrix} \boldsymbol{b_{1,1}} & a_{1,2} & a_{1,3} \\ \boldsymbol{b_{2,1}} & a_{2,2} & a_{2,3} \\ \boldsymbol{b_{3,1}} & a_{3,2} & a_{3,3} \\ \ldots & \ldots & \ldots \\ \boldsymbol{b_{N,1}} & a_{N,2} & a_{N,3} \end{bmatrix} \quad A_B^{(2)} = \begin{bmatrix} a_{1,1} & \boldsymbol{b_{1,2}} & a_{1,3} \\ a_{2,1} & \boldsymbol{b_{2,2}} & a_{2,3} \\ a_{3,1} & \boldsymbol{b_{3,2}} & a_{3,3} \\ \ldots & \ldots & \ldots \\ a_{N,1} & \boldsymbol{b_{N,2}} & a_{N,3} \end{bmatrix}$$

$$A_B^{(3)} = \begin{bmatrix} a_{1,1} & a_{1,2} & \boldsymbol{b_{1,3}} \\ a_{2,1} & a_{2,2} & \boldsymbol{b_{2,3}} \\ a_{3,1} & a_{3,2} & \boldsymbol{b_{3,3}} \\ \ldots & \ldots & \ldots \\ a_{N,1} & a_{N,2} & \boldsymbol{b_{N,3}} \end{bmatrix}$$

(3.16)

4. The A, B, and the d $A_B^{(i)}$ matrices in total specify $N(d + 2)$ points in the input space (one for each row). <u>Run the model at each point in the A, B, and $A_B^{(i)}$ matrices</u>, giving a total of $N(d + 2)$ model evaluations – the corresponding $f(A)$, $f(B)$ and $f(A_B^{(i)})$ values.

5. Calculate the <u>sensitivity indices</u> using the estimators below.

The accuracy of the estimators of course depends on N. The value of N can be chosen by sequentially adding points and calculating the indices until the estimated values reach some acceptable convergence. For this reason, when using low-discrepancy sequences, it can be advantageous to use those that allow sequential addition of points (such as the Sobol sequence), as compared to those that do not (such as Latin hypercube sequences).

Summarizing, for the estimation of the S_i and the S_{Ti} for every d input variables, $N(d + 2)$ model runs are required, with N denoting the number of model runs for each test. Since N is often of the order of hundreds or thousands of runs, the computational expense can quickly become a problem when the model takes a significant amount of time for a single run. In such cases, there are several techniques available to reduce the computational cost of estimating sensitivity indices, one of these techniques contemplate the use of **emulators**.

3.1.2 Emulators and Polynomial Chaos expansions

Emulators (also known as *meta-models*, *surrogate models* or *response surfaces*) are data-modeling/machine learning approaches that involve <u>building a relatively simple mathematical function, known as an *emulator*, that approximates the input/output behavior of the model itself</u>.

The underlying concept is known as "modelling a model" (hence the name "*meta-model*"). The idea is that, although computer models may be a very complex series of equations that can take a long time to solve, they can always be regarded as a function of their inputs $Y = f(X)$. <u>By running the model at a number of points in the input space, it may be possible to fit a much simpler emulator $\eta(X)$, such that $\eta(X) \approx f(X)$</u> within an acceptable margin of error.

Then, *sensitivity measures* can be calculated from the emulator (either with Monte Carlo or analytically), which will have a negligible additional computational cost. Importantly, the number of model runs required to fit the emulator can be orders of magnitude less than the number of runs required to directly estimate the sensitivity measures from the model.

The procedure of finding the *emulator function η* that is a sufficiently close approximation of the *model function f* usually requires the following steps:

1. Sampling (running) the model at a number of points in its input space.
2. Selecting a type of emulator (mathematical function) to use.
3. "Training" the emulator using the sample data from the model. This generally involves adjusting the emulator parameters until the emulator mimics the true model as well as possible.

Sampling the model can often be done with low-discrepancy sequences, such as the Sobol sequence or Latin hypercube sampling, although random designs can also be used, at the price of a small reduction of efficiency.

The selection of the emulator type and the training are intrinsically linked, since the training method will be dependent on the class of emulator. Some types of emulators that have been used successfully for sensitivity analysis include,

- *Gaussian processes* (also known as *kriging*), where any combination of output points is assumed to be distributed as a multivariate Gaussian distribution.

- *Random forests*, in which a large number of decision trees are trained, and the result is averaged.

- *Gradient boosting*, where a sequence of simple regressions is used to weight data points to sequentially reduce error.

- **Polynomial chaos expansions**, which use orthogonal polynomials to approximate the response surface.

- *Smoothing splines*.

In all cases it is useful to <u>check the accuracy of the emulator</u>, for example using cross-validation.

• *Polynomial Chaos*

Polynomial Chaos (**PC**), also called *Wiener chaos expansion*, is a <u>non-sampling-based method to determine the evolution of the uncertainty in a dynamical system</u> when there is probabilistic uncertainty in the system parameters. PC was first introduced by Norbert Wiener by the use of Hermite polynomials to model stochastic processes with Gaussian random variables. PC can be thought of as an extension of Volterra's theory of nonlinear functionals for stochastic systems and is defined as an infinite sum of products of the type:

$$\boxed{\underline{y}(\underline{x}) = \sum_{k=0}^{\infty} \beta_k(\underline{x})\, \Psi_k\left(\underline{\xi}\right)} \tag{3.17}$$

where: $\underline{\xi} = (\xi_1, \xi_2, \dots, \xi_d)$ is a set of d independent second order random variables with a given joint density;

$\left(\Psi_k\left(\underline{\xi}\right)\right)_{k \in \mathbb{N}}$ is a sequence of multidimensional <u>orthogonal polynomials</u>.

In order to obtain an orthogonal sequence, specific *polynomial bases* must be used according to the input distribution chosen. As an example, see Table 3.1.

For practical use, the sequence (3.17) is truncated at the polynomial order N_0:

$$P = \frac{(d + N_0)!}{d!\, N_0!} - 1 \quad \Rightarrow \quad \hat{\underline{y}} \approx \sum_{k=0}^{P} \hat{\beta}_k(\underline{x})\, \Psi_k\left(\underline{\xi}\right) \tag{3.18}$$

The knowledge of β_k <u>fully characterizes</u> $\underline{y}$.

Distribution	Polynomials
Uniform	Hermite
Gaussian	Legendre
Gamma	Laguerre
Beta	Jacobi

Table 3.1 – Polynomial bases used to build the Polynomial Chaos expansion according to input distributions.

Linking the Polynomial chaos theory to the Sobol indices computations, results in the following relations:

The expectation and the variance of the process are given by:

$$E\left[\underline{y}\right] = \beta_0(\underline{x}) \tag{3.19}$$

$$E\left[\left(\underline{y} - E\left[\underline{y}\right]\right)^2\right] = \sum_{k=0}^{\infty} \beta_k(\underline{x}) \left\|\Psi_k\right\|^2 \tag{3.20}$$

Sensitivity indices are calculated with the formula:

$$S_u = \frac{{\sigma_u}^2}{{\sigma_{\hat{y}}}^2} \tag{3.21}$$

where: $\sigma_{\hat{y}}^{\ 2} = \sum_{U \subseteq \{1,2,\dots,D\} \setminus \emptyset}[\sigma_u^{\ 2}]$

$\sigma_u^{\ 2} = \sum_{k \in K_u} \hat{\beta}_k^{\ 2} \left\|\Psi_k\right\|^2$

$K_u = \left\{k \in K \mid \Psi_k\left(\underline{\xi}\right) = \Psi_k\left(\underline{\xi} = \underline{\xi_u}\right)\right\}$, $K = \{0, 1, \dots, P\}$

It has been demonstrated that the generalized PC based methods are computationally superior to Monte-Carlo based methods in several applications. However, the method has a notable limitation. For large numbers of random variables, polynomial chaos becomes very computationally expensive and Monte-Carlo methods are typically more feasible.

3.1.3 **Implementation and examples**

In this thesis, the procedures introduced in 3.1.1 and 3.1.2 have been implemented in a computational code written in **Python** within the working environment **Anaconda**[7]. The output of the code has been post-processed using **MATLAB** to produce the plots.

•Python implementation

The python code is subdivided into the following main parts, see Figure 3.4:
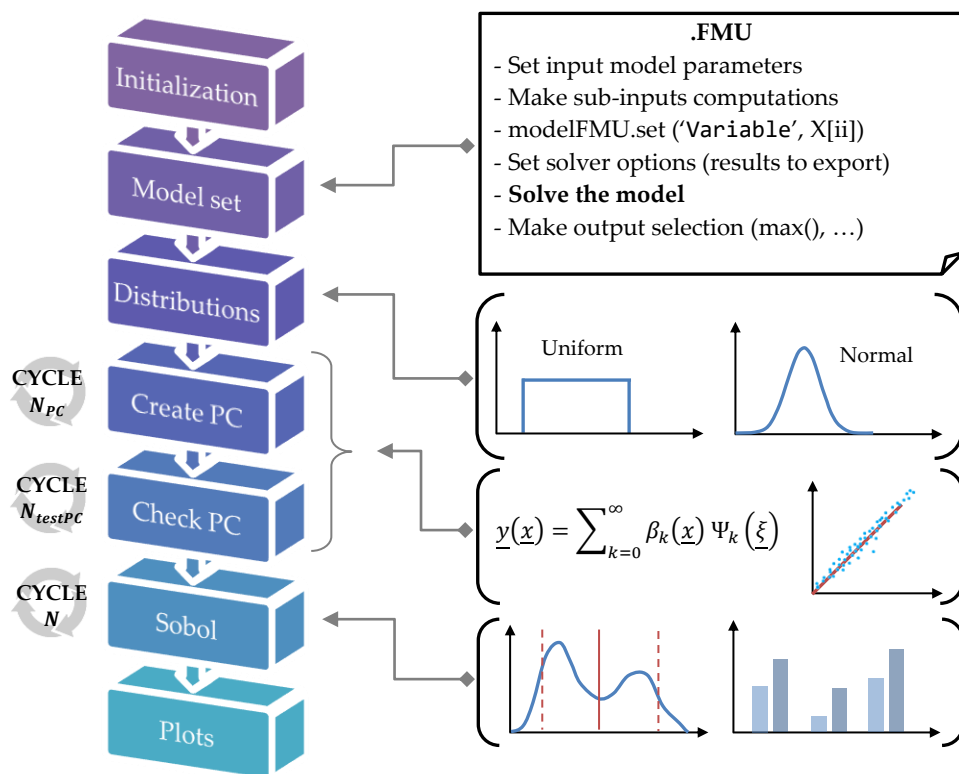
Figure 3.4 – Conceptual scheme of the Python code implemented to perform the sensitivity analysis.

- **Code initialization**: the libraries are imported, the global parameters are set, the sample sizes are set for the computation of the Polynomial Chaos expansion and for the subsequent simulation.

---

[7] https://www.anaconda.com/distribution/

- **Model setting**: the OpenModelica model is initialized as a class with the variables selected as arguments, the input and output variables are specified, and the computations for sub-inputs or output filtering are expressed.

- **Definition of the distribution**: the distributions of the inputs are declared.

- **Creation of PC expansion**: the model is run a N_{PC} number of times and the PC coefficients are computed.

- **Checking the PC expansion**: the generated meta-model is checked against the real model.

- **Sensitivity analysis – Sobol indices computation**: the Sobol indices are computed and reported.

- **Report of the results**: the information is reported and the graphs are plotted using MATLAB.

Some of the libraries used to develop the Python code are:

OpenTURNS[8], is the main statistical library used, an open source library for the Treatment of Uncertainties, Risks 'N Statistics. The mainly used classes are the `FunctionalChaosRandomVector` and `FunctionalChaosSobolIndices`, which evaluate the Sobol indices associated with the polynomial chaos decomposition of the model.

PyFMI[9], is a Python interface for loading, interacting, setting model parameters and evaluating model equations through Functional Mock-Up Units (FMUs), which are compiled dynamic models compliant with the Functional Mock-Up Interface (FMI). FMI is a standard that enables tool independent exchange of dynamic models on binary format. Several industrial simulation platforms support the export of FMUs, including, OpenModelica.

NumPy[10] is a library for the Python programming language, adding support for large, multi-dimensional arrays and matrices, along with a large collection of high-level mathematical functions to operate on these arrays.

---

[8] http://www.openturns.org/
[9] https://pypi.org/project/PyFMI/
[10] https://www.numpy.org/

•Examples of Polynomial Chaos approximation

In order to create a reliable Polynomial Chaos expansion which approximate with enough precision the model, a series of real model simulations are needed.

The real model is run a N_{PC} number of times where at each run the input is changed, in order to get many output results. Given the input values and the output values, the coefficients of the polynomial expansion that simulates the model behavior can be computed.
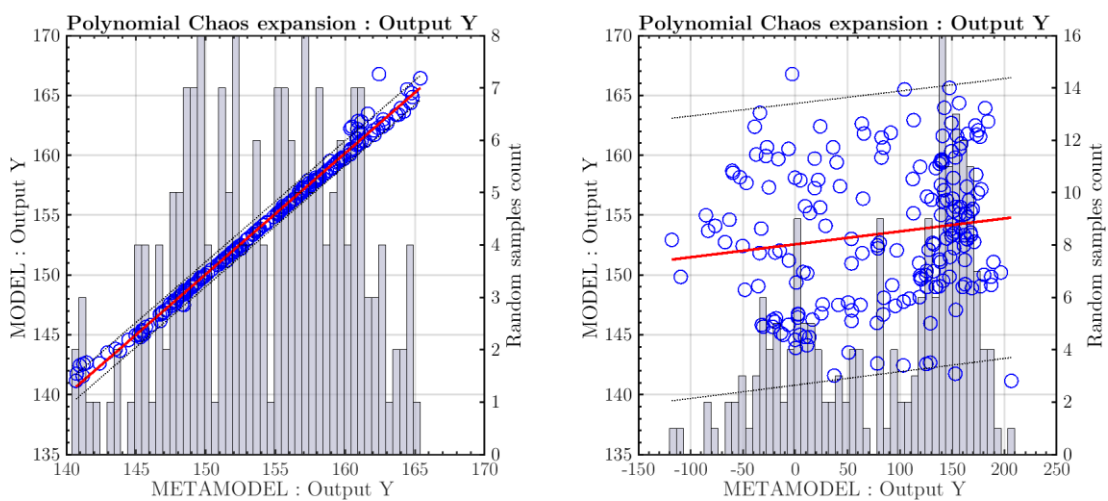
Figure 3.5 – Comparison between model outputs obtained with Polynomial Chaos expansions built with $N_{PC} = 50$ real model runs (on the left) and $N_{PC} = 20$ real model runs (on the right).

After the definition of the meta-model (based on the PC expansion), the meta-model must be tested against the real model with new simulations, for a user-defined N_{testPC} number of times.

Figure 3.5 shows the difference in the output results obtained from a PC-based meta-model built with 50 initial simulations of the real model, compared to the outputs of the same PC meta-model but built with only 20 initial simulations.

In each graph the circles represent the output values obtained for each testing run ($N_{testPC} = 200$) using both the PC meta-model and the real model. If the circles are aligned in a straight line, the output of the meta-model is able to reproduce exactly the real-model behavior. It can be seen that using $N_{PC} = 50$ simulations it is possible to obtain good results, with some small discrepancy at the end points of the output

distribution, whereas using $N_{PC} = 20$ does not permit to obtain a good meta-model since results go from negative values to very high values $Y_{meta} \in (-120 \div 210)$, while the real model is defined for $Y_{real} \in (141 \div 167)$. Note that Y is a fictitious output parameter of a model not of interest for the moment, used just as an example.
The histogram behind the scatter plot reports the meta-model output distribution.

Figure 3.6 reports a comparison between the input-output relation plot obtained with the two meta-model described above using $N_{PC} = 50$ and $N_{PC} = 20$ respectively.
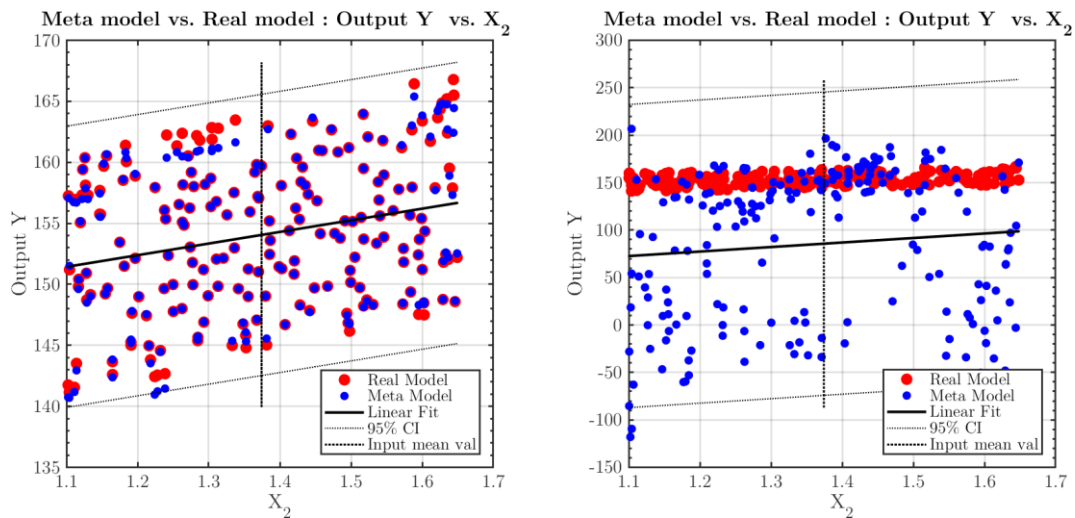
Figure 3.6 – Comparison between input-output graphs obtained with meta-models built with $N_{PC} = 50$ real model runs (on the left) and $N_{PC} = 20$ real model runs (on the right).

The y axis represents the output of the model Y, the x axis represents the considered input variable X_2. The bigger red dots are the real-model outputs, whereas the thinner blue dots are the meta-model results. Ideally the two set of dots should be completely superposed. We see that if $N_{PC} = 50$ the dots show small discrepancies concentrated at the boundaries, instead if $N_{PC} = 20$ the meta-model cannot simulate the real model behavior and the dots are spread all over the graph.

An example of Figure 3.5 and Figure 3.6 obtained with a better quality meta-model based on a PC built with $N_{PC} = 200$ real model simulations is reported in Figure 3.11 and Figure 3.13 respectively, in Section 3.2.

• Examples of Sensitivity analysis using Sobol indices

Figure 3.7 illustrates an example of graphical representation of the Sobol indices obtained with a sensitivity analysis of a system of which 3 fictitious input variables have been analyzed with respect to one output variable. The y axis reports the Sobol index value (from 0 to 1) and the x axis represents the considered input variables.
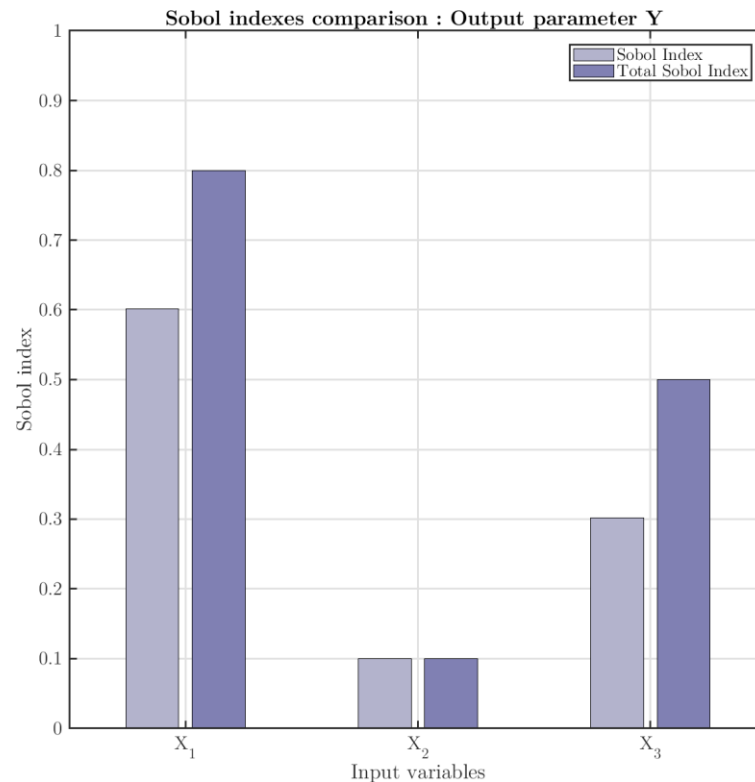
Figure 3.7 – Example of Sobol indexes analysis of 3 input variables (X_1, X_2, X_3) with respect to an output parameter Y.

The two columns represent the direct Sobol index S_i and the Total Sobol index S_{Ti}, for each variable.

- The **direct Sobol index** S_i indicates each input individual contribution to the output variance.

- The **Total Sobol index** S_{Ti} indicates each input contribution to the output variance when accounted together with the interactions with other parameters.

In this example the input variable X_1 is responsible for the 60% of the output variance, while X_3 and X_2 are responsible for the 30% and 10% respectively (each counted alone). The total sum of these direct Sobol indices is 100%.

The total Sobol indices of the variable X_1 and X_3 are greater than the direct index, this meaning that each of these variables are responsible for a greater output variance if accounted with their interaction with other variables. On the contrary, the variable X_2 has $S_i = S_{Ti}$, which means that this variable does not interact with other variables considered in this example.

3.2 Sensitivity analysis: Diastolic and systolic elastances

Taking as a reference the closed-loop model introduced in Chapter 2.1, a sensitivity analysis can be performed over a set of inputs with the aim of assessing their relative importance with respect to a defined output.

In this section, a sensitivity analysis is conducted over two sets of input parameters:

- $E_{D,L}$ and $E_{S,L}$ Left-ventricular diastolic and systolic elastances.
- $E_{D,R}$ and $E_{S,R}$ Right-ventricular diastolic and systolic elastances.

As explained in Section 2.1.1, these constants affect the ventricular capacitance of the closed-loop model, which characterizes the ventricular elastance in the heart.

The formula of the **variable capacitance** of the ventricle are here reported, see Table 2.2 for references:

$$\boxed{\Delta p = E(t) \cdot V}$$

$$C(t): \ E(t) = \begin{cases} E_L(t) = E_{D,L} + E_{S,L} \cdot A(t) \\[2mm] E_R(t) = E_{D,R} + E_{S,R} \cdot A(t) \end{cases}$$

(2.6)

where: $A(t)$ is the *activation function*, see (2.5).

The output parameter is set to be the **maximum ventricular pressure**:

- $\max(p_{LV})$ maximum left-ventricular pressure.
- $\max(p_{RV})$ maximum right-ventricular pressure.

► **Statistical parameters:**
For each sensitivity analysis, the number of runs of the real OpenModelica model used to build the Polynomial chaos expansion is set to $N_{PC} = 200$.

A number of tests $N_{testPC} = 200$ is performed over the meta-model with respect to the real model results.

A number of $N = 20'000$ simulations of the meta-model is performed, in order to get a reliable output variable distribution, and obtain reliable Sobol indices.

The PC expansion considers a maximum number of terms set to $maxPC_{terms} = 500$, with the most significant terms $minPC_{terms} = 50$, with a significance factor of $PC_{SF} = 10^{-8}$.

The input variables are considered **uniformly distributed** with mean value μ_{X_i} expressed in Table 3.2 and extension interval $[a; b] = [\mu_{X_i} - \alpha\,\mu_{X_i} \; ; \; \mu_{X_i} + \alpha\,\mu_{X_i}]$, see Figure 3.8.
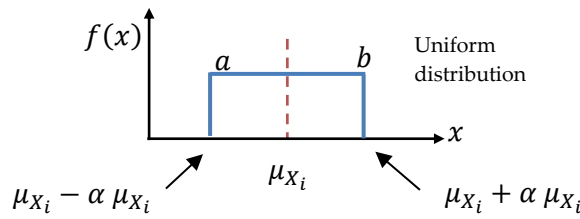
Figure 3.8 – Graphical representation of a uniform distribution.

Input variable	Distribution	Mean μ_{X_i}	Interval α	Units
$E_{D,L}$	Uniform	0.04	0.2	mmHg cm^{-3}
$E_{S,L}$	Uniform	1.375	0.2	mmHg cm^{-3}
$E_{D,R}$	Uniform	0.01	0.2	mmHg cm^{-3}
$E_{S,R}$	Uniform	0.23	0.2	mmHg cm^{-3}

Table 3.2 – Ventricle elastances input variables for sensitivity analysis.

The probability density function (PDF) associated with the above defined continuous uniform distributions is:

$$f(x) = \begin{cases} \dfrac{1}{b-a} & \text{for } a \leq x \leq b \\[2mm] 0 & \text{for } x < a \text{ or } x > b \end{cases}$$

(3.22)

with: $a = \mu_{X_i} - 0.2\,\mu_{X_i}$ and $b = \mu_{X_i} + 0.2\,\mu_{X_i}$

3.2.1 Maximum left-ventricular pressure depending on the elastances

Figure 3.9 reports the distributions associated with the chosen input parameters.
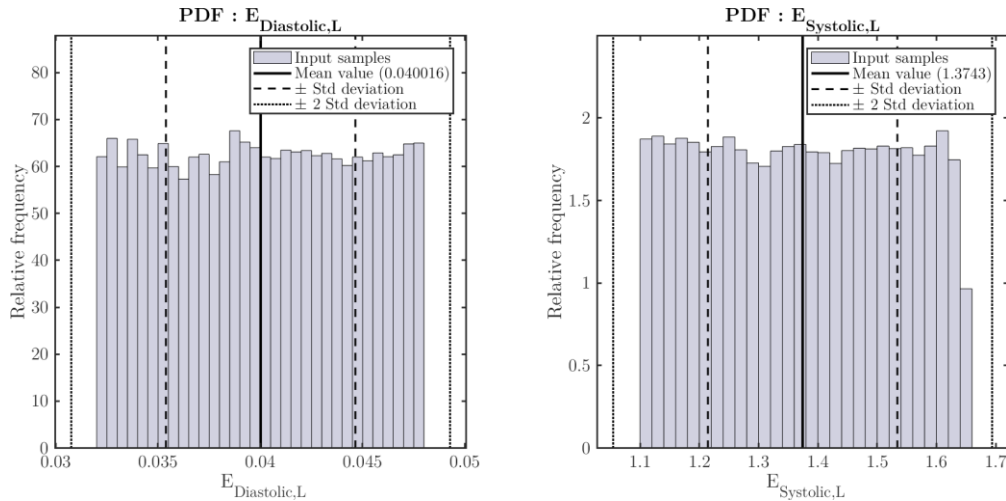
Figure 3.9 – PDFs associated with the input variables: $E_{diastolic,L}$ and $E_{sistolic,L}$.

The distributions of the inputs are uniform, and the means of the set of random values taken are sufficiently close to the imposed ones.

These inputs are used to perform $20'000$ simulations, using the PC expansion, to get the same number of output results. Figure 3.10 reports the distribution of the meta-model computed outputs. As an additional information, it can be seen that the shape of the output results resembles a Gaussian distribution.

In order to check if the results obtained in Figure 3.10 can be considered as reliable, additional simulations using both the real model and the PC-based meta-model are performed. In Figure 3.11, $N_{testPC} = 200$ simulation outputs are compared, and it can be seen that no deviation from the scatter line occurs. This means that a number of $N_{PC} = 200$ simulations are sufficient in order to get satisfying PC coefficients, and that the results obtained by using only the meta-model can be considered representative of the real model behavior.
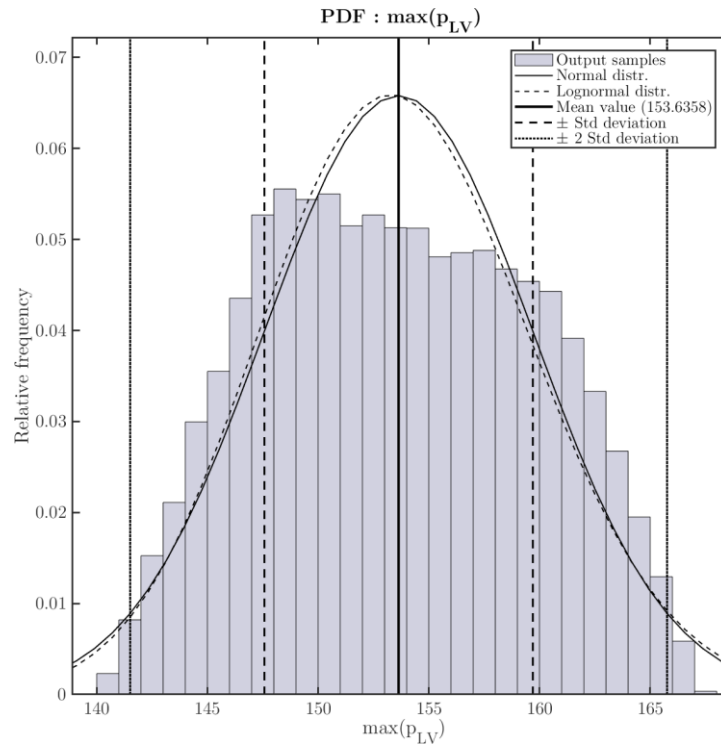
Figure 3.10 – PDF of the output variable: max (p_{LV}).

Using the results from these 200 additional simulations a graphical representation showing the relation between the input variables and the output can be plotted. In Figure 3.12 and in Figure 3.13 shows how the two considered input variables ($E_{D,L}$ and $E_{S,L}$) are correlated to the considered output max(p_{LV}).

More precisely, Figure 3.12 shows a negative linear correlation between the diastolic elastance of the left ventricle and the maximum pressure of the left ventricle, whereas Figure 3.13 shows a weaker positive correlation between $E_{S,L}$ and max(p_{LV}).

In addition, since these plots are based on the $N_{testPC} = 200$ testing simulations, it can be seen that the points associated with the meta-model are completely superimposed to the real model ones, confirming again the reliability of the considered meta-model.

Figure 3.11 – Comparison between the meta-model output results, generated through the polynomial chaos expansion, with respect to the real model outputs (circles and bold line, respectively). The meta-model output distribution counting the tested samples is reported in the histogram.

After checking the meta-model reliability, the results obtained in Figure 3.10 can be safely used to compute Sobol indices associated with the considered input variables. Figure 3.14 presents the direct Sobol indices and the Total Sobol indices associated with $E_{D,L}$ and to $E_{S,L}$.

It can be seen that the diastolic elastance alone is responsible for more than 85% of the maximum ventricular pressure variance, whereas the systolic elastance only contributes for less than 15%. In addition, it can be noticed from the Total Sobol indices that each variable contributes alone to the final output variance and does not interact with the other variable in any way.
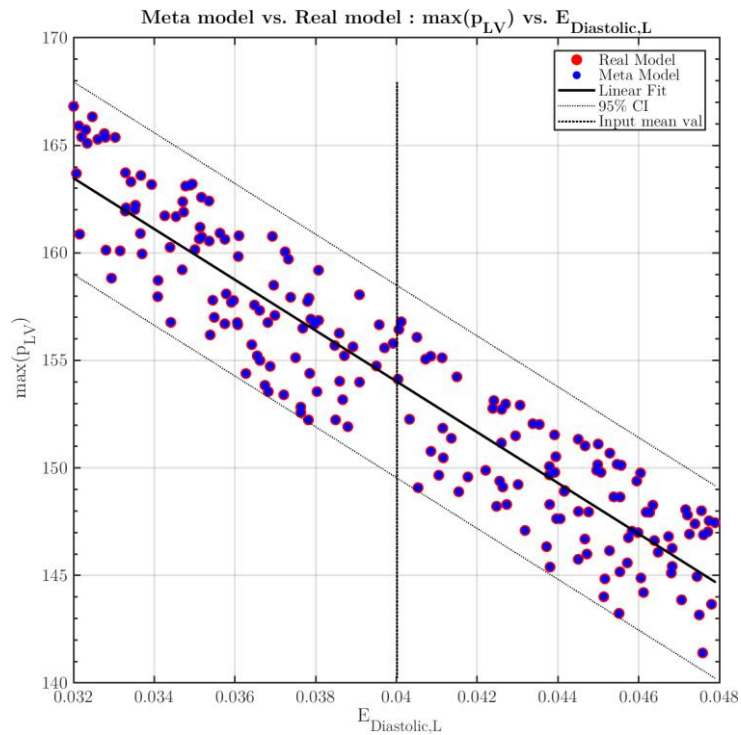
Figure 3.12 – Meta-model results compared with the real model. The x axis represents the input variable $E_{Diastolic,L}$ and the y axis displays the output variable $\max(p_{LV})$.
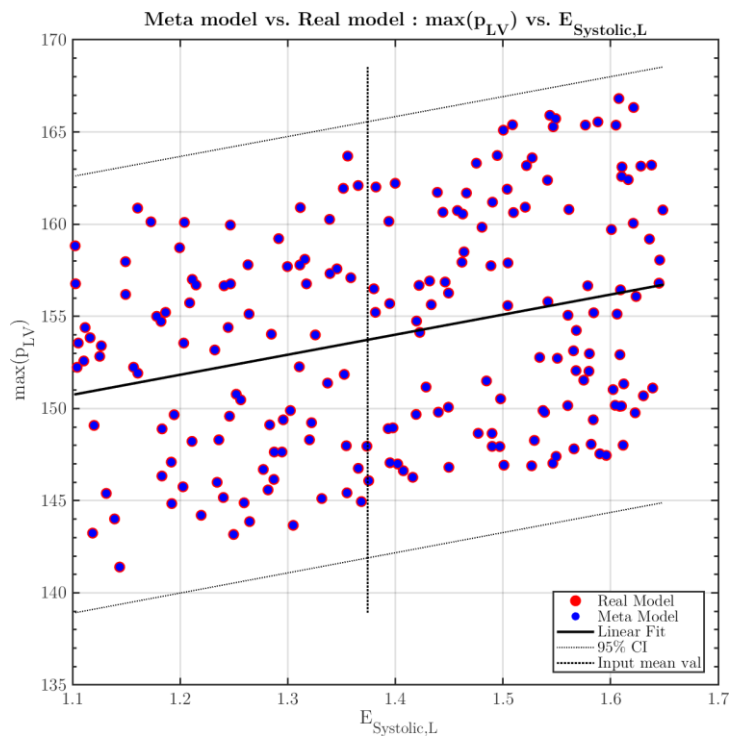
Figure 3.13 – Meta-model results compared with the real model. The x axis represents the input variable $E_{Systolic,L}$ and the y axis represents the output variable $\max(p_{LV})$.
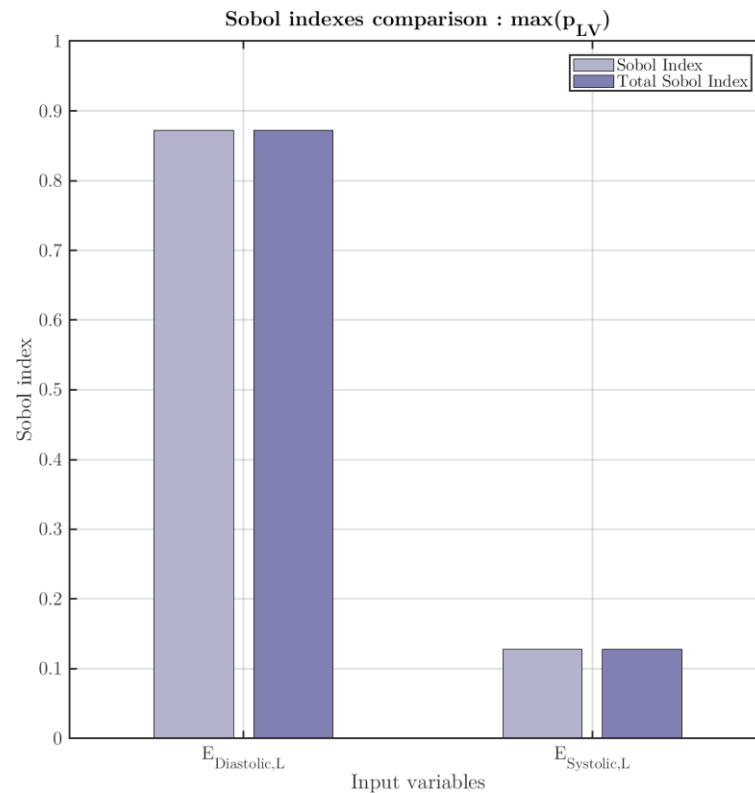
Figure 3.14 – Sobol indexes associated with the variation of the two input variables considered $E_{diastolic,L}$ and $E_{systolic,L}$ with respect to the output variable variation $\max(p_{LV})$.

3.2.2 Right ventricle maximum pressure given its elastances

Following the analysis performed in Section 3.2.1, in this section the same considerations are presented for the right ventricular part.

In Figure 3.15 the distributions of the two input variables are shown.

In Figure 3.16 the computed output variable distribution is reported. Again, it can be seen that it resembles (in a weaker way) a Gaussian distribution.
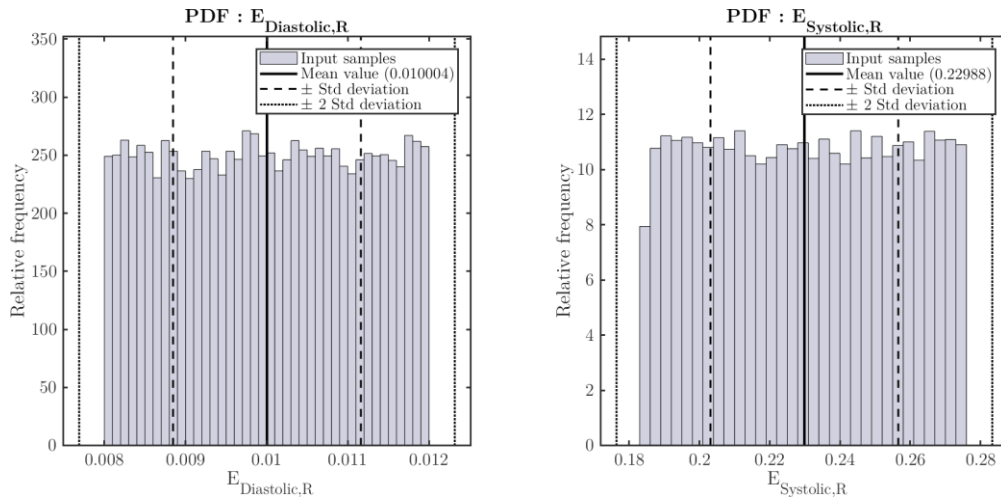
Figure 3.15 – PDFs of the input variables: $E_{diastolic,R}$ and $E_{systolic,R}$.
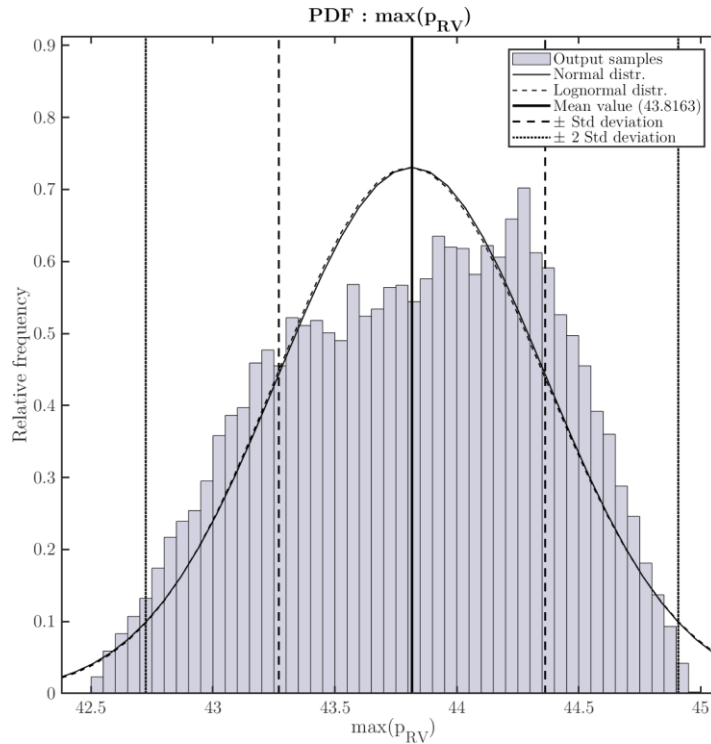
Figure 3.16 – PDF of the output variable: max (p_{RV}).

As done for the left ventricle, the quality of the newly computed PC is tested with $N_{testPC} = 200$ additional simulations, see Figure 3.17.
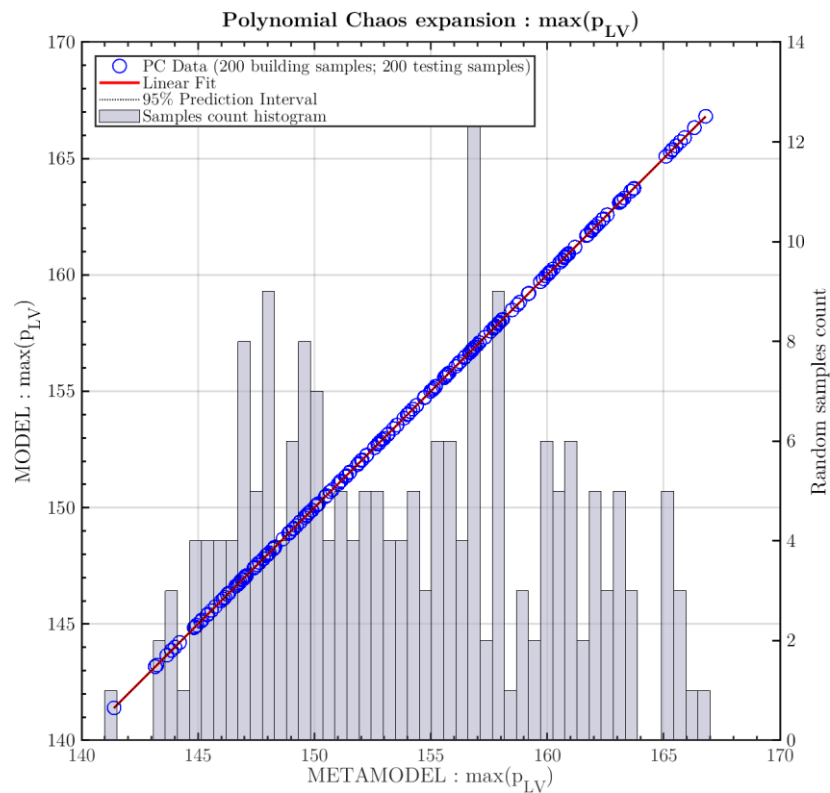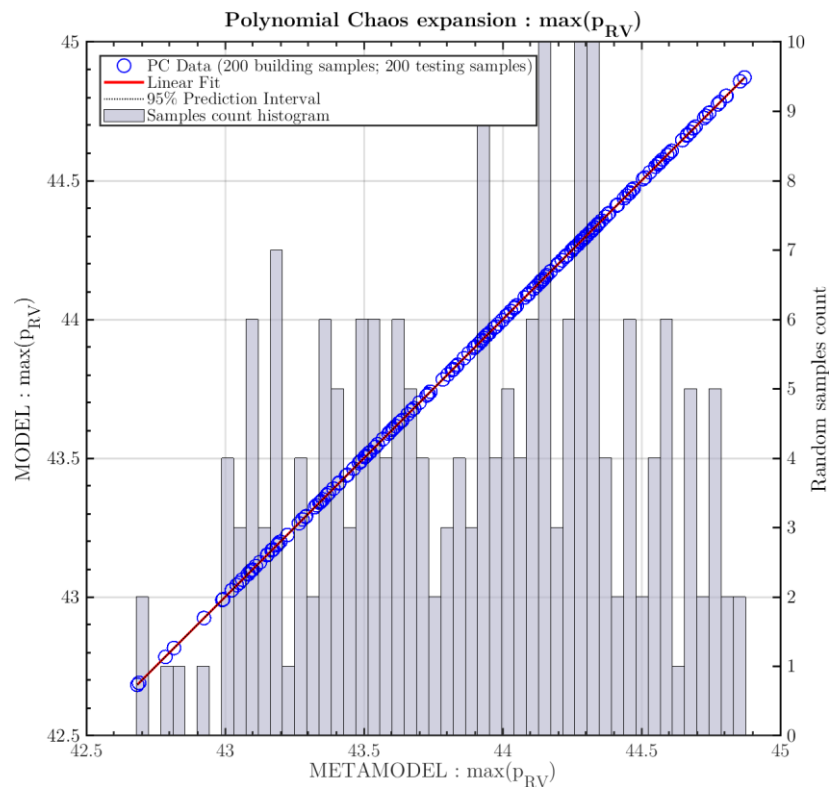
Figure 3.17 – Comparison between the meta-model output results, generated through the polynomial chaos expansion, with respect to the real model outputs (circles and bold line, respectively). The meta-model output distribution counting the tested samples is reported in the histogram.

In Figure 3.18 and Figure 3.19 the correlation between the inputs and the output is shown. Unlike the right ventricle, the diastolic elastance is weakly inversely correlated to the maximum right ventricle pressure, whereas the systolic elastance is positively well correlated.

In Figure 3.20 the Direct ad Total Sobol indices are computed and plotted. Results show a completely reversed situation (please note that the percentages of influence are not exactly the same) with respect to the left ventricle, in this case the systolic elastance affects for more than 85% the output variance, while the diastolic elastance the remaining part, around 15%. Again the two variables are not interacting with each other.
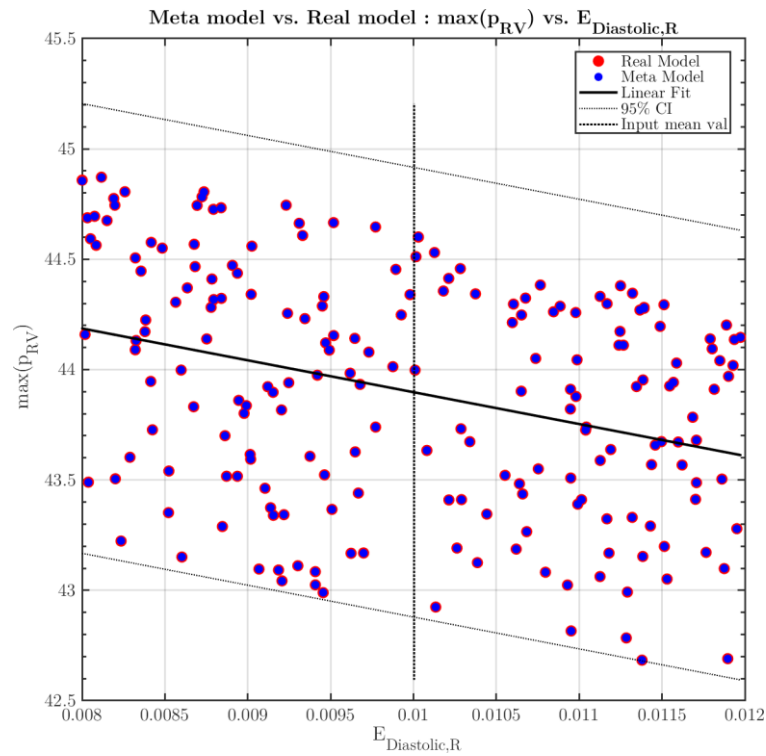
Figure 3.18 – Comparison between the meta-model results with respect to the real model ones. Correlation between $E_{D,R}$ with respect to the output variable.
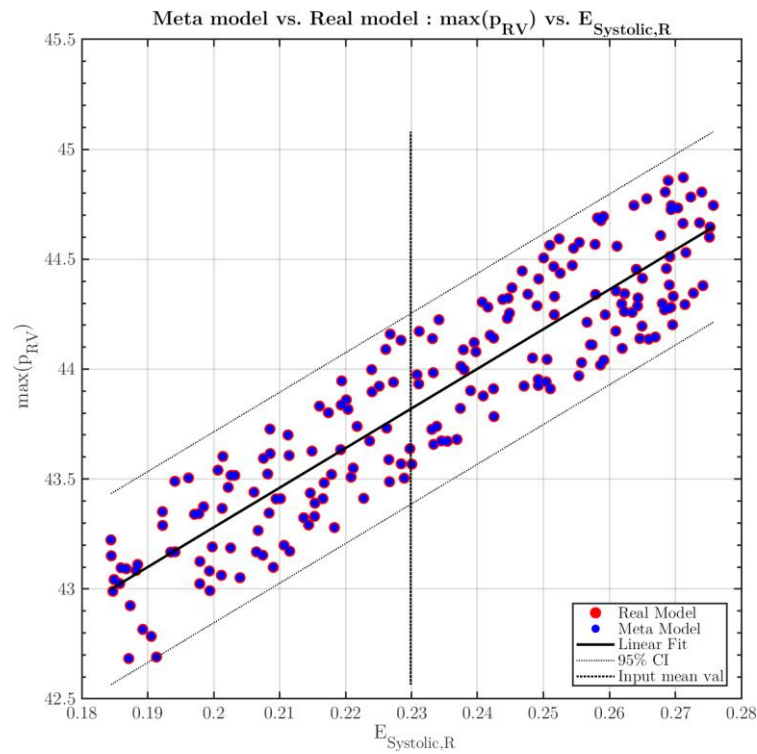
Figure 3.19 – Comparison between the meta-model results with respect to the real model ones. Correlation between $E_{S,R}$ with respect to the output variable.
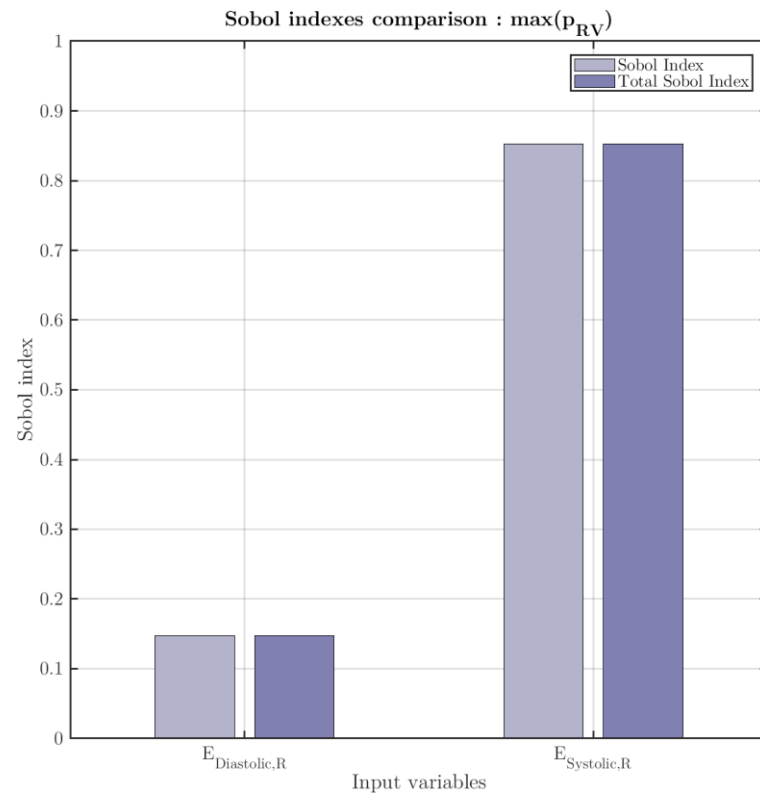
Figure 3.20 – Sobol indexes associated with the variation of the two input variables considered $E_{diastolic,R}$ and $E_{sistolic,R}$ with respect to the output variable variation $\max(p_{RV})$.

3.3 Sensitivity analysis: Arteries elastance

Another sensitivity analysis that can be performed is the influence of arterial stiffness, defined through the Young modulus E, on the pressure inside the left ventricle.

In particular, as defined in Section 2.1.1, the Young modulus E affects directly the capacitance of the main arteries of the model through the following relation:

$$\boxed{C = \frac{3\,l\,S\,(a+1)^2}{E\,(2a+1)}} \quad ; \quad \gamma = \frac{\delta}{C} \tag{2.4}$$

where:

C	is the capacitance constant;
γ	is the viscoelastic constant;
$a = r/h$	is the ratio between vessel radius r and wall thickness h;
l	is the vessel length;
$S = \pi\,r^2$	is the vessel cross-sectional area;
E	is the Young modulus of the vessel wall;
δ	is the viscoelastic parameter of the vessel wall.

As reported in Section 2.1.1, in (Guidoboni, et al., 2019), it is assumed that:

$$E = 4 \cdot 10^6\ [\text{dyne/cm}^2]$$

$$\delta = 1.56 \cdot 10^{-3}\ [s]$$

Since E is expressed in dyne/cm², a conversion factor must be used to express it in $mmHg$,

$$E[\text{mmHg}] = 0{,}000750062 \cdot E[\text{dyne/cm}^2]$$

The values of the remaining geometrical parameters utilized to determine R, L, C and γ for each of the main arterial segments have been adapted from (Noordergraaf & al., 1963) and are reported in Table 2.3.

Table 3.3 reports the characteristic values of the arterial compartments considered and the parameters used to compute the capacitance C. In the right column, the mean value of the capacitance is also reported. Note that it is called "mean" because obtained with the standard value of the Young modulus E, which will be taken as mean value for the input distribution.

Arterial Segment	L [cm]	R [cm]	H [cm]	A [-]	S [cm²]	C·E [cm³]	C$_{mean}$ [cm³/mmHg]
Ascending Aorta	4	1.44	0.158	9.114	6.514	415.8769	1.39E-01
Aortic Arch	5.9	1.25	0.139	8.993	4.909	456.9761	1.52E-01
Thoracic Aorta	15.6	0.96	0.117	8.205	2.895	659.4665	2.20E-01
Abdominal Aorta	15.9	0.85	0.105	8.095	2.270	521.0103	1.74E-01
Iliac artery	5.8	0.52	0.076	6.842	0.849	61.9043	2.06E-02
Carotid artery	20.8	0.39	0.064	6.094	0.478	113.7766	3.79E-02

Table 3.3 – Geometrical parameters and capacity calculations with respect to the Young modulus E for each considered variable compartment.

Inserting these values into the sensitivity analysis code, using $N_{PC} = 600$ simulations to capture the PC coefficient with high reliability, $N_{testPC} = 200$ testing simulations to check the PC against the real model outputs, and performing $N = 20'000$ simulations to assess the output distribution characteristics, brings to the results reported in the following.

The chosen input distribution of E is uniform, with limits sets to $\mu \pm 1.5\,\mu$, μ being the mean value of the considered input variable (the Young modulus E), see Figure 3.21.

Figure 3.22, instead, shows the distribution of the output variable. It can be seen that it is not possible to consider it normally distributed.

In Figure 3.23 the comparison between real model and meta-model is shown. It can be seen that $N_{PC} = 600$ simulations are sufficient to capture a reliable result.

Finally, in Figure 3.24 the input-output relation is shown. The behavior of the real model seems to be captured quite precisely by the built meta-model, since the dots are superposed, and an almost linear trend emerges from the results
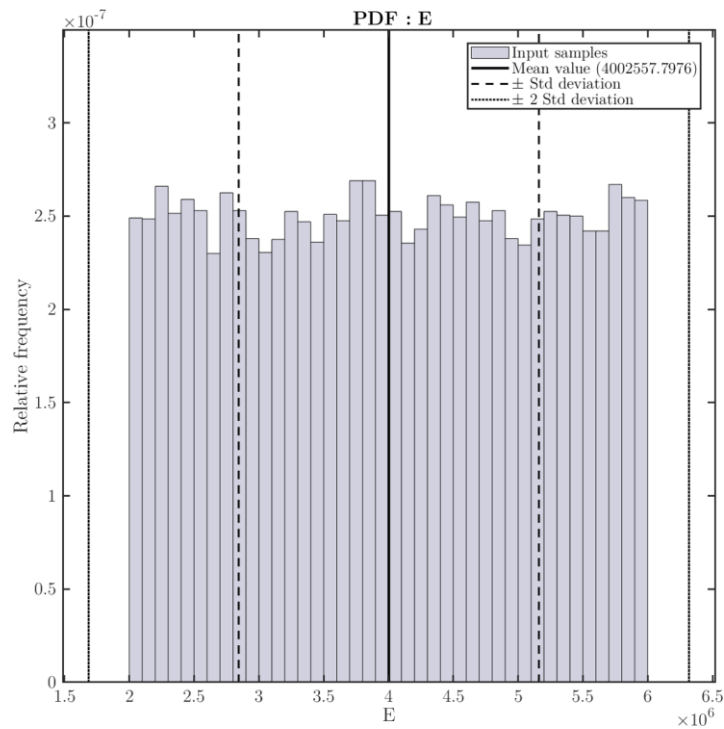
Figure 3.21 – PDF of the input variable: E.
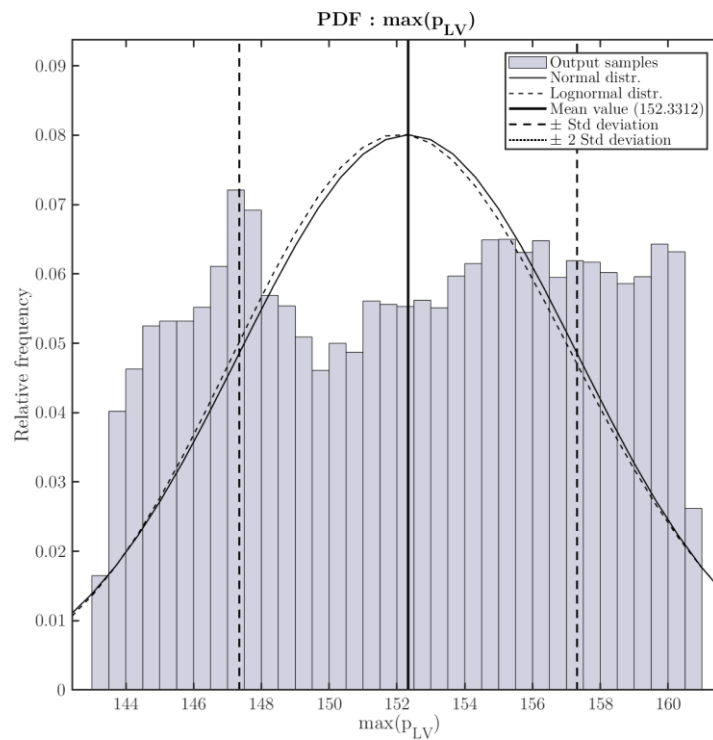
Figure 3.22 – PDF of the output variable: max (p_{LV}).
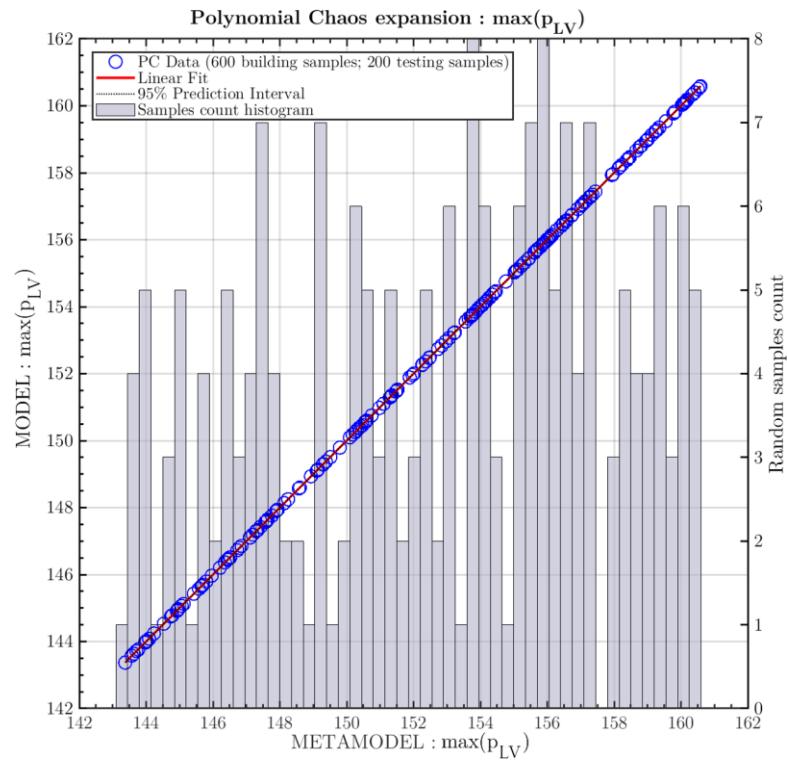
Figure 3.23 – Comparison between the meta-model output results, with respect to the real model outputs. The histogram represents the meta-model output distribution.
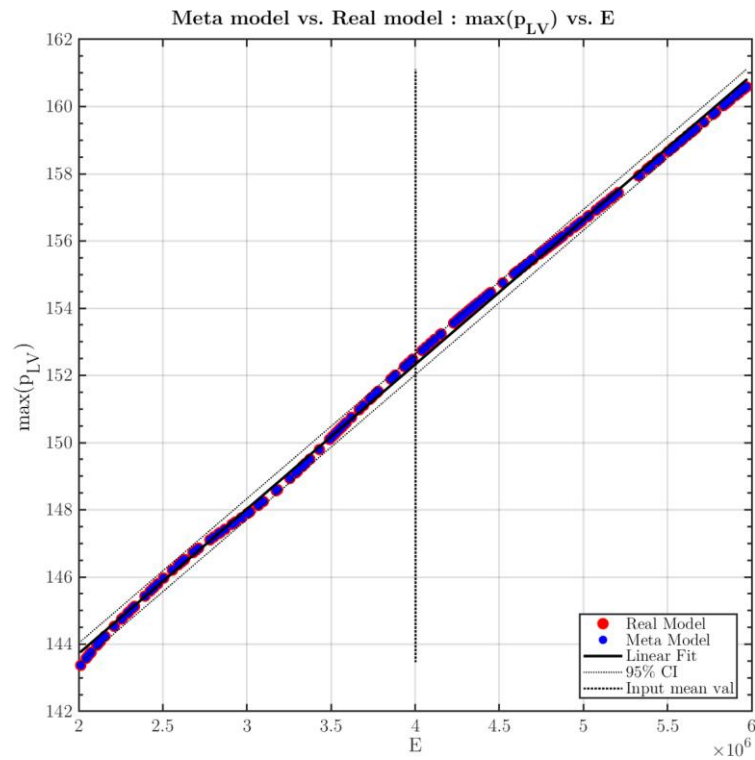
Figure 3.24 – Input-output relation. The x axis represents the input variable E and the y axis represents the output variable $\max(p_{LV})$.

PART II :

EXPERIMENTAL TESTS

4 – LOAD CELL SENSORS

In this chapter, we provide the details about how to measure the **ballistocardiogram (BCG)** associated with the <u>displacement of the center of mass of an individual</u>. This motion is mainly due to the inertial effects of the blood ejected by the heart into the aorta and its flow into the main arteries.

In particular, **load cells** (medical weighting scales, in this case) positioned under the four legs of a bed are used to retrieve the center of mass of the system composed by the bed frame and the person on the bed. The reconstruction of the motion of the center of mass leads to the measurement of the BCG.

In Chapter 2 a mathematical model capable of simulating the ballistocardiogram (BCG) curves given physiological data was described and analyzed. The final purpose of this chapter is to compare the theoretical result obtained in Chapter 2 with in-lab measurements. After this step, future experiments may assess precisely the causal-effect relationship between measured BCG curves and possible pathologies affecting the cardiovascular system, especially affecting the heart and the main arteries.

It should be noted that part of the work exhibited in this part has also been published in the chapter of the book (R. Invernizzi, 2021).
In particular, in that publication the link that exists between the ability to find the position of a weight placed on a bed and the ability to understand how the center of mass of a subject moves is exposed in a more synthetic and practical way.

4.1 Load cell sensors: mechanical and physical reasons

•*Measurement devices*

The original measurement device used by Starr and others was a lightweight **suspended bed** attached to the ceiling with long cables. The <u>blood flow of a subject lying on the suspended bed resulted in the bed swinging</u>; the capture of the swing was the BCG signal. This measurement device was impractical for standardized BCG measurements, especially compared to the electrocardiogram (ECG), which could be taken on virtually any platform using electric leads placed on the body in a standard configuration. The standardization of the ECG measurement has allowed clinical interpretation of the ECG waveform, such that it can be used to diagnose abnormalities in cardiac function.
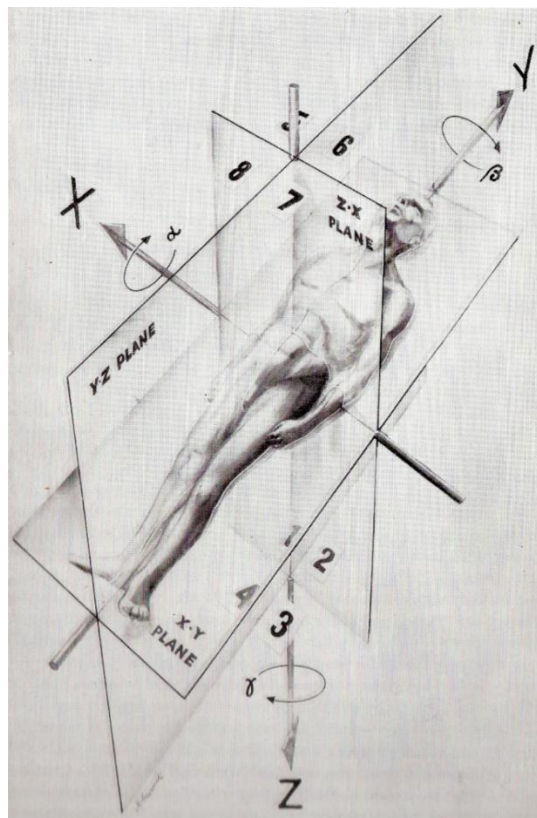
Figure 4.1 – Original drawing used by Starr and Noordergraaf with the nomenclature for the BCG axes. (Starr & Noordergraaf, 1967).

Recently, there has been a resurgence of BCG research, as new sensing devices (e.g., in the form of bed sensors) allow an <u>easier and noninvasive capture of the BCG signal</u>. In addition, the BCG offers advantages over the standardized ECG measurement, because direct body contact is not required and the signal reflects the status of the cardiovascular system as a whole, rather than of the heart only. These advantages provide intriguing possibilities of continuous passive monitoring of the cardiovascular system without requiring the patient to do anything.

There have been a variety of bed, chair, and other sensors proposed to capture the BCG; several of them are now available commercially (Inan & al, 2015). Much of this work has focused on monitoring heart rate along with respiration rate from the accompanying respiration signal, and other parameters for tracking sleep quality. Recent work has also investigated the BCG waveform morphology for the purpose of tracking changes in cardiovascular health (Pinheiro & al, 2010). This offers a special relevance and significant potential in monitoring older adults as they age. Identifying very early signs of cardiovascular health changes provides an opportunity for very early treatments before health problems escalate; very early treatment offers better health outcomes and the potential to avoid hospitalization (Rantz & al, 2015).

• *Load cells as bed sensors*

In the present work, particular weighting scales positioned under the four legs of a bed are used to retrieve the center of mass of the bed (when no one is laying on it), and the center of mass of the system composed of the bed frame plus the person lying on it.

Let R_1, R_2, R_3, R_4 be the forces transmitted by the bed legs to the four weighting scales (the reaction forces of the bed on the floor).

Let L and W be the measures of the major bed frame dimension and the smaller bed frame dimension respectively. These measurements are taken between the bed legs central points.

Finally, let W_{bed} be the total weight of the bed.

The **position of the centroid of the bed** can be found by enforcing the *rotational equilibrium* around two bed axes, see Figure 4.2, bringing to the following formulas:

$$x_c = W \cdot \frac{(R_1 + R_3)}{W_{bed}}$$

(4.1)

$$y_c = L \cdot \frac{(R_3 + R_4)}{W_{bed}}$$
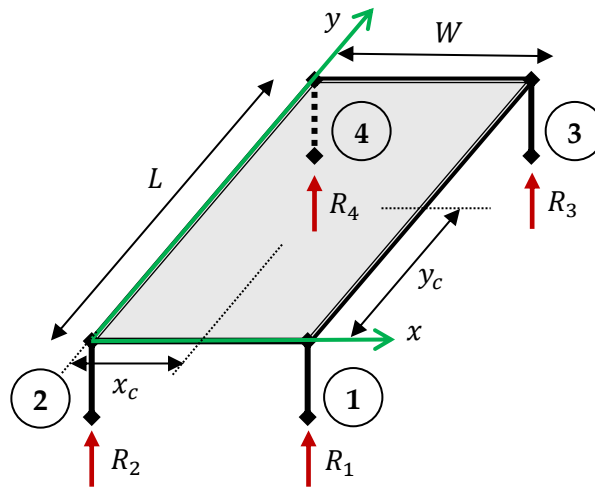
Figure 4.2 – Bed frame scheme. R_i are the reaction forces, $i = (1,2,3,4)$. L and W are the bed dimensions, x_c and y_c the coordinate of the center of mass of the bed.

These formulas allow us to compute the center of mass of the bed, see (R. Invernizzi, 2021).

In order to understand if this could actually be done, experimental tests are performed and reported in Section 4.2.

4.2 Load cell sensors: experimental tests

In this section experimental tests are carried out in order to understand if it is really possible to retrieve the position of the center of mass of a wooden bed using weighting scales positioned under the bed legs only.

For this purpose, a wooden bed was installed with 4 medical load cells under each bed leg at the *Center for Eldercare and Rehabilitation Technology*, established by Marjorie Skubic in the department of *Electrical Engineering and Computer Science* of the *University of Missouri*, See Figure 4.3.

Figure 4.3 – Image of the wooden bed frame used for the tests. Center for Eldercare and Rehabilitation Technology, University of Missouri.

The lead cells are produced by MinebeaMitsumi Inc. or NMB (Nippon Miniature Bearing), a Japanese multinational corporation and a major producer of machinery components and electronic devices.

Figure 4.4 – Detail of the weighting scales positioned under the bed legs.

The load cells are then numbered from 1 to 4 according to the scheme in Figure 4.2.

4.2.1 Load cells sensitivity to different weights

The first test consists in measuring many times some given weights. In particular, 15 tests are performed for each of the 9 calibration weights used, as shown in Figure 4.5.

The calibration weights are numbered according to Figure 4.5 and Table 4.1.
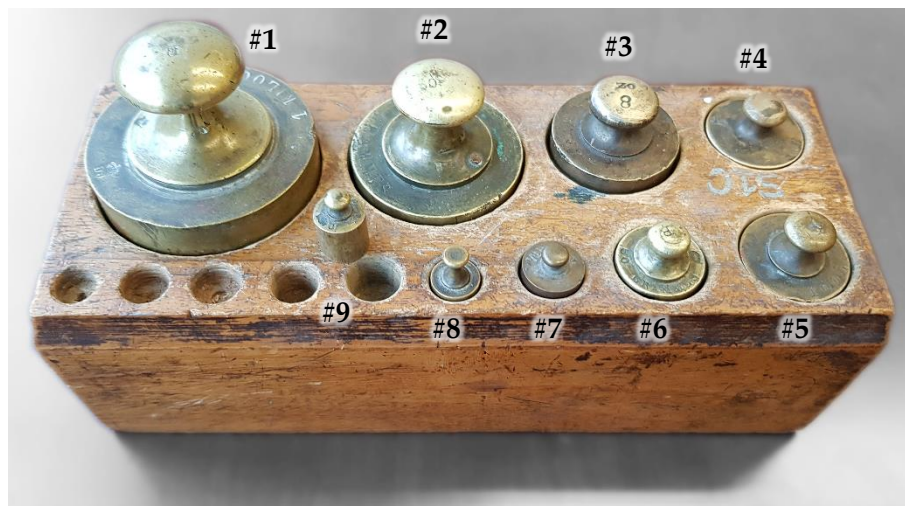
Figure 4.5 – Set of calibration weights used for the tests, numbered from 1 to 9.

The weights were positioned in 15 different locations on the bed frame as shown in Figure 4.6. The test was conducted by putting the weights over the wooden bed frame only, without mattress, pillows or bed sheets.
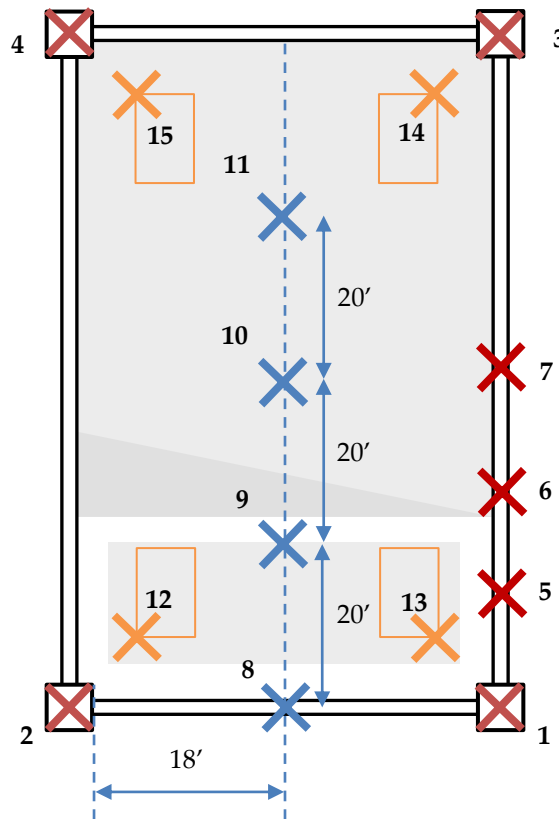
Figure 4.6 – Scheme of the weights positions on the bed frame.

The data from the load cells were recorded continuously, for each weight positioned in the 15 different locations, as shown in Figure 4.7. It can be noticed from the same figure that, as the position of the weight changes, the distribution of the reaction forces changes accordingly. In the first 4 tests, for instance, the weight is positioned exactly above the four legs, one at the time, and the measured signal given by the load cells is in fact predominant for the correspondent cell positioned under the corresponding weight.
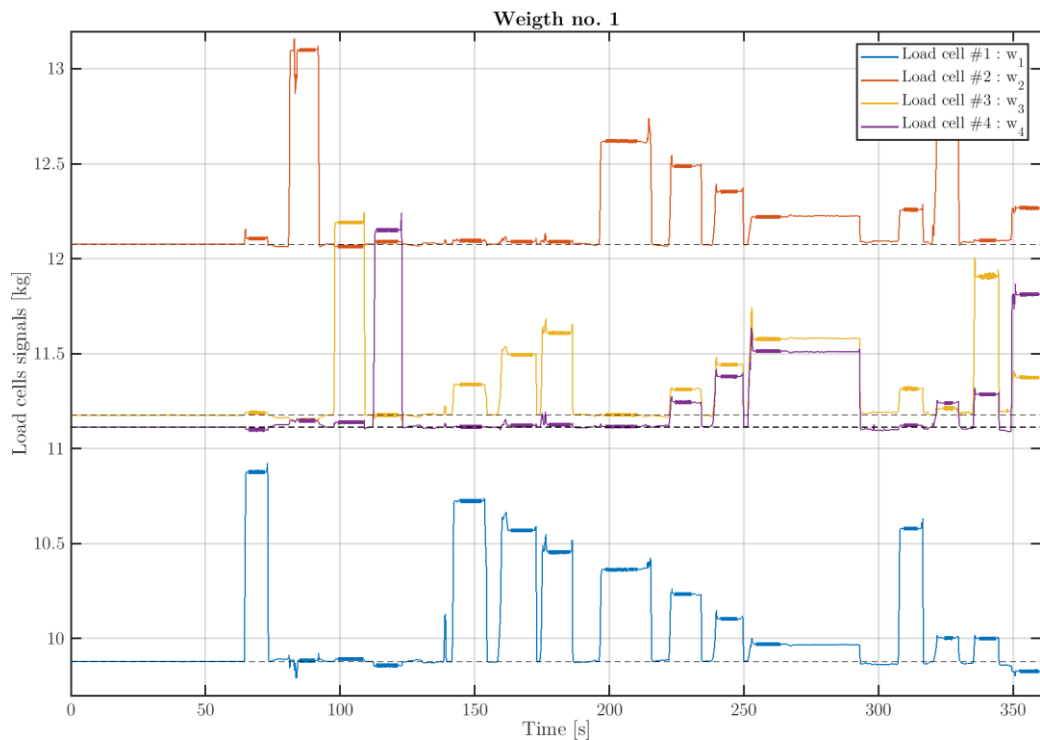
Figure 4.7 – Rough data obtained from the four load cells. Tested weight: 1kg. The thicker parts represent the stable measurements.

Summing up the signals from the 4 load cells, results in the total weight of the system composed by the bed frame plus the considered calibration weight. In Figure 4.8 the total weight graphs of 3 tested weights are reported.

It can be noticed that the weight of the sole bed frame is around 44.25 kg. For each tested weight the signal increases proportionally to the mass of the tested object and so its weight can be easily assessed considering the jump in the total weight signal.
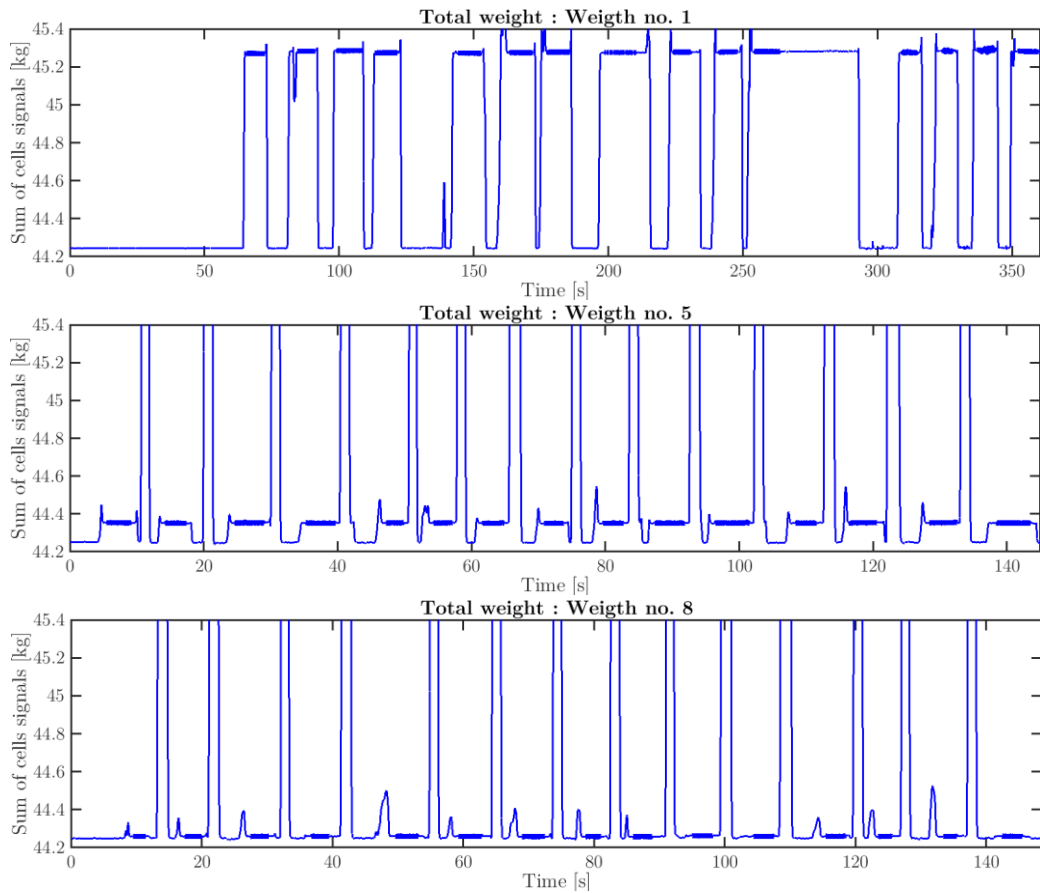
Figure 4.8 – Total weight obtained from the sum of the four load cells under the bed. The (I) refers to the weight no.1 (1kg), the (II) to the weight no.5 (100g), the (III) to the weight no.8 (10g).

NOTE: The high spikes present in the last 2 graphs are due to an enforced perturbation from one test to the other, useful to divide one experiment from the following one, especially in the case of small weights.

Table 4.1 and Figure 4.9 summarize the results of the weighting test.

It can be noticed that the real weight of the samples considered can be estimated with a limited variation (lower than ±1.5 %) until 50 g approximately, while for smaller weights the variability is higher (up to ±15 % with respect to the mean value).

Having assessed the precision of the weighting scales used, we ask ourselves whether it is possible to retrieve the position of the tested weights looking only at the load cells signals. This experiment is illustrated in Section 4.2.2.

Tested weight			Measured weight: 15 tests		
no.	Sign	Sign [g]	Mean [g]	Std. var [g]	
1	**1 kg**	1000.0	**1035**	±5	(±0.5%)
2	**500 g**	500.0	**525**	±7	(±1.4%)
3	**8 oz**	226.8	**234**	±1	(±0.5%)
4	**4 oz**	113.4	**104**	±1	(±1.2%)
5	**100 g**	100.0	**102**	±1	(±0.8%)
6	**50 g**	50.0	**52**	±0	(±0.9%)
7	**20 g**	20.0	**19**	±1	(±7.2%)
8	**10 g**	10.0	**11**	±1	(±9.8%)
9	**10 g**	10.0	**11**	±2	(±15.6%)

Table 4.1 – Results of the measuring weights test summed up.
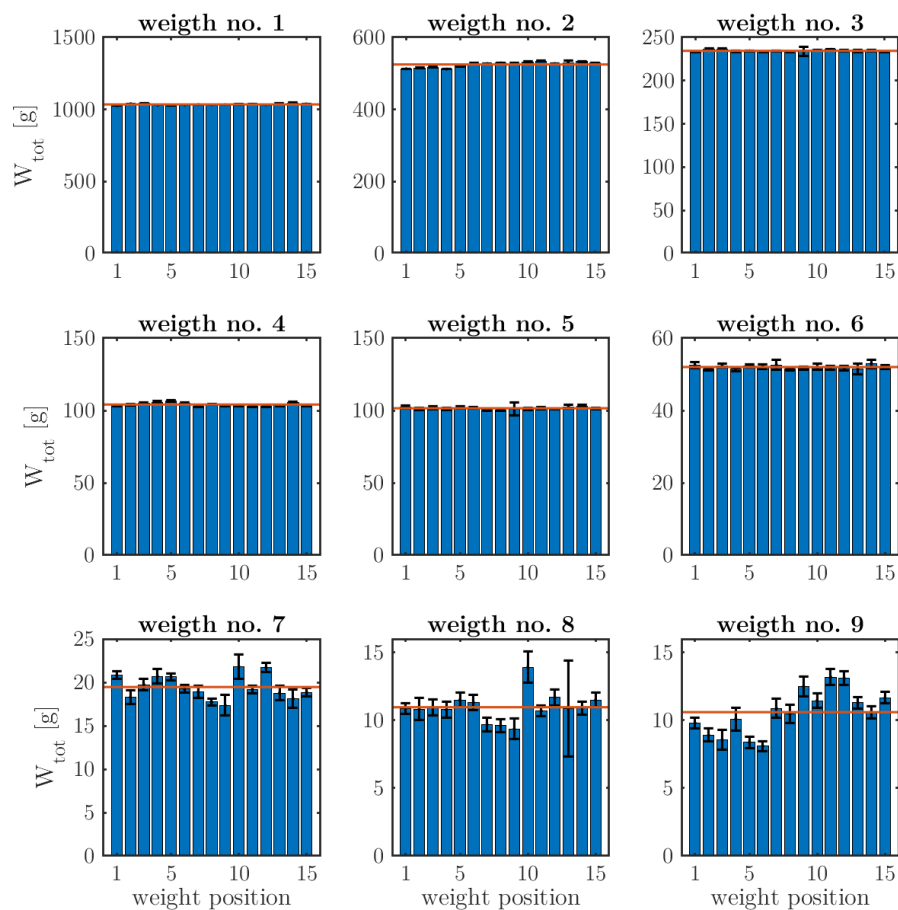
Figure 4.9 – Histograms showing the variability in estimating the weights.

4.2.2 Reconstructing weight position from load cells data

Following the conclusions of Section 4.1, and having the bed frame measures, it turns out that, in principle, it is possible to retrieve the position of a weight positioned on the bed frame considering only the signal from the load cells positioned under the bed legs.

With this purpose, the data obtained from Section 4.2.1 can be reused trying to estimate, a posteriori, the coordinates at which each calibration weight was positioned.

In Figure 4.10 raw data obtained from the load cells are reported in the case of the test of the weight no.5 (100 g).
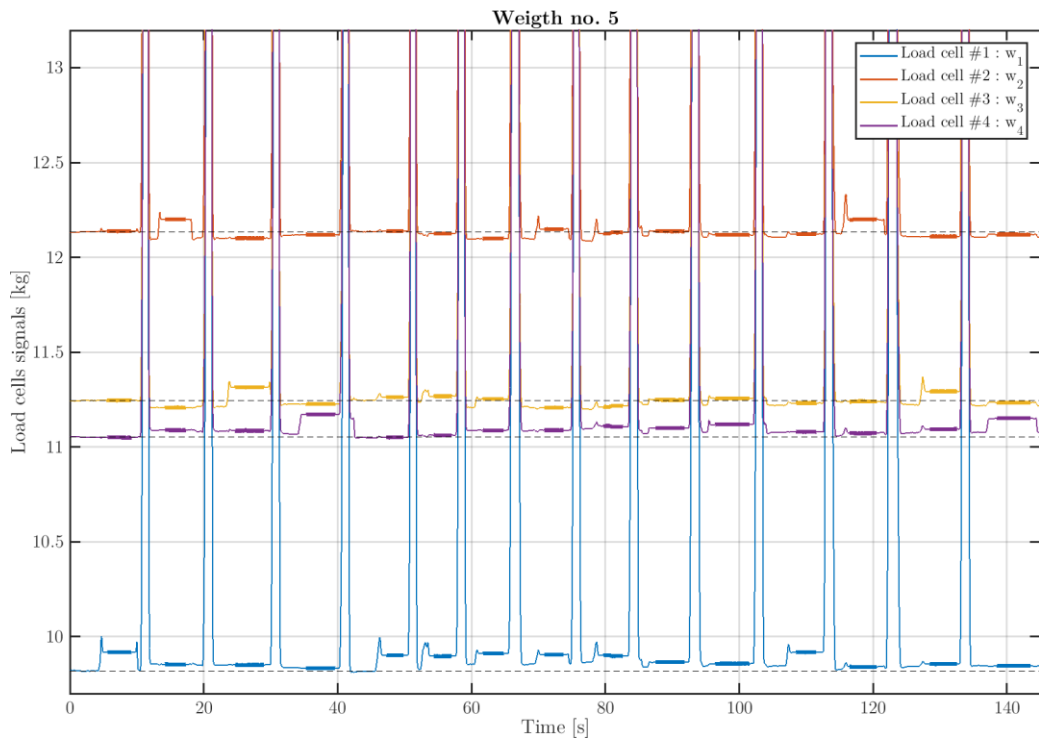
Figure 4.10 – Raw data obtained by the load cells with the weight no.5 (100g).

Taking these four signals associated with the load cells for each tested weights, it is possible to obtain the coordinate of the center of mass of the system composed by the bed frame and the tested weight by substituting in the equations (4.1) the following parameters:

Bed length: $L = 78" \ 12/16 \ (200.03 \text{ cm})$

Bed width: $W = 39" \ 2/16 \ (99.38 \text{ cm})$

Reaction forces at the legs: $(R_1, R_2, R_3, R_4) = (w_1, w_2, w_3, w_4)$

Total bed frame weight: $W_{tot} = (w_1, w_2, w_3, w_4)_{tot} = (W_{bed} + W_{weight})$

Using these data, the **center of mass of the whole system** composed by the bed frame and the weight on it can be easily assessed:

Bed + Weight: $(w_1, w_2, w_3, w_4)_{tot}, L, W, W_{tot} \rightarrow \boxed{(x_{c,tot} ; y_{c,tot})}$

Considering instead the signal of the load cells at the initial phase of the experiment, when no weight is rested upon the bed frame, the **center of mass of the sole bed frame** can be assessed:

Bed only: $(w_1, w_2, w_3, w_4)_{bed}, L, W, W_{bed} \rightarrow \boxed{(x_{c,bed} ; y_{c,bed})}$

where: $W_{bed} = (w_1, w_2, w_3, w_4)_{bed} \approx 44.25 \text{ kg}$
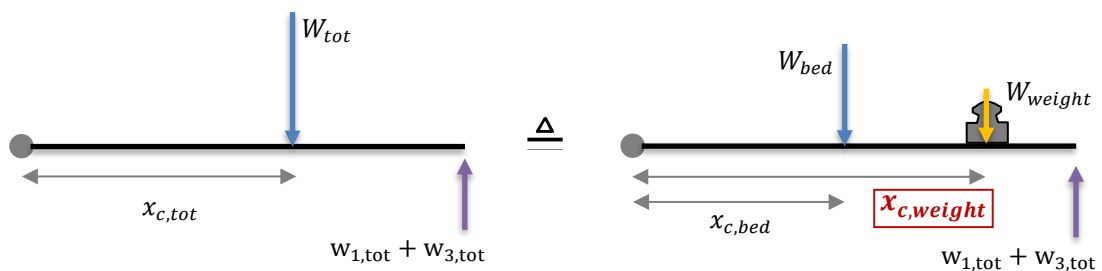
Figure 4.11 – Rotational equilibrium diagrams along the x axis. The total weight W_{tot} can be decomposed in $W_{bed} + W_{weight}$ to get the unknown $x_{c,weight}$.

Given these two centers of mass associated with the described conditions, the coordinates of the position of the deployed weight can be retrieved by using again the rotational equilibrium, see Figure 4.11, getting the equation (4.2):

$$\boxed{\begin{aligned} x_{c,weight} &= \frac{W_{tot}\, x_{c,tot} - W_{bed}\, x_{c,bed}}{W_{weight}} \\[2mm] y_{c,weight} &= \frac{W_{tot}\, y_{c,tot} - W_{bed}\, y_{c,bed}}{W_{weight}} \end{aligned}}$$

(4.2)

where: $W_{weight} = W_{tot} - W_{bed}$

In Figure 4.12 the reconstructed positions of the weights positions are shown compared to the real positions at which the weights were placed.
It can be noticed that the positions of weights over 100 g can be traced in a consistent way with a reduced margin of error with respect to the real positions. On the contrary weights around 50 g start to show discrepancies in their reconstructed positions, arriving to weights of the order of 10 g which cannot be traced in a precise manner and see their reconstructed positions no more close to the real ones.

In addition, results concerning the same test but performed with the mattress and the bed sheets on the bed frame are shown in Figure 4.13. In this case, even considering the case of the weights of 100 g, no precise positions can be retrieved. This is due to the fact that the rotational equilibrium equations assume the bodies rigid, which is definitely less true in presence of a mattress.
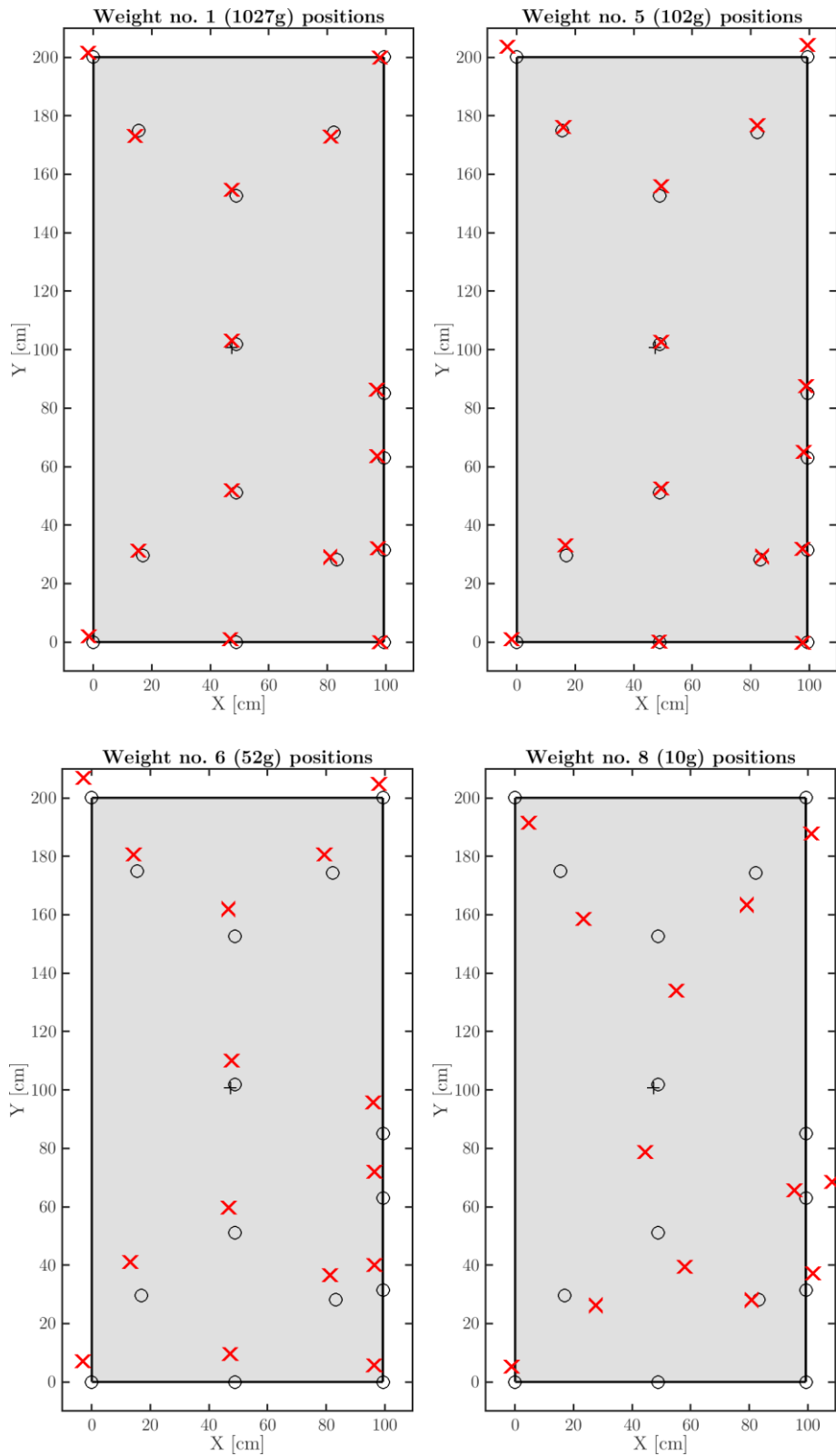
Figure 4.12 – Reconstructed weights positions.
(weights directly on the wooden board of the bed frame).
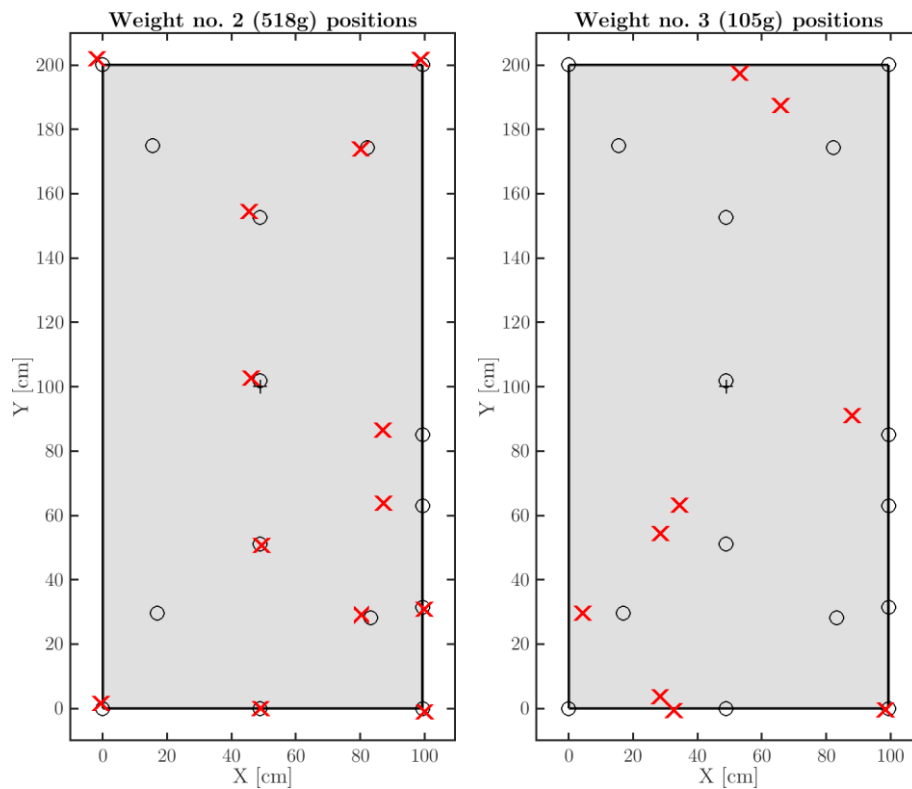
Figure 4.13 – Reconstructed weights positions.
(weights deployed over the mattress, on the wooden board of the bed frame).

•*Decremented load cells signals problem*

In Figure 4.14, a zoom of Figure 4.10 is reported. In that image raw data obtained from the load cells positioned under the bed legs, for the case of 100 g calibration weight test, can be observed.

It can be noticed that, especially in some parts, the <u>load signal of some of the load cells experiences a reduction of the measured weight</u> even when an additional weight is positioned on the bed.

<u>This apparently strange behavior can be explained by the fact that the static solution, in terms of reaction forces exerted by the bed legs at the four corners of a rectangular bed, is not unique.</u>
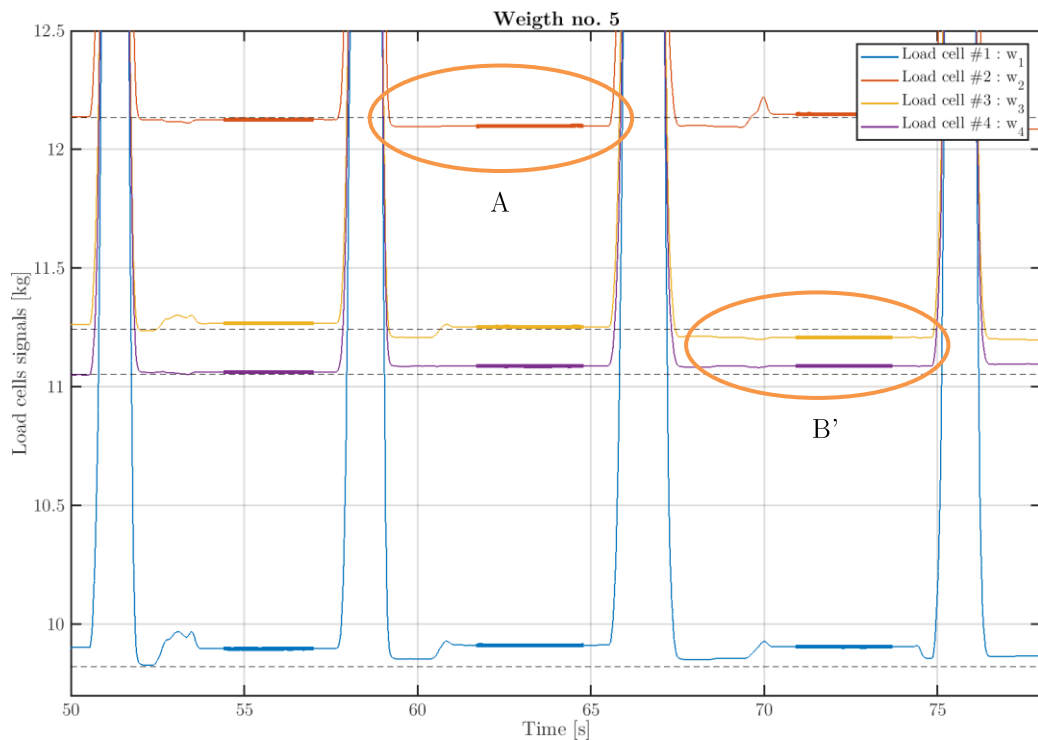
Figure 4.14 – Zoom of the raw data of Figure 4.10 with highlighted (A, B) the cells experiencing a reduction of weight with respect to their bed-frame-only reference values.

For this reason, negative measures experienced by 1 or 2 load cells during a test can be accepted and do not correspond to any problem in the measurements.

The following ideal experiment can be used to understand how this concept is common in practice. Let us take a very stiff rectangular board with 4 legs, one at each corner (as a very stiff bed). If two diagonally opposite legs are much longer than the other 2 (referring to Figure 4.6, assume that legs 2 and 3 are longer), they create a line of equilibrium. If the other 2 legs are shorter, dropping a weight on one triangular side of the board (for instance putting the weight close to leg no. 4) leads to a reduction of the reaction force exerted by the leg opposite to the triangular part chosen (in this case a reduction of the weight at the leg no. 1), bringing in some cases to the lifting of the bed corner with respect to its original position.

4.3 Load cell sensors: experimental tests on a person

4.3.1 **Experimental setup and measurement phases**

The sensitivity of the load cells used for the experiments of this chapter was assessed in Section 4.2. The next experiment consists in taking a healthy person, make him/her laying on the wooden board of the bed (directly on the wooden board in order to avoid any possible disturbances in the signal given by the transmission of the vibrational waves inside the mattress) and try to measure the displacement of his/her center of mass.
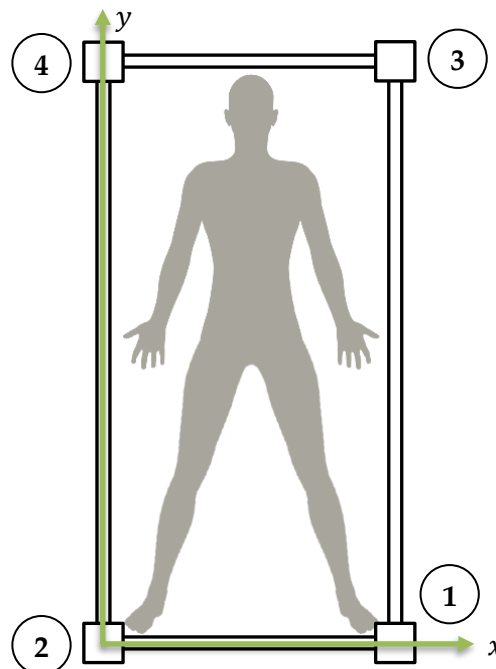
Figure 4.15 – Scheme of the load cells experiment on a person.

The same apparatus and the same formulas introduced in the previous sections can be used, to retrieve the position of the tested calibration weights.

Figure 4.16 shows raw data collected from the load cells positioned under the bed legs. The experiment consisted in measuring the four reaction forces of the bed legs having a person lying still in direct contact with the wooden board of the bed frame (without mattress, bed sheets or pillow to avoid possible signal modifications). The person is lying as schematized in Figure 4.15.
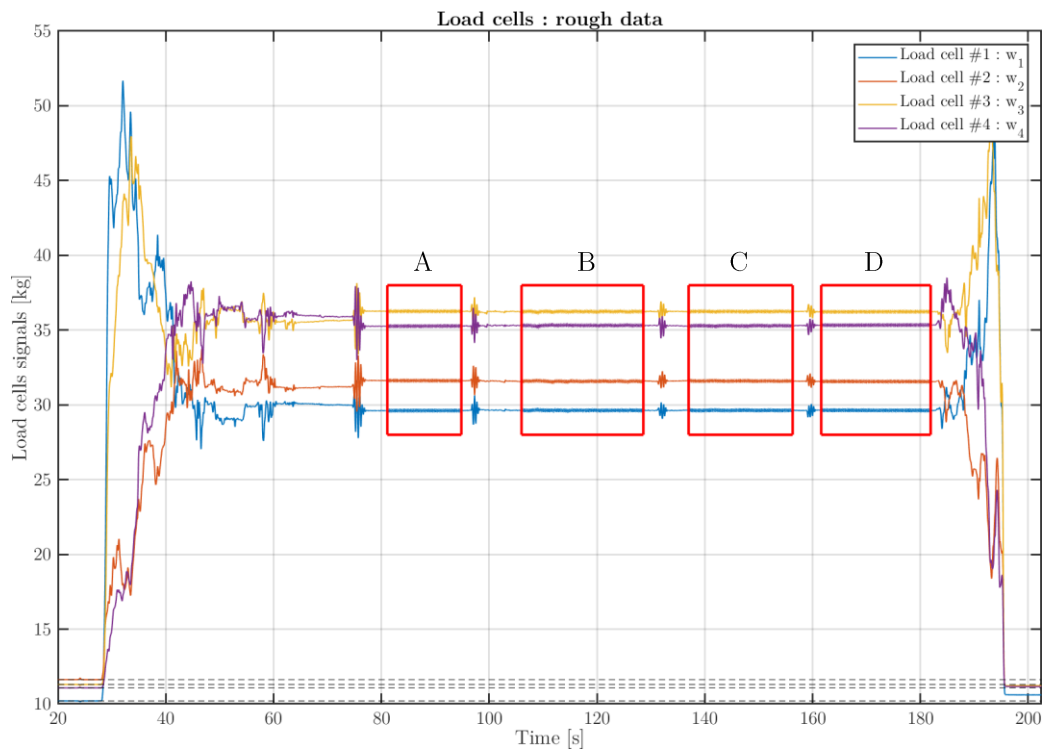
Figure 4.16 – Raw data of the load cells measuring a person still on the wooden board. Four phases were assumed: (A) no breathing, (B) normal breathing, (C) short and shallow breathing, (D) without breathing (as a control).

Following the signals in Figure 4.16 the whole experiment path can be identified. In the first part the **bed is empty**, without any persons on it, and the load cells measure the reference reaction forces related to the sole bed only $(w_1, w_2, w_3, w_4)_{bed}$. In the following part the **subject approaches the bed** and assumes the lying position on the bed starting to stay still. The next section refers to **4 different experimental situations** in which the subjet on the bed tries to stay still but modulates his/her breathing in order to recreate the following 4 conditions:

A. no breathing
B. short and shallow breathing
C. normal breathing
D. no breathing (as a control)

In the last part, the subject gets out of the bed and the load cells return to their original condition.

4.3.2 **Total weight analysis**

In Figure 4.17 the phases described above can be seen more easily due to the normalization of the weight. The graph shows the total weight obtained by summing up the four load cells signals normalized by subtracting the mean value of the total weight related to the first window (A). In this way the oscillations in the mean weight are more evident.
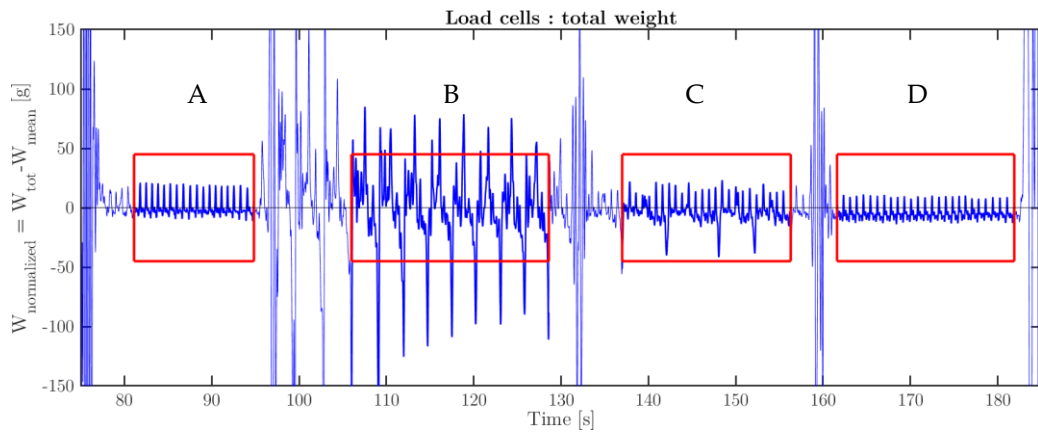
Figure 4.17 – Normalized total weight of a person lying still on the wooden board. Four phases were assumed: (A) no breathing, (B) short and shallow breathing, (C) normal breathing, (D) no breathing (as a control).

In Figure 4.18 to Figure 4.21 the four experimental conditions are individually enlarged.
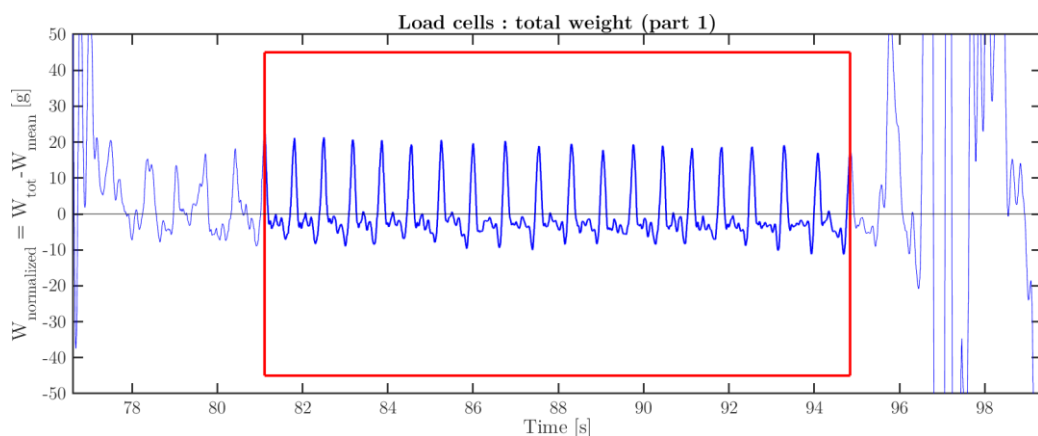
Figure 4.18 – Zoom of Figure 4.17, phase (A) – no breathing.
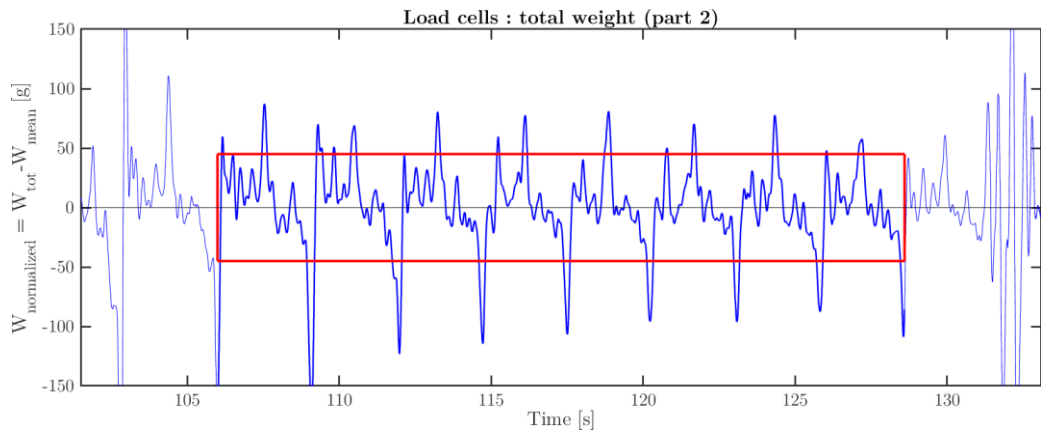
Figure 4.19 – Zoom of Figure 4.17, phase (B) – short and shallow breathing.
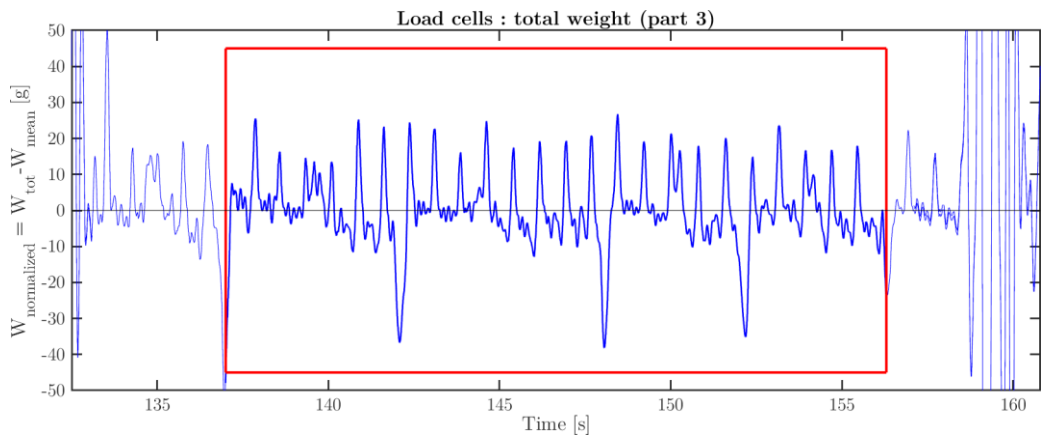
Figure 4.20 – Zoom of Figure 4.17, phase (C) – normal breathing.
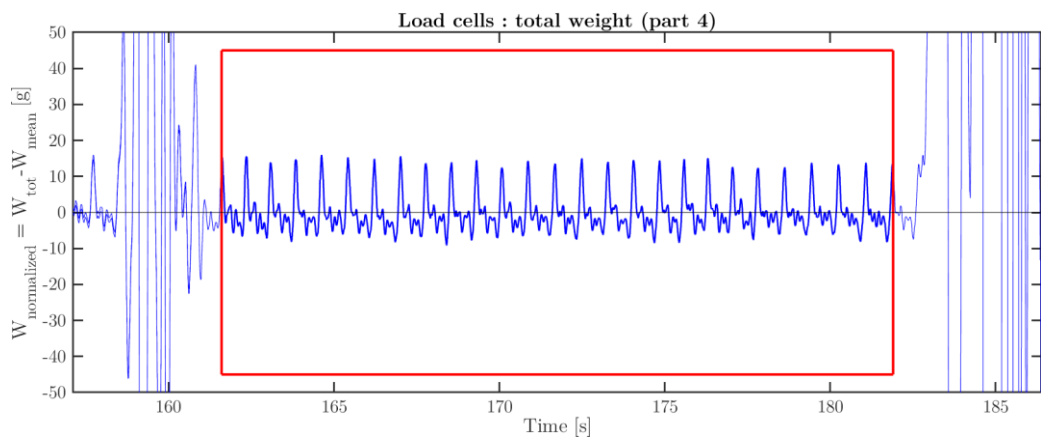
Figure 4.21 – Zoom of Figure 4.17, phase (D) – no breathing.

From Figure 4.18 it can be clearly seen that the **total weight of a person lying still on a rigid bed is not constant**. This measure indicates that the pumping of the heart exerts a dynamic effect on the body which makes the load cells experience a regular perturbation in the *z* direction.

4.3.3 Information obtained from the load cells

• *Heart beat*

By analyzing the peaks of the first condition associated with the absence of breathing (A), see Figure 4.22, it is possible to capture the **heart beat frequency** of the subject on the bed.
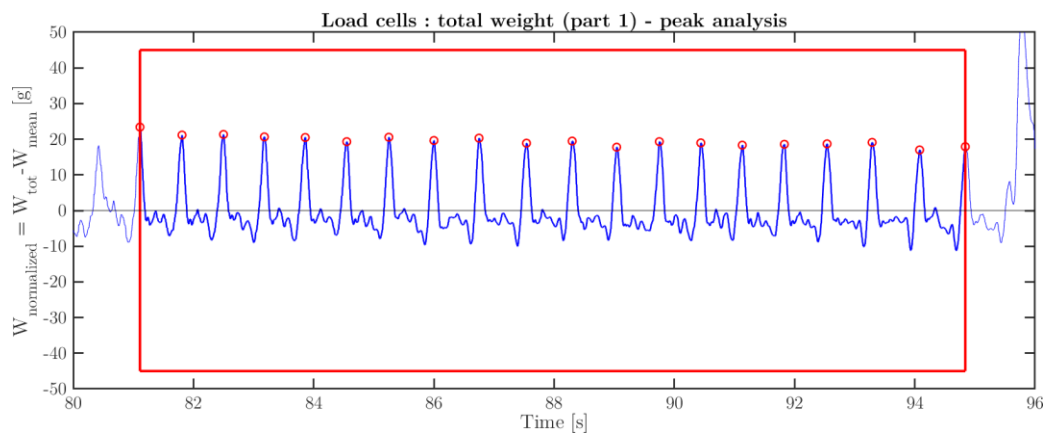
Figure 4.22 – Zoom of Figure 4.17, phase (A) with peaks highlighted by the circles.

In this case, the information derived from these peaks are:

Mean peak interval time:	0.78 ± 0.03 s
Mean peak frequency:	77.1 ± 2.6 bpm
Total peak amplitude:	~ 25 g

• *Respiration*

Taking the rough signals captured during the third condition, associated with a normal breathing pattern (C), see Figure 4.23, it is possible to see how the heart beating pattern analyzed before, is now modulated and added to the *respiratory forcing pattern* which periodically shifts the heart-only curve. Capturing the **breathing frequency** is more difficult with respect to the heart frequency because respiration is less constant.
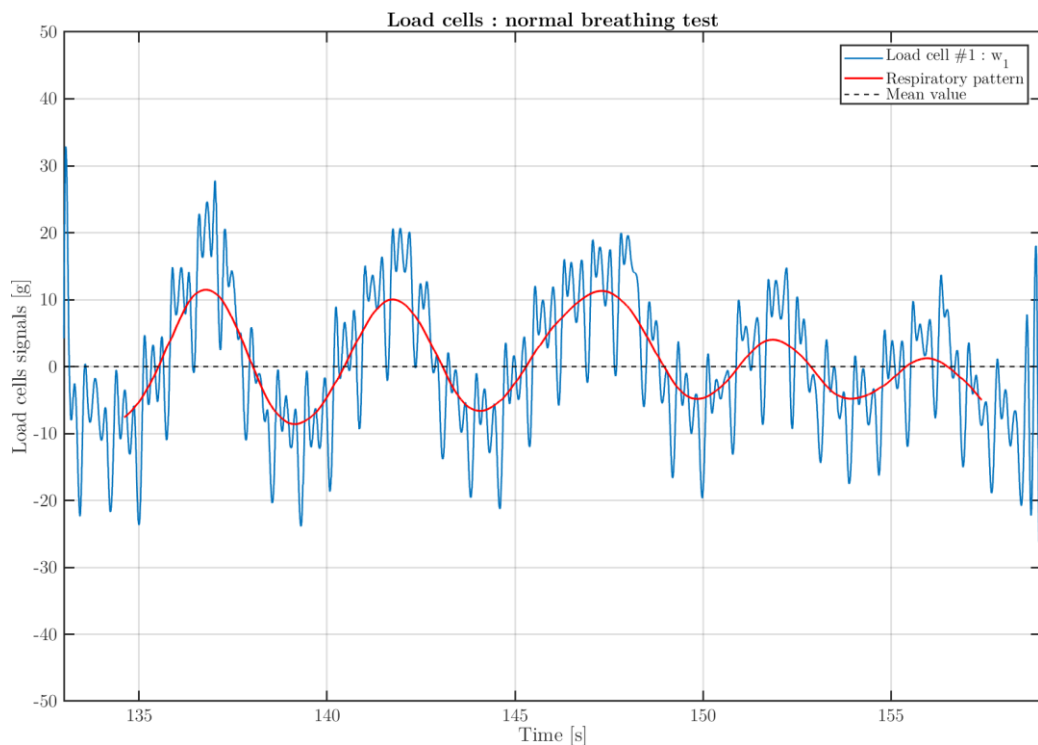
Figure 4.23 – Raw load cell signal, captured by the cell #1, during the third phase of the experiment (Phase C – normal breathing).

For the treated case the **respiration rate period** is around 5 s, thus the **respiratory frequency** is around 12 bpm. The total respiration amplitude is around 15 g.

•*Additional information*

In addition to the **heart frequency**, and to the **respiratory frequency**, it can also be noticed that the <u>information contained in the load cells signal is much richer</u>. As a matter of fact, the peaks are very easy to highlight and they seem to be a very consistent method in estimating heart rate, but considering the parts in between these peaks, <u>a repetitive pattern can be identified</u>.

In Figure 4.24 a superposition in time of the total weight signal is shown. The main peaks are taken as alignment point for each superposed part.
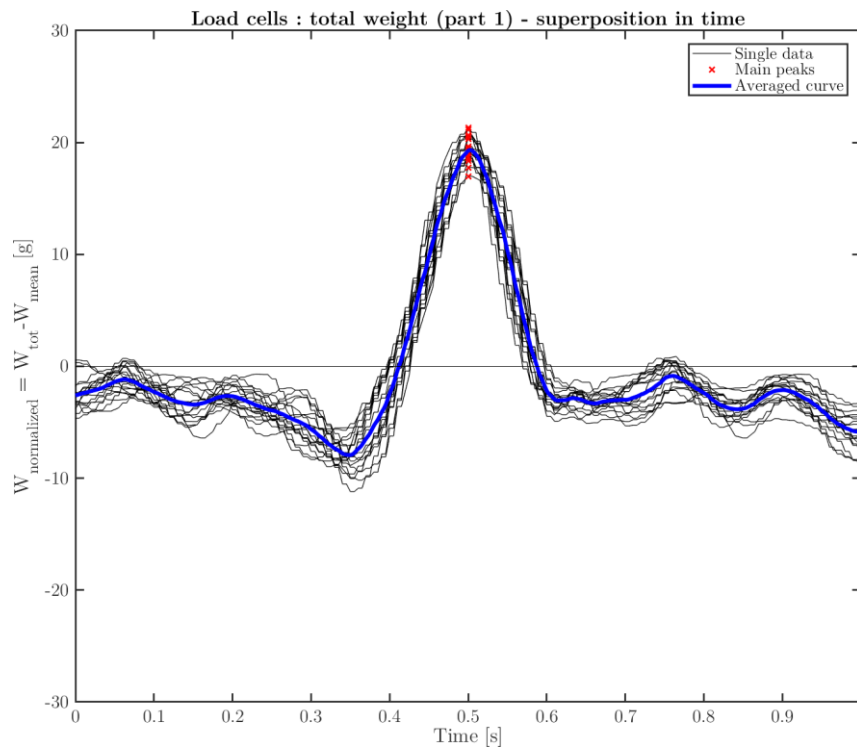
Figure 4.24 – Superposition in time of the total weight signal taking the main peak as alignment point.

It can be noticed the occurrence of a consistent pattern, with very limited variations from the averaged curve, confirming the <u>physically-related importance of this part of the signal which cannot be considered noise only</u>.

4.3.4 Experimental ballistocardiogram

• *Experimental BCGz*

Figure 4.24 reports the superposed pattern noticing from the measure of the total weight of a body laying still and without breathing over a rigid bed.

This pattern in the measured total weight can be interpreted as a **dynamic force acting on the bed frame** and experienced by the load cells. It should therefore be possible to express the measured total weight changes in terms of [dyne] ($1 \; dyne = 10^{-5} \; N$) by simply multiplying that weight expressed in grams by the acceleration of gravity $g \cong 9.81 m/s^2$ and by a conversion factor equal to 100. In addition, since the resulting curve represents a reaction force, it should be reversed in sign, see (4.3).

$$f_A \left[dyn = 10^{-5} N = 10^{-5} \; kg \; m/s^2 \right] = g \left[\frac{m}{s^2} \right] \cdot 100 \cdot W_{normalized} \; [g]$$

(4.3)

$$\boxed{f_A \; [dyn] \cong 981 \left[\frac{m}{s^2} \right] \cdot \left(- W_{normalized} \; [g] \right)}$$

Making this conversion, allows us to compare the obtained **experimental BCGz** to the theoretical one using the same unit of measure.

In Figure 4.25 the comparison between the theoretical BCGz, derived in Section 2.2.2, and the experimental BCGz, obtained by the procedure described above, shows a remarkable similarity in magnitude and also in shape. This result confirms the quality of the closed-loop model to reproduce physiological results.

144

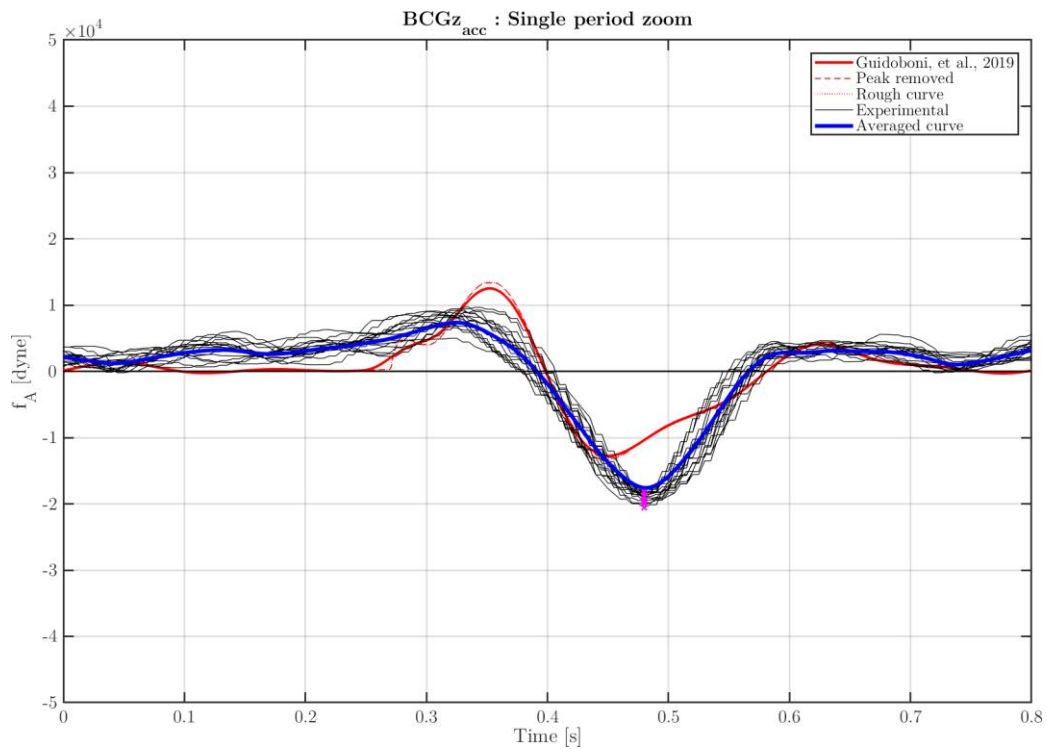Figure 4.25 – Superposition in time of the total weight signal obtained by taking the main peak as alignment point, changing its sign and expressing the result in [dyne], compared to the $BCGz_{acc}$ curve derived with the closed-loop model of Section 2.1.

Figure 4.26 – Simulated BCGz obtained with the closed-loop model described in Chapter 2.1 compared to the BCGz obtained using the load cells data.

The **velocity and displacement BCGz** are then derived by integration, see (4.4) and (4.5). For the treated case a trapezoidal integration rule is used to numerically compute the integral.

$$\boxed{f_{V,all} = \int_t f_A \, dt} \quad \rightarrow \quad \boldsymbol{f_V} = f_{V,all} - mean(f_{V,all}) \quad [\text{g} \cdot \text{cm/s}] \tag{4.4}$$

$$\boxed{f_{D,all} = \int_t f_V \, dt} \quad \rightarrow \quad \boldsymbol{f_D} = f_{D,all} - mean(f_{D,all}) \quad [\text{g} \cdot \text{cm}] \tag{4.5}$$

A **high-pass Butterworth filter** of order 4, with a normalized cut-off frequency of 0.007, is applied to each obtained auxiliary function to filter out the low frequency variations.

Other work should be done to better tune the model to catch each feature of the experimentally obtained BCGz curve. This is not treated in the present work, but this tuning work together with an experimental campaign may open the way to the interpretation of the BCG with respect to cardiovascular conditions.

• *Experimental BCGy*

Given the load cells data, it should be also possible to derive the BCGy, along the head-to-toe direction.

$$BCGy_{acc} = \frac{L}{H} \frac{g}{M_{body}} \cdot (R_1 + R_2) \quad [\text{cm/s}^2] \tag{4.6}$$

$$f_{A,all} = M_b \cdot BCGy_{acc} \quad \rightarrow \quad \boldsymbol{f_A} = f_{A,all} - mean(f_{A,all}) \quad [\text{dyne}] \tag{4.7}$$

where:
$L = 200.03$ cm	is the bed principal dimension;
$H = 38.735$ cm	is the bed height from the ground;
$g = 981$ cm/s^2	is the acceleration of gravity;
$W_{body} = W_{tot} - W_{bed}$	is the body weight;
R_1 and R_2	are the reaction forces measured by the load cells.

In addition, a high-pass Butterworth filter of order 4, with a normalized cut-off frequency of 0.007, is applied to filter out the low frequency variations.
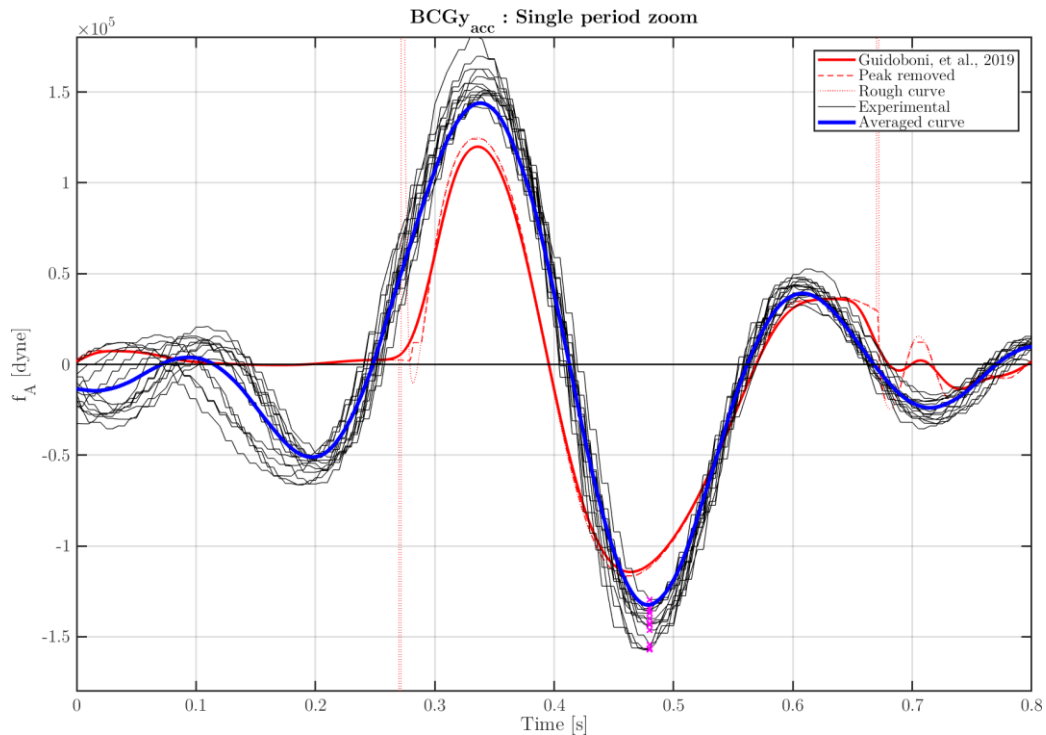
Figure 4.27 – Superposition in time of the measured $BCGy_{acc}$ taking the main peak as alignment point compared to the $BCGy_{acc}$ curve derived with the closed-loop model analyzed in Section 2.1.

The velocity and displacement BCG are then derived by integration, as done for the BCGz, see (4.4) and (4.5).

A comparison between the theoretical and experimental f_D, f_V and f_A is shown in Figure 4.28.

It can be noticed from the graph of the acceleration f_A how well the theoretical simulations obtained with the closed-loop model underline the experimental results superimposed in time taking as a reference the main peak point.

In the right part a variability in the experimental curves appears, this behavior is expected since the theoretical model considers a constant heart rate, while the physiological measurements could not get exactly-constant frequency. In addition, the parameters of the model have not been tuned considering specific individual characteristics such as body size, gender, age, and so on.
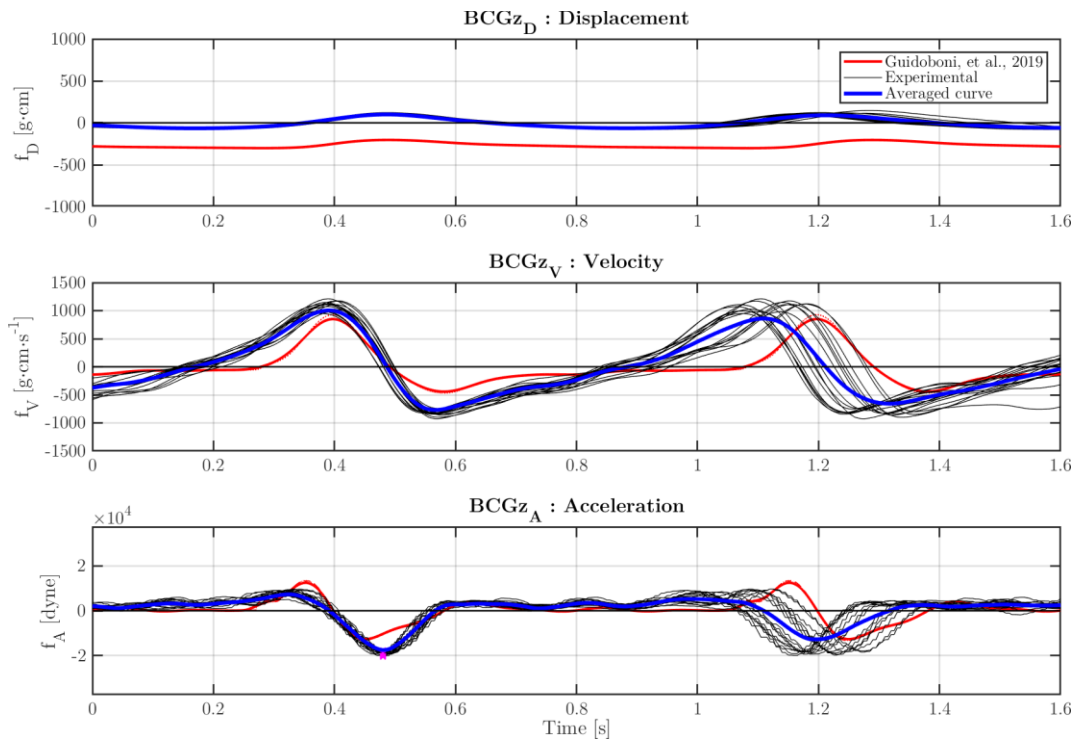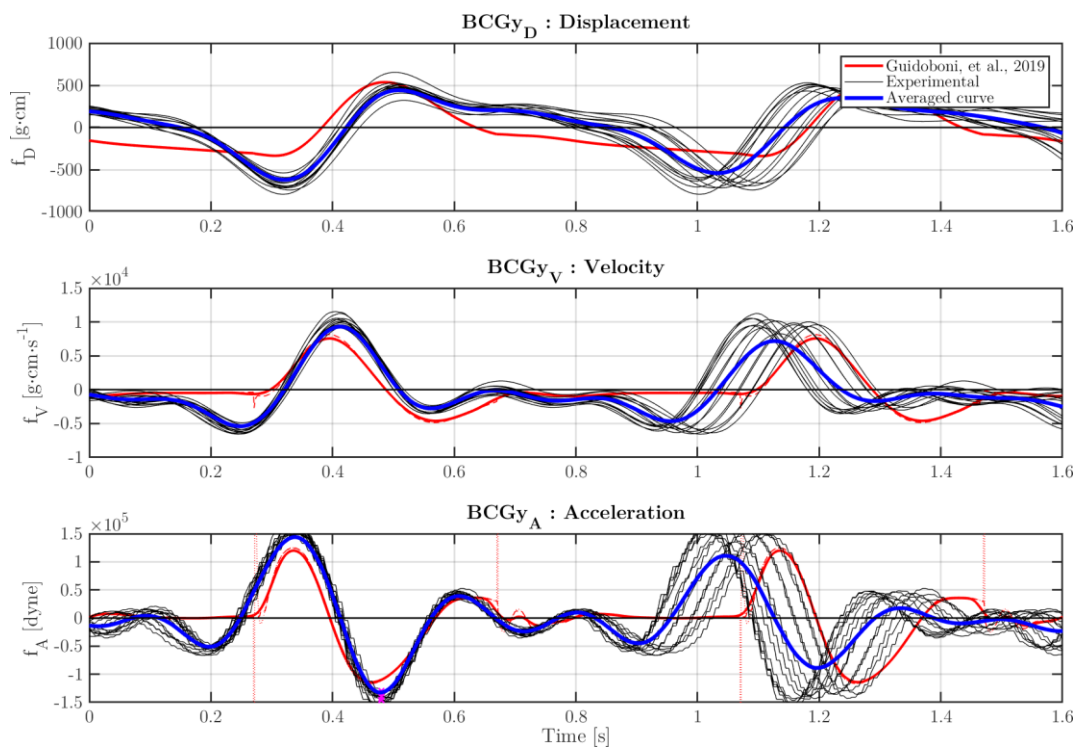
Figure 4.28 – Simulated BCGy obtained with the closed-loop model described in Chapter 2.1 compared to the BCGy obtained using the load cells data.

5 – MATTRESS TESTING

In Section 4.2.2, some measurements of load cells data positioned under the bed frame have been carried out. In particular, in that experiment, the positions of some testing weights positioned over the bed (while the load cells were acquiring data) were reconstructed, solely using the signals representing the reaction forces of the four bed legs.

Figure 5.1 – Image of the testing bed with the mattress, pillow and bed sheets on it.

That experiment was conducted in two phases: in the first phase, the weights have been directly put on the wooden board fixed to the bed frame; in the second phase the same weights have been put over a standard coil-spring mattress positioned over the board, see Figure 5.1. The results of the tests showed that in the case of the measurements using the mattress, the position of the weights was much more difficult to be retrieved, meaning that the presence of a mattress could have a significant importance in performing tests and acquiring signals (see Figure 4.13).

In Section 4.3 a person's ballistocardiogram was measured experimentally. Considered the results obtained with the weights positioning test (conducted before), the BCG recordings have been conducted with the subject directly lying on the stiff wooden board of the bed frame, without using any mattress. Since the aim of the BCG measurements is to capture the motion of the center of mass of a person without touching him/her and it should be continuous and less invasive as possible, it is evident that measurements should be taken with also the presence of a mattress on the bed.

In this chapter, **preliminary** testing results regarding the mechanical characterization of mattresses are reported. The aim of these investigations is to give the reader some preliminary reference values to investigate the influence of the mattress on BCG measurements.

The chapter is subdivided into two main sections. The first section regards the characterization of the elastic parameters by performing static tests. The second section illustrates the dynamical tests that have been performed to investigate the dynamical response and estimate the damping parameters.

5.1 Static behavior: assessing elastic parameters

The first test performed is a simple compression test. The mattress was put on a rigid plane (in this case the floor), with another rigid board on top of it (in this case a very stiff reversed table was used). By gradually increasing the weight on the upper board, a compression of the mattress can be noticed, and by recording the lowering of the upper board with respect to the floor, a force vs. deformation curve can be obtained.

The thinning of the mattress due to the weights applied was measured by hand, signing at each step with a pen the height from the floor on two vertical white boards fixed to heavy blocks. The mean of the two heights give the actual distance of the center of the upper part of the mattress from the floor.

Figure 5.2 – Compression test of the mattress by means of a rigid wooden board (a table) and weights on it (two subjects, in this case).

In Figure 5.3, the resulting measures obtained by the compression test of the lab mattress (a simple coil spring mattress), are reported.

On the top horizontal axis we use the measured vertical deformation of the mattress Δl in mm, while on the right vertical axis we have the corresponding mass applied on the upper board expressed in kg.
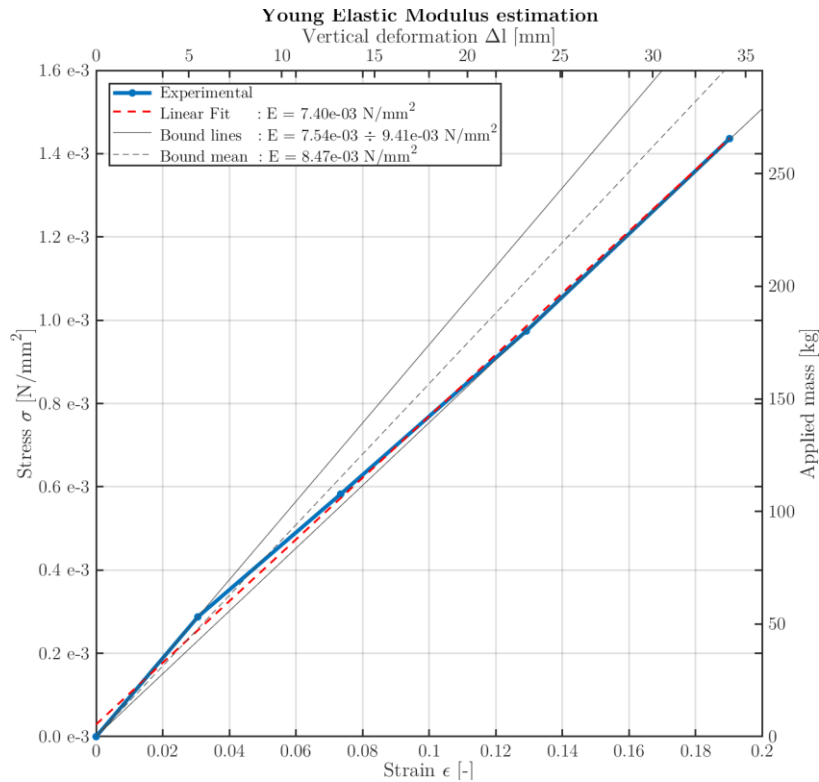
Figure 5.3 – Results of the compression test of the mattress no.1 (coil spring type).

In order to compare the results of this test with other tests, normalizing quantities are computed by which it is then calculated the elastic Young modulus E, these quantities are the strain ε and the stress σ, defined as in (5.1) and (5.2) respectively.

$$\varepsilon = \frac{\Delta l}{l_0}$$ (5.1)

$$\sigma = \frac{F}{A}$$ (5.2)

where: l_0 is the original mattress thickness $[mm]$;
$\Delta l = (l - l_0)$ is the difference between h_0 and the actual thickness $[mm]$;
$F = m \cdot g$ is the applied force $[N]$;
where m is the mass of the applied objects $[kg]$;
and $g = 9.81$ m/s^2 the acceleration of gravity.

152

$A = L \cdot W$ is the area of the mattress [mm^2], (L the length, W the width).

The Young modulus is thus the slope of the obtained line in the $\sigma - \varepsilon$ plot, see (5.3).

$$E = \frac{\sigma}{\varepsilon}$$

(5.3)

• *Different mattresses types*

In order to extend the possibility of comparisons, other mattress types are tested.

Besides the traditional and simple col spring mattress, in US houses two-sided pillow-top mattresses are also often used, see Figure 5.4. They are made by traditional coil springs bases, with above a "pillow" made of polyurethane soft foam.

Figure 5.4 – Two-sided, innerspring pillow-top mattress. A traditional spring mattress super-posed by an elastomer layer in memory foam.

Another type of mattress used, although not as popular as the other types, is the air mattress. In air mattresses a polyurethane foam surrounds one or more air-compressed chambers. In this type of mattresses the users can usually regulate the level of pressure in these chambers making the response more soft or more rigid.

In Figure 5.5, test results are shown for the pillow-top mattress, while in Figure 5.6 the results for the air mattress are shown.
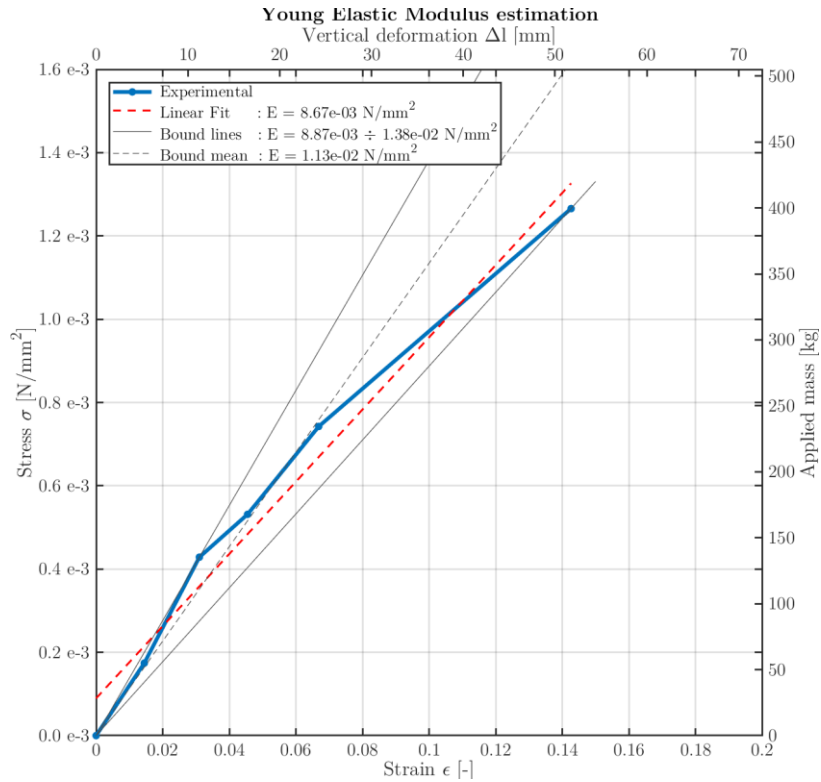
Figure 5.5 – Results of the compression test of the mattress no.2 (pillow-top type).

It can be seen from these plots that the response is not as linear as for the coil springs mattress, and the definition of an unique Young modulus becomes more difficult if not impossible. Each one of these 3 graphs is reported with the same scale for the strain and stresses axis. The stress reached by each mattress is similar, although the applied force is very different since the mattress no.1 is a single size, while the others are double size.
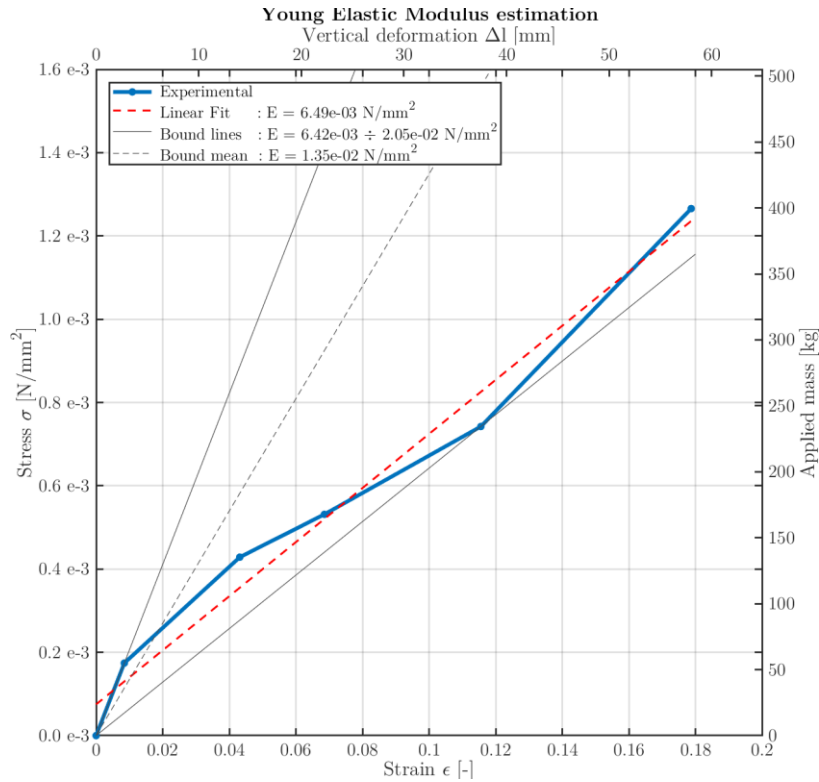
Figure 5.6 – Results of the compression test of the mattress no.3 (air mattress).

In Table 5.1, a summary of the obtained results is reported.

Mattress	No. 1	No. 2	No. 3
Type	Coil springs	Pillow-top	Air core
E (linear fit)	7.40 E-03	8.67E-03	6.49E-03
E (top bound)	9.41 E-03	13.80E-03	20.50E-03
E (low bound)	7.54 E-03	8.87E-03	6.42E-03
E (bounds mean)	8.47 E-03	13.30E-03	13.50E-03

Table 5.1 – Summary of the mattresses Young modulus tests [N/mm^2].

5.2 Dynamic behavior: assessing damping parameters

Another important mechanical characteristic of mattresses is how they behave dynamically. For this reason some tests are performed in order to assess how the mattresses damp out vibrations computing the damping ratio for the three type of mattress introduced in Section 5.1.
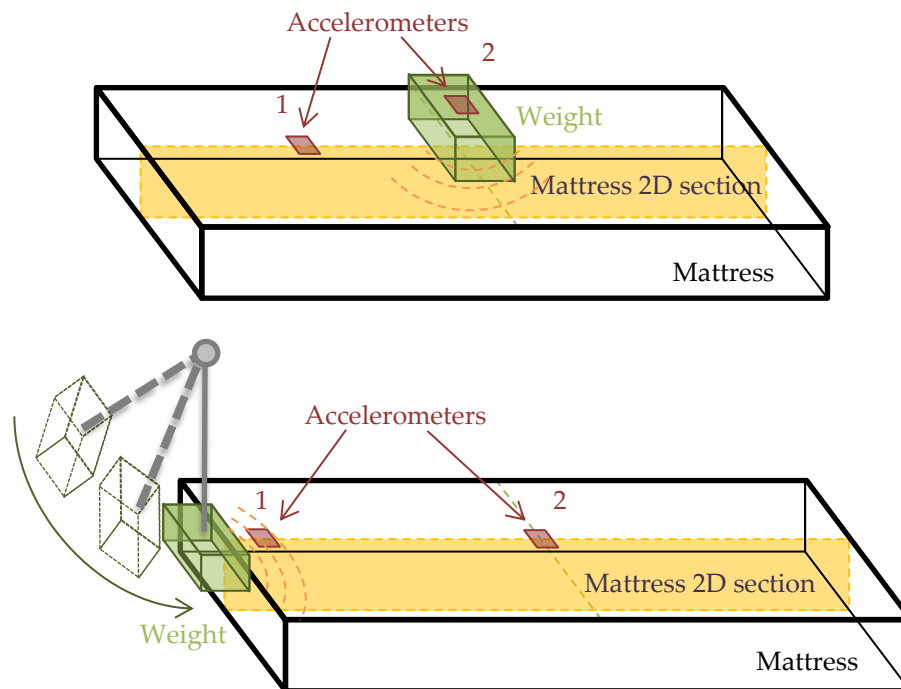
Figure 5.7 – Schematic view of the two tests performed: (on the top) Vertical weight drop test. (on the bottom) Lateral drop test.

In order to assess damping characteristics, 2 types of tests are performed:

- **Vertical drop test:** a heavy metal box is dropped on the mattress from a height of less than 1 cm from the surface. This is done to avoid bouncing effect of the box. During the test, two accelerometers positioned as in Figure 5.7 continuously record signals.
- **Lateral drop test:** the same heavy metal box is made swing, like a pendulum, and hits the side the mattress causing a shear perturbation. The bottom of the mattress remains fixed to the ground. Again, two accelerometers record signals.

In Figure 5.8 some pictures show the real experimental setup used, and the heavy metal box is shown in Figure 5.9.
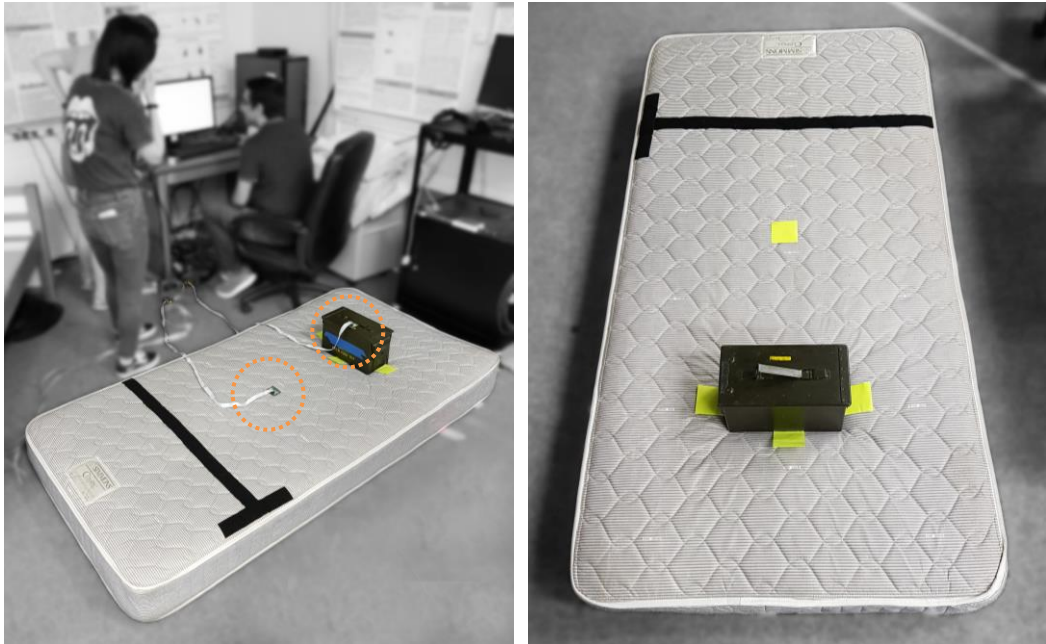
Figure 5.8 – Pictures taken during the drop test on the mattress no.1. The heavy green box is released on the mattress while the accelerometers (see the circles on the left image) measure the x, y and z accelerations.

Figure 5.9 – Picture of the heavy box used as weight for the drop test. 16 kg (35.2 lb.).

The experimental setup used is detailed shown in Figure 5.10.
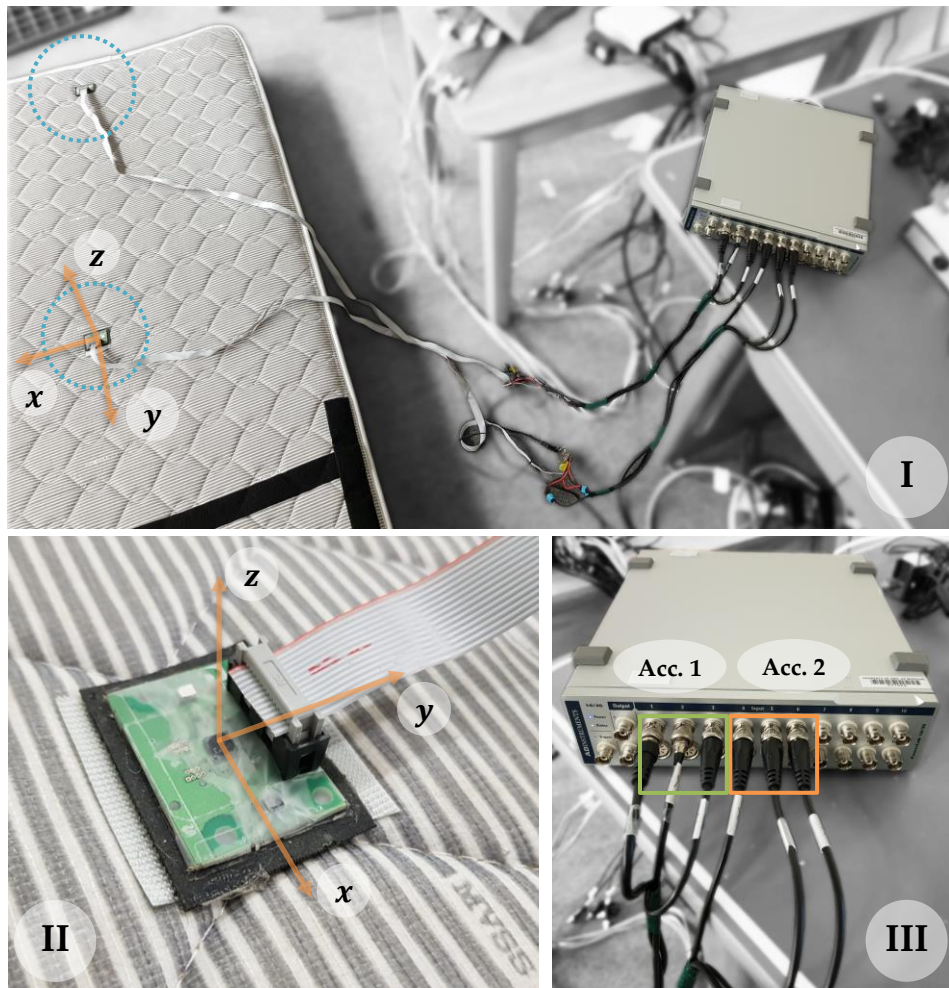
Figure 5.10 – Pictures of the experimental setup used to perform the dynamic analysis on the mattress no.1. (I) Comprehensive image of the instrumentation. (II) close up of the accelerometer fixed on the mattress by using Hook-and-loop fastener. (III) close up of the data acquisition board system.

The acquired data are reported from Figure 5.11 to Figure 5.16. The numbers assigned to the accelerometers and their positions are shown in Figure 5.7.

• **Mattress No. 1:**

Figure 5.11 – Vertical drop test: On top the 6 channels from of the accelerometers signals. On the bottom the signal zoom of the *z* axis of Accelerometer no.2.

Figure 5.12 – Lateral drop test: On top the 6 channels from of the accelerometers signals. On the bottom the signal zoom of the y axis of Accelerometer no.1.

• **Mattress No. 2:**

Figure 5.13 – Vertical drop test: On top the 6 channels from of the accelerometers signals. On the bottom the signal zoom of the *z* axis of Accelerometer no.2.

Figure 5.14 – Lateral drop test: On top the 6 channels from of the accelerometers signals. On the bottom the signal zoom of the *y* axis of Accelerometer no.2.

• **Mattress No. 3:**
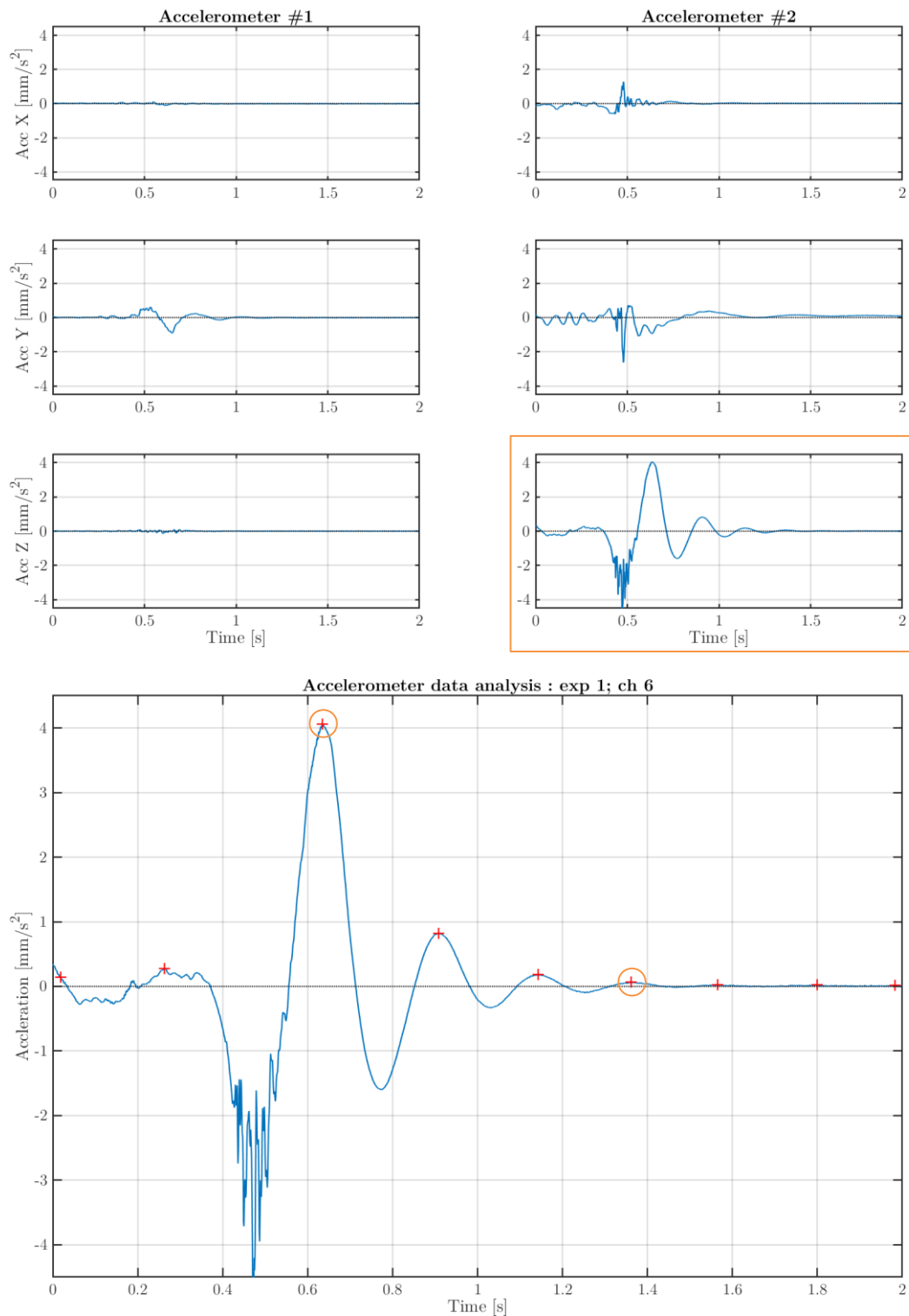
Figure 5.15 – Vertical drop test: On top the 6 channels from of the accelerometers signals. On the bottom the signal zoom of the *z* axis of Accelerometer no.2.

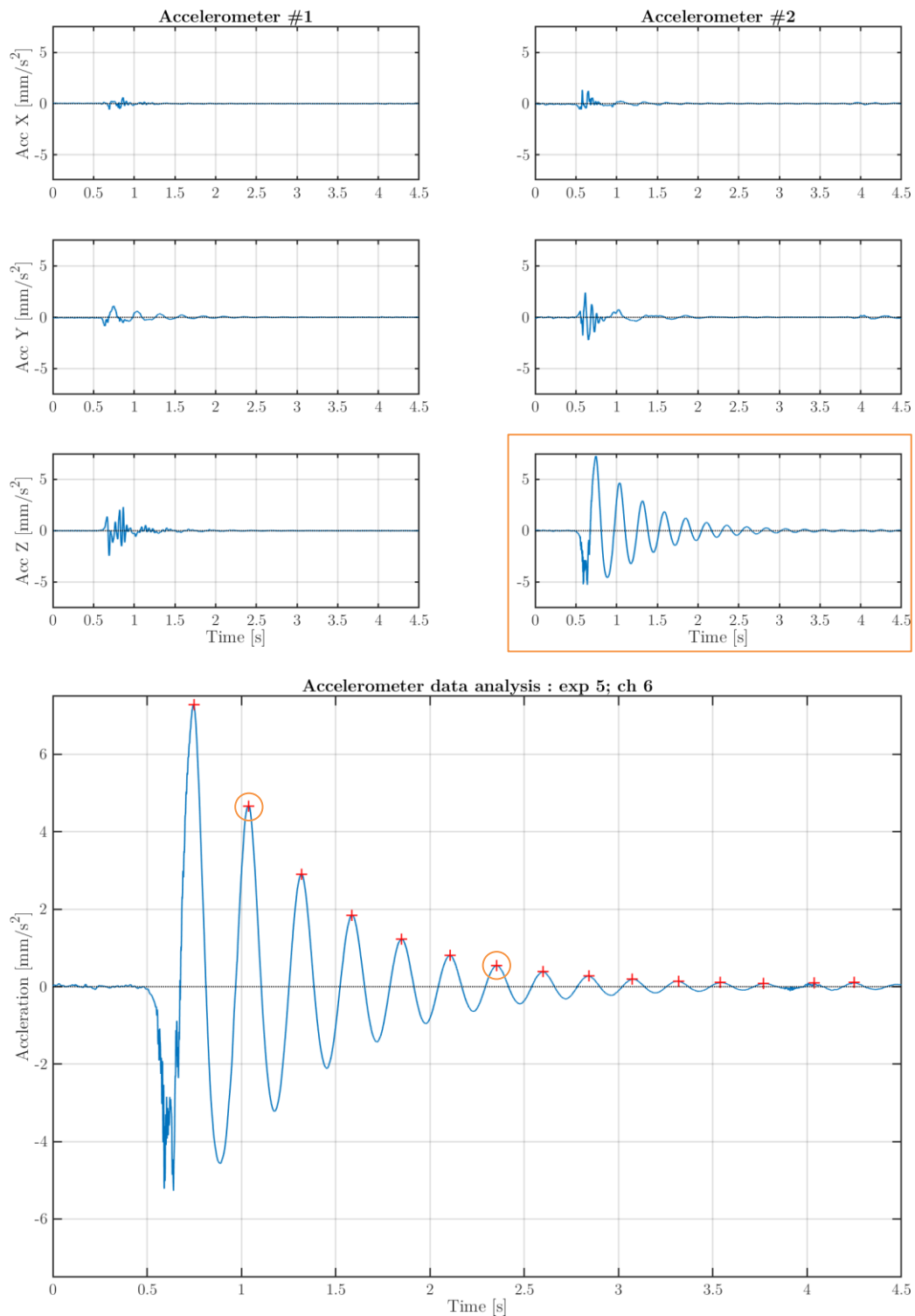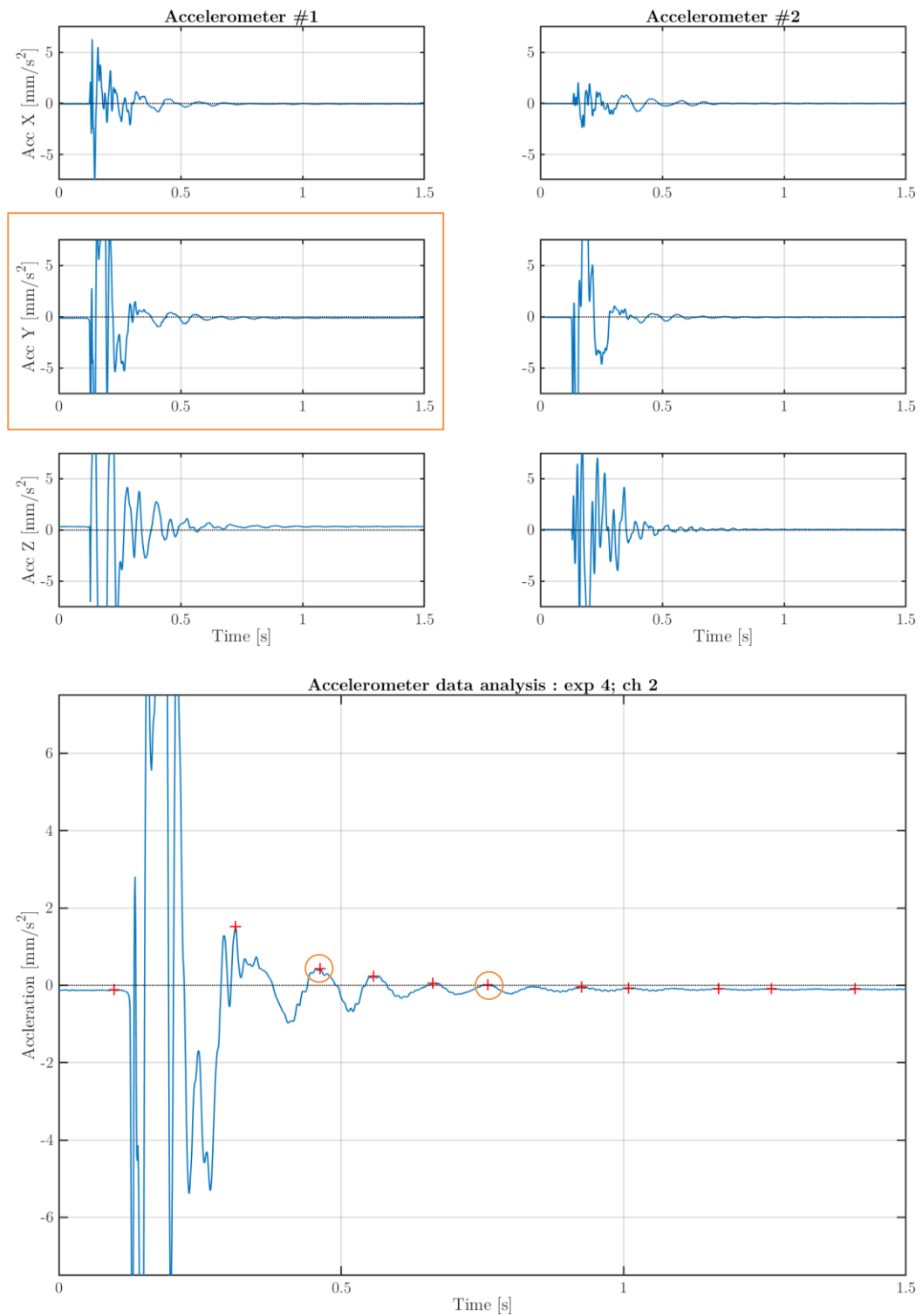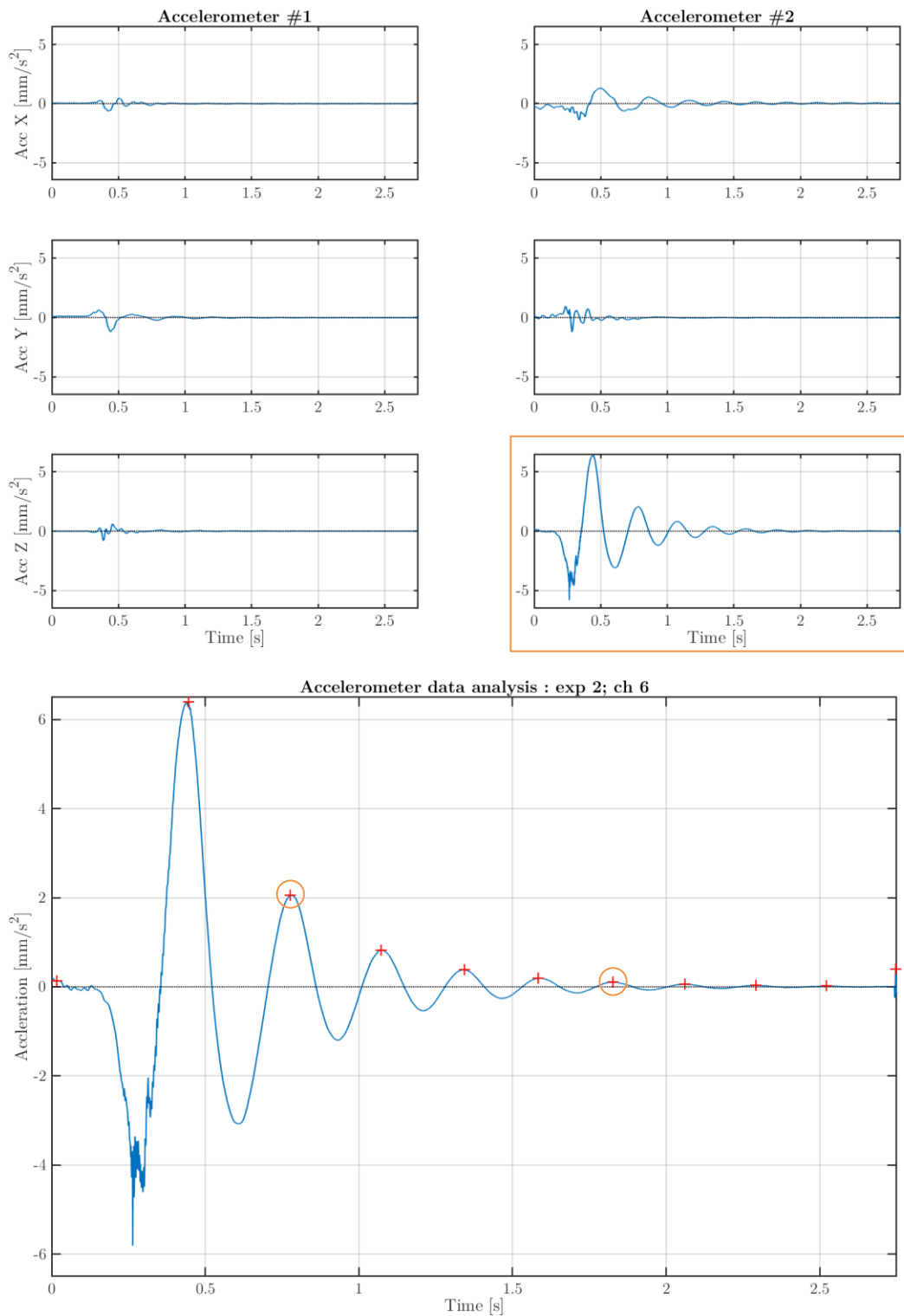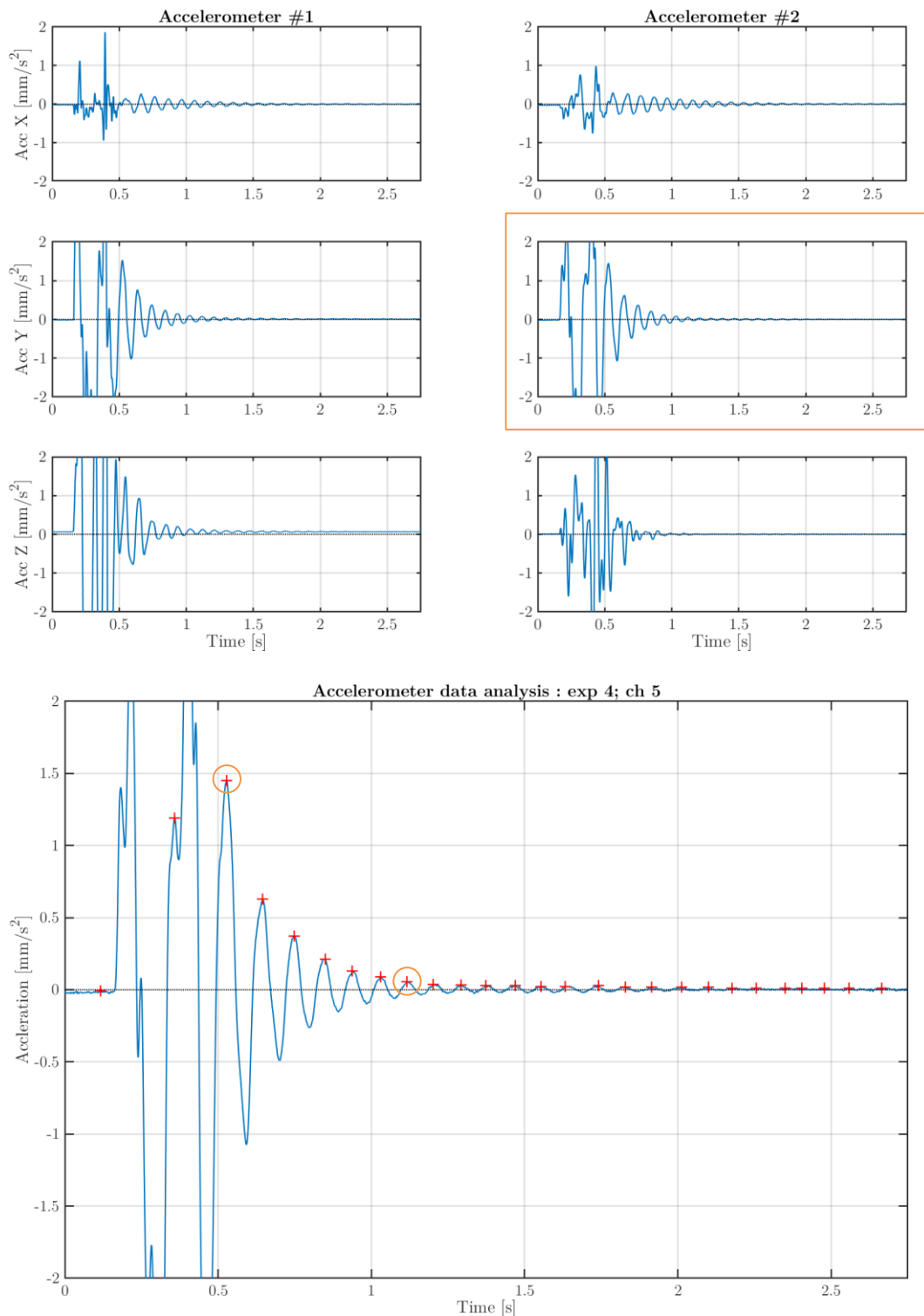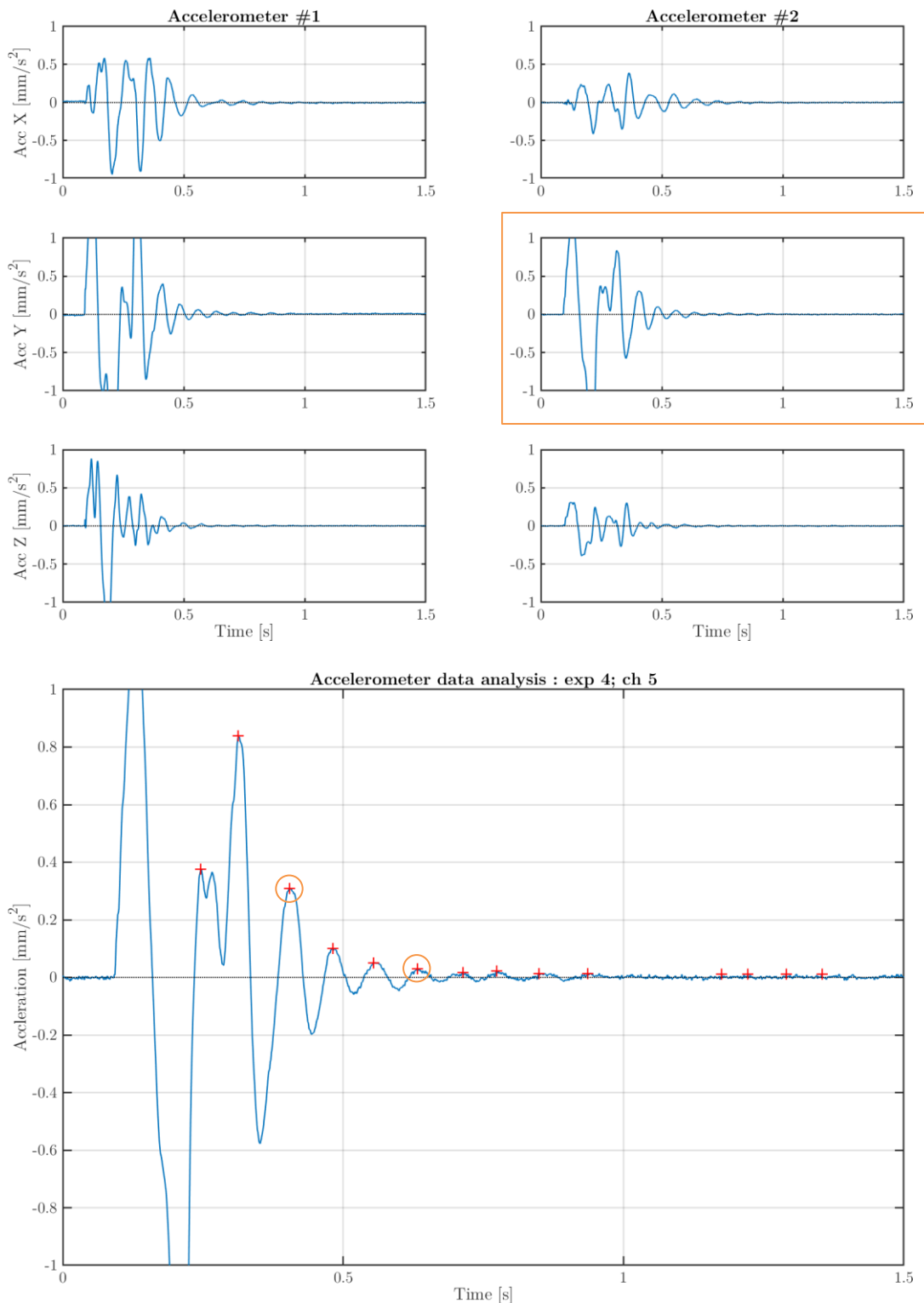Figure 5.16 – Lateral drop test: On top the 6 channels from of the accelerometers signals. On the bottom the signal zoom of the y axis of Accelerometer no.2.

Given the graphs reported from Figure 5.11 to Figure 5.16, and having highlighted with the circles some reference points, some damping-related parameters can be computed:
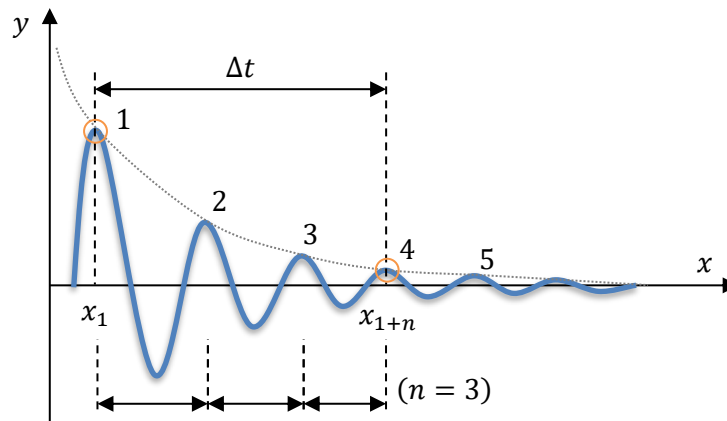
Figure 5.17 – General scheme of a damped signal.

Oscillatory frequency [Hz]

$$\omega = \frac{n}{\Delta t}$$

(5.4)

Logarithmic decrement [–]

$$\delta = \frac{1}{n} \ln\left(\frac{y_1}{y_{1+n}}\right)$$

(5.5)

Damping ratio [–]

$$\zeta = \frac{1}{\sqrt{1 + (2\pi/\delta)^2}}$$

(5.6)

where: n Is the number of periods considered;

$[\, x_1 \;\; x_{1+n}\,]$ Is the considered peaks locations;

$[\, y_1 \;\; y_{1+n}\,]$ Is the considered peaks amplitude;

$\Delta t = x_{1+n} - x_1$ Is the time delay between considered peaks.

Note: the radiant frequency conversion factor is 2π: ω [rad/s] $= 2\pi \cdot \omega$ [Hz].

Table 5.2 reports a summary of the computed quantities for the different tests, performed on the three mattress types.

Mattress	No.1		No.2		No.3	
Technology	Coil springs		Pillow-top		Air core	
Perturbation	Vertical	Lateral	Vertical	Lateral	Vertical	Lateral
Amplitude decay [mm/s^2]	4.66-0.54	0.43-0.01	2.06-0.11	1.45-0.06	4.06-0.06	0.31-0.03
Mean peak delay [s]	0.26	0.10	0.26	0.10	0.24	0.10
Frequency (ω) [Hz]	**3.80**	**10.1**	**3.81**	**10.19**	**4.13**	**13.1**
Logarithmic decrement (δ)	0.43	1.23	0.73	0.54	1.39	0.79
Damping ratio (ζ)	6.82%	19.30%	11.53%	8.55%	21.54%	12.40%

Table 5.2 – Damping tests results.

The ultimate purpose of this effort in estimating mechanical parameters of some mattresses, is to have some **base line values** useful to start a deeper analysis about the interaction provided by the mattress in performing bed measurements and investigating possible modifications in measuring BCG signals.

Conclusions

In this work the closed-loop mathematical model describing the cardiovascular system, taken as a reference from (Guidoboni, et al., 2019), has been extensively analyzed in several parts.

Through this analysis a deeper understanding of the influence on the BCG curve of the different model parts is now possible. A filtering-smoothing issue has been identified, and a sensitivity analysis has been carried out investigating the relation between some parameters and an output value.

Goals achieved:

In summary, the topics developed and treated in this work are:

- The capability of the originally proposed model has been expanded by proposing a **ballistocardiography computation also in the *z* direction**, BCGz.

- A **filtering-smoothing issue** has been raised and a standardizing solution has been proposed, in this way the analyzed model does not lose the possibility to detect oscillatory patterns due to arteries stiffening.

- The **causal effect relation between some model parts** and the BCG output has been assessed by considering different incrementally complex models.

- Concepts from **sensitivity analysis** have been applied to the specific case of the model tested, and reported results have assessed the model sensitivity with respect to some outputs given some inputs.

- **In-lab measurements** on a subject have been obtained experimentally. The idea of the author of taking these measurements without mattress but only with the wooden board of the bed frame has allowed to capture clean signals not disturbed by mattress interactions never obtained before. In addition the introduced 4-phases measurements protocol, in which the tested subject filtered himself from breathing has allowed an easier treatment of the acquired data and more reliable conclusions.

- The innovative **test method** implemented for this thesis has already allowed the **publication of a chapter** on a scientific book published by Springer. See (R. Invernizzi, 2021).

- The results obtained with the closed-loop model have been **compared to in-lab measurements** obtained through the use of load cells positioned under a bed. The remarkable similarity in shape found are a proof of the accuracy and reliability of the theoretical model as well as the **testing procedure**.

- **Mechanical characteristics of some mattresses** have been assessed and the related data could constitute a base for future developments.

Future developments:

Among the further possible developments of this study, the following directions can be identified:

1) Make an **experimental campaign** in order to get <u>several BCG curves measured in different context</u>. In this way several important topics could be further studied, for instance:
   - Develop a **standardized measurement protocol**.
   - Computing a **standardized BCG curve** (including variability between subjects)
   - Perform an **uncertainty analysis on the experimental BCG** curves, assessing the variations between subjects, and even trying to link these variability to some body characteristics of clinical influence.
   - By subdividing the healthy testing subjects from the non-healthy ones, a **validation of the virtual model** in the case of non-healthy cardiovascular condition can be performed.
   - Assessing the real influence of the mattress in measuring the BCG.

2) Perform a more extensive **sensitivity analysis on the virtual reference model**, in order to identify any critical model issues.

3) Precisely **model the mattress** to understand how the signals get modified passing through the mattress. In addition make tests considering several mattress types.

*"Ballistocardiography stands **now** where electrocardiography stood in the first quarter of this century. Sooner or later we shall be using it and we may as well get used to the idea."*

(Franzblau, January 1968)

References

[1] Avanzolini, G., Barbini, P., Cappello, A. & Cevenini, G., 1988. CADCS simulation of the closed-loop cardiovascular system. *International Journal of Bio-Medical Computing,* Volume 22(Issue 1), pp. 39-49.

[2] Bogaard, H. J. & al., e., 2009. The right ventricle under pressure: cellular and molecular mechanisms of right-heart failure in pulmonary hypertension. *Chest,* vol. 135(no. 3), p. pp. 794–804.

[3] Canic, S., Tambaca, J., Guidoboni, G. & Mikelić, A., 2006. Modeling viscoelastic behavior of arterial walls and their interaction with pulsatile blood flow. *SIAM Journal on Applied Mathematics,* vol. 67(no. 1), p. pp. 164–193.

[4] Desoer, C. A. & Kuh, E. S., 2010. *Basic circuit theory.* s.l.:Tata McGraw-Hill Education.

[5] Di Nisio, M. & al., e., 2016. Deep vein thrombosis and pulmonary embolism. *The Lancet,* vol. 388(no. 10063), p. pp. 3060–3073.

[6] Formaggia, L., Quarteroni, A. & Veneziani, A., 2009. *Cardiovascular Mathematics: Modeling and Simulation ofthe Circulatory System.* Italy: Springer–Verlag.

[7] Franzblau, S. A., January 1968. Ballistocardiography in Cardiovascular Research: Physical Aspects of the Circulation in Health and Disease. *JAMA The Journal of the American Medical Association,* Issue 203(2), pp. 157-157.

[8] Guidoboni, G. et al., 2019. Cardiovascular function and ballistocardiogram: a relationship interpreted via mathematical modeling. *IEEE Transactions on Biomedical Engineering.*

[9] Inan, O. T. & al, e., 2015. Ballistocardiography and seismocardiography: a review of recent advances.. *IEEE Journal of Biomedical and Health Informatics,* vol. 19(no. 4), p. pp. 1414–1427.

[10] Jolly, M. & Phillips, J., 2018. Pulmonary embolism: Current role of catheter treatment options and operative thrombectomy. *Surgical Clinics,* vol. 98(no. 2), p. pp. 279–292.

[11] Kim, C. S. et al., 2016. Ballistocardiogram: Mechanism and potential for unobtrusive cardiovascular health monitoring. *Scientific Reports,* Volume vol. 6, p. p. 31297.

[12] Klabunde, R., 2011. *Cardiovascular physiology concepts.* s.l.:Lippincott Williams & Wilkins.

[13] Lifesciences, E., 2014. Normal hemodynamic parameters and laboratory values. *Retrieved on April,* Volume vol. 9.

[14] Maceira, A. M. & al., e., 2006. Normalized left ventricular systolic and diastolic function by steady state free precession cardiovascular magnetic resonance. *Journal of Cardiovascular Magnetic Resonance,* vol. 8(no. 3), p. pp. 417–426.

[15] Maceira, A. M. & al., e., 2006. Reference right ventricular systolic and diastolic function normalized to age, gender and body surface area from steadystate free precession cardiovascular magnetic resonance. *European Heart Journal,* vol. 27(no. 23), p. pp. 2879–2888.

[16] McDonald, D., 1974. *Blood flow in arteries.* London: Edward Arnold.

[17] Noordergraaf, A. & al., e., 1963. The use of an analog computer in a circulation model. *Progress in Cardiovascular Diseases,* vol. 5(no. 5), p. pp. 419–439.

[18] Pinheiro, E. & al, e., 2010. Theory and developments in an unobtrusive cardiovascular system representation: ballistocardiography. *The Open Biomedical Engineering Journal,* Volume vol. 4, p. p. 201.

[19] R. Invernizzi, A. D. G. G. W. H. S. L. T. M. J. P., 2021. Modeling of biological systems: from algebra to calculus and computer simulations. In: *Foundation for Undergraduate Research in Mathematics (FURM).* s.l.:Springer.

[20] Rantz, M. J. & al, e., 2015. A new paradigm of technology-enabled 'vital signs' for early detection of health change for older adults,. *Nursing Outlook,* vol. 63(no. 6), p. pp. 650–655.

[21] Sacco, R., Guidoboni, G. & Mauri, A. G., 2019. *A Comprehensive Physically Based Approach to Modeling in Bioengineering and Life Sciences.* s.l.:Elsevier Science Publishing Co Inc.

[22] Starr, I. & Noordergraaf, A., 1967. *Ballistocardiography in cardiovascular research; physical aspects of the circulation in health and disease.* Amsterdam: North-Holland Pub. Co..

[23] Starr, I. & Wood, F. C., 1961. Twenty-year studies with the ballistocardiograph: the relation between the amplitude of the first record of healthy adults and eventual mortality and morbidity from heart disease. *Circulation,* Volume vol. 23, p. pp. 714–732.

[24] Wiard, R. et al., 2009. Estimation of central aortic forces in the ballistocardiogram under rest and exercise conditions. *Engineering in Medicine and Biology Society. EMBC 2009. Annual International Conference of the IEEE.*, p. pp. 2831–2834.